

ulm university universität
uulm

Studies of AlN grown by MOVPE for Electronic and Optoelectronic Applications

DISSERTATION

to obtain the academic degree of

DOKTOR-INGENIEUR
(DR.-ING.)

from the Faculty of Engineering and Computer Sciences
Ulm University

by

Sarad Bahadur Thapa
from Kathmandu, Nepal

Referees: Prof. Dr. Ferdinand Scholz
Prof. Dr. rer. nat. Albrecht Winnacker

Dean of the faculty: Prof. Dr.-Ing. Michael Weber

Ulm, 15 July 2010

Acknowledgment

The work presented in this thesis has been carried out at the Institute of Optoelectronics and Microelectronics Technology Center of Ulm University during 2005-2009. It has been a very rewarding experience to be a member of the GaN group led by Prof. Dr. Ferdinand Scholz. This thesis would not have possible without the trust, the guidance, the support and the help from many people inside and outside the university.

First of all, I would like to express my sincere gratitude to Prof. Dr. Ferdinand Scholz for giving me the opportunity to do Ph.D. in his group. He has been a truly awesome supervisor, continuously supportive, always providing invaluable advice and vision, while at the same time giving me freedom to explore my own ideas. Also, many thanks to him for the intensive discussions and corrections to this work.

I would like to thank Prof. Dr. rer. nat. Albrecht Winnacker of the chair of Materials for Electronics and Energy Technology at the Department of Materials Science and Engineering in the Friedrich-Alexander University of Erlangen-Nürnberg for giving his valuable time in my Ph.D. examination as a referee.

I am grateful to Dr.-Ing. Christoph Kirchner, a former member of the GaN group, for introducing me to MOVPE system at the Microelectronics Technology Center. I also thank him for carrying out RTA to some of my samples at the laboratory of Mattson Thermal Products GmbH, Dornstadt.

It gave me a great pleasure for sharing an office room with Dr.-Ing. Joachim Hertkorn at the institute in the period of my research work. We had a lot of fruitful discussions on many aspects of academic, professional and private matters. Thanks Joachim for creating such a congenial atmosphere and your well understanding.

I have enjoyed the company of all of my fellow group members Dipl.-Ing. Thomas Wunderer, Dipl.-Phys. Frank Lipski, Dipl.-Phys. Stephan Schwaiger, M.Sc. Mohamed Fikry, M.Sc. Kamran Forghani, Dr.-Ing. Peter Brükner, and Dr.-Ing. Barbara Neubert. I particularly miss our everyday lunch break and the coffee chat. Thank you very much for sharing a wonderful time in all in- and outdoor activities during my stay there. It would be very difficult for me to perform many of the tasks without your scientific and technological cooperation.

I hold to warmly thank Dr. Jürgen Mäahn, Dipl.-Ing. Rainer Blood, Dipl.-Ing. Rudolf Rösch, Dipl.-Chm. Susanne Menzel, and Dipl.-Ing. Dieter Kinzler for their technological supports in the clean room. Similarly, I would like to thank Sükran Kilic and Hildegard Mack for easing the administrative and bureaucratic procedures.

I am highly grateful to Dr.-Ing. Fernando Rinaldi who helped me learning X-ray measurements. I am indebted to Dipl.-Ing. Hendrik Roscher and PD Dr.-Ing. Rainer Michalzik, former advisers of my master thesis work, for their continuous support during my stay at the institute. I would like to thank all the colleagues and the members of the institute for lending their helping hands whenever needed and friendly accompanying on every occasions. I would like to mention especially two research groups from Ulm University for an intense collaboration to carry out this work. Without their contributions, this work would not have been realized. Many thanks go to Dr. Günther M. Prinz, Dipl.-Phys. Robert A. R. Leute, Dr. Martin

Feneberg, and apl Prof. Dr. Klaus Thonke of the Institute of Semiconductor Physics for CL, PL, and Raman investigations and Dipl.-Phys. Oliver Klein, Dr. Johannes Biskupek, Dr. Andrey Chuvilin, Ms. Sabine Grözinger, and Prof. Dr. Ute Kaiser of Transmission Electron Microscopy Group for TEM analysis of our samples.

I would also like to thank Dr. Hong Yin and Prof. Dr. Paul Ziemann of the Institute of Solid State Physics, and M.Sc. Mohammed Alomari and Prof. Dr.-Ing. Erhard Kohn of the Institute of Electron Devices and Circuits for providing us their lab facilities for high temperature electrical measurements. I highly appreciate Mr. Alomari for his endeavor on processing our structures for FETs. I am grateful to Dipl.-Ing. Alexander Minkow of the Institute of Micro and Nanomaterials for SEM measurements.

I would like to thank Dr. Lutz Kirste, T. Fuchs, and M. Grimm of the Fraunhofer Institute for Applied Solid State Physics, M. Trapp, P. Helm, and M. Gericke of RTG Mikroanalyse GmbH, Berlin, and Dr. Christoph Schnuerer-Patschan and Dr. Ulrich Ehrke of Cameca GmbH, Munich for SIMS measurements. A special thanks go to PD Dr. Matthias Bickermann of the Department of Materials Science and Engineering of the Friedrich-Alexander-University of Erlangen-Nürnberg for providing the AlN substrates. I am also grateful to Dietmar Schmitz of AIXTRON GmbH for providing me an opportunity to learn MOVPE technology in the laboratory of AIXTRON at the beginning of my Ph.D. work.

The work of my students Stefan Wabra, Hu Wenjie, Junjun Wang, Lu Xianming, and Evangelos Angelopoulos are highly appreciated.

I highly acknowledge the funding of Deutsche Forschungsgemeinschaft and express deep gratitude to Prof. Dr. Daniel Hofstetter of the Physics Institute of the University of Neuchâtel for partly financially supporting through Sofja Kolajewskaja Program of the Alexander von Humboldt foundation.

I feel a deep sense of gratitude for my parents and grand parents who formed part of my vision and taught me the good things that really matter in life. I am sincerely grateful to my sisters and the rest of our family members who tried to encourage me despite the distance. Their persistent love and support have given me the strength to persevere in reaching my educational goals.

Last, but not least, I would like to thank my wife, Pinky, for all her love and companionship. It would have been very difficult to complete this work without her presence. Being the person closest to me, she had to suffer through ups and downs of Ph.D. studies, but she never stopped bringing my life joy and happiness, which I needed the most. My wife Pinky and two lovely daughters Shreeya and Sneha receive my deepest gratitude and love all the time for their invaluable dedication and sacrifice in every part of my life.

A sad moment at the end was sudden death of my beloved grand father Chandra Bahadur Thapa and father-in-law Shankar Raj Bista with whom I wanted to share all my achievements. I dedicate this work to them.

Contents

1 Introduction **1**
1.1 Motivation . . . 1
1.2 Overview of Thesis work . . . 3

2 Fundamentals of III-Nitrides **5**
2.1 Physical Properties of Group-III Nitride Material System . . . 5
2.1.1 Crystallographic Structure . . . 5
2.1.2 Band Structure . . . 8
2.1.3 Polarization Effects . . . 10
2.2 Substrate Materials . . . 17
2.3 Defects . . . 20
2.4 Growth Techniques . . . 26
2.4.1 Hydride Vapor Phase Epitaxy . . . 26
2.4.2 Physical Vapor Transport . . . 27
2.4.3 Liquid Phase Epitaxy . . . 27
2.4.4 Pulsed Laser Deposition . . . 27
2.4.5 Molecular Beam Epitaxy . . . 28
2.4.6 Metal Organic Vapor Phase Epitaxy . . . 29
2.5 Characterization Methods . . . 30

3 Metal Organic Vapor Phase Epitaxy **34**
3.1 Basic Principle of MOVPE . . . 34
3.2 Precursors and Chemistry of Epitaxial Growth of AlN . . . 37
3.2.1 Precursors . . . 37
3.2.2 Chemistry of Epitaxial Growth of AlN . . . 39
3.3 MOVPE-System AIXTRON AIX 200 RF . . . 41
3.4 *In-Situ* Characterization in MOVPE . . . 44

4 MOVPE Growth of AlN **47**
4.1 Introduction . . . 47
4.2 Two-step Growth Process on Sapphire . . . 48
4.2.1 Desorption and nitridation of sapphire . . . 48
4.2.2 Medium-temperature nucleation layer . . . 50
4.2.3 Stage between Nucleation and Epitaxial Layers . . . 57
4.2.4 High Temperature Epitaxial Layer . . . 59

4.3 Structural and Spectroscopic Properties of AlN 72
4.4 Multi-step growth on sapphire 83
4.5 Using Indium as Surfactant 88
4.6 *In-situ* deposited SiN_x as defect-reducing interlayer 90
4.7 AlN on Different Substrates 93
4.7.1 Growth on SiC 93
4.7.2 Growth on native AlN substrate 96

5 Si Doping of AlN **99**
5.1 Introduction 99
5.2 Experimental 101
5.3 Effects on structural properties 102
5.4 Effects on spectroscopic properties 107
5.4.1 Influence on near-band-edge luminescence 108
5.4.2 Influence on violet band luminescence 111
5.5 Electrical Properties 112

6 MOVPE Growth of High Al Content AlGaN **117**
6.1 Introduction 117
6.2 Experimental 118
6.3 Al Composition in AlGaN 119
6.4 Structural and Spectroscopic Properties 123

7 Heterostructures for Potential Devices based on AlN **127**
7.1 Heterostructures for Electronic Devices 127
7.2 Heterostructures for Optoelectronic Devices 132

8 Summary and Conclusions **135**

Chapter 1

Introduction

This thesis deals with studies of the growth of undoped and silicon (Si)-doped aluminum nitride (AlN) epilayers using metal organic vapor phase epitaxy (MOVPE) technology, and their characterizations. To exploit the possibilities of using AlN in device structures, further studies on the growth and characterizations of high aluminum (Al) content aluminum gallium nitride (AlGaN) epitaxial layers and some AlN-based heterostructures are also carried out.

1.1 Motivation

In the last fifteen years, there has been a tremendous progress in the research and development of direct band-gap group-III nitride based semiconductor materials and devices, both in the area of optoelectronics and electronics. The group-III nitride family has the ability to tune the band-gap from 0.7 eV for indium nitride (InN) to 6.2 eV for AlN. They form a complete series of ternary alloys which spans the whole visible spectrum and extends well into the infrared (1.7 μm) and deep-ultraviolet (DUV) region (200 nm). This inherent property has made possible the fabrication of high-performance blue laser diodes (LDs) [1] and light-emitting diodes (LEDs) operating in the UV through green spectral range [2–5]. On the other hand, the strikingly large electronic polarization fields (in the order of MV/cm) in this material system affect the electronic properties (band diagrams, charge distributions) of layered structures in many ways [6]. The polarization induced electric field forms a two-dimensional electron gas (2DEG) at the hetero-interface of the layered structure based on this material system [7]. This property has been exploited for the fabrication of transistors with high output power-density operating at high frequencies [8, 9], although the polarization has deleterious effect on the performance of optoelectronic devices. Among the group-III nitrides, gallium nitride (GaN) has been extensively studied in the last two decades, especially after the invention of some groundbreaking technologies like employment of a low temperature nucleation layer during its epitaxial growth on sapphire substrate [10] and a successful p-type doping using magnesium [11]. Many devices based on GaN are already on the market since a decade. However, the demand of novel optoelectronic devices operating at shorter wavelength and electronic devices operating at

higher temperature and higher voltage/power is steadily growing for many scientific and technological applications. The challenge is now to open up new materials that enable the realization of a new generation of devices.

In recent years, AlN has attracted much attention because of its extremely outstanding chemical and thermal stability under hostile environment. AlN derives its technological importance from providing the large band-gap binary component of the $Al_xGa_{1-x}N$ ternary alloys exceeding even silicon carbide (SiC) and diamond. Thus, it is regarded as a promising candidate for novel optoelectronic and ultra-fast robust electronic devices. Due to its inherent superior electronic and mechanical properties, the realization of high-quality AlN epitaxial layers can widely extend the application field of group-III nitride materials. However, the epitaxial growth of AlN having excellent crystalline quality, smooth surface morphology, and good spectroscopic properties - as required for such device fabrication - is still a big challenge despite the stupendous advancement made in the epitaxial growth technologies, both in the process and the system. Thus, the full potential of this material has been limited by the material quality. One major problem during the epitaxial growth of AlN and high Al content $Al_xGa_{1-x}N$ is the parasitic gas-phase pre-reactions between ammonia (NH_3) and the metalorganic aluminum source TMAl (trimethylaluminum). Thus, the issue of pre-reactions should be effectively addressed. For these materials, native lattice matching substrates are not yet commercially available and therefore sapphire substrates have been widely used. However, the crystalline quality of the layer structures is adversely affected by a large lattice mismatch between substrate and nitride layer. The present insufficient quality of AlN is attributed to a high density of crystal defects, mainly threading dislocations above $10^{10}\,cm^{-3}$ that originate from the substrate. A significant reduction of dislocation density is mandatory to employ this material meritoriously into device structures. Meantime, it is quite difficult to achieve a growth mode for epitaxial and smooth AlN layers since the surface diffusion of the growth contributing species is low. Hence, the growth parameters and the process should be prudently optimized. While the process optimization is very reactor dependent, it is still imperative to identify some of the typical growth-related characteristics, e.g. growth rate, crystal mosaicity, etc. of MOVPE grown AlN epilayers that appear to be controlling the crystal quality of the epilayer.

In this work, we assess the influences of the various growth parameters and processes on the structural and spectroscopic properties of AlN. Afterward, we will determine optimum growth parameters and develop a growth process in our AIXTRON AIX200RF reactor which can be a good reference for the growth of AlN epilayers in other MOVPE reactors, too.

For device applications, not only the epitaxial quality but also the efficacious intentional doping is necessary. The achievement of sufficient electrical conductivity and the control of carrier concentrations in AlN epilayers are the critical issues still remaining to be addressed. Till today, only limited reports have been published describing the properties of intentionally doped pure AlN and high Al content $Al_xGa_{1-x}N$ ternary alloys [12–14] compared to GaN or indium gallium nitride (InGaN), due primarily to the difficulties on the epitaxial growth of high quality layers of this material. Especially the effective and efficient doping of such materials to obtain the required electrical conductivity for practical AlN based devices remains a key issue for the nitride researchers.

The intention of this work is to analyze the effects of n-type doping on the structural, spectroscopic and electrical properties of AlN and understand the limitations of doping mechanism and control.

Additionally, AlN can be employed not only in the active layer of the device structure but also in a buffer layer in $Al_xGa_{1-x}N$ based DUV structures because of its transparency to the operating wavelength and in electronic applications due to its intrinsic high resistivity and thermal conductivity characteristics. Other major fields of application are its use as a material for surface acoustic wave (SAW) applications [15] due to its high sound velocity and for film bulk acoustic resonators (FBIR) [16] in radio frequency (RF) filters due to its piezoelectric properties. Furthermore, thin AlN/GaN superlattices can be attractive structures to be used in optical devices operating at telecommunication wavelengths by exploiting intersubband transitions between bound quantum well states [17, 18].

1.2 Overview of Thesis work

In order to benefit from the excellent properties of AlN materials and realize the above mentioned applications, growth of high quality epitaxial layers with necessary electrical conductivity is indispensable. This thesis is basically divided into three parts, namely, discussion on fundamental material properties and MOVPE technology in the perspective of the growth of AlN, growth and characterizations of doped and undoped AlN, and finally a discussion on the high Al content AlGaN and heterostructures for potential AlN based optoelectronic and electronic devices.

In chapter 2, first we present some important characteristics of group III-nitrides mainly focusing on AlN. Next we discuss critical issues of structural and native defects. Then, various commonly used techniques for the growth of AlN crystals are shortly described followed by a brief introduction of the material characterization techniques employed in this work.

Chapter 3 presents the basic principle of the MOVPE technique along with a brief introduction to commonly used precursors and a review of growth chemistry. Additionally, we introduce our MOVPE system and present some modifications done in the conventional susceptor body design for AlN growth. A brief introduction to the *in situ* characterization technique is also given at the end of the chapter.

In this study, AlN epilayers are deposited on sapphire substrates. Optimization of the growth parameters of AlN epilayers was carried out in several growth steps. A lot of ambiguities are prevailing in the relation between basic epitaxial parameters, the respective growth kinetics and resulting crystal quality of AlN layers. In chapter 4, we report the effects of the variation of basic growth parameters in low-pressure MOVPE on the surface morphology, crystal quality, growth rate and consequently on the luminescence spectra of the AlN layers. A study on the reduction of threading dislocations and cracking of the epilayers is also presented. Finally, we report the results of AlN deposited on SiC and native AlN substrates.

In contrast to unintentionally doped GaN and InN, AlN layers are typically highly resistive. A number of theoretical studies predicted that it is essentially impossible

to overcome the insulating properties of AlN. Chapter 5 deals with the Si-doping of AlN for n-type conductivity. Here, we present the influence of Si concentration on structural, spectroscopic, and electrical properties of AlN. Finally, we report the measured conductivity of n-type doped AlN layers.

In this study, high Al content ($\geq 50\%$) AlGaN layers are grown under similar growth conditions as optimized AlN epilayers. Chapter 6 is dealing with the characterization results of these layers.

In chapter 7, we present heterostructures of AlN with $Al_xGa_{1-x}N$ and GaN in the context of potential AlN based electronic and optoelectronic devices. Band-gap simulations and experimental results of some heterostructures are also presented.

Finally, chapter 8 offers a comprehensive summary of our work and an outlook for the related future research.

The work of the author consisted of the growth and characterizations (atomic force microscopy, high resolution X-ray diffraction, scanning electron microscopy, and electrical measurement) of the material and the structures. The cathodoluminescence characterizations were carried out by Dr. Günther M. Prinz and Dipl.-Phys. Robert A.R. Leute of the Institute of Semiconductor Physics. High resolution transmission electron microscopy was performed by Dr. Johannes Biskupeck and Dipl.-Phys. Oliver Klein of the Transmission Electron Microscopy Group of Ulm University.

Chapter 2

Fundamentals of III-Nitrides

It is necessary to understand fundamental properties, e.g. the crystallographic and the electronic band structures, of a material system of interest before beginning a study of its growth and in-depth investigations. This introductory chapter provides a short review of some fundamentals of group-III nitride materials particularly with a focus on AlN followed by a short discussion on the substrates that are commonly used for the heteroepitaxial growth. Certain problems concerning the inherent defects of this material system and the evolution of structural defects during the growth are briefly discussed. A short introduction to some of the commonly employed crystal growth techniques for the growth of AlN is given. Finally, a section is dedicated to the various characterization methods used for evaluating the materials and the structures.

2.1 Physical Properties of Group-III Nitride Material System

Aluminum (Al), gallium (Ga) and indium (In), the group-III elements from the periodic table together with nitrogen (N), the group V element, form a III-V $(Al_xGa_{1-x})_yIn_{1-y}N$ compound semiconductor material system that consists of InN, GaN andAlN, and their ternary and quaternary alloys. This material system has a wide band-gap energy range from 0.7 eV for InN to 6.1 eV for AlN as shown in Fig. 2.1

Because of such wide band-gaps the group III-nitrides have increasing importance in the development of infrared to ultraviolet light emitters and high-temperature high-frequency transistors. The crystallographic and electronic band structures, and the polarization characteristics are explained below.

2.1.1 Crystallographic Structure

The group-III nitrides can crystallize in three structures, namely, the wurtzite (WZ), zinc blende (ZB), and rock salt. There are only a few reports on the successful growth of the ZB structure of AlN [19, 20], GaN [21, 22], and InN [23, 24] by epitaxial methods. The growth of rock salt structure is possible only under a high pressure. Among these structures, the WZ is the only thermodynamically stable structure under

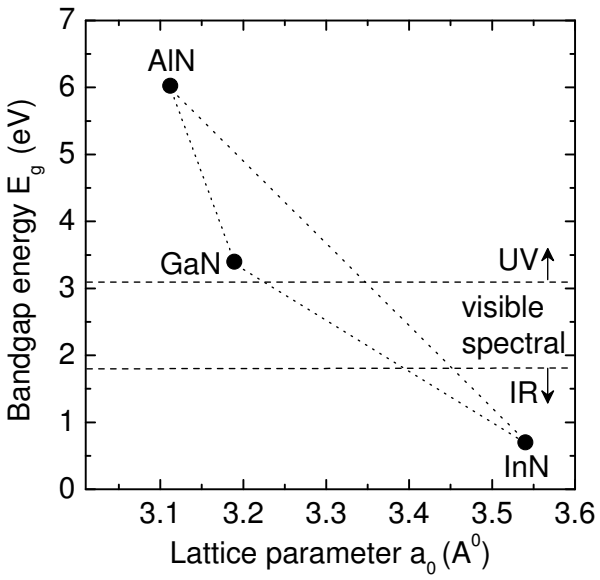

Figure 2.1: Band gap energy vs. lattice constant for binary group-III nitride material system.

ambient conditions. In this work, the WZ structure of AlN and its alloys with GaN are investigated.

The WZ structure is a hexagonal close-packed (hcp) lattice, comprising vertically oriented III-V units at the lattice sites. In this structure, each atom forms four bonds with tetragonal symmetry. It has a hexagonal unit cell and thus is represented by two lattice parameters, c and a, and the internal parameter u. The lattice constant c defines the spacing of two identical hexagonal lattice planes, and the lattice parameter a describes the distance of atoms in the hexagonal lattice plane. The cell internal parameter u is defined as the anion-cation bond length (also the nearest neighbor distance) divided by the c-lattice constant and provides information of the distortion of the unit cell. In an ideal WZ structure, the values of the tetragonal ratio and the cell internal parameter are $c/a = \sqrt{8/3} = 1.633$ and $u = 3/8 = 0.375$, respectively [25]. The space grouping for the WZ structure is $P6_3mc$ in the Hermann-Maugin notation. The group-III nitrides have partially covalent and partially ionic bonds. Because of the $1s^2 2s^2 2p^3$ electronic configuration of the N atom (the smallest and the most electronegative group-V element) or rather the lack of electrons occupying the outer orbitals, the electrons involved in the metal nitrogen covalent bond are strongly attracted by the Coulomb potential of the N atomic nucleus. This means that this covalent bond will have stronger ionicity due to the large difference in the electronegativities compared to other III-V covalent bonds, which means very high bonding energies (AlN = 11.5, GaN = 8.9, and InN = 7.7 $\frac{\text{eV}}{\text{atm}}$) [26] .

The structure of a hexagonal WZ unit cell of AlN is sketched in Fig. 2.2, where the sub lattices of Al and N atoms, shown in different colors, are tetrahedrally bonded to the nearest neighbors. This structure consists of a stacking sequence of alternating bi-atomic close-packed (0001) planes of Al and N pairs (marked by A and B) along

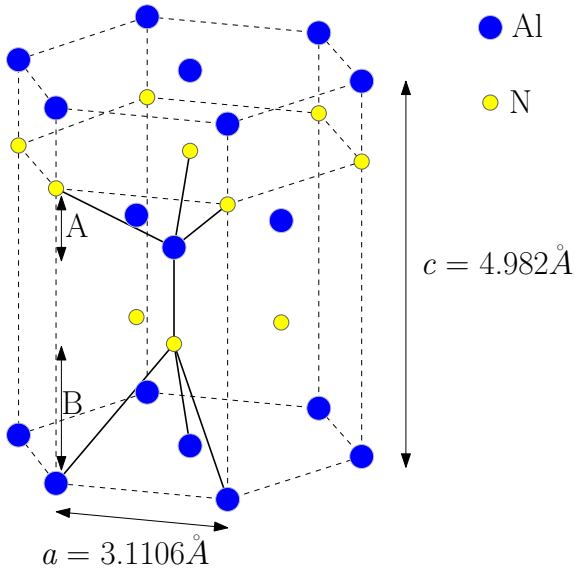

Figure 2.2: Illustration showing the wurtzite structure of AlN.

the c-axis. The presence of such bilayers A and B results in an internal asymmetry along the c-axis. This means that the direction of the atomic bonds are different along the [0001] and [000$\bar{1}$] directions. This results in an internal polarity of the film, and is defined by the direction of the group-III-N bond between the bilayers (along the c-axis) with respect to the surface normal of the film. If in this bond the nitrogen atoms are placed on top of the group-III atoms the film is called Al- or [0001]-polar (face) and if the group-III atoms are on top of N atoms the film is called N- or [000$\bar{1}$]-polar (face). The polarity of the films has a major effect on both the surface properties and on the piezoelectric field of the group-III nitrides. The effect of polarity has been widely investigated both theoretically and experimentally in [27,28]. Group-III nitrides grown on (0001) sapphire by MOVPE are typically group-III-polar [28].

The lattice parameters of nominally unstrained AlN are a = 3.1106 Å and c = 4.982Å, repectively [29]. Unlike GaN, AlN deviates significantly from the aforementioned ideal parameters: c/a = 1.601 and u = 0.379 due to the strong presence of ionic bonds [30]. This may be one of the reasons for the difficulties of AlN doping. GaN and InN have smaller ionicity than AlN [31]. Semiconductors with a large covalent component can form hydrogen-like shallow levels in the bandgap by substitution of a host atom with a donor or acceptor with one more or less electron, respectively. Therefore, GaN can be easily doped n- and p-type compared to AlN. We will extensively discuss the n-type doping of AlN in chapter 5. Inhomogeneities, strain, partial relaxation of strain, and high concentration of structural defects may distort the lattice constants from their intrinsic values and cause a wide dispersion among the reported values. The other binaries GaN, InN, and their ternaries and quaternaries have similar crystalline structure, in which group-III atoms occupy the sublattice shown with Al atoms in Fig. 2.2. Table 2.1 lists the theoretically calculated (for ideal crystal) as well as experimentally determined structural parameters discussed above, inclusive of the lattice parameters

Table 2.1: Theoretically (theo.) calculated and experimentally determined (expt.) structural parameters for AlN, GaN, and InN [29,32].

Parameters	AlN	GaN	InN
a (theo.) (Å) [32]	3.110	3.199	3.585
c/a (theo.) [32]	1.633	1.633	1.633
u (theo.) [32]	0.375	0.375	0.375
u (expt.) [32]	0.382	0.377	0.379
a (expt.) (Å) [29]	3.112	3.1896	3.548
c (expt.) (Å) [29]	4.982	5.185	5.705
c/a (expt.) (Å) [29]	1.60	1.626	1.608

for AlN, GaN, and InN [29,32].

2.1.2 Band Structure

The electrical and optical properties of semiconductors are mainly determined by the electronic band structure near the Γ point. Therefore, information regarding the electronic band structure of AlN is fundamentally important for the understanding of the basic properties of AlN and its device applications. In the group-III nitrides, all the binary materials and their alloys are wide direct bandgap semiconductors except zinc blende AlN. Among these, AlN has the widest direct bandgap of about 6.1 eV (at the Γ point) at low temperature (10 K) in the WZ structure [30,33,34] (see Fig. 2.3) and indirect (Γ to X) in the ZB structure [35] at the first Brillouin zone of the respective crystal structures. There has been a plethora of reports on theoretical studies of electronic band structure of AlN [34,36–39]. However, due to the lack of reliable experimental data, many details of these studies still need to be improved to provide an accurate band description. Approaches such as $\mathbf{k}\cdot\mathbf{p}$ model calculations including strain have been employed to calculate the band structure of WZ group-III nitrides. Fritsch *et al.* [34] calculated the electronic band structure of group-III nitrides within the empirical pseudopotential approach using ionic model potentials and the static dielectric screening function.

Li *et al.* [30] provided a coherent picture for the band structure parameters of wurtzite AlN near the Γ point from photoluminescence (PL) spectroscopy measurements and first-principle calculations. Under the influence of the crystal field and spin-orbit interactions, the Γ point valance band splits into three levels. Figure 2.4 shows the valence bands for AlN in increasing order of the transition energies: $\Gamma_{7vbm}(A)$, $\Gamma_{9v}(B)$, $\Gamma_{7v}(C)$, whereas for GaN the order is different: $\Gamma_{9vbm}(A)$, $\Gamma_{7v}(B)$, $\Gamma_{7v}(C)$ [40]. The main difference in the valance band structure of these two binaries is the differing order of A, B, and C bands. The band split between A and B is attributed to spin-orbit whereas the split of C is attributed to crystal field. The $\Gamma_{7vbm}(A)$ band on top of the $\Gamma_{9v}(B)$ band implicates a negative crystal field splitting of AlN which is larger than -200 meV. Such

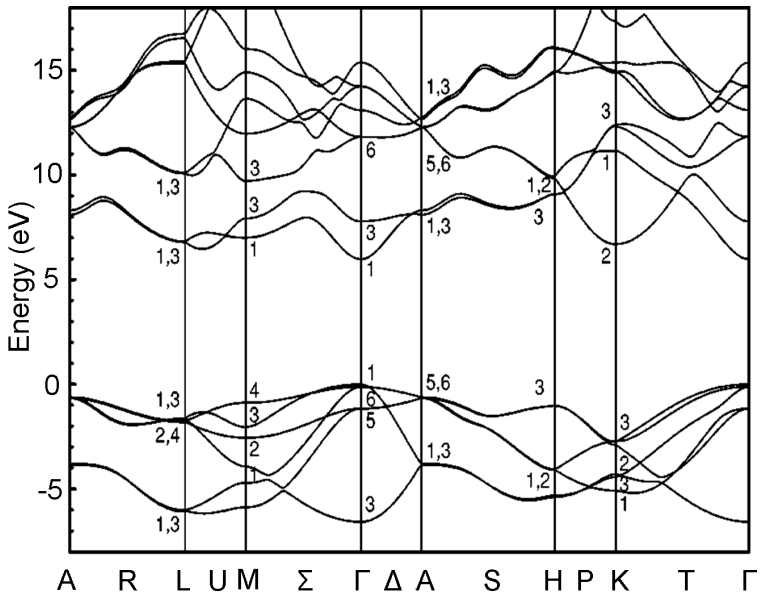

Figure 2.3: Calculated band structure of wurtzite AlN along high-symmetry lines in the Brillouin zone [34].

a negative crystal field splitting can be attributed to a much smaller *c/a* and larger *u* of AlN. The recombination between the conduction band Γ_{7c} electrons and the holes in the top most valence state $\Gamma_{7vbm}(A)$ is almost prohibited for the electric field component of the light *E* perpendicular to the *c*-axis of AlN epilayer $E \perp c$ (α polarization) whereas the recombination between the Γ_{7c} electrons and holes in the $\Gamma_{9v}(B)$ and $\Gamma_{7v}(C)$ are almost forbidden for $E \parallel c$. This is in sharp contrast to GaN in which the recombination between the Γ_{7c} electrons and the holes in the top most valence band $\Gamma_{9vbm}(A)$ is almost prohibited for $E \parallel c$. In many optical measurements such as absorption, transmission, and reflectance, the excitation light is polarized perpendicular to the *c*-axis $E \perp c$. This is why a larger bandgap of about 6.2 eV (at 5 K) for wurtzite AlN was reported earlier by Yim *et al.* [41] and Perry and Rutz *et al.* [42] as they measured the transition between the Γ_{7c} electrons and holes in the $\Gamma_{9v}(B)$ and $\Gamma_{7v}(C)$. This is in contrast to the case for GaN epilayers, in which the emission to the top most valence band is allowed for α polarization yielding generally the same band gap value in GaN for different optical measurements. Later on, Tang *et al.* [43] and Li *et al.* [30] estimated the bandgap of wurtzite AlN below 6.2 eV at low temperature cathodoluminescence (CL) and photoluminescence (PL) measurements, respectively. In the investigation of AlN epilayers, we obtained a free exciton at about 6.025 eV at low temperature (10 K) cathodoluminescence (CL) spectra which also indicates the bandgap of wurtzite AlN below 6.2 eV at 10 K. A detailed study of such spectra will be presented in chapter 4. However, despite the extensive research on the group-III nitride materials, until now many of the key band parameters of AlN have not yet been conclusively determined.

When the Al content is decreased from 1 to 0 in $Al_xGa_{1-x}N$ alloys, crystal-field splitting increases from -219 to 38 meV [30, 44] and the split-off $\Gamma_{9v}(B)$ band moves

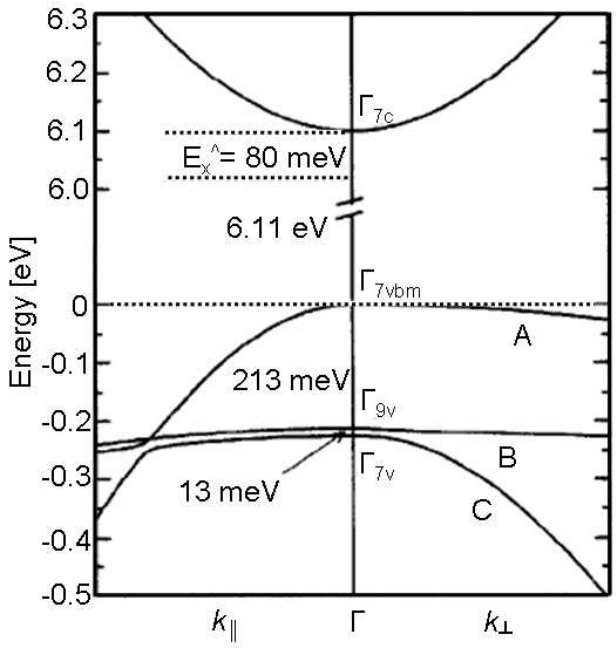

Figure 2.4: Calculated band structure of wurtzite AlN near the Γ point. At k=0, the top of the valence band is split by crystal field and spin orbit coupling into the $\Gamma_{7vbm}(A)$, $\Gamma_{9v}(B)$, $\Gamma_{7v}(C)$ states. The sign $\perp$ ($\|$) denotes the direction perpendicular (parallel) to the c axis of the AlN epilayer. The A band exciton binding energy is denoted as $E(X_A)$ = 80 meV [30]

up to be the top most valance band. It is reported to be zero when the Al content is approximately 73%...78% [45]. The dependence of the $Al_xGa_{1-x}N$ bandgap energy on the alloy composition can be described by a linear dependence on the Al mole fraction x and a nonlinear correction with a magnitude given by the bowing parameter b (0.8 to 1.0 eV) to yield:

$$E_g = xE_g{}^{AlN} + (1-x)E_g{}^{GaN} - bx(1-x), \tag{2.1}$$

where $E_g{}^{AlN}$ and $E_g{}^{GaN}$ are the bandgap of AlN and GaN, respectively. In chapter 6, we will present the structural quality of the $Al_xGa_{1-x}N$ ($0.5 \leq x \leq 1$) layers and estimate the Al compositions. However, a major factor complicating the interpretation of the experimental data is residual strain (see chapter 6.3).

2.1.3 Polarization Effects

As mentioned above, the group-III nitrides exhibit very strong polarization effects, comprising both intrinsic spontaneous polarization and strain-induced piezoelectric polarization.

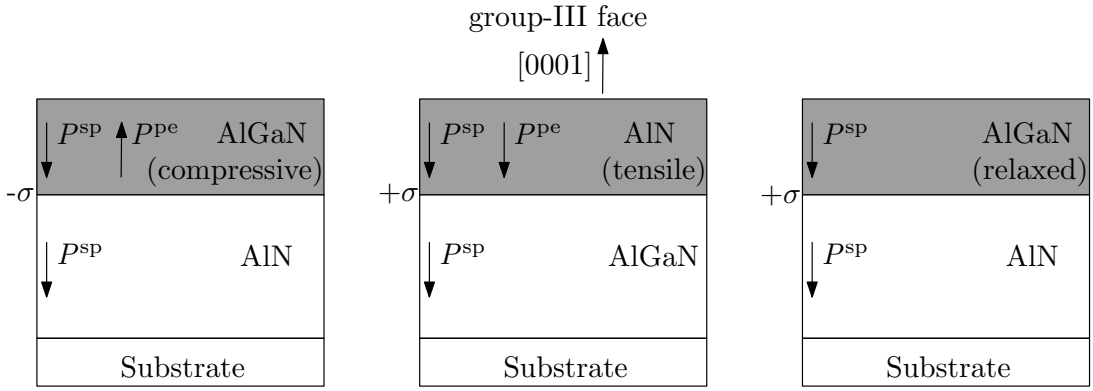

Figure 2.5: Schematic representation of polarization induced sheet charge density σ and directions of the spontaneous P^{sp} and piezoelectric P^{pe} polarization in Al-face strained and unstrained AlGaN/AlN and AlGaN/AlN heterostructures. If the charge density σ is positive, a 2DEG can be confined in the layer with the smaller bandgap close to the interface whereas a 2DHG can be confined if σ is negative.

Spontaneous polarization

The WZ structure of group-III nitrides lacks center of inversion symmetry along the [0001]-axis, the typical growth direction of choice for nitride epitaxy. Absence of this inversion symmetry, in addition to the strong ionicity of the metal-nitrogen bond, results in a strong electrostatic field. Since this field is built in the equilibrium lattice of the III-nitrides at zero strain, it is called spontaneous polarization, which is, in other words, caused by the deviation of the unit cell from the ideal hexagonal structure. Due to the crystal symmetry, the polarization is aligned along the [0001] direction with the positive direction pointing parallel to the [0001]-axis. The spontaneous polarization for GaN and AlN is negative [6], meaning that for Al or Ga-face layers, the spontaneous polarization is pointing towards the $[000\bar{1}]$-axis (see the direction of the polarization in each layers in Fig. 2.5). Because of the sensitive dependence of the spontaneous polarization on the structural parameters, there are some quantitative differences in the polarization for GaN and AlN. The non-ideality of the crystal structure going from GaN to AlN [u (expt.) being the anion-cation bond length along the [0001]-axis (Tab. 2.1)] corresponds to an increase in spontaneous polarization [7].

The spontaneous polarization parameters calculated for the binary group-III nitrides are given in Tab. 2.2. Assuming the linear interpolation, it can be expressed for $Al_xGa_{1-x}N$ alloys as

$$P^{sp}_{Al_xGa_{1-x}N} = xP^{sp}_{AlN} + (1-x)P^{sp}_{GaN}. \tag{2.2}$$

However, in reality, there are considerable effects of internal structural and bond alteration, volume deformation, and disorder on the bowing of spontaneous polarization. In this vain, any nonlinearity in the spontaneous polarization can be treated by using a bowing parameter $b_{Al_xGa_{1-x}N}$ ($0.0191\,Cm^{-2}$ [46, 47]) as commonly employed in

interpolating the bandgap of an alloy as given below

$$P^{sp}_{Al_xGa_{1-x}N} = xP^{sp}_{AlN} + (1-x)P^{sp}_{GaN} - b_{Al_xGa_{1-x}N}x(1-x). \tag{2.3}$$

The nonvanishing spontaneous polarization is noteworthy, particularly when heterointerfaces between two nitride layers with varying electronegativity are involved. In such heterostructure, polarization charge arises due to the difference between the spontaneous polarization of the two layers. This manifests itself as a polarization charge at heterointerfaces (see Fig. 2.5). The induced charge is a charge separation. It has both negative and positive parts.

Piezoelectric polarization

The existence of a polarization field in group-III nitrides implies the presence of internal electrical fields. In WZ nitrides, the preferred growth direction is the polar [0001] axis, so that any non-accomodated in-plane mismatch automatically generates piezoelectric effects along the growth axis. If pseudomophic growth occurs, the layer will be strained and therefore subjected to a piezoelectric polarization P^{pe}. It is related to the strain ϵ_{ij} through the piezoelectric constant e_{ij} as [6]

$$P^{pe} = e_{33}\epsilon_{33} + e_{31}(\epsilon_{11} + \epsilon_{22}). \tag{2.4}$$

The wurtzite symmetry reduces the number of independent components of the piezoelectric constant e_{ij} to two, namely, e_{33}, and e_{31} considering the polarization induced by a shear strain is not applicable for the epitaxially grown layer. For isotropic basal plane, the in-plane biaxial strain $\epsilon_{\parallel}$ is equal to ϵ_{11} and ϵ_{22} and given by

$$\epsilon_{\parallel} = \epsilon_{11} = \epsilon_{22} = \frac{a - a_0}{a_0}, \tag{2.5}$$

where a_0, and a represent the in-plane lattice constant for the relaxed (equilibrium), and the strained epitaxial layer of interest, respectively. Similarly, the expression for the out-of-plane strain $\epsilon_{\perp}$ is equal to ϵ_{33} and given by

$$\epsilon_{\perp} = \epsilon_{33} = \frac{c - c_0}{c_0}, \tag{2.6}$$

where c_0, and c represent the out-of-plane lattice constant for the relaxed (equilibrium), and the strained epitaxial layer of interest, respectively.

In hexagonal symmetry, out-of-plane strain can be expressed in terms of the in-plane (basal plane) strain through the use of Poisson's ratio ν as

$$\epsilon_{\perp} = -2\frac{C_{13}}{C_{33}}\epsilon_{\parallel} = -2\frac{\nu}{1-\nu}\epsilon_{\parallel}, \tag{2.7}$$

where C_{13} and C_{33} are elastic constants [48, 49]. Using Eqs. 2.4 and 2.7, the amount of the piezoelectric polarization P^{pe} in the direction of the [0001]-axis can be determined by

$$P^{pe} = 2\epsilon_{\parallel}(e_{31} - e_{33}\frac{\nu}{1-\nu}). \tag{2.8}$$

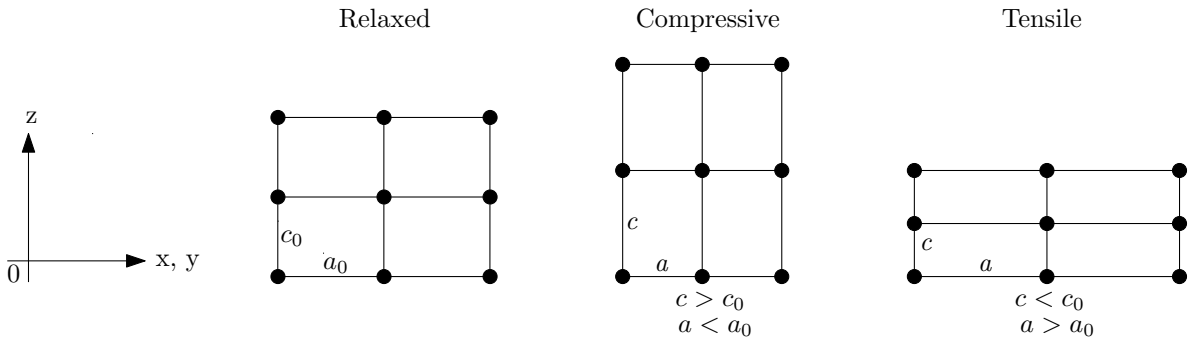

Figure 2.6: Schematic representation of a and c lattice constants of a crystal lattice under compressive (middle) and tensile strain (right).

Since $(e_{31} - e_{33}\frac{\nu}{1-\nu}) \leq 0$ for AlGaN over the whole range of compositions, the piezoelectric polarization is negative for tensilely and positive for compressively strained layers, respectively. Figure 2.6 shows a two dimensional schematic representation of relaxed, compressive, and tensile strain states of a crystal lattice where a_0 and c_0 are lattice constants of the underneath layer. The biaxial strain in the layer is due to the existence of a strong correlation between the c/a and the cell internal parameter u so that when c/a decreases, the u parameter increases in a manner to keep the four tetrahedral distances (bond distances) nearly constant through a distortion of tetrahedral angles (bond angles) [25].

Moreover, in the case of $Al_xGa_{1-x}N$ alloys, the piezoelectric polarization can be estimated using linear interpolation of Vegards law as [50]

$$P^{\text{pe}}_{\text{AlGaN}} = [x\overleftrightarrow{e}\text{AlN} + (1-x)\overleftrightarrow{e}\text{GaN}]\overrightarrow{\epsilon}(x). \tag{2.9}$$

where $\overleftrightarrow{e}$ and $\overrightarrow{\epsilon}(x)$ are the strain and the piezoelectric constants tensors. This expression contains terms linear as well as quadratic in x. This piezoelectric term is only present in pseudomorphic strained growth, and will typically tend to zero beyond the critical thickness at which strain relaxation sets in. However, the piezoelectricity in the nitride alloys is nonlinear. Contrary to spontaneous polarization, this nonlinearity hardly depends on the microscopic structure of the alloy. Bernardini and Fiorentini [51] put forward such argument by calculating piezoelectric polarization as a nonlinear function of the basal strain for all the binaries. Importantly, they concluded that Vegard's law still holds in calculating the piezoelectric polarization of group-III nitride alloys, provided that the nonlinearity of the bulk piezoelectric of the constituents is accounted for. The nonlinear piezoelectricity P^{pe} (in Cm^{-2}) of AlN and GaN can be described by the relations [32]

$$P^{\text{pe}}_{\text{AlN}} = -1.808\epsilon + 5.62\epsilon^2 \text{ for } \epsilon < 0, \tag{2.10}$$

$$P^{\text{pe}}_{\text{AlN}} = -1.808\epsilon - 7.888\epsilon^2 \text{ for } \epsilon > 0, \tag{2.11}$$

Table 2.2: Piezoelectric, dielectric, elastic constants, and spontaneous polarization of AlN, GaN, and InN [7,52].

Parameters	AlN	GaN	InN
e_{33} (C/m^2) [52]	1.46	0.73	0.97
e_{31} (C/m^2) [52]	-0.6	-0.49	-0.57
ϵ_{33} [52]	10.7	10.4	14.6
ϵ_{11} [52]	9	9.5	-
P^{sp} (C/m^2) [52]	-0.081	-0.029	-0.032
C_{13} (expt.) [7]	120	70	121
C_{33} (expt.) [7]	395	370	182

$$P^{pe}_{GaN} = -0.918\epsilon + 9.541\epsilon^2. \tag{2.12}$$

The calculation of the piezoelectric polarization of the $Al_xGa_{1-x}N$ alloys for any level of strain would proceed with first calculating the strain $\epsilon = \epsilon(x)$ for a given x using Vegard's law and the piezoelectric polarization by

$$P^{pe}_{Al_xGa_{1-x}N} = xP^{pe}_{AlN} + (1-x)P^{pe}_{GaN}, \tag{2.13}$$

where P^{pe}_{AlN} and P^{pe}_{GaN} are the end binary strain dependent piezoelectric polarizations for a given strain, $\epsilon(x)$. The piezoelectric, dielectric, and elastic constants of binaries of the group-III nitrides are tabulated in Tab. 2.2.

Piezoelectric coefficients in nitrides are almost an order of magnitude larger than in many of the traditional group-III-V semiconductors [6].

Besides the lattice mismatch induced strain, the thermally-induced strain also plays a profound role in the piezoelectric polarization. The thermally-induced strain is caused by differences in the thermal expansion coefficients of the nonnative substrate and the epitaxial layer when cooling down from the elevated growth temperature. The thermal expansion coefficients (α_{th}) of the group-III nitride binaries and some of the common substrates at room temperature (300 K) are listed in Tab. 2.3 [1]. However, α_{th} is a temperature dependent parameter.

The thermally-induced strain ϵ_{th} can be determined from the following expression:

$$\epsilon_{th} = \Delta T \Delta\alpha_{th} = (T_{gth} - T_{rt})(\alpha_{th,epi} - \alpha_{th,subst}), \tag{2.14}$$

where ΔT is the difference between growth T_{gth} and room temperature T_{rt} and $\Delta\alpha_{th}$ is the difference between the thermal expansion coefficients of the epitaxial layer $\alpha_{th,epi}$ and the substrate $\alpha_{th,subst}$. Sapphire and SiC, the dominant substrates used in the group-III nitride growth, both introduce sizeable thermal mismatch. However, the type of induced strain (tensile or compressive) is different for different binaries and ternaries depending upon the epitaxial relationship between the epitaxial layer and the substrate used. The following subsection presents the epitaxial relationship between AlN and

different substrates.

Polarization in heterostructures

The polarization charge arises from two sources: piezoelectric effects due to strain (piezo component), and the difference in spontaneous polarization between two different layers, i.e. heterointerface of nitrides even in the absence of strain (spontaneous component) (see above). These charges exist in nitride layers to varying degrees unless compensated by surface charges or impurities. At the heterointerface involving two layers $Al_xGa_{1-x}N$ and $Al_yGa_{1-y}N$ ($x \neq y$), the total polarization P^{total} is the sum of piezoelectric and spontaneous polarizations and can be expressed as

$$P^{\text{total}} = P^{\text{pe}} + P^{\text{sp}}. \tag{2.15}$$

The spontaneous polarization can cause very high electric fields in the group-III nitride crystals, and strain in pseudomorphically grown $Al_xGa_{1-x}N/Al_yGa_{1-y}N$ ($x > y$) or InGaN/GaN heterostructures can cause an additional piezoelectric field. Generally, the $Al_xGa_{1-x}N$ layer on top of $Al_yGa_{1-y}N$, if $x > y$, is coherently tensile strained. The piezoelectric and the corresponding difference in the spontaneous polarization between the two layers are negative and in the same direction. The alignment of the piezoelectrical and spontaneous polarization is parallel in the case of tensile strain, and antiparallel in the case of compressively strained top layers. In Fig. 2.5, the directions of the spontaneous and piezoelectric polarization are given for Al-face strained (compressive and tensile) and unstrained AlGaN/AlN heterostructures.

These very high polarizations and resulting electric fields inextricably produce a high density of polarization-induced free carriers σ at the interface that significantly increases the sheet carrier concentration n_s and a narrower confinement of the two dimensional electron gas (2DEG) [7,50]. Figure 2.7 shows an illustration of conduction band profile (solid line) in a single $Al_xGa_{1-x}N$ (top layer)/ $Al_yGa_{1-y}N$ (bottom layer) ($x > y$) heterostructure and the 2DEG distribution (n_s) at the interface. The polarization-induced sheet charge density σ in such structure can be expressed by

Table 2.3: Thermal expansion coefficient of AlN, GaN, InN, Sapphire, and SiC at room temperature (300 K) [1].

Material	$\alpha_{\text{th}}(10^{-6}/\text{K})$	
	α_a	α_c
AlN	4.2	5.3
GaN	5.59	3.17
InN	5.7	3.7
Sapphire	7.5	8.5
6H-SiC	4.0	4.68

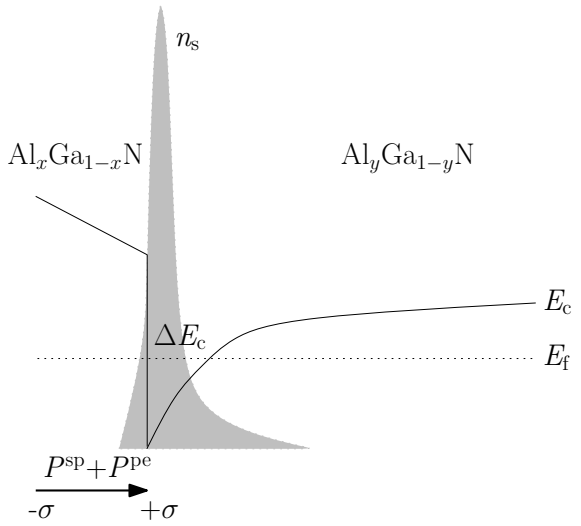

Figure 2.7: llustration of conduction band profile (solid line) in $Al_xGa_{1-x}N$/ $Al_yGa_{1-y}N$ ($x > y$) heterostructure and 2DEG distribution (n_s) at the interface.

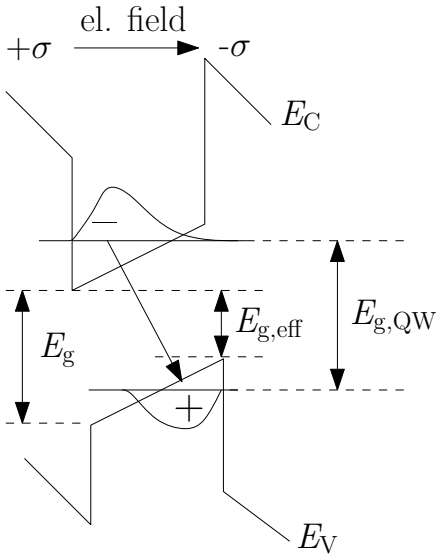

Figure 2.8: Influence of the electrical field in a quantum well. The wavefunctions of electrons and holes are separated.

$$\sigma = P^{\text{total}}_{Al_yGa_{1-y}N} - P^{\text{total}}_{Al_xGa_{1-x}N}. \tag{2.16}$$

It is obvious that σ increases with increasing difference between Al compositions in the two layers. The piezoelectricity in AlN/GaN heterostructures is the largest among the AlGaN-based heterostructure system. Furthermore, the electric field at the interface of the AlN barrier confines the 2DEG wave function tightly. Therefore, the magnitude of the polarization charge converted into number of electrons for AlN/GaN heterointerfaces should be relatively high in the range of mid-10^{13} cm^{-2} (see simulation results in chapter 7). However, a huge lattice mismatch between these two layers consequently may generate cracks on the top AlN layer, therefore, the thickness is a limitation for this type of heterostructure. If the AlN barrier layer is not pseudomorphic but partially relaxed (by misfit dislocations for example) then the piezoelectric effect would be reduced but the spontaneous polarization would still be present. In this case, the density of polarization charge may not be significantly improved as expected in AlN/GaN heterostructure in comparison to the high Al content $Al_xGa_{1-x}N$/GaN heterostructure [32]. The alloy scattering, intermixing of layers and the rough interface between layers may limit the carrier density and the mobility in the latter structure. This results in poor transport properties. In contrast, the mobility and sheet carrier density in AlN/GaN can be expected to be high because the interaction between the 2DEG wavefunction and the binary AlN barrier reduces alloy scattering. Therefore, it is imperative to address the issue of a high crystalline quality and critical-thickness of AlN barrier layer to achieve a higher carrier density.

There are many devices based on AlGaN/GaN [53] and InGaN/GaN heterostruc-

tures [1,54] but the devices based on AlN/AlGaN heterostructures as an active layer are yet to be realized. We will focus our studies on such a heterostructure and discuss the possibility/constraint of realization of electronic and optoelectronic devices based on such heterostructures in chapter 7.

The polarization induced electric field is beneficial for the formation of 2DEG in electronic devices such as high-electron mobility transistors (HEMTs), modulation-doped field effect transistors (MODFETs), etc. without the need of doping. However, the built-in electric field created within quantum wells (QWs) of optoelectronic device leads to a spatial separation of electron and hole wavefunctions, and results in the quantum-confined Stark effect (see Fig. 2.8). The consequences of this effect are an increased carrier lifetime, a decreased recombination efficiency, and a red-shift of emission due to a change in effective bandgap energy, thus limiting the performance of the optoelectronic devices [55,56]. Hence, the polarization of wurtzite nitrides has a deleterious effect on the performance of optoelectronic devices.

2.2 Substrate Materials

In theory, the best substrate selection for group-III nitride epitaxy would be the native substrate itself. However, this is barely ever approached in practice since there are no large quantities, good quality, and low cost native group-III nitride wafers commercially available. In recent years, there is a tremendous progress in the hydride vapor phase epitaxy (HVPE) growth of GaN substrates but there are only a few reports on the growth of AlN or high Al content $Al_xGa_{1-x}N$ substrates, although the early work on producing bulk AlN looked promising [57]. Therefore, foreign substrates have been employed in the heteroepitaxial growth of AlN and the rest of the group-III nitride layers. Despite the lack of matched substates, remarkable progress in the growth of high-quality GaN has been achieved using MOVPE, MBE, and HVPE techniques. However, efforts are still underway to grow high-quality AlN and high Al content AlGaN layers. The substrate plays a vital role to achieve a high-quality material. It should have similar properties to the film to be grown over it. The substrate determines the growth plane and hence the crystal structure and/or orientation of the film e.g. AlN will grow hexagonal on hexagonal substrates like (0001) sapphire (Al_2O_3) and may be cubic on cubic substrates like (001) galliumarsenide (GaAs). The substrate is, normally, chosen in such a fashion that the lateral lattice parameters are nearly equal to those of the film to grow. When the film and substrate lattice parameters differ more substantially, either the two lattices strain to accommodate their crystallographic differences or, if this is not possible, dislocation defects form at the interface and the epitaxial layer is relaxed. Hence, lattice-mismatched substrates lead to a substantial density of misfit and threading dislocations. Moreover, the perfect substrate does not exist, therefore, strain will be present in all heteroepitaxially grown group-III nitride thin films. Strained-layer epitaxy generally prevails during the early film formation stages irrespective of crystal structure to match the substrate crystallography (such growth is called *pseudomorphic*).

Another influential parameter of the substrate is the lateral thermal expansion co-

Table 2.4: Lattice and thermal parameters of the different types of substrates and mismatches with AlN

Material	Lattice parameters (Å)	Lattice mismatch %	Thermal expansion coefficients (10^{-6}/K)	Thermal mismatch %
AlN	a = 3.112		$\alpha_{th,a}$ = 4.2	
	c = 4.982		$\alpha_{th,c}$ = 5.3	
GaN	a = 3.189	-2.4	$\alpha_{th,a}$ = 5.59	-2.5
	c = 5.185	-3.9	$\alpha_{th,c}$ = 3.17	6.7
Sapphire	a = 4.758	-34.6	$\alpha_{th,a}$ = 7.5	-44
	c = 12.991	-61.65	$\alpha_{th,c}$ = 8.57	-38.1
SiC-6H	a = 3.0817	0.98	$\alpha_{th,a}$ = 4.2	0
	c = 15.1123	-67	$\alpha_{th,c}$ = 4.68	13.25
ZnO	a = 3.2496	-4.2	$\alpha_{th,a}$ = 4.75	-11.6
	c = 5.2065	-4.3	$\alpha_{th,c}$ = 2.9	82.7
Si (cubic)	a = 5.4301	-42.7	$\alpha_{th,a}$ = 3.59	17

efficient which should be matched with the film to be grown to avoid cracking of the film during the cool-down. Extra strain may be added when film and substrate have different thermal expansion coefficients, resulting in elastic or plastic deformation as described in the previous section. Furthermore, the substrate should be also chemically stable.

Two of the most popular substrates for the epitaxial growth of group-III nitrides are sapphire and SiC. Table 2.4 lists the lattice parameters and thermal characteristics of a number of prospective substrate materials.

Sapphire, which is used in this thesis, continues to be the principal substrate due to its low cost, the availability of 2-in. diameter crystals of good quality, ease of handling, its stability at high temperature and the fact that films of sufficient quality for device fabrication can be grown on it despite its poor structural and thermal match to the group-III nitrides. Group-III nitride films have been grown on different sapphire planes: c-plane (0001), a-plane ($11\bar{2}0$), r-plane ($1\bar{1}02$), and m-plane ($1\bar{1}00$). The basic structure of sapphire consists of hexagonal close-packed (hcp) planes of oxygen intercalated with aluminum planes. The aluminum planes have a similar hexagonal close-packed arrangement but with 1/3 of the sites vacant, giving rise to an Al/O ratio of 2/3. Each Al atom is surrounded by 6 oxygen atoms, and each oxygen atom has 4 Al neighbors [1]. In the case of group-III nitride films grown on c-plane sapphire, the hexagonal closed packing of the oxygen in the sapphire substrate is continuous with the hcp of N in AlN or GaN and Al or Ga atoms occupying all of the upward tetrahedral sites [58]. Since AlN and GaN lattice parameters are similar, it has been assumed by many researchers [58,59] that AlN would have the same epitaxial relationship as of GaN. We will present the epitaxial relationship of AlN film on sapphire using high-resolution TEM studies in

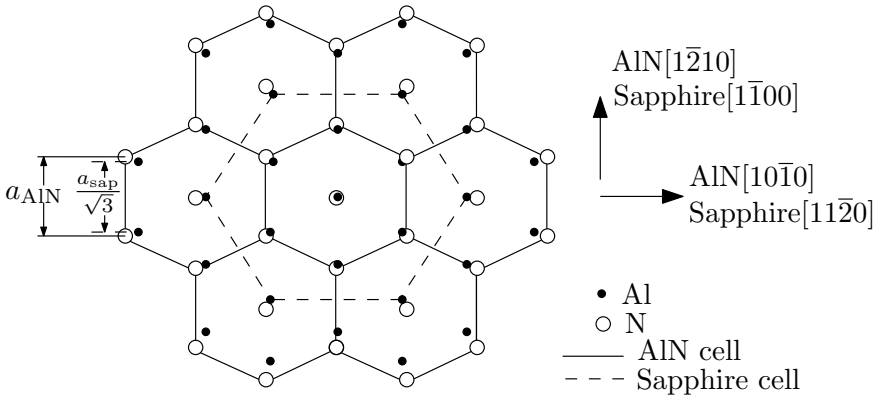

Figure 2.9: Schematic of the growth orientation of AlN cation positions on the *c*-plane (0001) sapphire. The circles represent Al-atom positions and dashed lines show the sapphire basal plane unit cells. The open circles represent the N-atom positions and solid lines show the AlN basal plane unit cell. The AlN unit cell is rotated by 30 ° around the *c*-axis as compared to that of sapphire.

chapter 4.

The calculated lattice mismatch between the basal AlN and the basal sapphire plane is larger than 34%. However, the small cell of Al atoms on the basal plane of sapphire plane is oriented 30 ° with respect to the larger sapphire unit cell. Lattice mismatch is caused when N generated from NH_3 is combined with Al ion to make a tetrahedron together with the oxygen on the sapphire surface. The chemical bonds change gradually from their ionic nature to a covalent nature: the bonding between the Al ion and the O ion of sapphire is ionic, and the Al atoms and N atoms make sp^3 hybrid orbitals with a more covalent nature. Lattice mismatch can be calculated from the change of Al − Al atomic distances between AlN and sapphire. Therefore, the actual mismatch is smaller (13.29 %) [58] as calculated by

$$\frac{\sqrt{3}a_{AlN} - a_{sap}}{a_{sap}} = 0.1329. \tag{2.17}$$

This smaller lattice mismatch is calculated in the same way as the lattice mismatch for GaN [60] is calculated to be 16 %. The atomic arrangement of the (0001) planes of AlN and sapphire is schematically represented in Fig. 2.9. Here (0001)AlN||(0001)sapphire, and [1$\bar{2}$10]AlN||[1$\bar{1}$00]sapphire, and [10$\bar{1}$0]AlN||[11$\bar{2}$0]sapphire are indicated.

In addition to lattice mismatch, a large thermal expansion coefficient mismatch between AlN and sapphire is another limitation (see Tab. 2.4). Due to thermal and lattice mismatch, growth has to be started with a thin polycrystalline nucleation layer which incorporates a high threading dislocation density into the material. In recent years, many researchers have been employing different growth techniques to improve the quality of epitaxial layers of AlN on sapphire. In chapter 4, we describe the thorough growth optimization to alleviate strain and reduce intrinsic defect densities that yields a very high quality of AlN on sapphire. Nowadays, as-received sapphire wafers are

epi-ready, therefore, no need to surface preparation prior to the growth.

In contrast to sapphire, hexagonal SiC has a better lattice and thermal expansion coefficient match with the group-III nitrides. The cleavage planes of SiC coincide with those of c-plane group-III nitrides. This property makes SiC a very attractive substrate. It has a much higher thermal conductivity compared to sapphire, which makes heat dissipation for high-power devices a much simpler issue. In this work, only a few experiments were carried out on this substrate because of the cost issue.

Few groups have grown group-III nitride films on Si substrates [61,62]. The growth on Si is gaining much interest because of its high thermal conductivity. Meanwhile, Vogg *et al.* [63] have also reported a high quality AlN on diamond. However, the quality of such films are still not comparable to the films grown on sapphire or SiC.

A good quality AlN bulk crystal is not commercially available. M. Bickermann *et al.* of the Friedrich-Alexander-University of Nuernberg-Erlangen have provided us a small piece of bulk AlN. We will discuss the properties of homoepitaxially grown AlN in chapter 4.

2.3 Defects

The properties of semiconductor materials are often controlled by defects and the incorporation of impurities. The heteroepitaxial layers of group-III nitrides contain large densities of structural and native defects in comparison to other III-V materials (arsenides, phosphides). The crystallite imperfections due to such defects give rise to electronic states throughout the band gap which is reflected in the luminescence properties of the layers. Among the structural defects, threading dislocations (TDs), nanopipes, inversion domains, and pyramidical planar defects can cross the whole epitaxial layer. Differences in the stacking orders of the epitaxial growth planes may form planar defects, namely, stacking faults (SFs). Point defects including vacancies (missing atoms), self-interstitials (additional atoms incorporated on sites other than substitutional sites), and antisites (in a compound semiconductor, a cation sitting on a nominal anion site, or vice-versa) are native defects and intrinsic to the semiconductor. It is also possible for point defects and impurities to agglomerate and form complexes.

Dislocations may be grouped into misfit dislocations (MDs) generated due to the lattice and thermal expansion coefficient mismatches, and TDs due to the tilt and twist of crystal grains. Below a certain epilayer thickness, called the *critical thickness*, an epilayer may be grown pseudomorphically on a substrate, while a relaxation of misfit strain via plastic flow occurs for the epilayer exceeding the critical thicknesses. The most common mechanism of plastic relaxation is through the formation of MDs. Such dislocations have edge components and move across the layer. Figure 2.10 shows a crystallographic model, presented by Masu *et al.* [64], at the AlN/sapphire interface illustrating periodical MDs which are indicated by white arrows due to lattice mismatch between lattice constants of N-N and O-O. From TEM image as shown in Fig. 2.11, Uehera *et al.* [65] actually observed periodical MDs indicated by white arrows and argued that MDs exist only within a few monolayer thickness from the interface due to a large lattice mismatch of 13.4% between the lattice constants of N-N and O-O. MDs

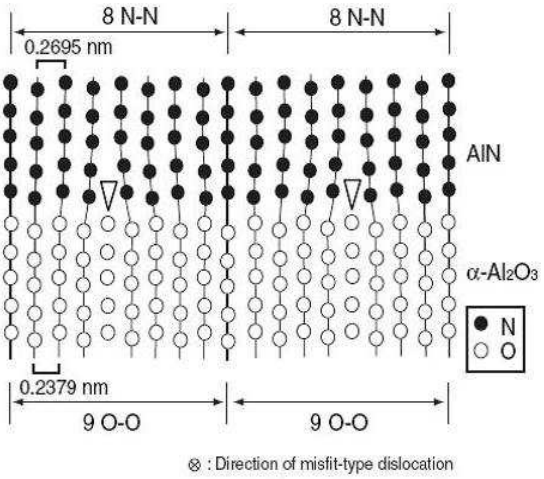

Figure 2.10: Crystallographic model illustrating the accomodation of the lattice misfit by dislocations [64]. The AlN epitaxial layer is totally relaxed.

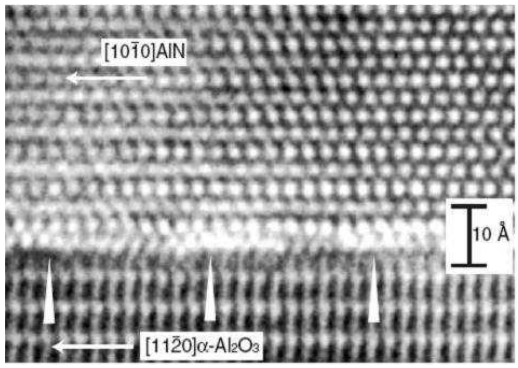

Figure 2.11: Cross sectional image of AlN/sapphire interface by high-resolution TEM [65].

are usually introduced in regular intervals of 8 atomic planes in terms of the AlN lattice or 9 atomic planes in terms of the Al_2O_3 lattice.

This was verified by Kehagias *et al.* [66] by cross-section HR-TEM images. Using Fourier filtering, it was possible to visualize the edge component of one set of misfit dislocations as terminating fringes of the corresponding substrate lattice planes. Figure 2.12 shows a filtered image using the in-plane Fourier spatial frequencies, where $11\bar{2}0$ Al_2O_3 lattice fringes terminate at the interface in nine fringe intervals. Terminating Moiré fringes and dislocation density measurements suggest the association of misfit and threading dislocations at the epitaxial/substrate interface. An average dislocation density is estimated to be approximately $1.15 \times 10^{11}\,cm^{-2}$ for an AlN layer grown on sapphire substrate. A semiconductor layer with such a high density of defects is not

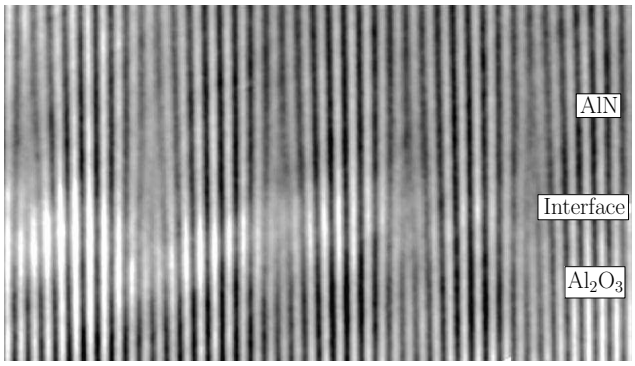

Figure 2.12: Fourier filtered image using the inplane Fourier spatial frequencies, where $11\bar{2}0$ Al_2O_3 lattice fringes are shown to terminate at the interface in nine fringe intervals [66].

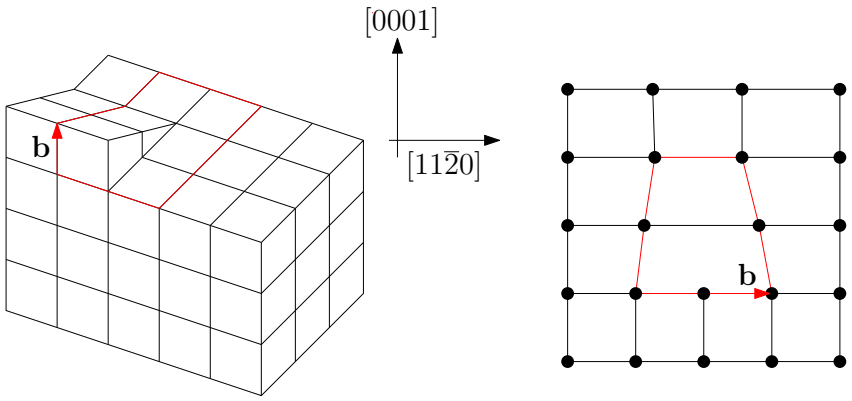

Figure 2.13: Schematic representation of a screw-(left) and edge-(right) type dislocation with the respective Burger vector **b**.

suitable for optoelectronic and electronic applications. Therefore, a reduction in the dislocation density is indispensable. In this work, we have optimized various growth parameters at different growth stages and developed a growth procedure preferentially reducing the dislocation density (see chapter 4).

During crystal growth, unevenness of the substrate surface or the collision of growth islands leads to the nucleation of dislocations with line direction parallel to the direction of the growth. These dislocations thread the epilayer, therefore, are termed as TDs and reach the surface of the film except those that annihilate each other. The presence of TDs adversely affects the device properties causing non-radiative recombination [67, 68], carrier scattering effects [69], and diffusion of dopants and impurities [70]. Moreover, given the affinity of AlN for oxygen and the presence of hydrogen in MOVPE growth, it is likely that dislocations in AlN will be decorated with these impurities, too. There are few theoretical studies of dislocations in AlN. Wright *et al.* [71] investigated the structures and formation energies of neutral and charged edge dislocations in AlN via density-functional-theory calculations and concluded that the formation energy of Al vacancies at an edge dislocation is lower than in the bulk layer. This may arise because atoms near the dislocation core are more easily able to relax their positions and find optimum bonding geometries. The atoms surrounding a bulk vacancy, on the other hand, are likely more constrained in terms of their ability to relax.

The character of the TDs is given by the type of the Burgers vector **b**, a mathematical vector that represents the magnitude and direction of the distortion in a dislocation in a crystal lattice (Fig. 2.13). There are basically three types of TDs present in the nitride films, namely, edge-type dislocations (a-type), screw-type dislocations (c-type), and mixed-type dislocations (c+a-type) corresponding to Burger's vector **b** = 1/3<11$\bar{2}$0>, <0001>, and 1/3<11$\bar{2}$3>, respectively. The schematic Burger vectors of these dislocations are illustrated in Fig. 2.14.

In the case of epitaxial growth of GaN on sapphire, the lattice mismatch results in extremely high dislocation densities near the interface and the isolated TDs of edge, screw or mixed type generally persist beyond approximately 0.5 μm above the interface

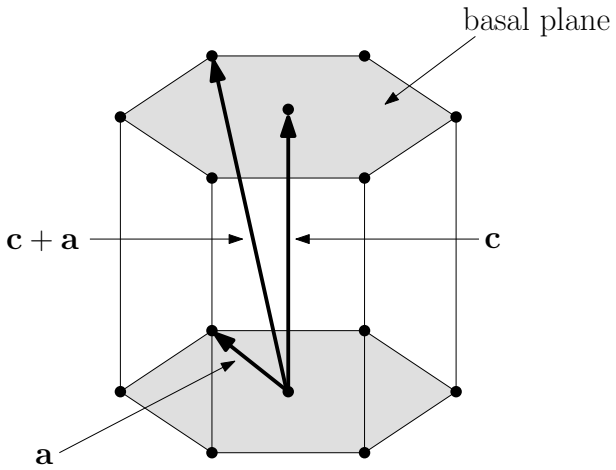

Figure 2.14: Schematic showing the Burgers vectors of the three types of dislocation observed in (0001) group-III nitride layers.

region [72,73]. The nucleation layer (NL) and its growth conditions critically impact the evolution of TDs into the subsequently grown layer. The growth process is nucleated in islands and the structure is often described by the model of mosaic crystals as illustrated in Fig. 2.15 [1]. The mosaic crystals consist of many small hexagonal grains of high crystalline quality. However, these grains are slightly misoriented with respect to each other and have a distribution of out-of-plane tilt and in-plane twist within the nitride film. Although the tilt and twist boundaries of these grains can have a mixed character,

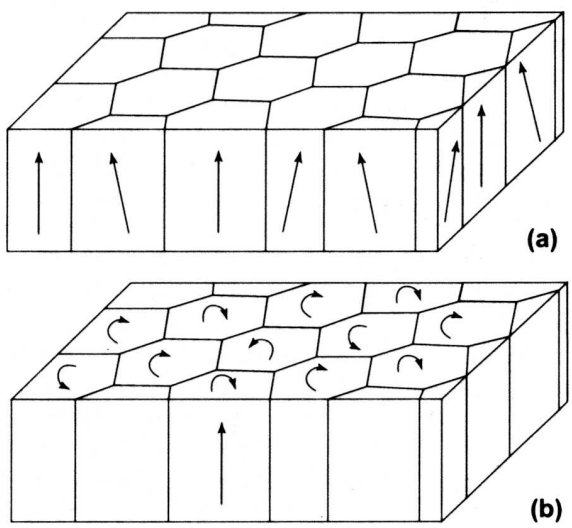

Figure 2.15: Columnar model for the group-III nitride film consisting of a mosaic of vertical columns or grains. Illustration of a slight distribution in intergrain orientation with two components: (a) tilt and (b) twist [1].

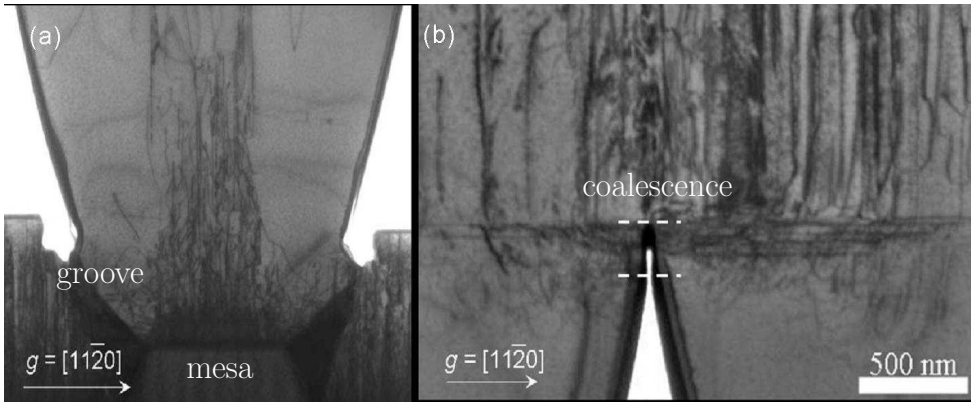

Figure 2.16: Bright-field TEM micrographs in cross section of AlN stripes before coalescence (a) and after coalescence of stripes (b) [80]. High TDs with an edge component originating at the substrate mesa compared to the TDs in the lateral grown area (a). Generation of new TDs after coalescence of the strips (b).

i.e. have both edge as well as screw components of TDs, in the more general case, they can be explained in terms of screw and/or edge-type dislocations, respectively.

Several methods, e.g. epitaxial lateral overgrowth (ELO) using silica (SiO_2) masks [74, 75] or *in situ* deposition of silicon nitride (SiN_x) intermediate layer as a dislocation filter [76–78] are successfully employed to reduce the TDs in GaN layers. Some groups have reported that, unlike in GaN, such approaches are not effective to reduce TDs in the case of AlN or high Al content AlGaN epitaxy because of the tendency to deposit polycrystalline AlGaN on the silica (SiO_2) masks and poor lateral growth rate associated with increasing aluminum content [79]. We will present the results of AlN layers that were deposited on sapphire using this approach in chapter 4. Mei *et al.* [80] grew a mask-less ELO of AlN films on shallow-grooved (0001) sapphire substrates using a pulsed lateral overgrowth (PLOG) technique. As shown in Fig. 2.16(a), a high density (more than $10^{10}\,cm^{-2}$) of TDs was observed in the region above the mesa, whereas the density of TDs was reduced to $10^{8}\,cm^{-2}$ in the lateral growth region across the groove. The reduced TDs in the laterally overgrown AlN demonstrates that the lateral growth is a necessary growth condition for obtaining a high quality of AlN layer. However, after coalescence, (Fig. 2.16(b)), new TDs of the same nature and order of magnitude as those observed in the mesa region were generated and there is no reduction of the density of TDs as a whole. Imura *et al.* [81] have reported a very high-temperature (1400 °C) growth of AlN and observed that smaller grains were incorporated into bigger grains resulting in much larger grains. The growth mode was much more lateral and dislocations were filtered or bent during the incorporation process of grains.

While it is understood to some extent that TDs are caused by the lack of a suitable, i.e., thermally and lattice matched substrate, the electronic structure of these defects is not well understood. Studies that explicitly address defects in AlN are rare so far, therefore, it is still a topic of studies. We will investigate the behavior of TDs using TEM and their correlation with the full width at half maximum (FWHM) of X-ray

diffraction peaks from symmetric (002) and asymmetric (102) reflections in chapter 4. The determination of the Burgers vector **b** of a dislocation is not a straightforward operation. It is observed that sometimes dislocations are visible and at other times they are not. In this work, TDs in the AlN layers are investigated and analyzed by Dipl.-Phys. Oliver Klein *et al.* of the Transmission Electron Microscopy Group of the University of Ulm after unambiguous determination of **b** in the hcp lattice using the well-known $|\mathbf{g} \cdot \mathbf{b}|$ criterion where **g** is the diffraction vector. As reported earlier by others, the edge-type and the mixed-type TDs are found to be the dominating TDs in AlN layers similar to GaN and InN layers. Many researchers have employed various growth techniques to reduce the TDs in AlN layers at least to the same range of density of TDs present in GaN layers. However, it is a surmount task for the epi-growers.

Besides TDs, nanopipes may also be present in an AlN film, however, it is very difficult to identify such defects. Nanopipes, in the technical sense, are empty or filled holes that exhibit a dislocation character. They can extend up to a few tens of nanometers and are usually limited by $10\bar{1}0$ planes. They have been reported to start from V-shaped indentations [82]. Further, the nanopipe density increases with higher concentrations of impurities or dopants, for example, O, Mg, and Si. We have observed an increase of the density of V-pits with increasing Si concentrations in the AlN layer while doping. However, the V-pits observed in AlN layers are similar to the the V-defects observed in InGaN/GaN or AlGaN/GaN multi-quantum well structures which are associated with either mixed or edge character TDs [83, 84]. Nanopipes above a certain diameter may be subject to chemical attack, and be visible as pits after chemical etching. However, a high quality AlN layer is not easily etched by most chemicals. Additional crystalline defects besetting the layers include inversion domain boundaries (IDBs) and stacking faults. Such defects manifest themselves as energy states in the forbidden energy bandgap producing scattering centers.

The native defects are critical for the group-III nitrides, especially AlN. While there have been several theoretical and experimental studies of point defects in GaN [85, 86], less work has been done on AlN. The structural and point defects cause impurities to diffuse more readily along threading dislocations, and carrier transport is either impeded, as in lateral transport, or aided, as in vertical transport. The high density of defects also leads to boundary-limited transport making the important basic parameters such as diffusion constant and mobility nearly impossible to measure. The extended defects in nitrides also lead to inhomogeneities in electric potential because of the high piezoelectric constants of AlN. Electrically active defects induced either directly or indirectly by extended defects cause excess leakage that is detrimental to both optical devices (in the form of dark current in detectors and reduced quantum efficiency in emitters) and electrical devices (in the form of increased gate current leakage and output conductance in FETs).

First-principles calculations of formation energies of native defects in AlN were performed by Mattila and Nieminen [87], Fara *et al.* [88], and Stampfl and Van de Walle [89]. The main conclusions are similar to those for GaN: Self-interstitials and antisites are high in energy in wurtzite AlN, and only vacancies have low enough formation energies to occur in high enough concentrations to affect the electronic properties. Stampfl and Van de Walle [89] reported that under n-type conditions (large E_F values), the

triply negatively charged aluminum vacancy V_{Al}^{3-} has the lowest formation energy that acts as an effective compensating center for shallow donors (e.g., O and Si), inhibiting successful n-type doping. This is a severe problem in achieving n-type conductivity in AlN. The behavior of the Al vacancy is similar to the case of the gallium vacancy in GaN. However, because of the larger band gap of AlN, the formation energy of V_{Al}^{3-} is significantly lower than V_{Ga}^{3-}. The defect level of V_{Al} lies close to the valence-band maximum. The problem of achieving electrical conductivity in the AlN layer may be attributed to self-compensation by such native defects at a large extent. There is no experimental report on the relationship between native defects and the n-type electrical conductivity so far. We will present our findings about the relationship between the defect related low-temperature CL peaks (the violet luminescence band) and the electrical conductivity of Si doped AlN layers in chapter 5.

2.4 Growth Techniques

Practically all well-known growth techniques have been investigated for the growth of group-III nitrides. It may be said that the different epitaxial growth techniques have stimulated each other's development. Here, we will discuss some of the common techniques employed for the growth of good quality AlN crystals by different researchers. MOVPE and MBE are, unanimously, the most popular techniques for the growth of AlN films in the recent times.

2.4.1 Hydride Vapor Phase Epitaxy

There are several earlier reports about the HVPE growth of bulk AlN crystals [41,57,90]. Like the growth of GaN freestanding wafers which have already been utilized as the substrates for blue laser diodes, HVPE is expected to become a commercial process of AlN freestanding substrates in the near future. In the case of GaN, HVPE is usually carried out in a hot-wall quartz (SiO_2) reactor by passing hydrogen chloride (HCl) gas over Ga metal to form GaCl gas, which is then mixed with NH_3 gas to form GaN. However, hot AlCl gas generated by the reaction between Al and HCl reacts violently with quartz and destroys the reactor. Thus, HVPE of AlN is very difficult. On the other hand, there are other aluminum chlorides such as $AlCl_2$, $AlCl_3$ and $(AlCl_3)_2$ which have less reactivity with quartz glass. Kumagai *et al.* [91] reported that the HCl gas is introduced to react with Al metal pellets at 500 °C to produce $AlCl_3$ gas in the upstream region (source zone) of the reactor. A substrate (sapphire or SiC or AlN/Sapphire or AlN/SiC template) is placed in the downstream region of the reactor (growth zone), in which $AlCl_3$ and NH_3 are separately introduced and mixed to grow AlN at 1100 °C. This technique can produce a thicker AlN layers. Unfortunately, unlike GaN, the standard HVPE technique suffers from severe cracking of the AlN layer when its thickness exceeds few microns. However, Soukhoveev *et al.* [92] have reported the crack free growth of 75 μm and 15 μm thick AlN layers on 2-inch and 3-inch SiC and sapphire substrates, respectively. This growth technique is suitable to the growth of substrates rather than thin layers.

2.4.2 Physical Vapor Transport

Another special technique to fabricate single crystals is PVT (physical vapor transport). Bickermann *et al.* [93] have successfully grown AlN single crystals using the PVT technique by sublimation of an AlN charge placed in the hot zone of a tungsten crucible and subsequent condensation of vapor species in a cooler region. The growth temperature of the crucible lid is about 2100 °C. We have used such AlN bulk crystals to deposit AlN epilayers in this work (see chapter 4). Lu *et al.* [94] reported a sublimation growth of 500-900 μm thick and 20 mm diameter AlN single crystals on SiC (0001) seeds at the growth rate of approximately 8-18 μm/hr with dislocation densities on the order of 10^6-10^7 cm^{-2}. The growth environment, which is very critical in this process, can significantly interfere the crystallization process, not only in a way that reflects impurities (O and C) incorporation but also by yielding crystallites of different nucleation and morphological characteristics [95]. Furthermore, Tuomisto *et al.* [96] have observed vacancy defects in PVT grown AlN single crystals. These defects are tentatively identified as negatively charged Al vacancies, as well as negative non-open volume centers. Such vacancy defects are also observed in our MOVPE grown AlN layers. We will discuss these defects in detail in chapter 4.

2.4.3 Liquid Phase Epitaxy

There have been a few reports on AlN single crystal growth in the liquid phase using an AlN melt under a high pressure of N_2 [97]. Isobe *et al.* [98] used liquid-phase epitaxy (LPE) growth technique to synthesize AlN grains by varying the flux composition (Ca:Sn) and the ratio of Al to flux under the relatively mild conditions of 900 °C and nitrogen gas pressure of 5 atm in a time period of 96 hr. However, the material quality of the AlN crystal is very poor. Furthermore, the growth of multilayer structures with abrupt interfaces is difficult by LPE. In addition, the thickness uniformity of epitaxial layers grown by LPE is generally poor.

2.4.4 Pulsed Laser Deposition

Many researchers have reported successful epitaxial growth of AlN using pulsed laser deposition (PLD) technique in high vacuum and in a nitrogen ambient of a few mbar [99, 100]. In this growth technique, the AlN film is grown either by the direct laser ablation of an AlN target or by reactive laser ablation of an Al target with a laser beam using either a partial nitrogen atmosphere (in a pressure of 10^{-2} to 10^{-1} mbar), or a nitrogen plasma. In both cases, the oxygen (O) incorporation (concentration around 10% [100]) in the growing films is found as the main problem during laser ablation of the AlN film. Employment of UHV conditions and very pure nitrogen sputtering gas yielded reduced impurity levels to the extent that O contamination was reported to be 3.5×10^{18} cm^{-3} [101].

2.4.5 Molecular Beam Epitaxy

Molecular beam epitaxy growth of group-III nitrides is still limited to the research arena, contrary to the metalorganic vapor phase epitaxy (MOVPE) which is used to grow the material of the main commercialized III-nitride components, i.e. LEDs, LDs, and transistors. In MBE, thin films are formed in vacuum on a heated substrate through various reactions between thermal molecular beams of the constituent elements on the substrate. In the growth of the group-III nitrides, high purity metal species are provided by respective thermal effusion cells and nitrogen is provided either by plasma-induced fragmentation sources (DC, radio frequency (RF), electron cyclotron resonance (ECR)) [22] or the dissociation of gaseous NH_3 [102]. Solid or gaseous dopant sources of Si and Mg are used to achieve controlled n and p-type conductivity. The synthesis of group-III nitrides involves a metastable growth process, which is controlled by a competition between the forward reaction (incorporation of group-III species and N into the film and epilayer forms) and the reverse reaction (decomposition of nitrides). For a net growth to take place, the rate of film formation must be larger than the rate of decomposition. The film growth by MBE is a nonequilibrium kinetic process in which rate-limiting steps affect the growth modes (two-dimensional(2D), islands, or mix of 2D and islands).

One advantage of MBE technique is that the materials can be grown at a comparably low growth temperature which results in low thermal stress upon cooling, less diffusion, and reduced alloy segregation. Another advantage of MBE is the absence of atomic hydrogen species during the growth, therefore, hydrogen passivation of the deposited layer can be avoided. The processes like deposition, desorption, and surface diffusion in MBE determine the eventual interface morphology of a growing film. Therefore, MBE allows for a fine control of composition, thickness, and doping of the growing structure at monolayer level. Furthermore, the ultra high vacuum (UHV) environment allows the use of reflection high-energy electron diffraction (RHEED) for the *in situ* characterization (surface reconstruction and growth modes).

However, despite these advantages, there are several difficulties in the MBE growth technique of group-III nitrides. The growth of the group-III nitrides needs a relatively high growth temperature. Semiconductor thin films are typically synthesized at half to two thirds of the material melt temperature to ensure adequate surface diffusion for single crystal growth. In case of GaN, the growth by MBE cannot be performed at high temperatures due to the rapid decomposition of the compound in the ultrahigh-vacuum MBE environment. For this reason, the sample temperature is restricted to below 900 °C and MBE growth of GaN invariably produces material with high threading-dislocation densities on all practical substrates [103]. Unlike GaN, the AlN growth temperature is rate limited by the reactant sticking coefficient at around 1200 °C rather than by epilayer decomposition [104, 105]. The growth rate decreases at near-zero sticking coefficient at around 1200 °C. The threading-dislocation density is extremely high if the growth temperature is low. In MBE, one of the most difficult parameters to control is the substrate temperature particularly at high growth temperatures where thermal radiation losses are high [106]. Uniformity across the wafer is difficult to achieve due to radiation loss at the edge of the wafer and by variations in the refractory metal coatings

applied to the back of the transparent substrates like sapphire and SiC.

Although the MBE growth of AlN was already reported in 1979 [107], only a few groups have reported a successful growth of it so far. Heffelfinger *et al.* [108] have focused on the initial stages of AlN growth on (0001) oriented sapphire substrates by MBE. For a film thickness of about 25 nm, AlN forms islands of varying alignments with respect to the sapphire substrate. Such islands with an alignment other than the predominant orientation (i.e. [0001] plane) disturb the growth near the AlN/sapphire interface and create displacements along the [0001] direction of AlN in overlaying AlN grains. These misaligned AlN grains cause planar defects to form in the epitaxial AlN films. Faleev *et al.* [109] have reported a MBE grown AlN layer with a very low (1.75–8.5 $\times 10^5$ cm^{-2}) density of screw type threading dislocations. However, the largely present edge type dislocations in the AlN epitaxial layer is still not addressed by this technique. Similarly, Shen *et al.* [110] have reported the achievement of ultra-flat surface morphologies of AlN with rms as small as 0.12 nm in AFM measurements and high crystalline quality with the full-width at half maximum of the (002) peak less than 80 arcsec in high-resolution X-ray diffraction measurements. Although there are reports on clear near-band edge cathodoluminescence emission of such MBE grown AlN layers, the broad FWHM (>50 meV at 77 K) of the emission peak shows the poor optical quality of these layers.

2.4.6 Metal Organic Vapor Phase Epitaxy

In recent years, metal organic vapor phase epitaxy (MOVPE) has become a mainstream technique for the research, development and production of optoelectronic and electronic devices based on group-III nitrides. State of the art performance has been demonstrated for a number of categories of devices, including lasers, LEDs, PIN photodetectors, FETs, HEMTs, solar cells, etc using this growth technique. The MOVPE is characterized by large-area growth capability, high surface mobility of the precursor gaseous molecules, good layer uniformity, precise control of the epitaxial deposition, reproducibility, and excellent reconfiguration flexibility. These reasons together with the higher growth rate, made the MOVPE the favorite growth method for industrial purposes, too. MOVPE offers unequalled flexibility that encompasses a wide range of operating conditions: temperature, pressure, and source materials. The group-III MOVPE growth typically involves high growth temperatures that result in complex gas phase and surface reactions. By this technique, the gas phase growth precursors are transported by a carrier gas to a heated substrate, where the precursors are pyrolized and the nitride film is deposited. The diffusion of the active materials to the substrate is favored by the depletion at the surface and the consequent concentration gradient of the materials in the gas phase, due to their consumption during the growth. The obtained byproducts are then transported out from the reactor together with the unused reactants. MOVPE is performed at much higher pressures than MBE, allowing the group-III nitride films to be synthesized at significantly higher temperatures more than 1050 °C under conditions at which the compound is thermodynamically stable. This simple thermochemical argument is believed to be the primary reason why MOVPE group-III nitride material is superior in performance for commercial optoelectronic de-

vice applications. High-quality epitaxial group-III nitride films and heterostructures for devices have been accomplished using this growth technique. Compared to MBE, it has high throughput and no ultra high vacuum is needed, therefore, it is economically advantageous.

Nevertheless, several problems still remain in this technology, including the need for a large number of parameters that must be precisely controlled to obtain the necessary quality, uniformity, and reproducibility. Unlike the MBE system, RHEED is not suitable for *in-situ* characterization in the relatively high-pressure environment of MOVPE. RHEED requires a high electron mean free path, which can be only achieved in UHV conditions. The growth process is therefore monitored by normalized optical reflectometry and reflectance anisotropy spectroscopy (RAS). A detailed description of the MOVPE system used in this work will be given in the following chapter.

The first demonstration of the MOVPE growth of GaN and AlN films on sapphire and SiC substrates was carried out by Manasevit *et al.* [111] in 1971. A great advance in crystal growth was achieved in 1986 when Amano *et al.* [10] used a low-temperature (LT) buffer layer that enabled the realization of high-quality GaN films. Currently, the LT-buffer technique is one of the most popular standard methods for the growth of GaN on sapphire by MOVPE. However, due to the severe gas-phase pre-deposition reactions between the group-III and -V precursors (typically trimethylaluminum (TMAl) and ammonia) leading to the reduction in the growth efficiency, limited lateral growth of the AlN layer, and active chemical behavior of Al atom, so far no de-facto-standard methods have been developed for the growth of AlN or high Al content AlGaN films by MOVPE. Several growth processes, including high-temperature (HT) direct growth [112], multiple modulation of V/III ratio at HT direct growth [113], switching of the precursor flows ON and OFF during the growth [114, 115], two-step temperature growth (LT buffer and HT layers) [116, 117], and so on, have been explored by many researchers. However, there have been no unanimous results reported on the crystalline, surface, luminescence, and electrical properties of high quality AlN layers grown by either of the above mentioned processes. Therefore, the establishment of a de-facto-standard method for the MOVPE growth of a high quality AlN layer is still a challenging task for the MOVPE growth researchers. A detailed study of the MOVPE growth and characterization of AlN layers will be presented in chapter 4.

2.5 Characterization Methods

A brief overview of the characterization techniques used in this study is provided in the following subsections.

X-ray Diffraction

X-ray diffraction (XRD) is a widely-used powerful and non-contact method in order to understand the structural properties of a solid material. In this study, various informations about crystal structure, strain state and material composition of the MOVPE grown epilayers have been obtained using different setup geometries of the X-ray

diffractometer.

For the current study we worked with a Siemens D5000 diffractometer. Incorporating a copper (Cu) source for X-ray generation, it uses the Cu-K_α emission line (λ = 0.154 nm) with the help of a 4-crystal germanium (Ge) monochromator, in order to achieve extremely narrow line-width in arcsec.

The line width of a rocking curve measurement (ω scans) i.e., the full width at half maximum (FWHM), determines the crystalline quality of the material. There are two components which govern the perfection of the epilayer structure: (i) tilt, i.e. out-of-plane rotation, between the crystalline columns with respect to the substrate normal (due to the dislocations present which can propagate in the growth direction) and (ii) twist, i.e. in-plane rotation, of the columns orientation about the substrate normal (due to the edge dislocations that lie on the basal planes) [118].

The measured FWHM of X-ray rocking curves β_{hkl} can be expressed as

$$\beta_{hkl}^2 = (\beta_S \cos\chi)^2 + (\beta_E \sin\chi)^2 + \frac{(2\pi/L)^2}{K_{hkl}^2}, \tag{2.18}$$

where β_S and β_E are the tilt and the twist angles, χ is the angle between the reciprocal lattice vector K_{hkl} and the (001) plane, and L is the lateral coherence length [119]. The FWHMs for (002)- and (102)-reflections are used to estimate β_S and β_E, respectively. For simplicity, we have omitted the contribution of L and added about 20% errors in the calculations [119]. Since $\chi = 0$ for (002)-reflection, the value of β_S is simply equal to β_{hkl} which is the measured FWHM for (002)-reflection. β_E is calculated from Eq. 2.18 by substituing the values of β_S, β_{hkl} which is the measured FWHM for (102)-reflection, and χ for (102)-reflection. The tilt and twist of lattice planes are related to the densities N_S and N_E of the screw and/or mixed and the edge and/or mixed components, respectively, of the TDs [120]. We calculate the TD densities using well-known classical formula from Dunn and Koch [121]

$$N_S = \frac{\beta_S^2}{4.35|\mathbf{b}_S|^2}, \tag{2.19}$$

$$N_E = \frac{\beta_E^2}{4.35|\mathbf{b}_E|^2}, \tag{2.20}$$

where $\mathbf{b}_S$ and $\mathbf{b}_E$ are the Burgers vectors of the screw ($\mathbf{b}_c$ = 0.4982 nm) and edge ($\mathbf{b}_a$ = 0.3112 nm) components, respectively.

AFM

The investigation of the surface morphology of the grown epilayer was carried out using atomic force microscopy (AFM). The AFM measurements were performed with a Veeco Dimension 3100 scanning probe microscope equipped with a Nanoscope III-A controller unit. The maximum scanning range for the x-y direction is 90 μm and for the z-direction 5.5 μm. The AFM dynamic non-contact mode was used, according to which the cantilever is externally oscillated close to its resonance frequency not touching the surface and the effects of the interaction forces (mainly attractive Van der Waals) are

transferred directly to the oscillation characteristics, such as the amplitude or phase and are recorded by the detection system.

SEM

Scanning electron microscope (SEM) facility we used was the LEO-982, product of a Zeiss and Leica group cooperation. The electron beam is generated from a Schottky Field Emitter (S-FE) and can be accelerated by voltages ranging from 0.2 to 30 kV, resulting to resolutions of 4 nm and 1 nm respectively. LEO-982 is equipped with both a secondary and a backscattered electron detector and the sample stage can be moved in the x-y axis, rotated by 360 ° and tilted from 0 ° to 90 °. The controller unit offers a lot of possibilities, such as image storage, distance measurements, etc.

TEM

Transmission electron microscopy (TEM) investigations of our samples were carried out by Dr. Johannes Biskupek and Dipl.-Phys. Oliver Klein of the Transmission Electron Microscopy Group of Ulm University with a Philips CM-20 microscope. To image dislocations and distinguish the different dislocation types, cross-sectional weak beam dark field method (WBDF) images close to the $[01\bar{1}0]$ zone were analyzed by exploiting the $\mathbf{g} \cdot \mathbf{b}$ criterion. According to this criterion, only c-type and (a+c)-type dislocations are visible in the WBDF image when using the (0002) reflection. Exploiting the $(2\bar{1}\bar{1}0)$ reflection, only a-type and (a+c)-type TDs give rise to a contrast. To determine Burgers vectors directly, HRTEM images were recorded at the $[01\bar{1}0]$ zone as well as in the [0001] plane-view projection.

CL

The spectroscopic properties of our samples were evaluated using cathodoluminescence (CL) measurements. Dr. G.M. Prinz and Dipl.-Phys. R.A.R. Leute of the Institute of Semiconductor Physics of Ulm University carried out these measurements in their lab set-up using a continuous He-flow cryostat with an effective sample temperature below 10 K. The samples were excited using a RHEED electron gun with an acceleration voltage of 6 kV. The emitted light was dispersed by a monochromator with a focal length of 30 cm, equipped with a grating with 1200 rules/mm and resolution of 0.2 nm. The spectra were detected with a nitrogen cooled CCD camera. The spot diameter of the electron beam on the sample is around 0.5 mm with an estimated penetration depth of 370 nm in AlN epilayers.

Electrical Measurements

To evaluate the electrical properties of our Si-doped samples and the heterostructures, we performed two-point current-voltage (*I-V*) measurements from room temperature to 1000 °C at the lab of Institute of Electron Devices and Circuits and Institute of

Solid State Physics of Ulm University. In order to evaluate the carrier concentrations and mobility, we performed Van der Pauw Hall measurements on $5 \times 5\,\mathrm{mm}^2$ pieces of the samples in our lab set-up.

Chapter 3

Metal Organic Vapor Phase Epitaxy

The purpose of this chapter is to understand the basic MOVPE phenomena from the perspective of the AlN growth in a MOVPE reactor. As briefly discussed in chapter 2.4.5, MOVPE is unquestionably the most versatile and economic technique for the production of devices requiring large areas, such as LEDs, photocathodes, ulta-high speed transistors, integrated circuits, and solar cells. In this chapter, first its basic principles will be reviewed. In contrast to the growth of GaN and low Al content AlGaN layers, for which the epitaxial growth process is well established, the MOVPE growth of AlN and high Al content AlGaN layers is more crucial. The peculiarities of the MOVPE growth of AlN and the specific configuration of the substrate positioning in the reactor is briefly described. A short review of the general properties of the precursors employed in this study is presented. Finally, a discussion of the *in-situ* monitoring of epitaxial growth employed in our system is presented.

3.1 Basic Principle of MOVPE

MOVPE is a non-equilibrium growth technique which relies on vapor transport of the precursors and subsequent reactions of highly supersaturated alkyl, [organic radical (R) + metal from group-III (M)] and hydride [hydrogen compound from group-V (EH)] in a heated zone resulting in epitaxial growth of a thin solid film which finally establishes the equilibrium of the system. In a simplistic manner, the general reaction of the MOVPE process can be written as follows

$$R_3M^{(g)} + EH_3^{(g)} = ME^{(s)} + 3RH^{(g)}. \tag{3.1}$$

It involves complex homogeneous and heterogeneous reactions of the group-III and group-V source molecules in the gas phase and on the solid surface as well as growth related surface processes such as adsorption/desorption of the chemical species, diffusion and surface migration. The steps of an MOVPE growth process are schematically shown in Fig. 3.1.

The fundamental processes occurring during the MOVPE crystal growth are commonly subdivided into three components, namely, thermodynamics, kinetics, and hy-

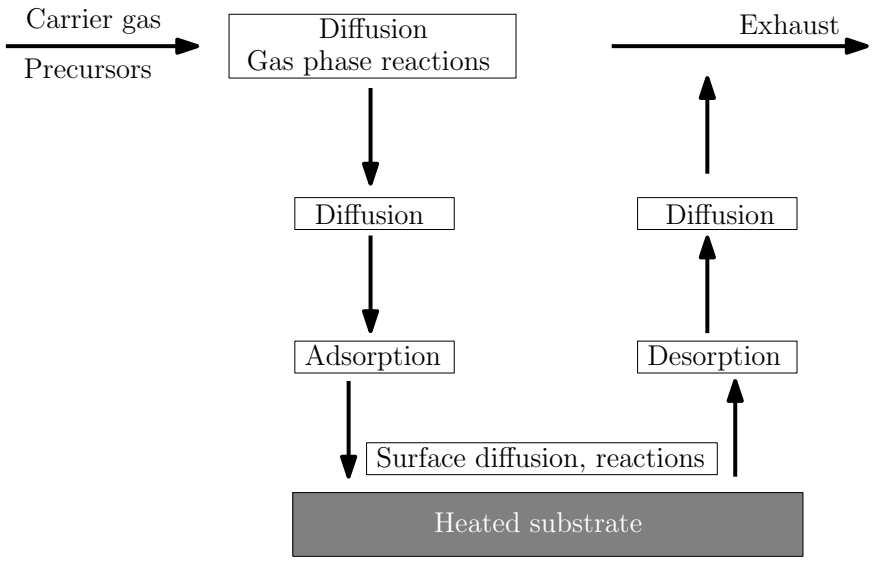

Figure 3.1: General reaction steps in an MOVPE process.

drodynamics. Thermodynamics, which is underlying the MOVPE growth process, determines the driving force to the overall epitaxial growth, maximum growth rate, and number and compositions of the equilibrium phases on the surface. It is concerned with the energy of the system in the initial and final equilibrium states. Kinetics gives insight into how the chemical reactions occur, including the determination of reaction rates, reaction mechanisms and the identification of rate determining steps. Hydrodynamics controls not just the mass transport of the species to the growing solid/vapor interface but also the temperature distribution, the velocity profile and total pressure in the reactor. Each of these components will dominate some aspect of the overall growth process. Modeling and a detailed description of the general MOVPE growth process can be found elsewhere [122–124]. However, most of the MOVPE growth parameters are reactor dependent, i.e. the growth being dependent on the reactor geometry coupled with the fluid dynamics and heat and mass transfer. This makes the translation of experimental data from one reactor to another reactor type and also the scale-up of reactors very uncertain. In these circumstances, despite their disadvantages (time consuming, high costs), the trial-and-error methods are still important in developing new MOVPE growth processes. A similar approach is taken in this work to establish the AlN growth process in the existing commercial reactor.

In a classic paper, Shaw [125] showed a general categorization of MOVPE growth process into three growth temperature regimes, namely, kinetically limited, mass transport limited, and thermodynamically limited. A plot imaging the growth rate versus reciprocal temperature is shown in Fig. 3.2.

In the kinetically limited regime at low temperatures, the chemical kinetics (surface reactions) are slower than mass transport and will limit the overall growth rate, which will increase exponentially with the temperature. In the mass transport limited regime at intermediate temperatures, the chemical kinetics become faster, and the mass transport (gas diffusion to and away from the surface) is the rate limiting step. The diffusion

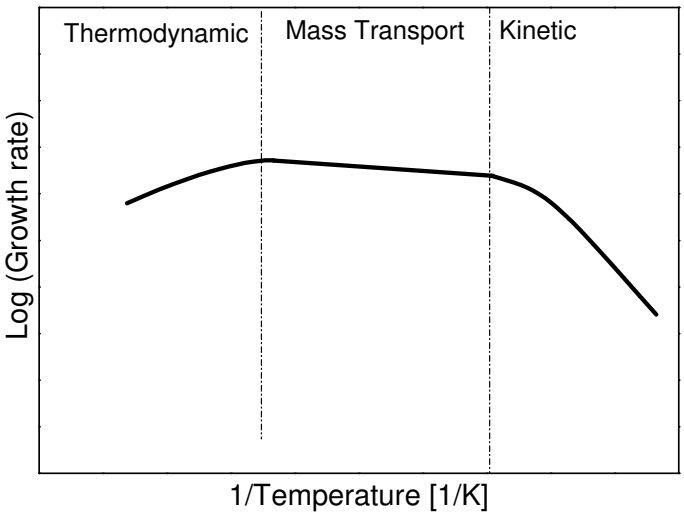

Figure 3.2: Qualitative temperature dependence of the growth rate for an MOVPE process.

is also comparably fast. That is why the mass flow into the reactor is the limiting factor. Since the mass transport has only a weak temperature dependence, the growth rate is nearly constant. In the thermodynamically limited regime at high temperatures, the thermodynamics will try to restore the equilibrium (through increased desorption rate, gas phase reactions and depletion of the reactants on reactor walls), limiting the growth rate which will decrease as the temperature increases.

Beside temperature, for each growth regime there are also other factors which may influence the overall growth process. For the thermodynamically limited regime where the overall growth rate decreases as the temperature increases due to possible depletion routes (adduct formation, wall deposits), parameters such as reactor geometry and, importantly, the time residence may influence considerably the growth. When the mass transport limits the overall growth rate, parameters such as total flow which enters the reactor, flow velocity and reactor pressure must be taken into account. In the kinetically limited case, where the surface plays an important role, the substrate issue, including the initial orientation or surface treatments must be considered.

In contrast to the conventional compound semiconductors, such as arsenides, phosphides, and antimonides, the MOVPE growth of group-III nitrides is challenging. Because of the high group-III-N bond strength, the growth of group-III nitrides requires typically high growth temperatures for the growth of high-crystalline-quality material. Typically, the mass transport is the most favorable regime for the growth of group-III nitrides, specially the growth of (In)GaN and low Al content AlGaN layers. However, the growth of good quality AlN layers needs a very high temperature. Therefore, we expect the shift of favorable growth regime towards the thermodynamically limited regime. In the following chapter, we will address this issue during the growth optimization of AlN layers.

3.2 Precursors and Chemistry of Epitaxial Growth of AlN

The commonly used precursors for the growth of group-III nitrides are trialkylcompounds of the group-III elements as metalorganic (MO) precursors and NH_3 as N_2 precursor. There can be severe pre-reactions between the trialkylcompounds of group-III and NH_3. The metalorganic (MO) precursors readily form Lewis acid-base type adducts with NH_3. The adducts have low vapor pressure and their presence leads to changes in the composition of the gas phase as well as depletion of the actual growth precursors that can result in degradation of growth uniformity and efficiency, and material quality. Such consequences are much more serious for the growth of AlN and high Al content AlGaN layers because of the high reactivity of Al-adducts. Similar to the MOVPE growth of other III-V compounds, the group-III nitride MOVPE growth process is complex and involves both gas-phase and surface reactions. The difficulties related to the chemical nature of group-III nitride MOVPE growth arise mainly from the peculiarities of the process: (i) the possible pyrolysis of both MO precursor and NH_3 and the reactions between them as well as the reactions between the resulted decomposition fragments can occur both in the gas (homogeneous reactions) and at/on the substrate surfaces or reactor walls (heterogeneous reactions); (ii) the chemical species involved are very unstable at the employed reactor temperatures and pressures or are present at concentrations that vary depending on the position in the reactor (near to or far from the heated substrate). Accordingly, qualitative and especially quantitative analysis of the chemical species are difficult and can give conflicting results depending upon the modalities used for sampling the gas mixture and the experimental conditions employed during the growth process.

The next sections will briefly review the general properties of the precursors employed in this study of MOVPE growth of AlN and $Al_xGa_{1-x}N$: trimethylaluminium (TMAl), trimethylgallium (TMGa) and NH_3. Furthermore the chemistry which governs the MOVPE growth for AlN and $Al_xGa_{1-x}N$ using these precursors will be described.

3.2.1 Precursors

Trimethylaluminium (TMAl)

TMAl is one of the most often employed Al precursors in MOVPE growth of AlN and $Al_xGa_{1-x}N$. It has the chemical formula of $(CH_3)_3Al$. It is a very strong electron acceptor (Lewis acid) due to the tendency of aluminum to use completely its valence orbitals and readily form intermolecular bonds by self-association such as the dimeric molecule or adducts with other electron donor molecules (Lewis bases) in which Al has a fourfold coordination. Specially, when TMAl evaporates, it contains a dimeric molecule, i.e. every molecule in the vapor contains two Al atoms as shown here: $(CH_3)_6Al_2$ [25,126]. One of the crucial parameters of MO precursors is the vapour pressure that governs the concentrations of MOs entering the reactor, and subsequently the rate of deposition in MOVPE process. The vapor pressure depends on the bubbler temperature, and material constants. The molar flow rate of MO precursor can be calculated using the vapor pressure. In this work, we have maintained the TMAl

bubbler temperature at 17 °C (liquid state) and the vapor pressure is calculated to be 9.77 mbar. One should take into account the dimeric property of TMAl while calculating the incorporation efficiency of Al and Ga species in the $Al_xGa_{1-x}N$ layers. We will present this study in chapter 6. However, a monomer-dimer equilibrium has been observed in the vapor form from 100 °C to 160 °C the heat of dissociation into 2 moles of $(CH_3)_3Al$ being 85.3 kJ/mol [127, 128]. It means the gas-phase decomposition of TMAl is a complex reaction chemistry. There are several studies concerning the pyrolysis of this compound [129, 130]. TMAl decomposition has been proposed to occur through the loss of CH_3 radicals and formation of different -CH_n (n < 3) fragments in the intermediate stages. The chemistry of the growth of AlN and $Al_xGa_{1-x}N$ will be given in the following subsection.

Trimethylgallium (TMGa)

Despite of the fact that Ga follows Al in the group-III, the Ga-compound does not present the same chemical properties of Al-compound. TMGa ($(CH_3)_3Ga$) is less reactive and a weaker electron acceptor than TMAl. Due to the Lewis acid character, TMGa is also susceptible to form adducts, even at room temperature, with different donor molecules, like NH_3 in MOVPE. However, it does not show the tendency for stabilization by dimerization, therefore, it has monomeric property in both vapor and liquid phases. The bubbler temperature of TMGa was maintained at -4 °C (liquid state) and the corresponding vapor pressure is 69 mbar. Experimental and theoretical studies on the thermal decomposition of TMGa are reported in [131–133].

Ammonia (NH_3)

It is the most commonly employed nitrogen source in the group-III nitride growth. It has a very poor cracking efficiency without catalyst. The lone pair of electrons enables NH_3 to act as a Lewis base in interactions with the MO precursors, forming adducts which may influence the growth process. In the growth of GaN, great amounts of NH_3 are typically employed in order not just to generate active species containing nitrogen for growth but also to compensate the high volatility of nitrogen from the growing layer. In contrast, a small amount of it is employed in the growth of AlN because the Ga species at the gas/solid phase are less reactive than the Al species. Although a small amount of NH_3 undergoes homogeneous decomposition in the gas phase, most of it undergoes heterogeneous decomposition on the surfaces, generating active species containing nitrogen for growth. In MOVPE growth environment, non-decomposed NH_3 in gas phase can reach the growth surface where its dissociative chemisorption occurs [134]. Generally, once chemisorbed on the surface, NH_3 will dissociate generating H and NH_x ($x < 3$) species. The adsorbed NH_x species can either dissociate to adsorbed N and H atoms or combine with adsorbed H to reform NH_3 [135, 136].

3.2.2 Chemistry of Epitaxial Growth of AlN

MOVPE of group-III nitrides involves complex gas-phase and surface reactions combined with flow, heat transfer, and mass transfer processes. The results of these physical and chemical rate processes determine the quality of the deposited layers. In MOVPE, the NH_3 excess should be high enough to achieve a good crystalline quality of the material. At the same time, the MO supply should be sufficient to provide reasonable growth rate of the epitaxial layers. However, during the growth of AlN, high TMAl and NH_3 flow rates may promote severely parasitic gas-phase pre-reactions between these precursors [137,138]. In addition, the high temperatures required to deposit high-quality material can further increase the rate of such parasitic chemical reactions [139]. These reactions ultimately lead to nanoparticle formation and consume a significant fraction of the group-III precursor [140–142]. Creighton *et al.* [142] directly observed AlN nanoparticles in the reactor by in situ laser light scattering. Particles are carried away from the reactor by the flow, removing material from the gas-phase and thus diminishing growth efficiency. There are several reports on the effect of parasitic reactions [139,143–145]. The prominent effect is the reduction of both the Al concentration in the solid and AlGaN growth rate with increasing NH_3 flow rate. It was also mentioned that the surface roughness is dependent on parasitic reactions [144]. It was suggested in Ref. [144] that small clusters of atoms, existing in the growth volume in excess at high rates of pre-reactions, reach the wafer, resulting in poor surface morphology. We have also observed similar effects of parasitic reactions on our AlN layers. We will explain in detail in the proceeding section and the following chapter how such problems were dealt in our studies.

Mihopoulos *et al.* [140] proposed a theoretical kinetic model of the gas-phase and surface chemistry in MOVPE during the growth of AlN as illustrated schematically in Fig. 3.3.

The adduct TMAl:NH_3 formation between TMAl and NH_3 occurs instantaneously upon mixing followed by the elimination of methane to give a DMAl:NH_2 species and

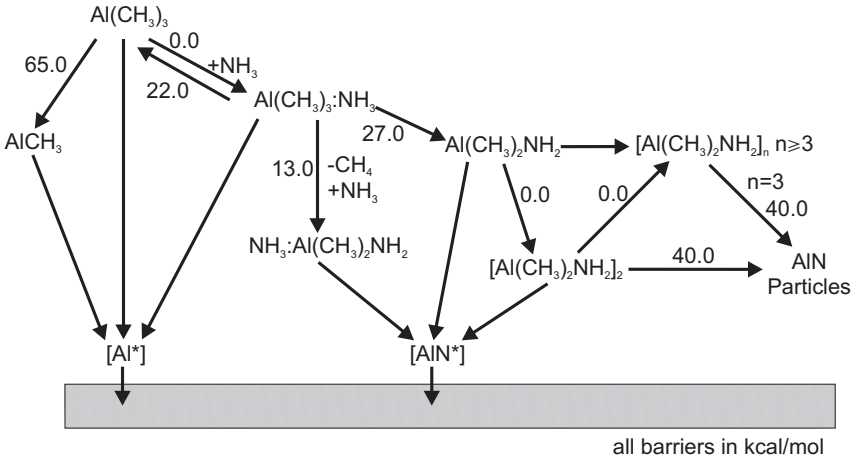

Figure 3.3: Schematic of the AlN deposition and reaction pathways [140].

formation of oligomers. The kinetic mechanism of particle formation was reconsidered by Yakovlev *et al.* [146]. It was assumed that AlN particles nucleate through the interaction between AlN gaseous molecules originating from decomposition of dimers and trimers containing both Al and N. Subsequent growth of solid particles is due to the reactions between AlN nuclei and Al-containing species such as $DMAlNH_2$ and $[DMAlNH_2]_2$.

Lobanova *et al.* [147, 148] from STR Group Soft-Impact Ltd., St. Petersburg, Russia carried out computer simulations of AlN growth in MOVPE by considering our growth conditions and parameters. They proposed a model [1] that explains the observed tendencies by the competition between two reaction pathways: an adduct-to-TMAl no-losses pathway and an adduct-to-monomer pathway responsible for particle formation. At low NH_3 flow rates, the growth is primarily governed by the adduct-to-TMAl pathway. Mixing of TMAl and NH_3 gives rise to $TMAl{:}NH_3$ adduct at the reactor inlet (Eq. 3.2). Then, $TMAl{:}NH_3$ decomposes back into TMAl downstream at elevated temperatures. Consequently, AlN layers grow on the wafer without any losses, owing to effective transport of TMAl to the susceptor.

$$TMAl + NH_3 \rightleftarrows TMAl : NH_3. \tag{3.2}$$

At high NH_3 flow rates, the adduct-to-monomer pathway prevails. Adduct coordination with a second NH_3 molecule intensifies the methane elimination reaction giving rise to $DMAl{:}NH_2$ monomeric species (Eq. 3.3). The monomer is responsible for the subsequent formation of dimers (Eq. 3.4) and high-order oligomers (Eq. 3.5). At enhanced temperatures, the dimers and trimers, in turn, eliminate methane radicals to form AlN vapor, responsible for nucleation of AlN particles (Eq. 3.6). According to the model, large amounts of the monomer, dimer and AlN vapor promote subsequent particle growth.

$$TMAl : NH_3 + NH_3 \rightarrow DMAl : NH_2 + CH_4 + NH_3. \tag{3.3}$$

$$2DMAl : NH_2 \rightarrow [DMAl : NH_2]_2. \tag{3.4}$$

$$n \cdot DMAl : NH_2 \rightarrow [DMAl : NH_2]_n,\ n = 3, 4, ... \tag{3.5}$$

$$[DMAl : NH_2]_2, [DMAl : NH_2]_3 \rightarrow AlN(vapor) \rightarrow AlN(solid). \tag{3.6}$$

[1] **Modelling of AlN growth:** Modeling includes detailed 3D calculations of fluid dynamics, heat transfer and species transport, gas-phase and surface chemistry, as well as nucleation, growth and transport of AlN nanoparticles. The gas-phase chemistry model is based on the paper by Mihopoulos *et al.* [140]. The kinetic mechanism of particle formation was reconsidered by Yakovlev *et al.* [146]. The effect of thermophoresis on particle transport was taken into account. To simulate the surface chemical processes, the quasi-thermodynamic model [149] has been applied. The model considers adsorption/desorption to be the limiting stages of the deposition process, whereas other stages are assumed to proceed under near-equilibrium conditions. The computations were performed using the CVDSim software package [http://www.str-soft.com]. The AlN MOVPE model was previously verified on the data obtained in various reactors [147, 150].

To minimize pre-reactions, a balance between TMAl and NH_3 flow rates is necessary. We have experimentally determined the effect of flow rates on the growth rate and the quality of the AlN layers in chapter 4. Meanwhile, the growth pressure, total flow, and the reactor geometry are other influencing factors on the pre-reactions of precursors. We have carried out a systematic studies on this issue and determined an optimum growth condition of AlN in our MOVPE reactor.

3.3 MOVPE-System AIXTRON AIX 200 RF

In this work, the growth of AlN and $Al_xGa_{1-x}N$ layers was carried out in a AIXTRON AIX200RF system (Fig. 3.4) utilizing the state-of-the-art MOVPE technology. This system is one of the first commercial reactors manufactured by AIXTRON for the growth of AlGaAs. Later on, the system was modified for the growth of GaN. It is equipped with a water-cooled quartz glass horizontal reactor as illustrated in Fig. 3.5 (upper). The reactor is structured in a co-axial form using quartz tubes: the inner (liner), inside which the susceptor (a massive body made from graphite and coated with SiC to hold the wafer) is positioned, surrounded by another pair of outer quartz tubes. The



Figure 3.4: Image of AIXTRON AIX200RF MOVPE system .

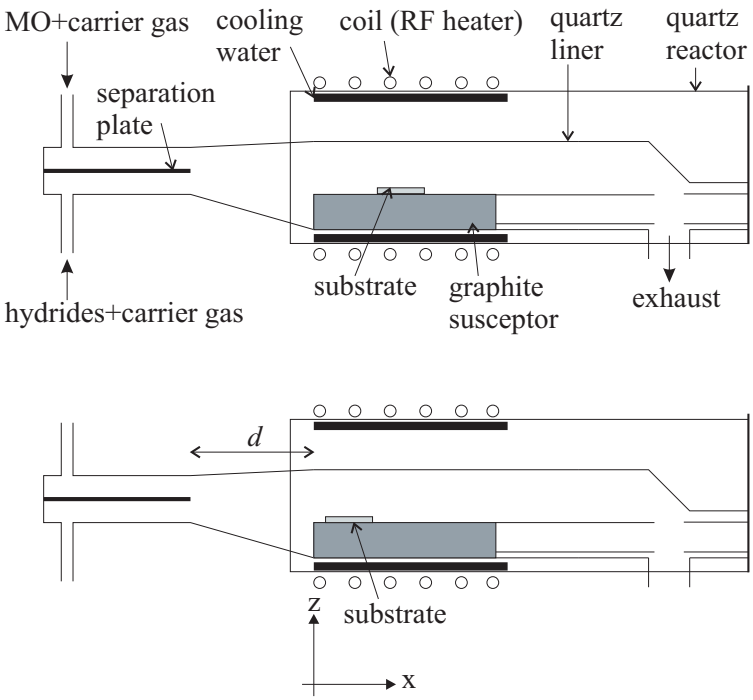

Figure 3.5: Schematic of AIXTRON AIX200RF MOVPE reactor. Conventional susceptor where the substrate is placed at the rotating disk on the center of the body (upper). Modified susceptor where the substrate is placed on the gas inlet part of the reactor for the growth of AlN (below).

cooling water is channeled through the outer pair of the quartz tubes. The required high temperatures (upto 1200 °C) are achieved by inductive heating of the susceptor by using a radio-frequency (RF) spiral coil with the spirals distributed equidistant along the reactor ensuring a uniform temperature distribution over the wafer. Two thermocouple elements are inserted inside the body of the susceptor to control the temperature. All growth temperatures mentioned in this work are thermocouple temperatures which may differ from the real susceptor surface and substrate temperatures due to a temperature gradient inside the susceptor body.

In the conventional design, the susceptor consists of a rotating disk at the middle of its body (Fig. 3.6). The rotating disk is rotated by gas foil rotation technique using N_2 or H_2. An infra-red pyrometer is used to measure the temperature of the rotating disk. We observed that the surface temperature of the rotating disc was lower than the body temperature of the susceptor by approximately 30 °C. This result is expected because the rotating disk is lifted by the gas during the rotation. It causes the electromagnetic coupling of the disk with the induction coil to be different from the massive body of the susceptor.

Meanwhile, it is expected that the heated graphite block can influence the transport of the chemical species participating in the growth and subsequently affect the surface reactions. As mentioned above, the rate of NH_3 decomposition is very high on the solid interface. The front part (5 cm long) of the susceptor may facilitate the decomposition

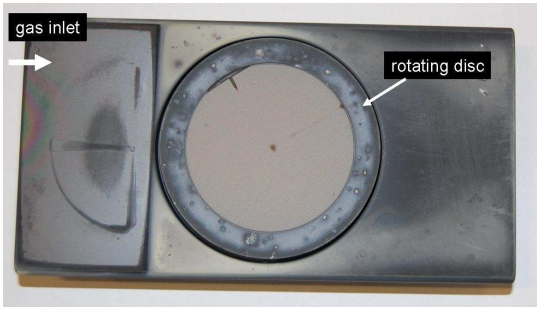

Figure 3.6: Conventional SiC coated graphite susceptor used in AIX200RF reactor. The rotating disc is shown at the center.

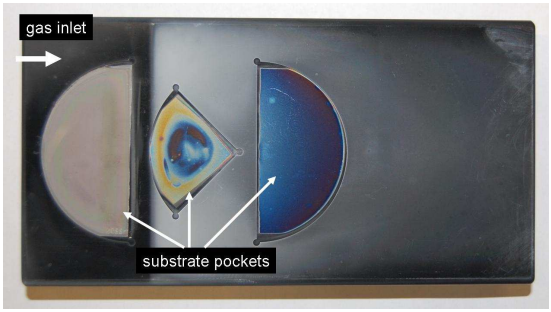

Figure 3.7: Modified SiC coated graphite susceptor for the growth of AlN in AIX200RF reactor. Half of a two inch wafer is placed at the substrate pocket on the gas inlet side of the susceptor for the growth. Provisions of other substrate pockets are also shown.

of NH_3. A longer residence time of the precursors at the heated zone of the reactor further increases the rate of parasitic pre-reactions between already decomposed NH_3 and TMAl species. Thus, to minimize the effect of parasitic reactions, the substrate positioning was changed from the conventional downstream middle place of the susceptor to the upstream gas inlet position as shown in Fig. 3.5 (below).

The modified susceptor for the growth of AlN is shown in Fig. 3.7 at which a half of a two-inch wafer is placed at the substrate pocket near to the gas inlet part of the reactor. There are also provisions for other substrate pockets at different places. The MOVPE growth of AlN using such a modified susceptor has several advantages. First,

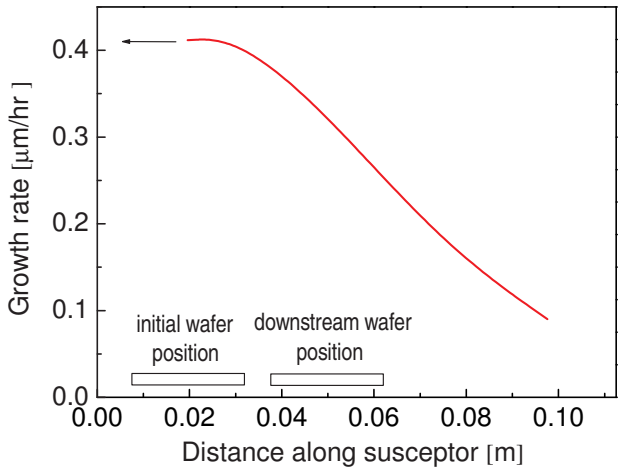

Figure 3.8: Calculated growth rate distribution along the susceptor [148].

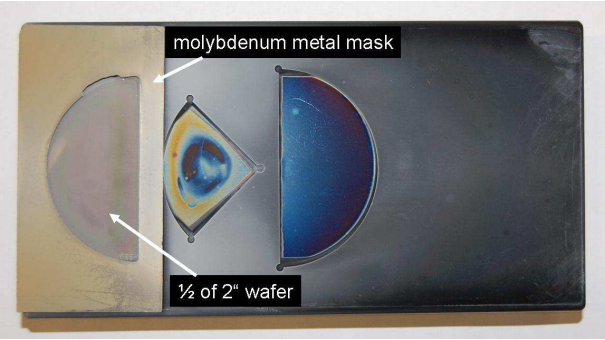

Figure 3.9: Molybdenum metal mask at the substrate pocket.

the residence time of the precursors at the heated zone of the reactor is decreased. Hence, the surface reactions at the front part of the susceptor are dramatically reduced. Secondly, the surface temperature of the substrate pocket in the new susceptor is approximately 30 °C higher than the surface temperature of the rotating disc. However, the most significant advantage of using rotating disc in a MOVPE growth, i.e. obtaining on-wafer homogeneity and thickness uniformity of the grown layer, was entirely sacrificed in this arrangement. Nevertheless, this arrangement has helped fulfilling the main objective of this study, i.e. obtaining a good crystalline quality of AlN layer in the existing reactor. Thus, the layer uniformity is not considered here.

Figure 3.8 shows the variation of the calculated growth rate of AlN using the modified susceptor [148]. The initial wafer position was the substrate pocket near the gas inlet part of the reactor and the downstream position was the conventional position. A clear advantage of higher growth rate is observed while using the modified susceptor. We obtained similar results in our AlN growth experiments.

Furthermore, a molybdenum metal mask was placed at the substrate pocket as shown in Fig. 3.9. The susceptor temperature was further increased by approximately 20 °C by using the metal mask. This is basically due to the electromagnetic coupling of the metal to the RF heating coil. Heat losses due to the radiation of susceptor was suppressed underneath the metal mask. Therefore, the metal mask confined more heat in the vicinity of the substrate. Consequently, the substrate temperature was further increased. With all these arrangements as described above we were able to grow AlN at relatively high temperature in our system.

In this MOVPE system, the growth pressure can be adjusted between 25 and 900 mbar. The carrier gases are N_2 or H_2. Further details of this system can be found in [124].

3.4 *In-Situ* Characterization in MOVPE

In this work, normalized optical reflectometry has been used for *in-situ* monitoring the epitaxial growth. The normal reflectance signal offers a convenient method for the growth rate determination. It is also a useful tool for monitoring the growth

steps. Our MOVPE system is equipped with a commercially available reflectometer system consisting of a white light source and a CCD spectrometer (Filmetrics F 30) as shown in Fig. 3.10. The spectrometer is a 512-element photodiode array with a spectral range of 400-1000 nm with a resolution of 2 nm. A detailed description of the installed reflectometer in our MOVPE system is found in [124].

The thickness of the layer which is grown during one oscillation of the reflectometry curve can be approximately calculated using the following equation [1, 124]

$$d_{\mathrm{AlN}}[\mathrm{nm}] = \frac{\lambda_m}{2\overline{n}}, \tag{3.7}$$

where λ_m is the measuring wavelength of the spectrometer in nm and $\overline{n}$ is the refractive index of AlN at the measuring wavelength. The oscillations are resonances of the layer system, where the resonator is formed by the AlN layer and the refractive index steps of the transitions AlN/sapphire and AlN/gas phase, respectively. The refractive index of AlN at the spectrometer wavelength of 580 nm is 2.4 [29] and does not change much with temperature [1]. Thus the values of the thickness calculated during growth (hot substrate) agree well with the data measured at room temperature using SEM. *In-situ* reflectometry provides direct information on any change of growth parameters (pressure, temperature, fluxes) affecting either growth rate (change of oscillation width) and/or surface roughness (change of oscillation amplitude). Development of the surface

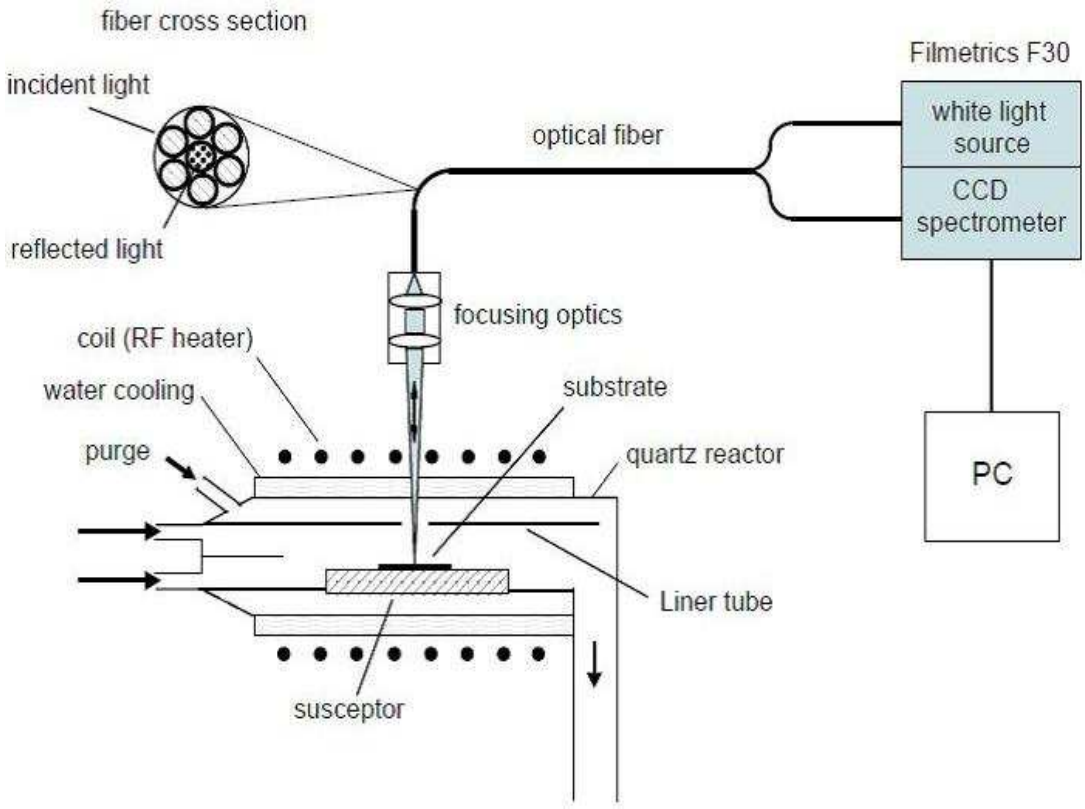

Figure 3.10: *In-situ* reflectance setup at the AIX 200 RF horizontal MOVPE reactor.

morphology is indicated by the course of amplitudes in the reflectance spectrum. Figure 3.11 shows the *in-situ* reflectance curves obtained from two different AlN epi growth processes. The oscillations of the first curve (1) have an almost equal amplitude and the curve is horizontally aligned. It is an indication of the emerging flatness of the grown epilayer surface. The second curve (2) has a downward slope and the amplitude of the oscillations is also decreasing. This is an indication of the roughness of the grown epilayer surface.

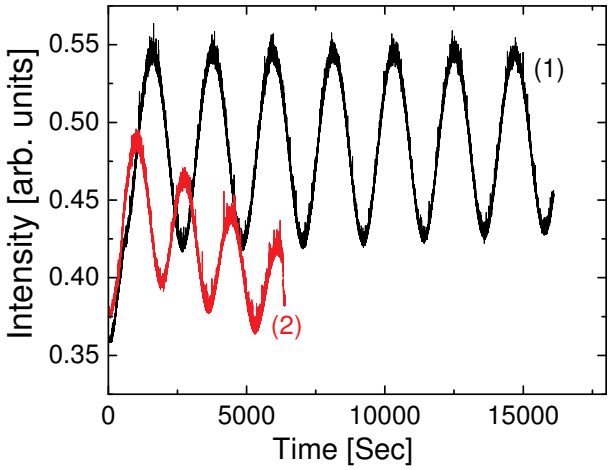

Figure 3.11: *In-situ* reflectance curves obtained from two different AlN epi growth processes.

Chapter 4

MOVPE Growth of AlN

As mentioned in the previous chapters, the growth of high quality epitaxial layers of AlN is still a big challenge for the nitride researchers. The difficulties arise predominantly from the high AlN bond strength of 2.88 eV. As a consequence, pre-reactions increase, and the adsorbed Al-species possess a low surface mobility due to high adsorption energies. In this chapter, we will describe the epitaxial growth of AlN layers on sapphire substrate using MOVPE technique in our AIXTRON AIX200RF system and investigations of the structural and spectroscopic properties using the characterization techniques described in chapter 2. The different growth stages are analyzed and the influence of independent growth parameters such as precursor flows, V–III ratio, total flow-rate, carrier gas composition, growth temperature and pressure on the nucleation and final layers of AlN are investigated. Finally, an optimum growth condition is empirically determined. The epitaxial layers were evaluated using indirect *ex situ* techniques like AFM, HRXRD, and CL. At the end, we will present the results of AlN epilayers grown on SiC and native AlN substrates.

4.1 Introduction

In this study, c-plane sapphire (0.3 ° miscut towards m-plane) was used as a primary substrate for the growth of AlN layers. The economy and the easy availability were prime reasons for the use of sapphire despite a large lattice mismatch and large difference in thermal expansion coefficients. However, few experiments were carried out on SiC and native bulk AlN substrates, too. TMAl and NH_3 were used as group-III and group-V precursors, respectively. H_2 was used as a carrier gas and the growth was carried out in H_2 and N_2 ambient.

Amano *et al.* [10] reported a successful growth of high-quality GaN films using a two-step growth process for the first time in 1986. Now, this process, as illustrated in Fig. 4.1, is almost established as a standard method for the heteroepitaxial growth of group-III nitrides by MOVPE. In this work, we employed two-step, multi-step, and direct growth processes.

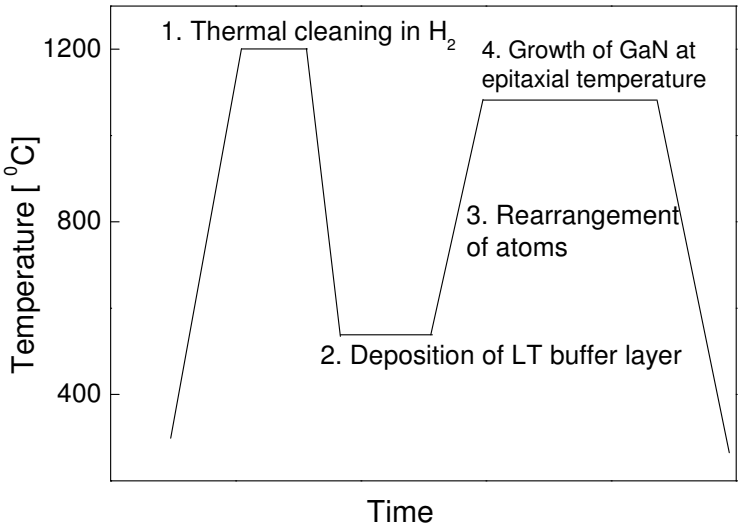

Figure 4.1: Temperature sequence of the MOVPE growth of GaN and the process of the LT buffer layer.

4.2 Two-step Growth Process on Sapphire

We started the optimization of the growth of AlN by employing a so-called two-step growth process similar to GaN. Although it is called a two-step process, the entire growth process in fact was a succession of more than two steps. The optimization process is, basically, divided into four parts, namely

- Desorption and nitridation of sapphire
- Medium-temperature (MT) nucleation layer (NL)
- Stage between nucleation and epitaxial layers
- High-temperature epilayer.

During optimization of each of the above mentioned parts, the growth condition of the other parts was kept constant. The basic structure of the sample contains an approximately 500 nm thick undoped AlN epilayer deposited over approximately 20 nm thick MT AlN NL.

4.2.1 Desorption and nitridation of sapphire

In the first step of the growth process, the as received sapphire substrates were heated at a high temperature of 1150 °C in H_2 environment for about 5 to 10 minutes. The organic molecules would be desorbed if there was any contamination. Therefore, this

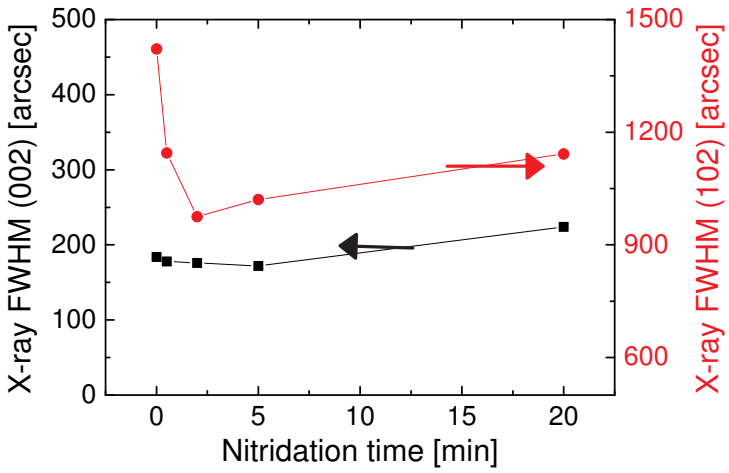

Figure 4.2: The effect of nitridation time on the symmetric (002), and skew-symmetric (102) FWHM of X-ray rocking curve.

step is also called desorption. When the thermal treatment is done in the presence of NH_3, then it is called nitridation.

Nitridation initiates nucleation of AlN islands and forms a very thin nucleated layer. Various conflicting results have been reported on the state of such a nucleated layer. Some studies showed that this layer was amorphous AlN_xO_{1-x} [151, 152], however, some presented the evidence of the formation of crystalline AlN [153–155]. It was speculated that one or two monolayers of the nucleated layer might be crystalline AlN. Because of the limitations of chemically active Al atoms, excessive nitridation cannot prominently increase the nitridated layer thickness [156]. Instead, excessive NH_3 induces un-stoichiometric growth which may degrade the nitridated layer crystal structure. Meanwhile, the density of nucleated islands decreases with increasing time period of nitridation upto an optimum value [114]. This is due to the lateral growth of islands for a certain time period of nitridation. Furthermore, Yeadon *et al.* [155] reported the transition of the nitridated layer into a polycrystalline phase with excessive nitridation duration (120 min).

In our case, we did not observe a clear impact of nitridation on the structural and surface quality of AlN epilayers when the growth was proceeded with a deposition of medium-temperature (MT) AlN nucleation layers. However, we observed a deteriorating surface quality of AlN layers with increasing nitridation time when grown directly on sapphire without nucleation layer. Others [157–159] also reported similar observations. Paduano *et al.* [114] reported that nitradation often consists of mixed Al- and N-polarity domains. Because of the significant differences in growth rate, AlN epilayers with such mixed polarity domains exhibit rough surface morphology. Since Al-polarity domains normally grow faster than N-polarity domains in the [0001] direction, the N-polarity layer does not typically have a smooth surface morphology. Longer nitridation increases the N-polarity domains and it may be another reason for the increase of surface roughness. The intrinsic in-plane tensile strain and the formation of cracks were other critical problems in directly grown samples. Therefore, such

problems necessitate the deposition of a mid-temperature nucleation layer prior to the growth of the high temperature AlN layer. However, a shorter duration of nitridation has a positive impact on the crystal quality of the directly grown layers. Figure 4.2 exhibits the effect of the nitridation time on the FWHM of symmetric (002), and skew-symmetric (102) X-ray rocking curves. The FWHM of both rocking curves was varied with the nitridation time, showing a seemingly optimum value for a moderate nitridation time of 2 minutes. Broadening of the rocking curves in prolonged nitridation depicts the fact that lack of a correct nitridation leads to samples with poor crystalline quality.

4.2.2 Medium-temperature nucleation layer

To overcome the problems of a large lattice mismatch and a large thermal expansion coefficient difference between the wurtzite group-III nitride and sapphire, a low-temperature (LT) (below 600 °C) nucleation layer (NL) of AlN [10] or GaN [160] is employed as an initial growth step before the deposition of the final epilayer. The NL acts as a buffer layer between the sapphire and the epilayer. More interestingly, Kuhn and Scholz [161] earlier reported that a slightly oxygen doped MT AlN NL gives an excellent result for the GaN epilayer. In this study, we have also tried medium temperature (MT) (above 800 °C) NL with oxygen doping during AlN nucleation and found a positive impact on the succeeding high-temperature (HT) (above 1100 °C) AlN epilayer. It is noteworthy to mention here that the surface of the MT-AIN NL might be covered by a thin molten layer of Al when a HT layer is deposited because the wettability of Al on AlN is much better than that on sapphire [162, 163]. It is expected because the supply of NH_3 for the growth of AlN is very low in comparison with the growth of GaN.

In the beginning, samples were desorbed in H_2 ambient at 1150 °C for 10 minutes, nitridated at 1000 °C for 3 minutes, then the nucleation was started. Next, a 10 minutes annealing step was carried out under H_2 and N_2 ambient with a constant flow of NH_3. The growth temperature of the AlN epilayer was set to 1150 °C. During the optimization of the NL, the growth conditions of the subsequently deposited AlN epilayers were kept constant as given in Tab. 4.1. The range of growth parameters of the NL is also shown in the table.

Oxygen from t–Butanol (t-CHO) used as a liquid source in conventional bubbler configuration was supplied in the form of pulses (2 sec ON, 28 sec OFF) whereas TMAl and NH_3 were turned ON throughout the nucleation process. The precursor flow time line is illustrated in Fig. 4.3. This source of oxygen was then readily available in our MOVPE system. As we need a very small amount of oxygen doping during the NL growth, the pulsed supply could be an effective method to precisely control the amount. This method offers a good controllability as we can vary both the pulse width and the period in addition to the mass flows.

We started the optimization process of the NL by fixing its deposition time at 10 minutes and employing 21 cycles of oxygen pulses as mentioned above. At this growth condition, the NL thickness was expected to be approximately 35 nm. Growth parameters like the precursor flows, the reactor pressure, the deposition temperature

Table 4.1: Growth conditions of subsequently deposited AlN epilayer on NL and range of growth parameters for NL optimization.

Growth Parameters	Subsequently grown AlN epilayer	Range for nucleation layer optimization
Growth Pressure	35 mbar	35 - 100 mbar
Growth Temperature	1150 °C	820 - 930 °C
V–III Ratio	2000	500 - 18000
N_2–H_2 Ratio	1.3	0.8 - 4.0
Total Flow	2500 sccm	1500 - 5000 sccm

and the growth duration were varied in order to find the optimal parameter window. One of the most critical parameters was the NL thickness. It should not be very thick otherwise not only the NL but also the successive layer may become polycrystalline. However, the layer thickness is dependent not only on the growth time but also on other growth parameters like the precursor flows and the reactor pressure. By changing the precursors flows, the rate of pre-reactions is changed which consequently affects the thickness of the deposited material. Similarly, by lowering the reactor pressure, the pre-reactions can be suppressed and the layer thickness can also be increased. Therefore, the variation in these growth parameters ultimately varies the layer thickness.

The quality of the NL was reflected in the structural properties of the succeeding AlN layer. The controlled figures of merit were: The rocking curve FWHM of the AlN (002)-reflection, and the surface roughness.

To observe the pre-reactions between NH_3 and TMAl, we fixed the TMAl flow at 5 μmol/min (minimum flow) and decreased the NH_3 flow in several steps from 3000 sccm to finally 150 sccm. Other growth parameters: the growth temperature, the reactor pressure, N_2-H_2 ratio, and the total flow were fixed at 850 °C 100 mbar, 2.0, and 2500 sccm, respectively. Figure 4.4 (left) illustrates the influence of the NH_3

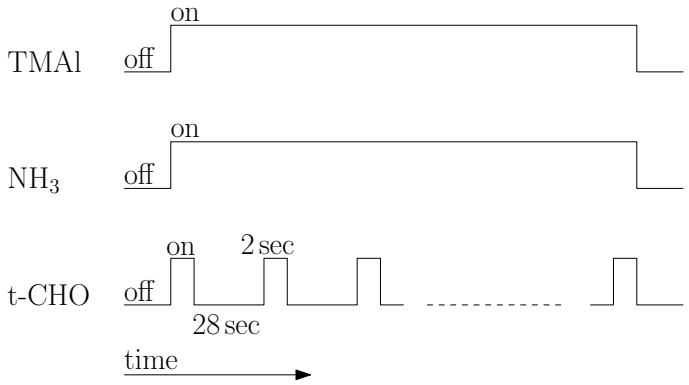

Figure 4.3: Illustration of precursors (TMAl, NH_3, and t-CHO) flow time line.

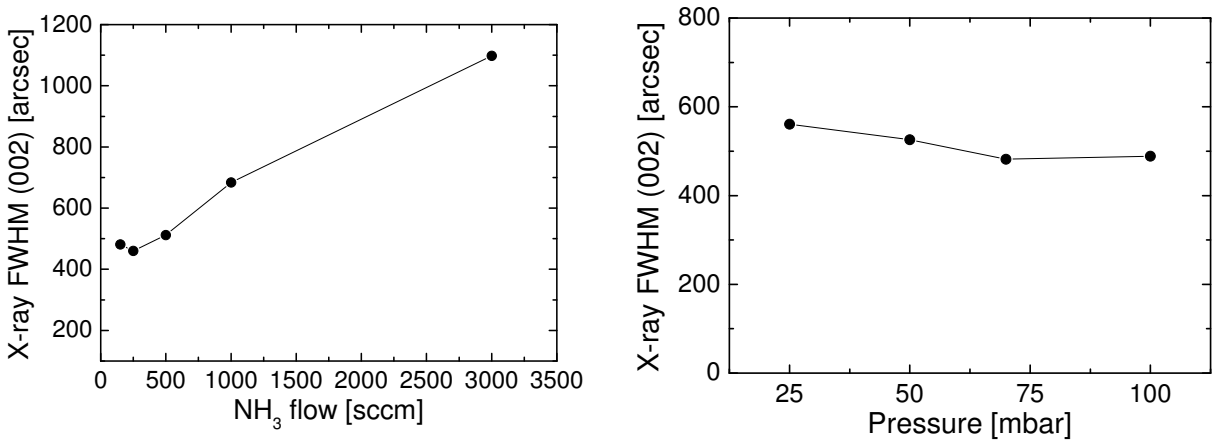

Figure 4.4: HRXRD rocking curve FWHM of the (002)-reflection in dependence of the NH_3 flow at a constant TMAl flow of 5 μmol/min (left) and the reactor pressure (right).

flow during the NL growth on the AlN crystal quality. The FWHM of the symmetric (002)-reflection (HRXRD) was reduced from 1098 arcsec (3000 sccm) to a minimum of 460 arcsec (250 sccm). However, it was slightly increased when the NH_3 flow was further reduced to 150 sccm. The surface of all samples was heavily pitted and it was not possible to analyze the effect on the surface morphology using AFM.

Next, we changed the reactor pressure by keeping the NH_3 flow fixed at 250 sccm and the rest of the growth parameters constant as given above. We observed that the FWHM of the symmetric (002)-reflection (HRXRD) was slightly decreased at 70 mbar and then increased again with decreasing pressure as shown in Fig. 4.4 (right). By reducing the reactor pressure, the parasitic reactions can be suppressed which causes the increase in layer thickness. The broadening of the rocking curve might be attributed to the thicker NL. The surface of the AlN epilayer was again heavily pitted.

In the next step, we varied the growth time while keeping the reactor pressure fixed at 70 mbar and the rest of the parameters constant as before. The switching rate of oxygen supply was also kept fixed (Fig. 4.3). Both the RMS surface roughness and the FWHM of HRXRD for the (002)-reflection of the AlN epilayers were minimum when the growth time was 2 min 30 secs. and the number of oxygen pulses was 5 in comparison to the NL without and with the supply of larger number of oxygen pulses (longer growth times) (Fig. 4.5 (left)). We deposited a NL without oxygen for a time period of 2 min 30 secs, exactly the same time period as of 5 oxygen pulses. in this case, the NL thickness was estimated to be about 10 nm. Figure 4.6 (left) shows an AFM image of a sample with 20 pulses of oxygen (growth time: 10 min). It shows the presence of a large number of hexagonal pits having large diameter ($\geq$ 20 nm). A similar result was observed on the sample without oxygen supplied into the NL.

Next, the growth period of NL was further extended without oxygen supply after the supply of 5 pulses of oxygen at the beginning of the nucleation process as demonstrated in the inset of Fig. 4.5 (right). The plot in this figure shows the RMS surface roughness and the FWHM of X-ray (002)-reflection of the AlN epilayers against the extended growth time periods of the NL without oxygen pulses. We observed a

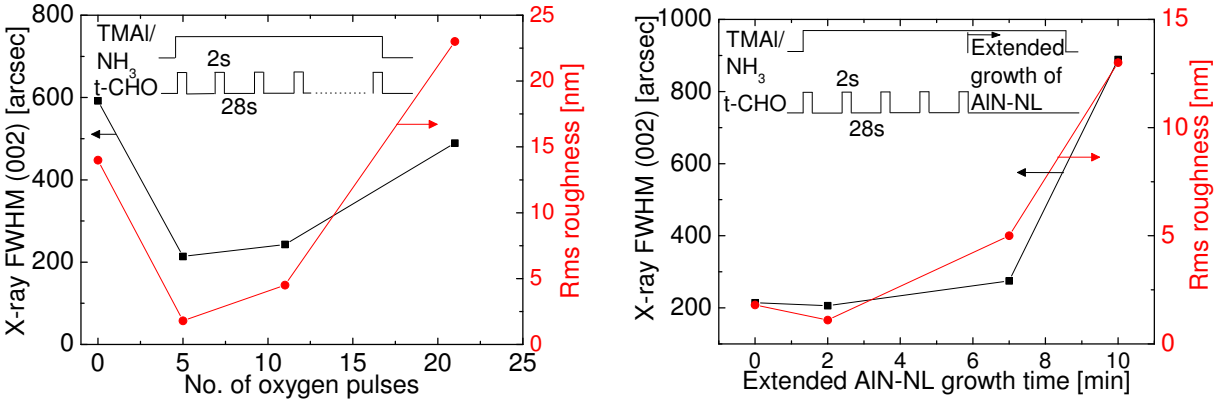

Figure 4.5: FWHM of HRXRD for the (002) reflection and RMS surface roughness of AlN epilayers: Plots for different numbers of oxygen pulses supplied during the NL growth (left), extended growth of the AlN NL after the supply of 5 pulses of oxygen at the beginning of the nucleation process (right).

slight improvement in the AlN epilayer quality if the growth period was extended by 2 minutes. However, longer times (more than 2 minutes growth) produced a negative effect on both the surface and the crystal quality. Figure 4.6 (right) shows an AFM image of the AlN epilayer after 2 min extended growth of the AlN NL. The large pits (dia $\geq$ 20 nm) are drastically reduced (below $10^9 cm^{-2}$) but the surface is still rough with small pits (dia $\leq$ 1 nm) with a pit density of approx. $8{\times}10^{10} cm^{-2}$. With these results, we confirmed that oxygen doping is needed just at the beginning of the NL growth. The total thickness of the NL should be approximately 20 nm to obtain a good quality of AlN layer where only the first part (nearly 10 nm) is doped with oxygen.

Recently, Bläsing *et al.* [164] and Hertkorn *et al.* [78] confirmed the growth of a very high quality GaN film on a 25 nm thick oxygen-doped AlN (AlN:O) NL. The argument was: a large amount of oxygen ions (O^-) replaces nitrogen atoms that results in a homogeneous NL with respect to the strain distribution, i.e. a homogeneous distribution of the stress-releasing edge dislocations in oxygen doped NL. In case of GaN, the correlation peak for the (002)-reflection of the AlN NL extends to the subsequently grown GaN epilayer and is visible as a sharp peak superimposed on a broad background (see Fig. 4.7 (left)). The correlation behavior of the AlN buffer layer is adopted by the thick GaN layer on top. Therefore Bläsing *et al.* [164] explicitly stated that it is not correct to take the FWHM of the correlation peak as a direct measure for the structural quality. However, the X-ray rocking curves did not exhibit such a sharp peak in our samples (see Fig. 4.7 (left)). It means the correlation peak of the AlN NL was not extended to the succeeding AlN epilayer. Therefore, we assume that the FWHM of X-ray rocking curve measures the structural quality of the AlN epilayer. It may be attributed to the non-perfectness of the epilayer so that the correlation peak vanished.

The AlN NL nucleates with 3D islands. The interface between a 3D island and sapphire was almost smooth and the layer was atomically grown as seen in the HR-TEM image of Fig. 4.8 (left). The AlN NL as a whole is an aggregate of such 3D islands. These islands were grown parallel to the c-plane of the sapphire which is confirmed

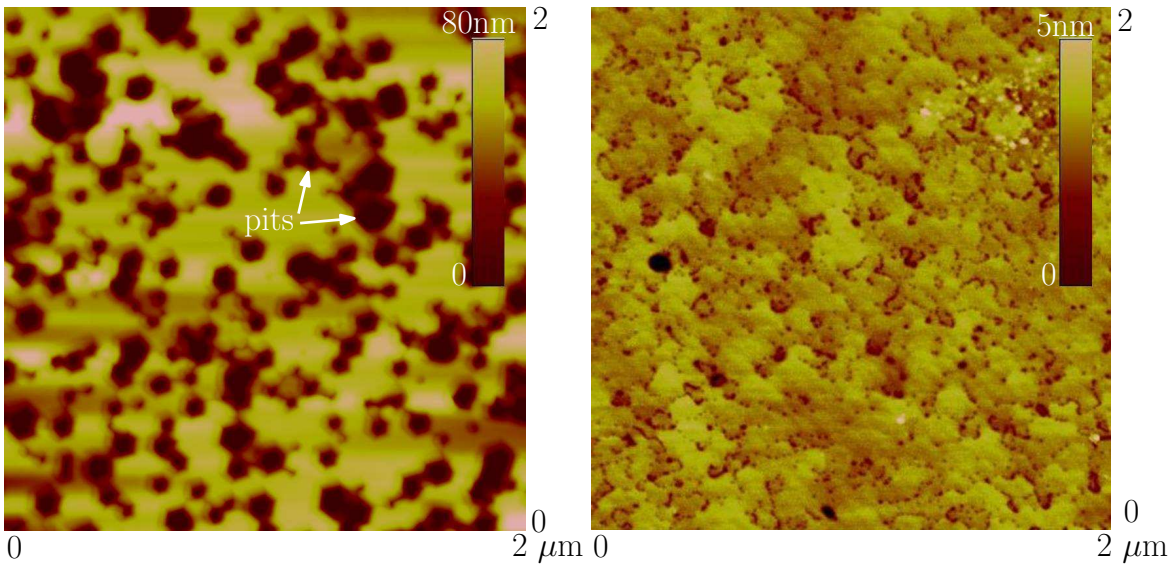

Figure 4.6: AFM images showing surface morphology of AlN epilayer deposited over AlN NL with 20 oxygen pulses (left) and 5 oxygen pulses and 2 min extended growth without oxygen (right). The large pits (dia ≥ 20 nm) are drastically reduced in the right image but the surface is still rough with a high density of small pits (dia ≤ 1 nm) approx. in the range of $8{\times}10^{10}$cm^{-2}.

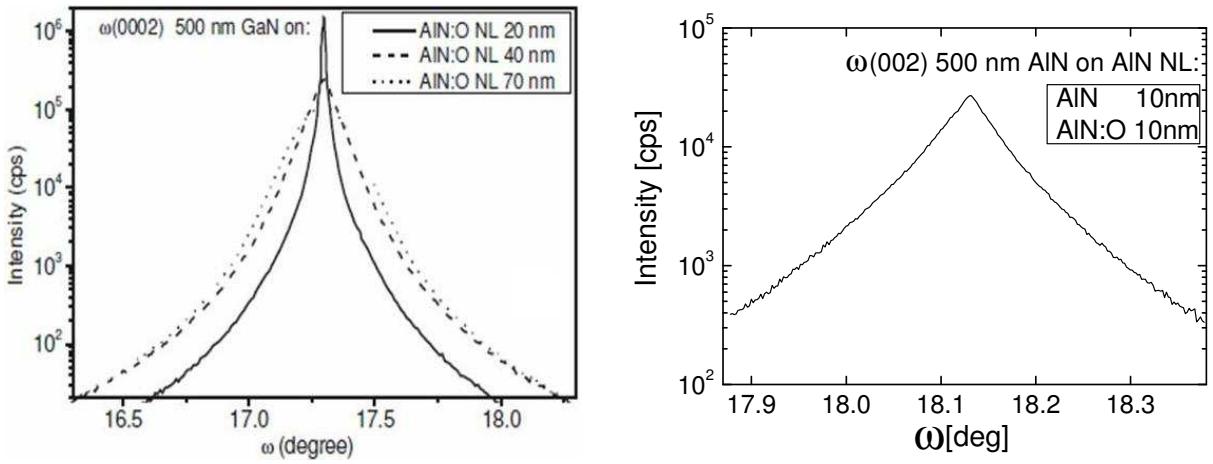

Figure 4.7: ω scan at (002)-reflection of X-ray rocking curve on GaN epilayer (left) [164] and on AlN epilayer (right) on AlN:O NL.

by the selected-area-electron-diffraction (SAED) pattern in the inset of Fig. 4.8 (right). The SAED pattern from the $[01\bar{1}0]$ cross-section of the AlN sample shows an epitaxial relationship of $[0002]\text{AlN}||[0006]\text{Al}_2\text{O}_3$. Since the 3D nucleation islands were twisted with respect to each other, a huge number of dislocations is emerging form the NL as exhibited in the bright field (BF) TEM image of Fig. 4.8 (right). A detailed study of such dislocations is discussed in the coming sections.

Finally, we optimized the NL growth temperature which is a very important parameter since the pyrolysis of the precursors, homogeneous and heterogeneous reactions,

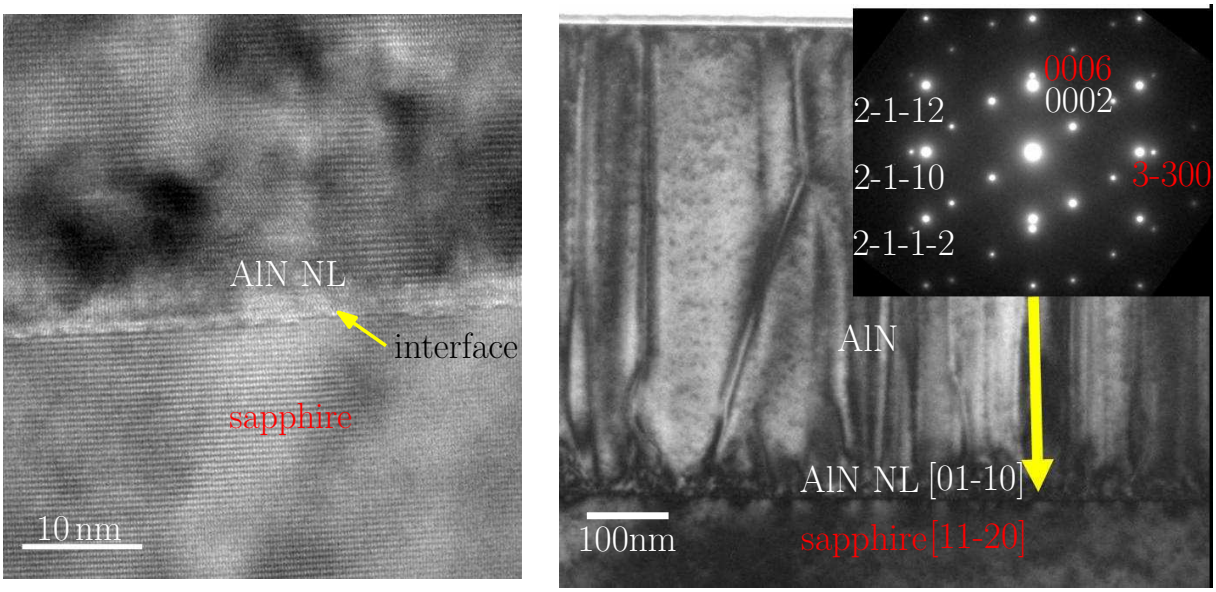

Figure 4.8: HR-TEM image at the interface between the AlN NL and sapphire (left). BF TEM image of AlN on sapphire (right) exhibiting a huge number of dislocations emerging from the NL. SAED image at the inset shows diffraction from AlN and sapphire at their interface.

Table 4.2: Optimized growth parameters for the nucleation layer.

Growth Parameters	Optimized value
Growth Pressure	70 mbar
Growth Temperature	870 °C
V–III Ratio	2500
N_2–H_2 Ratio	1.9
Total Flow	2000 sccm

and the mobility of the precursor species on the substrate are strongly temperature dependent phenomena. In order to investigate the influence of the growth temperature, we fixed other growth parameters at the optimum value as described above and varied the temperature between 820 °C and 930 °C. We found a window of the growth temperature from 850 °C to 870 °C with respect to a better surface morphology of the grown layer. The surface was heavily pitted when the growth was carried out at other temperatures. Furthermore, the FWHM of X-ray (002)-reflection showed a minimum of 179 arcsec at the growth temperature of 870 °C (Fig. 4.9).

A summary of the optimized growth parameters of our oxygen doped AlN NL is given in Tab.4.2.

Secondary ion mass spectroscopy (SIMS) measurements[2] were carried out to find

[2]SIMS measurements were carried out by L. Kirste, T. Fuchs, and M. Grimm of the Fraunhofer

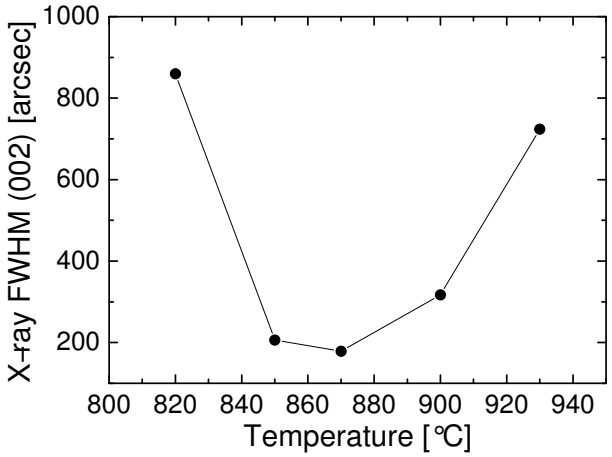

Figure 4.9: HRXRD rocking curve FWHM of the (002)-reflection in dependence of the NL growth temperature.

out the oxygen profile in the AlN NL layer, but it was not possible to detect the distribution of oxygen due to the surface and interface effects of the underlying Al_2O_3 substrate. However, an overall profile of oxygen concentrations in doped and undoped samples was sketched out in Fig. 4.10. Curve I shows the oxygen concentration in an AlN epilayer grown over AlN NL without oxygen doping. In the NL region, oxygen concentration is sharply decreased from the sapphire interface. However, interestingly, oxygen concentration in the AlN epilayer was very high, in the range of 10^{20} $\frac{\text{atoms}}{\text{cm}^3}$ in this sample. The layer surface was very rough and full of large hexagonal pits (see Fig. 4.6 (left)). The chances of oxygen incorporation at the facets of such pits are relatively very high. SIMS measurement confirms that rough and heavily pitted samples incorporate a large quantity of oxygen. Similar observations were also made in the samples grown by J. Hertkorn [165]. Curve II and III show oxygen concentrations in AlN epilayer grown over optimized AlN NL with oxygen doping as described above and on the oxygen-doped AlN NL template provided by J. Hertkorn [78, 165], respectively. Both curves exhibit similar profiles i.e. the oxygen concentration is high in the NL region and in the range of 1–2 $\times 10^{18}$ $\frac{\text{atoms}}{\text{cm}^3}$ in the AlN epilayer region. However, a slight penetration of oxygen concentration into the epilayer from the NL is observed. It may be due to a possible memory effect in the reactor or interface effects of the underlying AlN:O NL. Nevertheless, these experiments show that a proper oxygen doping in the NL has positive impacts in reducing the oxygen concentrations in the subsequently deposited AlN epilayers.

Moreover, instead of the pulsed supply arrangement of oxygen from the conventional bubbler, we implemented a controlled but continuous supply of oxygen from a gas source that contained a mixture of nitrogen (99.7 %) and oxygen (0.3%) during the NL growth. The characterization results of AlN epilayers deposited under this arrangement were inferior to the epilayers that were deposited under the pulsed supply arrangement. Therefore, we continued our growth process with our old arrangement.

Institute for Applied Solid State Physics, Freiburg.

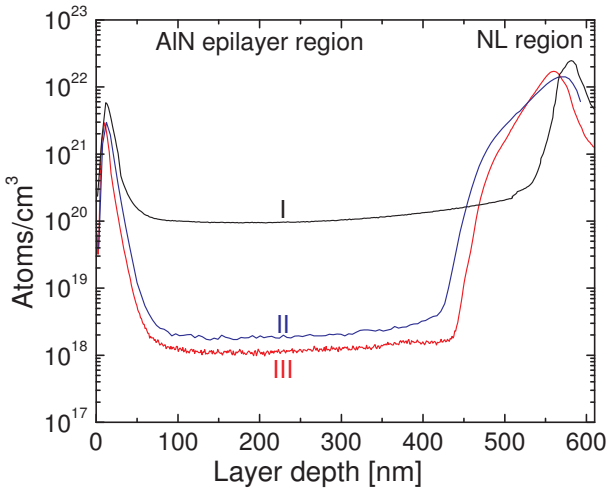

Figure 4.10: SIMS measurement for oxygen in the AlN epilayer: without oxygen doped AlN NL (I), with oxygen doped optimized AlN NL (II), and with oxygen doped AlN NL grown by J. Hertkorn [78, 165] (III).

4.2.3 Stage between Nucleation and Epitaxial Layers

Next, we carefully examined the stage between the MT NL and the main epilayer growth. In the case of a conventional LT (< 600 °C) NL, the crystalline quality of the NL is very poor, therefore, a heat treatment is typically applied in an H_2 and NH_3 ambient to rearrange the atoms after the NL growth as shown in Fig. 4.1 (step 3) [10]. The formed small islands start to coalesce in larger and the coalescence is completed during the growth of the subsequent layer [166].

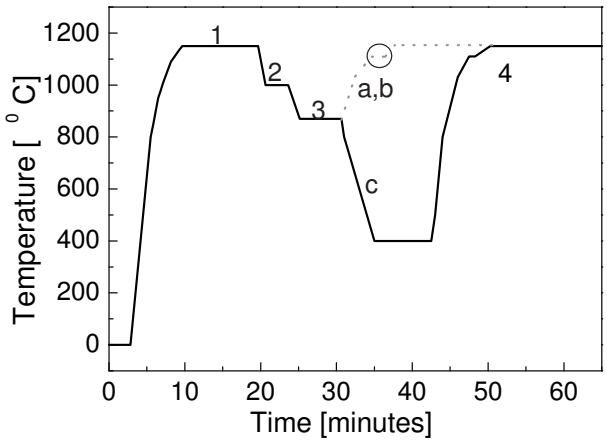

Figure 4.11: Schematic showing different steps (1. Desorption, 2. Nitridation, 3. Nucleation, and 4. final epilayer growth) in the growth of AlN layer with various temperature sequences. The stage between nucleation and final epilayers shown by a (thermal annealing), b (continuous growth), and c (cooling down, and annealing).

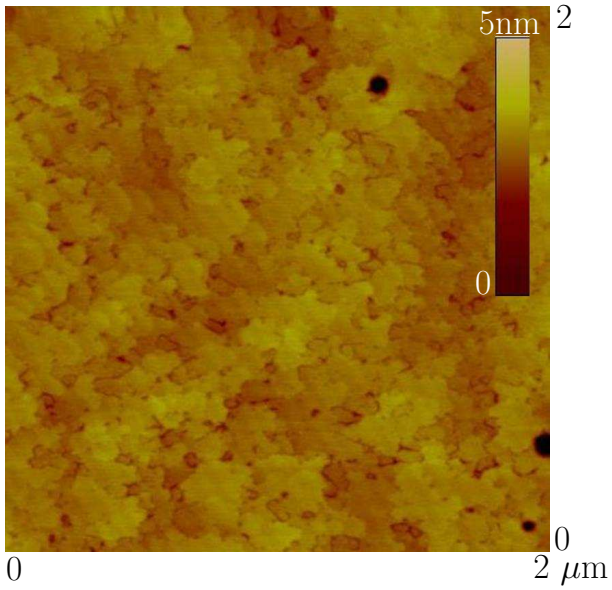

Figure 4.12: AFM image showing surface morphology of AlN epilayer after optimization of the stage between the NL and final epilayer growth. Although the surface is relatively smooth, large pits (diameter ≥ 20 nm), and points and networks of small pits (diameters ≤ 1 nm) are also visible.

However, our NL was grown at 870 °C which is higher than the conventional LT NL growth temperature. At this temperature, the layer may already be nucleated in the form of large islands. We implemented three different procedures at the stage between the nucleation and bulk layer growth (schematically shown in Fig. 4.11). Those were: (a) annealing of the NL under NH_3 before final AlN epilayer growth similar to the conventional group-III nitride growth process, (b) continuous growth of AlN epilayer after the NL during ramping up of the temperature, and (c) cooling the nucleation layer down to 400 °C in NH_3 ambient and ramping the reactor temperature up to the final epilayer growth temperature followed by a short pre-flow of NH_3 before epilayer growth. We employed the same optimized growth conditions of the NL as given in Tab. 4.2 and the growth conditions of the subsequently deposited AlN epilayers were kept constant as given in Tab. 4.1.

In the first step (a), we used a temperature ramp from 870 to 1110 °C in 2 minutes, hold there for 3 minutes, and finally ramped up to the growth temperature of 1150 °C in 1 minute (see plot a in Fig. 4.11). We changed the holding time (shown by a circle in Fig. 4.11) at 1110 °C from 30 seconds to 10 minutes as a characteristic parameter. The entire thermal treatment was performed in NH_3 ambient. Although the longer holding time of thermal treatment improved slightly the FWHM of X-ray (002)-reflection, it had a negative effect on the surface quality of the subsequently grown AlN epilayer. The surface was full of pits and very rough in AFM observation. The measured RMS roughness of 2×2 μm^2 scan was more than 1 nm. A long duration of thermal annealing in NH_3 ambient results in recrystallization and decomposition of the NL [166] which promotes the formation of N-polarity AlN. As described in chapter 3.2.1, this ultimately

degrades the surface quality of the succeeding layer. Similar observations were also reported by J. Hertkorn [78].

Next, we carried out a continuous growth of the AlN layer after the NL growth during ramping up of the temperature (see plot b in Fig. 4.11). The impact of this growth process on both, the surface and the crystal quality, was very negative. We measured a broad X-ray rocking curve (more than 1000 arcsec for the (002)-reflection) and observed a polycrystalline like surface morphology in AFM.

Therefore, we changed the growth process as depicted by plot c in Fig. 4.11. In this process, first, the nucleation layer was cooled down to 400 °C in NH_3 ambient, then the reactor temperature was ramped up to the final epilayer growth temperature. The growth of the AlN epilayer was proceeded by a short (15 seconds) pre–flow of NH_3. This growth process enhanced both the surface and the crystal quality of the AlN epilayer further. Cooling down of the NL might relax the stress induced by thermal mismatch earlier. Hence, the effect of thermal strain on the subsequently grown AlN epilayer was minimized. The short pre–flow of NH_3 before the growth of the bulk layer may assist the re–crystallization and further coalescence of AlN islands of the NL at very high temperature which in effect transforms the 3D growth mode of the NL to 2D growth of the final epilayer. The surface morphology of the AlN epilayer grown after the optimization of the stage between the NL and the final epilayer is shown in the AFM image in Fig. 4.12. The surface is relatively smooth compared with the sample grown with conventional annealing in NH_3 ambient after the NL (see Fig. 4.6 (right)). However, large pits (dia $\geq$ 20 nm), and points and networks of small pits (dia $\leq$ 1 nm) are still present in the range of $10^8 cm^{-2}$ and $5{\times}10^{10} cm^{-2}$, respectively. Although, the atomic steps are not clearly visible, the final layer might be grown in 2D growth mode. The measured RMS value of the surface roughness of this layer at $2{\times}2\,\mu m^2$ scan was 0.5 nm.

4.2.4 High Temperature Epitaxial Layer

The AlN epilayer growth occurs at high temperatures (higher than 1100 °C). At the early stage of this study, our AlN layers exhibited random three-dimensional (3D) nucleated growth features of rough grains. The surface showed either whisker-like features of rough grainy characteristics, or columnar textures. Hexagonal pits of varying size, depth and diameter (similar to Fig. 4.6 (left)) were largely observed. The crystalline quality (as measured by the FWHM of HRXRD) of the layers was also inferior. In the initial stage of the growth process, the rearrangement of the atoms form agglomerations of hexagonal islands. The emergence of a high pit density on the surface was the result of columns protruding through the entire layer from the inception of the epilayer as shown in the SEM micrograph in Fig. 4.13. After optimization, the epilayer is expected to grow simultaneously both laterally and vertically in a 3D growth mode on the previously deposited NL. The 3D islands should start to coalesce and at the end of the coalescence, the growth mode rapidly changes from 3D to two-dimensional (2D) which allows the further growth of a smooth AlN epilayer with improved surface and crystal qualities. The *in-situ* reflectometry method employed during the AlN growth is capable to provide qualitative information on the surface roughness of the growing

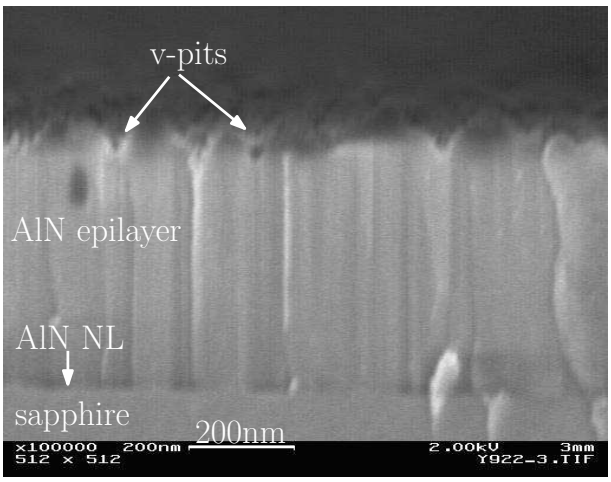

Figure 4.13: SEM image of AlN epilayer before optimization.

layer and the growth rate. The growth of high quality epilayers entails several characteristic growth parameters, namely, precursors flow-rate, ambient gas (H_2 and N_2) compositions, reactor pressure, and the growth temperature to be optimized. In order to analyze the influence of each of these characteristic growth parameters on the AlN epilayer, we varied only one parameter at a time keeping the rest of the parameters fixed.

Effect of precursors flow-rate

As mentioned in the preceding chapter, the parasitic reactions between TMAl and NH_3 promote the formation of AlN nanoparticles in the gas phase [141] causing a sinister impact on both the quality and the growth rate of the AlN epilayer. Indeed, we observed the presence of a remarkable amount of white microparticles on the susceptor and a coating of a white layer on the liner sidewalls. This confirms the occurrence of inherent strong parasitic pre-reactions during AlN epilayer growth. To minimize the adverse effects of such pre-reactions, it is customary to carry out a precise optimization of the flow-rates of both precursors, TMAl and NH_3. We carried out several growth experiments with different V–III ratios by varying the TMAl and NH_3 flow-rate while the rest of the growth parameters was kept constant (see Tab.4.3). In these experiments, the preliminary growth conditions and stages were also kept fixed. The thickness of all the layers was approximately 500 nm.

In the first set of experiments, TMAl flow-rate was varied from 5.5 to 45 μmol/min and NH_3 flow-rate was kept constant at 22.3 mmol/min (505 sccm). The growth rate of AlN epilayers acquired from experiments and computation [147] with respect to the change in TMAl flow-rates is plotted in Fig. 4.14 (left). It also shows an extrapolated data which was derived from the normalization of the growth rate at low flow (5.5 μmol/min). The growth rate increases as expected up to $\sim$ 12 μmol/min, then it is lower than the expected value at larger flows. As seen in the figure, the deviation of the experimental growth rate from the extrapolated data is increased with increasing flows and it is more than 31% when the TMAl flow-rate was 45 μmol/min. Such deviation is

Table 4.3: Characteristic parameters for the growth of high temperature AlN epilayer. Here, the precursors (TMAl and NH_3) flow-rate was a variable.

Growth Parameters	Value
Growth Pressure	35 mbar
Growth Temperature	1110 °C
N_2–H_2 Ratio	1.26
Total Reactor-flow	2500 sccm

explained by material losses due to the formation of AlN nanoparticles. Meanwhile, we observed an increase of the surface roughness with the increase of the TMAl flow-rate (see Fig. 4.14 (right)). It can be attributed to the increased nanoparticle formation. These nanoparticles may nucleate and form small clusters on the surface (on the defect places such as threading dislocations, for instance), resulting in a transition from step-flow to 2D or even 3D growth mode and the emergence of large hexagonal pits at the epilayer surface. We observed a similar degradation at reduced growth rates, too, when the wafer was placed at a different downstream position (see Fig. 3.8 in chapter 3). Computations by A.V. Lobanova show that the growth rate decreases in flow direction due to an increased formation of AlN nanoparticles. Therefore, it is not only the higher growth rate but also, primarily the parasitic reactions that are responsible for the surface degradation. Furthermore, the high TMAl flow-rate allows only a shorter diffusion length of the Al species which hinderances the lateral migration of Al adatoms resulting in a poor surface quality. On other hand, the FWHM of the X-ray rocking curve for the (002)-reflection decreases with the increase of TMAl flow as illustrated in Fig. 4.15. At higher TMAl flows, the growth in vertical direction is higher than in

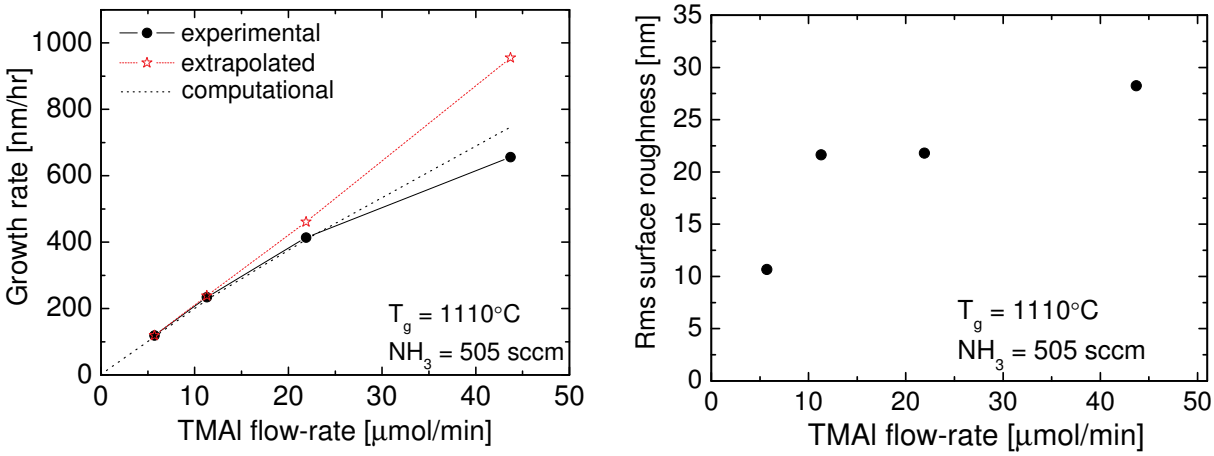

Figure 4.14: Change in the growth rate (left) and the RMS surface roughness (right) with respect to TMAl flow-rate. NH_3 flow-rate was kept constant at 22.3 mmol/min (505 sccm).

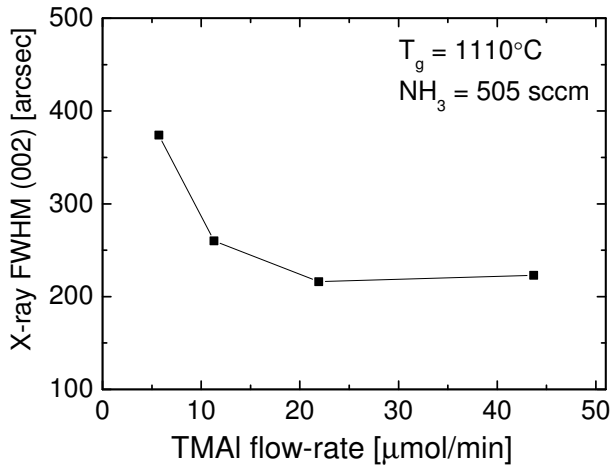

Figure 4.15: Change in FWHM of X-ray rocking curve for the (002)-reflection with respect to TMAl flow-rate. NH_3 flow-rate was kept constant at 22.3 mmol/min (505 sccm).

the lateral direction that results in columnar structures protruding through the entire layer. One reason for narrow X-ray peaks might be the presence of a strong correlation effect of ordered columnar structures at (002)-reflections. The reduced out-of-plane tilt of such crystal structures with increasing growth rate in the vertical direction could be another reason. However, a FWHM of the (102)-reflection of more than 2000 arcsec was for all samples in this set of experiments, not steadily dependent on TMAl flow. Such large in-plane twist (as reflected by the X-ray (102)-reflection) is attributed to the high initial island density.

Next, we varied the NH_3 flow-rate from 155 to 1005 sccm (7 to 45 mmol/min) and the TMAl flow-rate was kept constant at 11.3 μmol/min The growth rate of AlN is decreased

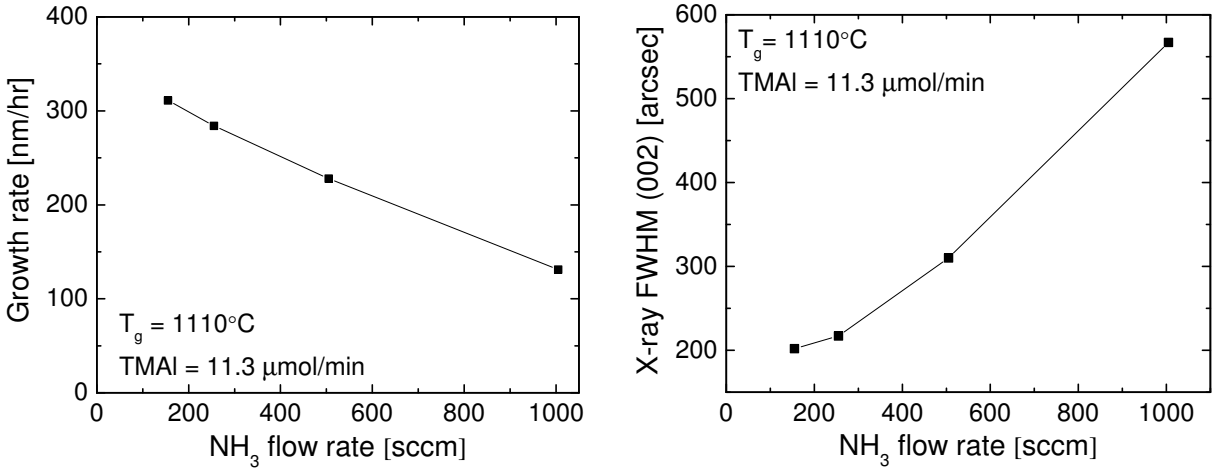

Figure 4.16: Change in the growth rate (left) and the FWHM of X-ray rocking curve for the (002)-reflection (right) with respect to NH_3 flow-rate. TMAl flow-rate was kept constant at 11.3 μmol/min

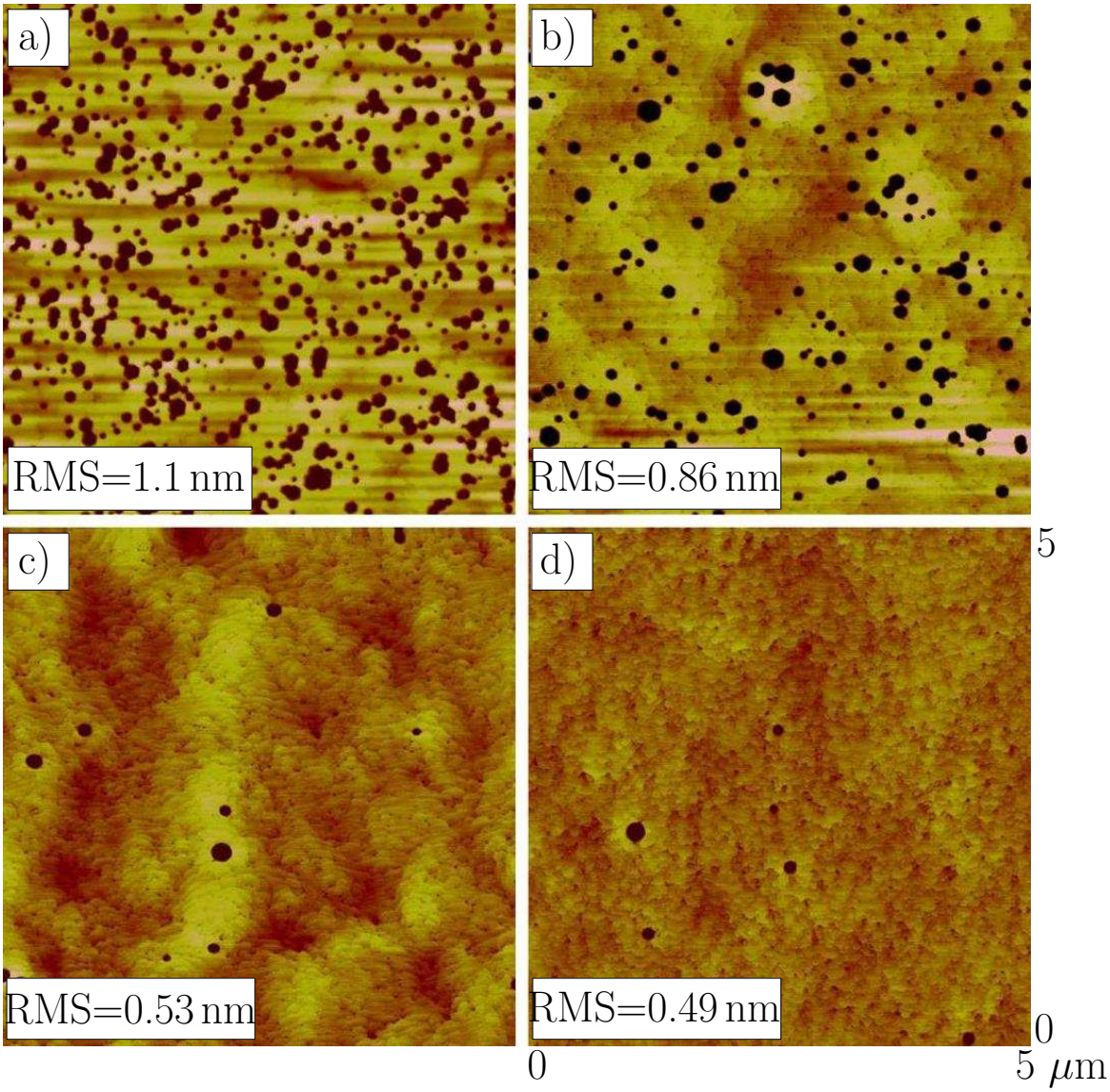

Figure 4.17: $5 \times 5\,\mu m^2$ scanned AFM images exhibiting surface morphology of AlN epilayer grown at different NH_3 flow-rate: (a)1005 sccm, (b)505 sccm, (c)255 sccm, and (d)155 sccm. TMAl flow-rate was kept constant at 11.3 μmol/min The surface morphology is improving with decreasing NH_3 flow-rate.

with the increase of NH_3 flow-rate as shown in Fig. 4.16 (left). At high NH_3 flow, the low growth rate shows a loss of Al due to more parasitic pre-reactions. Furthermore, it has been reported that NH_3 can reduce the potential energy barrier of trimer and higher n-mer formation [167]. Therefore, with the increase of the NH_3 flow-rate, the quantities of trimer and higher n-mer which do not contribute to the growth will increase and the growth rate of AlN will decrease. At low NH_3 flow, the high growth rate shows a negligible loss of Al. The FWHM of X-ray rocking curve for the (002)-reflection is increasing with NH_3 flow-rate (see Fig. 4.16 (right)). It can be explained with similar

arguments for the higher growth rates while varying TMAl flows as mentioned above. However, the surface morphology of the AlN epilayer is significantly improved with the decrease of NH_3 flow-rate. Figure 4.17 shows AFM micrographs ($5 \times 5\ \mu m^2$ scan) of the samples that were grown with NH_3 flow-rates between 1005 sccm, and 155 sccm. Both, the density and the size of pits decrease with decreasing NH_3 flow-rate. The density of large-size hexagonal pits is reduced to less than $1 \times 10^8 cm^{-2}$ when the NH_3 flow was at a minimum of 150 sccm. Since the parasitic pre-reactions were escalated with increasing NH_3 flow, the resulting high pit density can be attributed to the nanoparticle formation. The measured RMS surface roughness of the $5 \times 5\ \mu m^2$ scanning of samples grown under NH_3 flow-rate of 155 and 255 sccm was approximately 0.5 nm whereas it was approximately 1.0 nm when NH_3 flow-rate was 505 and 1005 sccm. From these results we conclude that a low NH_3 flow is advantageous for reducing pre-reactions between TMAl and NH_3 in the gas phase. The low NH_3 flow-rate allows a longer diffusion length of the Al species which enhances the lateral migration of Al adatoms resulting in an improvement of the surface roughness.

Since the suppression of the pre-reactions between the precursors and the surface diffusion of Al atoms during the growth process are the key factors in determining the surface morphology, the growth process was hence optimized by decreasing both, NH_3 and TMAl, flow-rate and apparently lowering the V–III product. Lowering the flow-rate of both precursors decreases parasitic reactions and lowering the growth rate enables more surface migration. We observed similar effects of precursors flow-rate on the surface and crystal quality of AlN epilayers when the growth temperatures were higher than 1110 °C.

Effect of N_2-H_2 composition

We have used H_2 as a carrier gas for the transportation of the MO precursors. However, a significant amount of N_2 was introduced as a pusher gas. Hence, the growth ambient was a mixture of N_2 and H_2. The growth ambient, especially the presence of different gases in the reactor, plays an important role in the MOVPE growth of group-III nitrides. Due to the unique thermo–chemical (entropy, specific heat) and

Table 4.4: Characteristic parameters for the growth of high temperature AlN epilayers. Here, the N_2-H_2 gas composition is a variable.

Growth Parameters	Value
Growth Pressure	35 mbar
Growth Temperature	1190 °C
NH_3 flow-rate	250 sccm
TMAl flow-rate	11.3 μmol/min
Total flow	2000 sccm

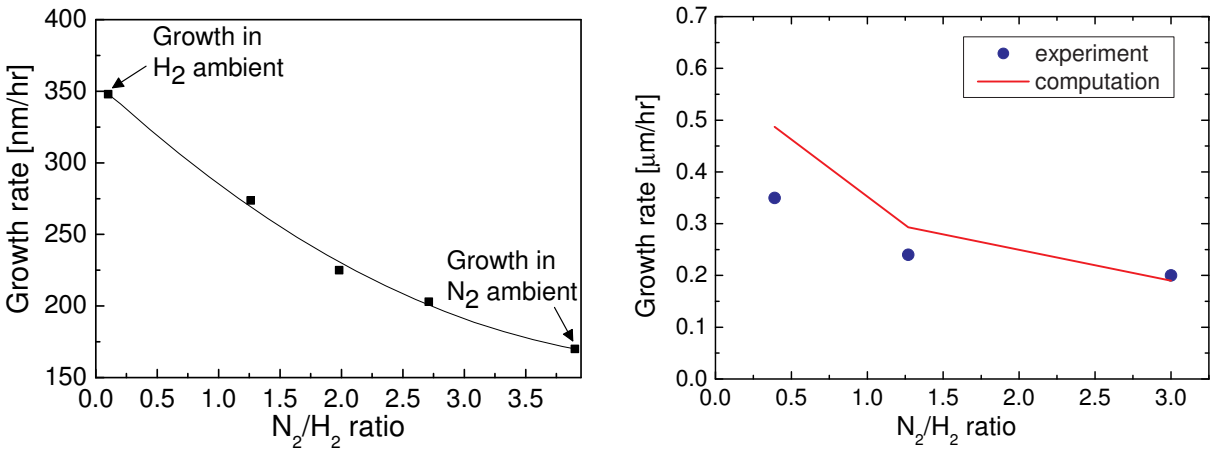

Figure 4.18: Change in the growth rate with respect to the N_2-H_2 ratio for the samples grown at the same temperature: 1190 °C (left) and 1110 °C (right). The computational data for the samples grown at 1110 °C is also shown.

transport (diffusivity, thermal conductivity, viscosity) properties, impacts of each gases on both temperature distribution in the gas phase and heat transfer between the gas phase and the solid surfaces of the reactor (susceptor, walls) influence the chemical reaction mechanism in the gas phase and at the surface as well. There are several reports on the influences of H_2 and N_2 on the growth of GaN [168, 169] but we hardly find such reports for the growth of AlN. In this study, we performed few experiments to see the distinct heating effect of N_2 and H_2 on the susceptor by introducing these gases separately into the reactor. The temperature of the susceptor was monitored using a pyrometer and a direct coupling of thermocouple sensor element in it. Similar to others [170], we observed that the reactor temperature in N_2 ambient was lower than in H_2 ambient by 40 °C while supplying the same electrical power to the RF generator to heat the susceptor to 1150 °C. The specific heat capacity $C_{p,\mathrm{m}}$ of N_2 (29.12 $\mathrm{Jmol^{-1}K^{-1}}$) is higher than that of H_2 (28.82 $\mathrm{Jmol^{-1}K^{-1}}$). Therefore, a higher energy is needed if the ambient is dominated by N_2. The thermal conductivity k of N_2 (0.0026 $\mathrm{Wm^{-1}K^{-1}}$ at room temp.) is lower than that of H_2 (0.18 $\mathrm{Wm^{-1}K^{-1}}$ at room temp.). When the gases from the gas-inlet side enter into the hot reactor ambient, H_2 is heated a bit faster than N_2 because of its high thermal conductivity. Due to a large volume of gas flow into the reactor, the lowly heated N_2 may form a cold-finger effect [171] into the growth region of the susceptor which causes the temperature fall down further. Therefore, relatively a higher electrical power is needed to heat the susceptor in N_2 ambient.

We carried out several growth experiments in the ambient of different N_2-H_2 gas compositions. Other growth parameters were kept constant as listed in Tab.4.4. We found that the N_2-H_2 gas composition is one of the growth-rate-limiting factors and remarkably inflicts the surface quality of the AlN epilayer.

It was observed that the growth rate increases with the decrease of the N_2–H_2 ratio (with increasing H_2) as illustrated in Fig. 4.18. A similar trend was observed in both the experimental and the computational studies (carried out by Lobanova *et al.* [147]) when the samples were grown at a relatively low growth temperature of 1110 °C (Fig. 4.18

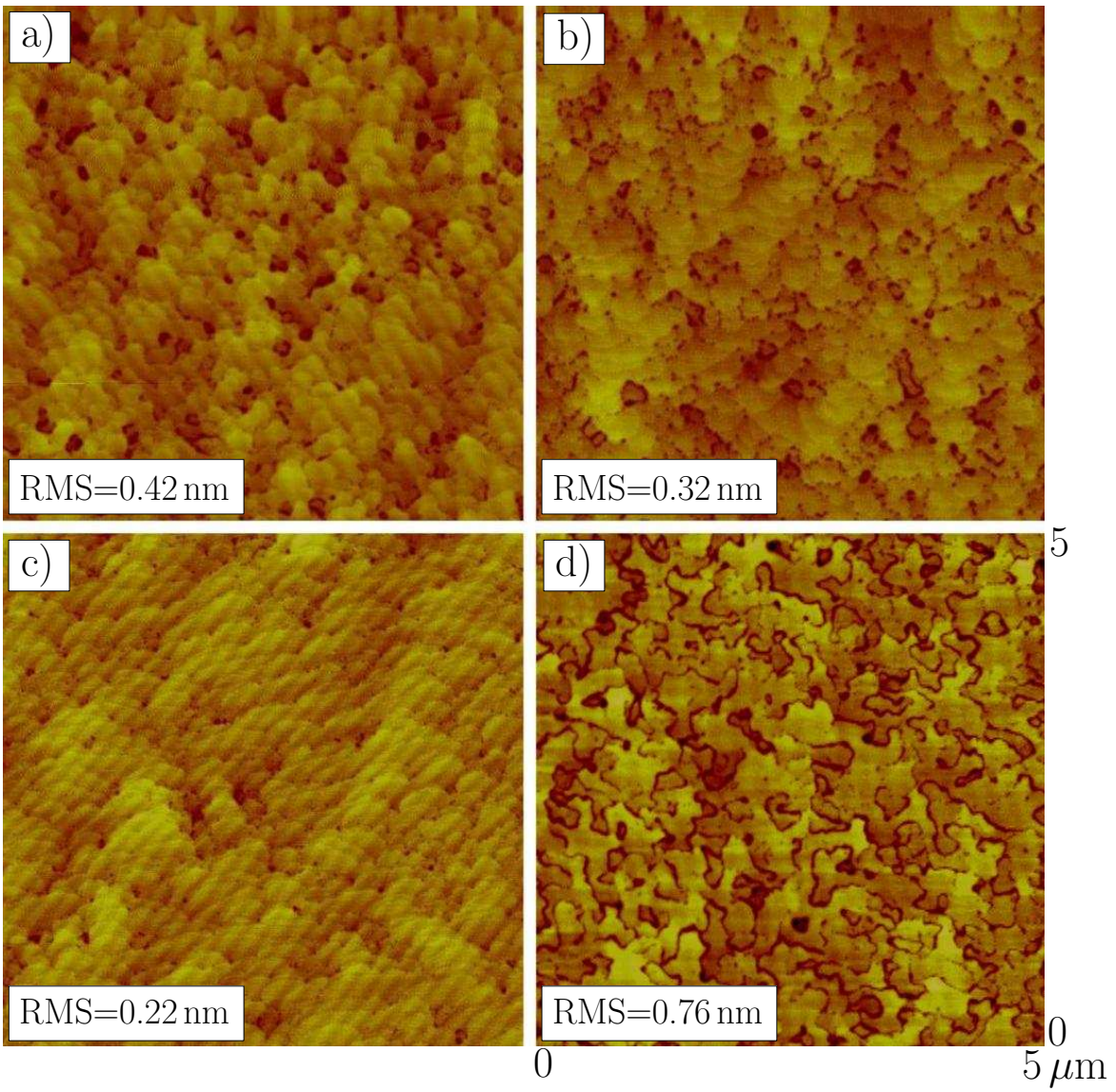

Figure 4.19: $2 \times 2\,\mu m^2$ scanned AFM images exhibiting surface morphology of AlN epilayer grown at different gaseous ambient: (a) pure N_2, (b) N_2–H_2 = 2.7, (c) N_2–H_2 = 2, and (d) pure H_2.

(right)). However, this result is somewhat contrary to the observations made by other groups [172, 173] in the high-temperature GaN growth where the growth rate was decreased with increasing H_2 flow-rate. Our results clearly show that the growth rate of AlN is not only transport limited but also largely ambient dependent. The variation in the gas composition changes both the ambient and the substrate temperatures that ultimately influence the gas phase and surface reactions. Although the susceptor temperature was kept constant by regulating it with the thermocouple, the diffusivity of precursor species may also depend upon the ambient gases. Higher growth rates in H_2 rich-ambient are caused by a faster diffusivity of the Al-containing species in

H_2 atmosphere. The change in surface morphology due to different growth ambients is exhibited in Fig. 4.19. The samples grown in pure N_2 (a) or H_2 (d) ambient show inferior surface morphology in comparison to the samples grown in mixed ambient (b) and (c). Although the temperature of the ambient is substantially increased in pure H_2, the morphology degradation due to enhancement of parasitic reactions seems to be stronger than the morphology improvement due to enhanced surface diffusion of Al atoms. The pure H_2 ambient resulted in a very rough surface that contains a mesh of closed networks of tortuous grooves arising from nano-pits. However, a very smooth morphology is obtained for the sample grown at a N_2–H_2 ratio of 2 (c). Such improvement in the surface morphology might be the compensation of two counteracting effects: reduced gas phase parasitic reactions due to relatively lower ambient temperature and reduced growth rate. Earlier, Wagner *et al.* [174] reported that the lateral growth velocity of GaN is enhanced by increasing the N_2 content in the mixture of N_2 and H_2 during HVPE growth of GaN. The AFM investigation of our samples reveals that the grain boundary area as highlighted by small nano-pits network is expanded in the sample grown at a N_2–H_2 ratio of 2. It evidences the enhancement of the coalescence of 2D islands at this gas ratio. However, the surface quality is relatively deteriorated as shown in (b) for higher N_2 content. Hence, we found that the surface morphology of AlN epilayers can be improved by proper adjustment of N_2-H_2 gas composition. However, we did not observe much impact of the growth ambient on the FWHM of the X-ray rocking curve for the (002)-reflection.

Effect of Reactor Pressure

The reactor pressure is one of the highly influencing parameters for the growth of AlN. To study the effects, we varied it from 25 to 70 mbar while the rest of the growth parameters were kept constant as listed in Tab. 4.5.

A longer residence time of the gas phase species in the reactor enhances the parasitic pre-reactions between the precursors. Decreasing the reactor pressure reduces the residence time and increases the growth rate of the AlN epilayer as illustrated in Fig. 4.20 (left). With even lower reactor pressures, a higher growth rate might be

Table 4.5: Characteristic parameters for the growth of the high temperature AlN epilayer. Here, the reactor pressure is varied.

Growth Parameters	Value
Growth Temperature	1190 °C
NH_3 flow-rate	250 sccm
TMAl flow-rate	11.3 μmol/min
N_2–H_2 ratio	2
Total flow	2000 sccm

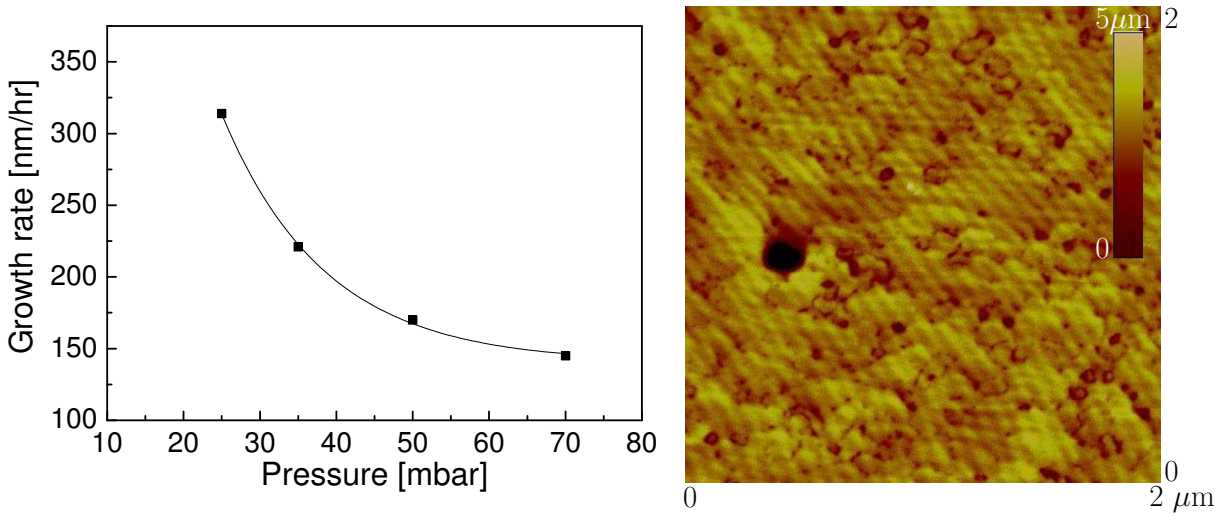

Figure 4.20: Change in the growth rate with respect to the reactor pressure (left). $2 \times 2\ \mu m^2$ scanned AFM image exhibiting the surface morphology of an AlN epilayer grown under a reactor pressure of 25 mbar (right).

reached, but the minimum reactor pressure in our MOVPE is limited by the pumping system.

We observed a deterioration of the surface morphology with the emergence of large hexagonal pits with increasing reactor pressure from 35 mbar. Uehara *et al.* [175] also reported the increase of surface roughness with the increase of reactor pressure. At higher reactor pressure, the increase of surface roughness is attributed to the enhanced parasitic pre-reactions. We also observed a bad surface morphology at a low pressure of 25 mbar as exhibited in Fig. 4.20 (right). This is attributed to a higher growth rate. Although the parasitic reaction is largely minimized at a low growth pressure of 25 mbar, the growth mode might be transformed from 2D to quasi-2D or 3D. At such a low pressure, the rate of arrival of precursor species at the substrate may be higher than the rate of surface diffusion. This might be a possible explanation for the change in the above mentioned growth modes and the exponentially increased growth rate at low reactor pressure. During a very low pressure growth, the employment of a very high temperature or decrease of the growth rate by lowering the TMAl flow might avert such changes in the growth modes and suppress the hexagonal pits. Moreover, we did not observe any remarkable impacts on the FWHM of X-ray rocking curve for the (002)-reflection due to the change in reactor pressure in the above mentioned ranges. We found the reactor pressure around 35 mbar is the optimum value for the growth of AlN in our reactor under the given growth conditions.

Effect of Growth Temperature

It is an empirical rule that a material with high melting point requires a high growth temperature for the crystal formation. A long time back, Dryburgh [176] theoretically estimated the minimum growth temperature for the crystal growth of AlN and GaN from the gas phase to be 1099 °C and 894 °C, respectively, considering the standard heat

Table 4.6: Characteristic parameters for the growth of AlN epilayer. Here, the growth temperature is varied from 1110 °C to 1199 °C.

Growth Parameters	Value
Growth Pressure	35 mbar
NH_3 flow-rate	250 sccm
TMAl flow-rate	11.3 μmol/min
N_2–H_2 ratio	2
Total flow	2000 sccm

of formation ΔH_f^0 of 76 kcal/mol and 26.2 kcal/mol for AlN and GaN, respectively, at atmospheric pressure. This estimation clearly manifests the necessity of the employment of a very high temperature reactor for the growth of a high quality AlN epilayer using MOVPE. In this study, the influence of the growth temperature was analyzed in a range between 1110 °C and 1199 °C (maximum achievable temperature in our reactor). The temperature was measured indirectly, underneath the susceptor (where the sapphire substrate is located) using a thermocouple element sensor and is not the real surface temperature of the substrate. Other growth parameters were kept constant as listed in Tab.4.6.

Koukitu and Kumagai [177] reported theoretical studies of the deposition of AlN without etching and droplet modes at 1200 °C or even higher. In our studies, we experimentally observed that the growth rate of AlN slightly decreases with the increase of growth temperature from 1150 °C (Fig. 4.21 (left)). Our observation is in contrast to the reports by Imura *et al.* [81] and Ohaba and Hatano [178]. The decrease of the growth rate with increasing temperature may be attributed to the increased parasitic pre-reactions in the gas phase and simultaneous etching effects on the solid surface with temperature. Figure 4.21 (right) illustrates an Arrhenius plot of the growth rate. Two types of rate-determining steps were clearly observed. It shows that the growth rate of AlN in our MOVPE reactor is not only mass transport limited but also temperature dependent when the growth temperature was higher than 1150 °C. An activation energy value corresponding to the higher temperature range was estimated to be approximately 52 kJ/mol (0.54 eV per atom).

It is assumed that AlN decomposition should not take place in this temperature range due to the high equilibrium pressure of N. However, NH_3 is in fact highly reactive. It provides not only the N precursor, but also an active H that might reduce Al and cause the decomposition of the layer. The thermodynamics will try to restore the equilibrium (through an increased diffusivity), limiting the growth rate which will decrease as the temperature increases. Thus, the growth of AlN at the above mentioned range of temperatures is on the thermodynamically limited regime although the mass transport has a significant influence on the growth rate at this regime, too.

However, below 1150 °C, the growth rate is almost constant and simply controlled by the arrival rate of the Al and N species at the vapor-solid interface. Here, the

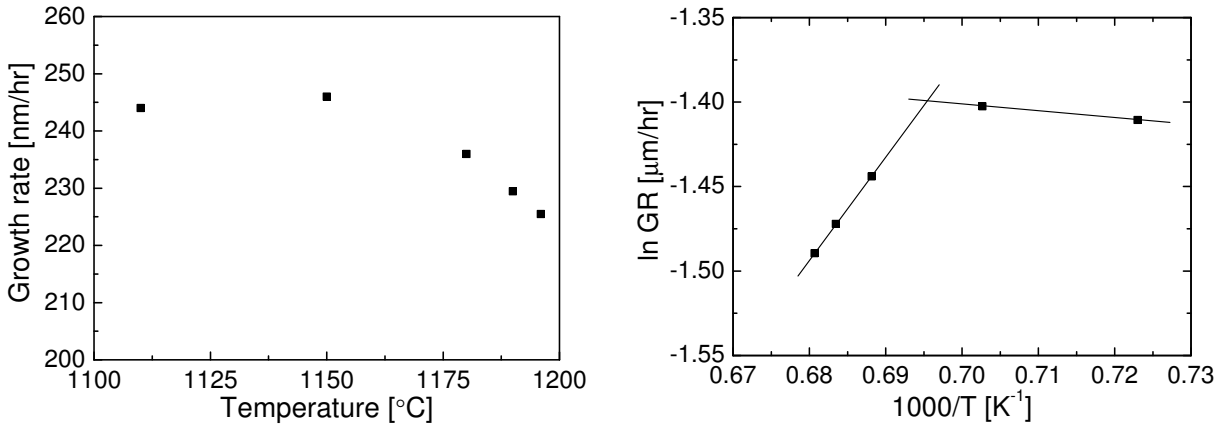

Figure 4.21: Change in the growth rate with respect to the reactor temperature(left) and corresponding Arrhenius plot (right).

diffusion of the gas species to and away from the surface limits the growth process. The temperature dependence of the growth rate in this range is weak, therefore, AlN growth at this range of temperature is on the mass transport limited regime. Moreover, the N_2-H_2 gas composition in the growth ambient remains an influencing growth parameter for both growth regimes.

The change in growth temperature has substantially influenced the surface morphology of the AlN epilayer. The adsorbed Al-species possess a low surface mobility due to the high adsorption energies. The degree of surface roughness is a result of kinetic processes involving the surface diffusion. The mean diffusion length (λ_s) of atoms can be written [179,180]

$$\lambda_s = (D\tau)^{1/2}, \tag{4.1}$$

where D is the surface diffusion coefficient and τ is the mean residence time of atoms at the surface. Increasing the growth temperature leads to a larger D, hence increasing the diffusion length. On the other hand, assume that the mean residence time is only limited by the atom incorporation process, then reducing the growth rate should also increase λ_s. Therefore, not only a higher growth temperature but also a lower growth rate should increase the diffusion length and thus reduce the surface roughness. However, the surface diffusion of Al adatoms during the growth process has not thoroughly been studied yet.

We observed that the surface of the sample grown at low temperature was very rough and heavily pitted with large hexagonal pits of varying diameters from few tens of nm to hundreds of nm. The low surface mobility of Al adatoms prevents the formation of large islands in the initial stage of growth. The low surface mobility may cause grain growth and leads to a rough surface. Samples grown at 1110 °C exhibited an RMS surface roughness of approximately 20 nm in a $2 \times 2\ \mu m^2$ AFM scan and 3.5 nm when the pits were excluded. The pit density was in the range of $10^9\ cm^{-2}$. The surface mobility of the adsorbed species can be enhanced by increasing the deposition temperature. Then, both, the surface roughness and the pit density, were drastically

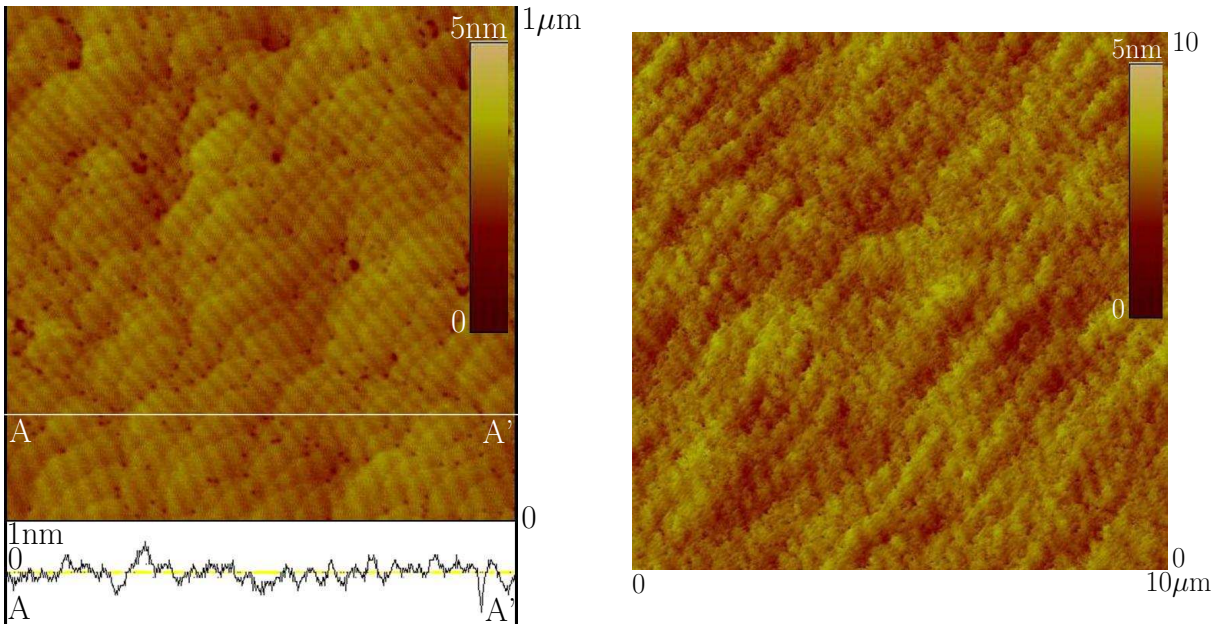

Figure 4.22: $1\times1\,\mu m^2$ (left) and $10\times10\,\mu m^2$ (right) scanned AFM micrographs of the optimized AlN bulk layer grown at 1199 °C. The cross-section plot at AA' exhibits the terrace width and atomic step height on the surface. Small pits are seen but no large hexagonal pits are observed.

reduced. For a sample grown at 1199 °C, we measured an RMS surface roughness of 0.21 nm on a $1\times1\,\mu m^2$ AFM scan (Fig. 4.22 (left)). We rarely found large hexagonal pits on small area scans, however, small pits (diameter ≤1 nm) are clearly resolved due to the smoothness of the surface. The density of such small pits is counted in the range of 2 to $5\times10^{10}\,cm^{-2}$. These small pits can be correlated with the opening of edge-type threading dislocations on the epilayer surface. The AFM image exhibits stepped terrace surface features reflecting a step-flow like growth. The small pits are located at the edges of these meandering atomic step terraces. At the end of some of the terraces, we observed slightly larger pits which might be an intersection of two or more threading dislocations (edge-, screw- or mixed-type) with the surface. Since surface diffusion and step incorporation kinetics during the growth are the key factors in determining the surface morphology, such step-flow-like growth of AlN film suggests that the ratio between the migration barrier energy and the thermal energy is sufficiently reduced for the surface mobility of Al adatoms. From the AFM analysis, it is possible to resolve the step dimensions. The average terrace width and the average step height are estimated to be about 40 nm and one or two monolayers, respectively. With these values, we obtain the tilt angle of the AlN surface plane to be about 0.4 °. This value is very close to the sapphire misorientation angle i.e. 0.3 ° miscut to the m-plane. The error bar is due to the measurement artifacts. Although an irregular bending and curves of the edge of the terraces are seen in the image, the surface plane of our AlN is almost parallel to the substrate plane confirming the atomic step growth of our epilayers. The irregular edge of the terraces may be attributed to the twist of the crystal structures. Considering the flatness of the surface, it may be assumed that the

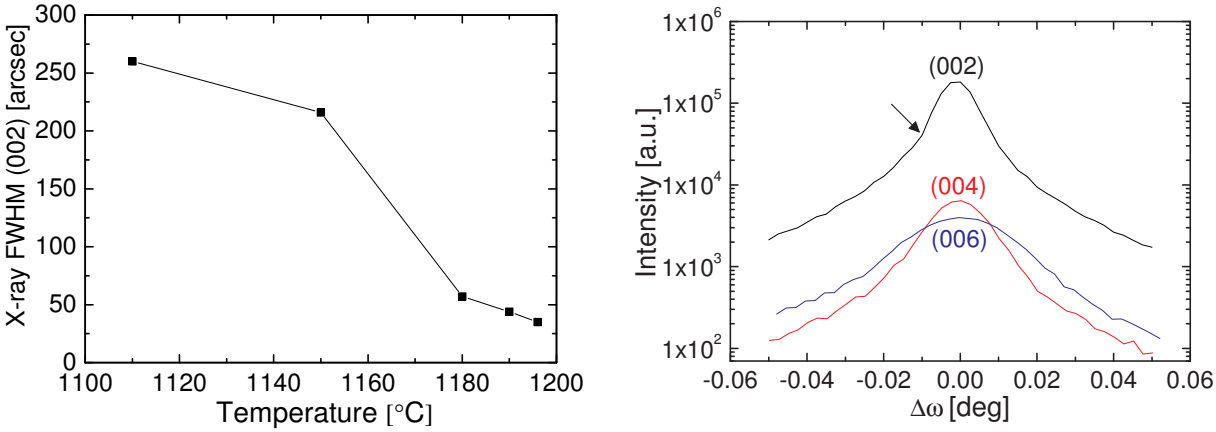

Figure 4.23: Change in the FWHM of X-ray rocking curve for the symmetric (002)-reflection with respect to the growth temperature (left) and X-ray rocking curves for the (002)-, (004)- and (006)-reflections of AlN (right). The arrow marks a kink at the lowest order (002)-reflection. No sharp peak is visible for the (006)-reflection curve.

mean diffusion length λ_s of atoms was larger than the terrace width. If λ_s was smaller than the terrace width, then 3D growth mode with rough surface morphology could be realized. Figure 4.22 (right) exhibits a $10 \times 10\,\mu m^2$ AFM scan with a measured RMS surface roughness of 0.31 nm. We occasionally observed one or two large hexagonal pits on such a large area AFM scan and estimated the average density of such pits to be in the range of $10^4\,cm^{-2}$. The remarkable reduction in the density of large hexagonal pits is particularly attributed to the high growth temperature. These AFM observations elucidate an improvement in the surface quality of the AlN epilayer when it was grown at the highest possible temperature in our reactor.

Similarly, we observed an improvement in the crystalline quality of our AlN epilayers with increasing growth temperature. Figure 4.23 shows a plot of the FWHM of the X-ray rocking curves of the symmetric (002)-reflection with respect to the growth temperature. The FWHM is decreasing with increasing growth temperature. We measured very narrow X-ray rocking curves (FWHM $\leq$ 50 arcsec) for the (002)-reflection on higher temperature grown samples.

4.3 Structural and Spectroscopic Properties of AlN

In this section, we will discuss more detailed structural and spectroscopic properties of our 500 nm thick optimized AlN epilayers.

Structural Properties

The investigations of the surface morphology of AlN epilayers were already discussed in previous sections. Here, we will analyze the crystal quality in detail using X-ray and TEM investigations.

As discussed earlier, we measured very narrow X-ray rocking curves (FWHM $\leq$

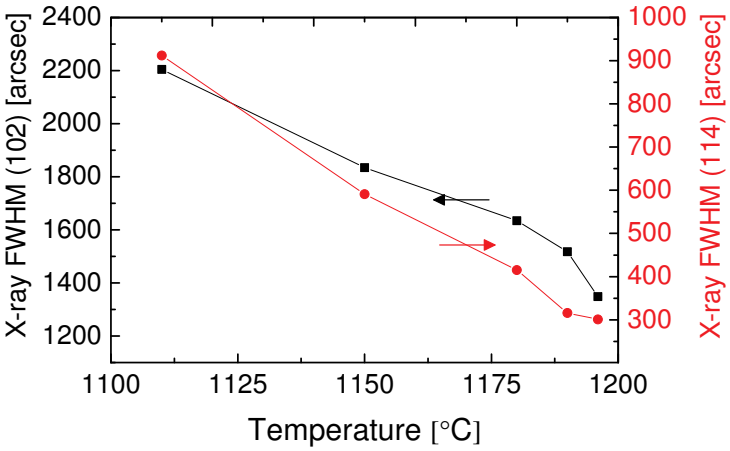

Figure 4.24: Illustration of change in FWHM of X-ray rocking curves of skew-symmetric (102)- and asymmetric (114)-reflections with respect to the growth temperature.

50 arcsec) for the (002)-reflection. However, it cannot be ruled out that there is no contribution of the correlation peak in such a low value of the FWHM for the (002)-reflection. Higher order (004)- and (006)-reflections for an AlN epilayer grown at 1199 °C are also illustrated in Fig. 4.23. The FWHM for the (002)-, (004)-, and (006)-reflections are 41, 61, and 108 arcsec, respectively. The shape of the (002)-reflection consists of two contributions: a very sharp peak and a broad background which is almost three times broader than the sharp region. A kink at the plot is shown by an arrow which is the transition from the broad background to the sharp peak. In addition, for the higher order (006)-reflection, the sharp component is attenuated and only the broader component is visible. In case of the (004)-reflection, it is not possible to distinguish the transition. The sharp peak of the (002)-reflection might be coming from the correlation effect of the underlaying oxygen-doped AlN NL. However, we did not observe the correlation effect in the samples grown at lower temperatures. The inferior crystalline quality of the overgrown epilayer absorbs the correlation effect of the underlying NL. Therefore, the appearance of the correlation effect in the low order X-ray reflection also evidences the high crystalline quality of the overlaying epilayer although the measured value of FWHM might be exaggerating the real structural quality.

Meanwhile, we measured the skew-symmetric (102)- and asymmetric (114)-reflections (Fig. 4.24) to obtain detailed information on the structural imperfections present in the AlN film. Like for the (002)-reflection, the FWHM of both, (102)- and (114)-, reflections is decreased with increasing growth temperature. The measured FWHM for the (102)- and (114)-reflections of our optimized 500 nm thick AlN layer are 1359 and 301 arcsec, respectively. We calculated the out-of-plane strain $\epsilon_{\perp}$ of this epilayer to be -0.05% using Eq. 2.6. It shows that the epilayer is under in-plane tensile strain which is expected due to the thermal expansion coefficient and the lattice parameters mismatches between AlN and sapphire substrate. The values of FWHM for the (002)- and (102)-reflections are used to estimate the density of screw and/or mixed components N_S and the edge

Table 4.7: Calculated threading dislocation densities from the FWHM of X-ray rocking curve measurements for AlN layers grown at various temperatures.

Sample	Growth Temperature	N_S cm^{-2}	N_E cm^{-2}
Y937	1110	1.5×10^{8}	3.8×10^{10}
Y1008	1150	1.0×10^{8}	2.7×10^{10}
Y1019	1180	7.1×10^{6}	2.1×10^{10}
Y1153	1190	4.2×10^{6}	1.8×10^{10}
Y1176	1199	2.7×10^{6}	1.4×10^{10}

and/or mixed components N_E of threading dislocations (TDs) in the AlN epilayer using Eqs. 2.19 and 2.20. Table 4.7 lists the estimated TD densities.

Dipl.-Phys. Oliver Klein of the Transmission Electron Microscopy Group of Ulm University carried out TEM investigations on sample Y1153 (grown at 1190 °C). He also developed and verified a dislocation model for the pure edge a-type TD in AlN with the help of weak beam dark field (WBDF) and HR-TEM investigations on this sample by comparing the experimental images with the calculated ones, obtained by applying a multi-slice algorithm on the dislocation model [181]. The cross-sectional bright field TEM (BFTEM) image in Fig. 4.25 shows an overview of the dislocation structure where the TDs of all types, edge (a-type), screw (c-type), and mixed ((a+c)-type), are visible. Large numbers of dislocations were created at the nucleation layer-sapphire interface, and they decreased as the epilayer thickness increased. The SAED pattern obtained from three different regions (sapphire, AlN-sapphire interface, and AlN epilayer) of the sample from the $[01\bar{1}0]$ zone-axis of AlN and $[11\bar{2}0]$ zone-axis of sapphire are also shown. The diffraction spots without streak suggest no stacking disorders in the layer.

The cross-sectional WBDF images of Fig. 4.26 (top) and (bottom) were recorded from the same sample area under $\mathbf{g} = 0002$ and $\mathbf{g} = 2\bar{1}\bar{1}0$ conditions, respectively, to make clear the differences of dislocation behavior. Using the $\mathbf{g} = 0002$ diffraction condition, we can observe dislocations with a [0001] (screw-type TDs) and $1/3[2\bar{1}\bar{1}3]$ (mixed-type TDs) type Burgers vectors $\mathbf{b}$. Similarly, using $\mathbf{g} = 2\bar{1}\bar{1}0$ diffraction condition, we can observe additional dislocations with a $[2\bar{1}\bar{1}0]$ (edge-type TDs) type $\mathbf{b}$. In these images, dislocations correspond to white lines and, in particular, thick white lines may be a bundle of dislocations in the direction of the depth. It is clearly shown that most dislocations formed are pure edge dislocations of type $1/3[2\bar{1}\bar{1}0]$ along the c axis, whereas the number of [0001] pure screw and/or $1/3[2\bar{1}\bar{1}3]$ mixed dislocations is very small. Furthermore, it is observed that the dense edge-type dislocations starting at the nucleation site thread the entire epilayer thickness and terminate at the surface with openings. A high edge-type TD density is related to the low surface mobility of the Al species during deposition, which prevents the formation of large islands in the initial stage of growth. Small pits (diameter ≤1 nm) in the AFM image in Fig. 4.22 (left)

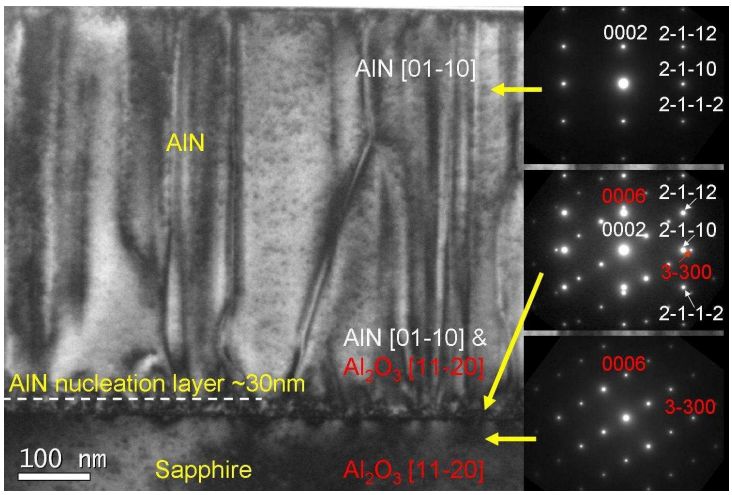

Figure 4.25: Bright Field TEM (BFTEM) image showing an overview of the dislocation structure. SAEDs at three different areas of the sample are also shown.

correspond to the openings of such edge-type dislocations at the surface. The density of such small pits in AFM is approximately $4{\times}10^{10}\text{cm}^{-2}$ which is close to the edge-type dislocation density estimated from TEM analysis. This is verified by counting the pits in AFM image and the number of dislocations per length in the cross-sectional WBDF image considering the depth of the TEM sample. This estimation is further confirmed by a planar-view TEM investigation. Figure 4.27 shows a planar-view BFTEM image exhibiting the dark marks arising from dislocations along c-direction in the AlN layer. The inset shows an unclosed Burgers circulation around the dislocation core in the filtered HR-TEM micrograph identifying the TD as a pure edge dislocation with **b** =

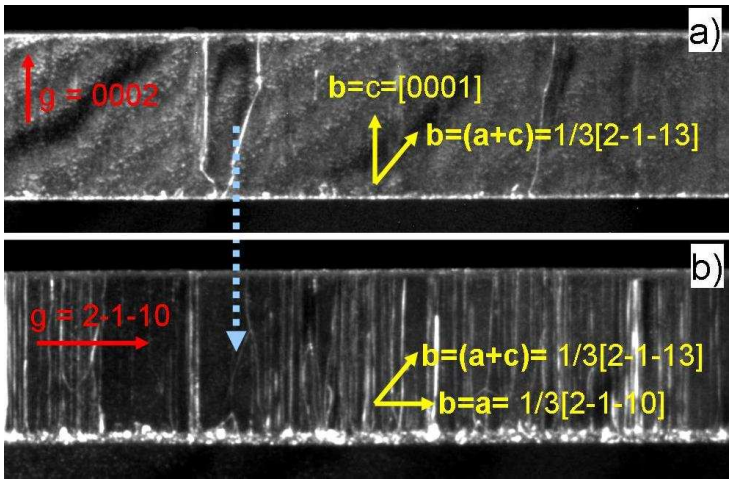

Figure 4.26: TEM dark images using the WBDF technique exploiting the (0002) (on top) and $(2\bar{1}\bar{1}0)$ (on bottom) reflections from the same area of the sample. The Burgers vectors **b** of the TDs in the respective WBDF image are also illustrated.

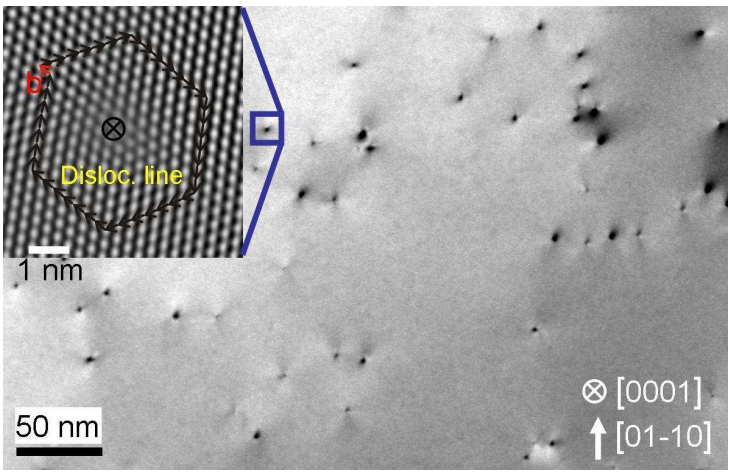

Figure 4.27: Plane-view [0001] BFTEM image exhibiting the dark marks arising from dislocations along c-direction in the AlN layer. Inset shows unclosed Burgers circulation around the dislocation core in the filtered HR-TEM micrograph identifying the TD as a pure edge dislocation with **b** = 1/3 [$2\bar{1}\bar{1}0$].

1/3 [$2\bar{1}\bar{1}0$]. The formation of the pure edge a-type TDs in AlN can be described as a cut along the [$01\bar{1}0$] direction with subsequent displacement at b = 1/3 [$2\bar{1}\bar{1}0$]. The edge-type dislocation density in this sample is measured to be approximately 3.4×10^{10}cm^{-2} which is nearly equal to the small pit density in AFM image. Thus, as most threading dislocations in our samples are of pure edge-type there is no doubt that the small pits in AFM images are connected to pure edge-type dislocations. As mentioned in chapter 2, we have not considered the contribution from the lateral coherence length in the calculation of the X-ray measurements. Therefore, the actual value of dislocation density is normally determined from the planar-view TEM analysis which is almost a factor of two higher than the calculated N_E from X-ray rocking curve measurement.

Similarly, we measured the screw type dislocation density by counting the number of dislocations per length in the cross-sectional WBDF image and the depth of the TEM samples which is almost equal to the calculated N_S from the X-ray rocking curve measurement. Moreover, the larger hexagonal pits (diameter ≥ 10 nm) in AFM image may be corelated to the screw and/or mixed-type TDs [182].

Spectroscopic Properties

First, we will discuss near-band-edge (NBE) luminescence studies of our two samples Y968 and Y973 grown under two different NH_3 flows of 255 and 155 sccm, respectively, whereas the TMAl flow was fixed at 11.3 μmol/min The growth temperature of these samples was 1150°C and the rest of the growth parameters was kept constant as given in Tab. 4.3. The nucleation layer and all the growth conditions were the same for both samples. These samples were investigated by Dr. G.M. Prinz [183] using CL. The NBE transitions such as free exciton or bound exciton recombination are characteristic of high quality materials with lower impurity concentration and lower defect density.

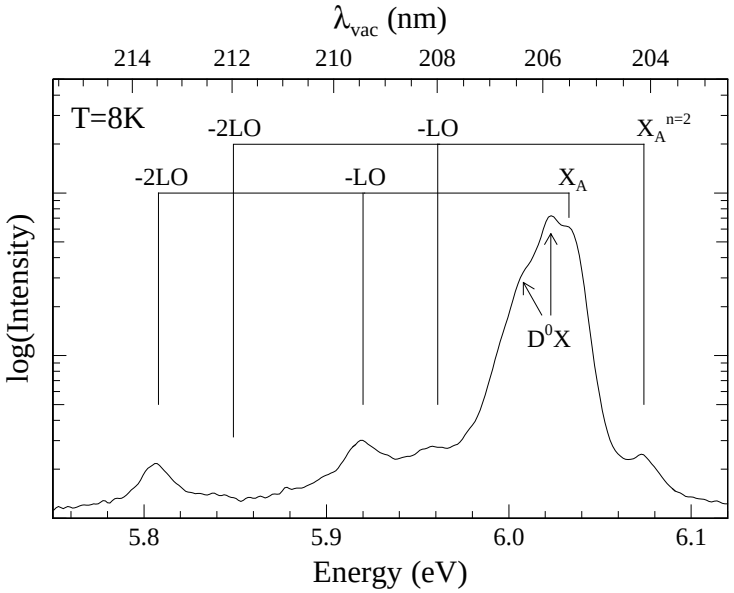

Figure 4.28: Low temperature spectrum of sample Y968. Three main contributions are seen in the near-band-edge luminescence. Additionally, a weaker line at about 6.073 eV and its LO-Phonon replica are also observed.

Heavy doping or high density of defects in the samples generate strong localized fields. That is why exciton luminescence can only be observed in high quality materials. At a temperature of about 8 K, we observed strong luminescence peaks at the vicinity of 6.0 eV and these peaks are well-resolved in both samples.

Figure 4.28 shows a low-temperature (T = 8 K) spectrum of sample Y968 where the intensity is plotted in logarithmic scale. The spectrum shows three main contributions at 6.033, 6.022, and 6.007 eV. Two dominant transitions at 6.022 eV and 6.007 eV are assigned to the recombination of excitons bound to neutral donors (D^0, X). However, the donors for these transitions are still in question. From a temperature dependent CL measurement (from 30 K to room temperature, as shown in Fig. 4.29) one can confirm the transition at 6.033 eV is due to the recombination of free excitons with holes from the A-valence band (X_A).

In addition to these three main contributions of the NBE luminescence, LO-phonon replica (-LO and -2LO) of the free A exciton X_A are recognized at approximately 110 meV lower side of the luminescence line. The presence of such replica is an indication of a good crystalline quality of the AlN epilayer. Moreover, a weaker transition at about 6.073 eV is also seen on the higher side of the luminescence line. The reason for this specific transition is not clearly known. However, this transition disappeared in temperature dependent CL measurement with increasing temperature. Several different models can be considered as a possible reason for this transition. It might be assigned to an excited free excitons $X_A^{n=2}$ [184]. LO-phonon replica (-LO and -2LO) to this transition are recognized at approximately 110 meV lower side. From the energetic distance of the two transition positions of X_A and $X_A^{n=2}$, the binding energy of the free A exciton X_A can be calculated as [183]

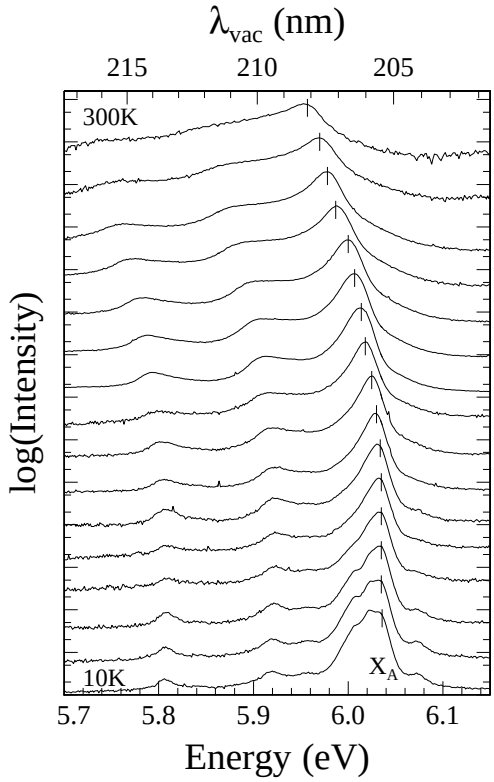

Figure 4.29: Temperature dependent (from about 30 K to room temperature) CL measurements of the sample Y968. The luminescence from the recombination of free excitons is dominating.

$$R_y(X_A) = 4/3 \cdot E(X_A^{n=2}) - E(X_A) = 53\,\text{meV}, \tag{4.2}$$

.

Although this value is lower than the value reported by Li *et al.* [30] (80 meV), it is still larger than that in GaN due to the larger effective masses of electrons and holes in AlN. The estimated full width at half maxima (FWHM) of the free A exciton X_A and excitons bound to neutral donors (D^0, X) lines is approximately 25 meV.

Figure 4.30 shows a comparison of the CL-spectra of samples Y968 and Y973 (grown under low NH_3 flow). A shift of the NBE luminescence to smaller energies for Y973 can be clearly seen. The free A exciton X_A position of Y973 is at 6.000 eV which is 33 meV lower to the X_A position of Y968. This shift explicitly evidences that a reduction of the NH_3 flow leads to an in-plane tensile strain of the samples. The (002)-reflection rocking curve peak shift to higher ω angle in HRXRD and E_2^{high} phonon mode shift to lower wave numbers in Raman measurements (see Fig. 4.31) further confirm the higher in-plane tensile strain situation in Y973 in comparison to Y968. We estimated -0.12% and -0.3% out-of-plane strain $\epsilon_\perp$ in Y968 and Y973, respectively. Moreover, a large number of crack lines were also visible on the surface of Y973. Such cracks might be possibly due to the residual in-plane tensile strain in the sample. These observations

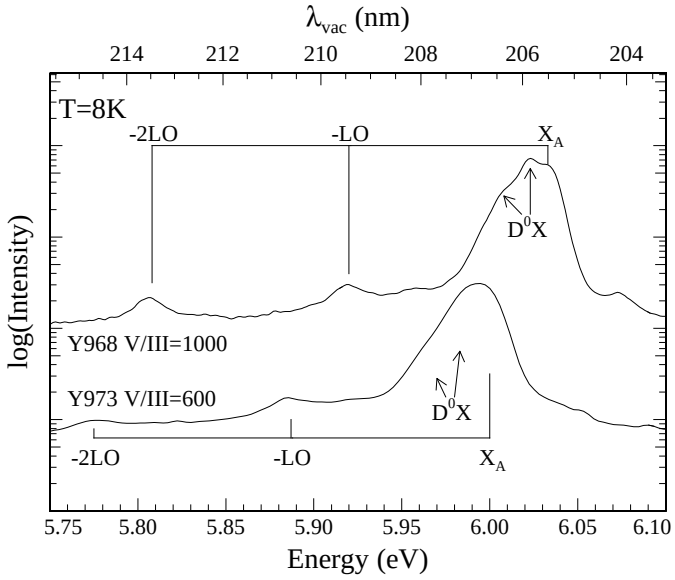

Figure 4.30: Low-temperature spectra of the two samples of Y968 and Y973. A clear shift of the band edge related luminescence at smaller energies for Y973 sample is seen.

show that the flow-rate of NH_3 is a very critical issue in the growth of AlN epilayers. We empirically found that an implication of a very small flow of NH_3 can be a good choice but the growth of a crack-free unstrained thick layer can not be accomplished due to the formation of residual strain on the layer. Therefore, we implied 11 μmol/min (0.13 sccm) of TMAl and 250 sccm of NH_3 (11.2 mmol/min) as quintessential growth parameters for the growth of a nominally thick AlN epilayer.

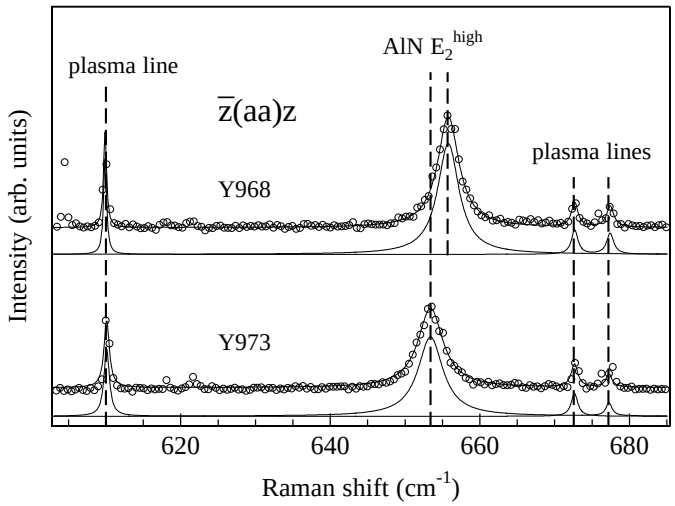

Figure 4.31: Raman spectra of the two samples Y968 and Y973. Besides the E_2^{high} phonon mode, plasma lines of the Ar^+-laser are also shown. A shift of the E_2^{high}-mode to smaller wave numbers visible for sample Y973.

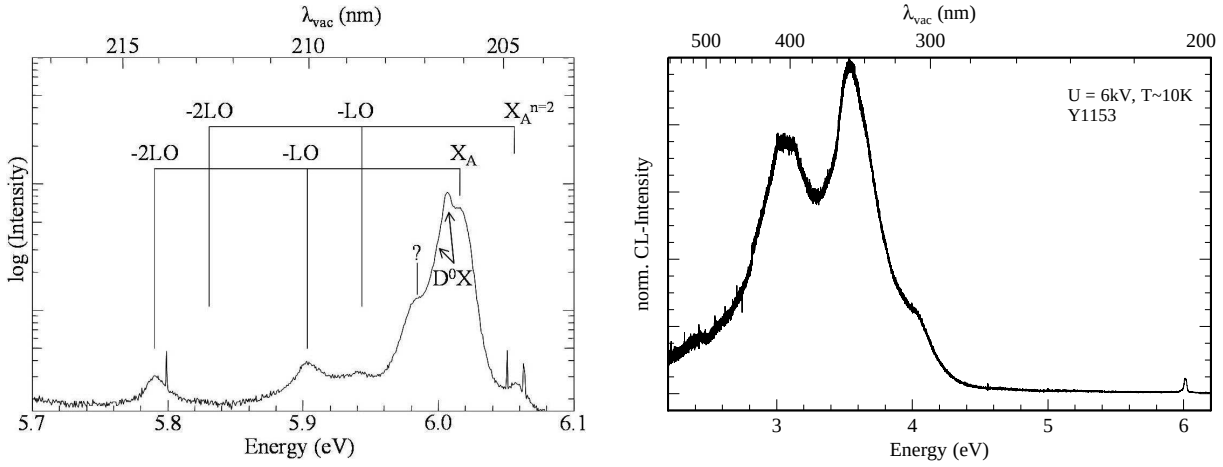

Figure 4.32: Low temperature spectrum of an AlN sample exhibiting near-band-edge luminescence (left) and overall view (right). The deep-level transitions (DLT) at about 3.05 eV, 3.55 eV, and a shoulder at about 4.06 eV are visible.

Next, the NBE luminescence of sample Y1153 (grown at 1190°C) was carried out in addition to the deep level luminescence studies. Figure 4.32 (left) shows a low temperature (T = 8 K) spectrum of this sample. Like in sample Y968 (grown at 1150 °C with similar growth conditions and thickness), we observed three main contributions: at 6.017 eV corresponding to X_A (confirmed by temperature series CL measurements), and at 6.007 eV and 5.84 eV corresponding to D^0, X. Here, the X_A peak is shifted to lower energy by 16 meV in comparison to the position of X_A in sample Y968. Such shifting corroborates the fact that a high temperature growth leads to in-plane tensile strain of the epilayer under similar growth conditions. Similar to sample Y968, -LO and -2LO of the X_A are recognized at approximately 110 meV lower energy of the luminescence line. A weaker transition at about 6.0573 eV is also seen on the higher energy of the luminescence line due to the $X_A^{n=2}$. Using the energy at these transitions in Eqn. 4.2, we have calculated the binding energy of X_A approximately 54 meV which is similar to the value obtained for the sample Y968 (grown at 1150 °C). Moreover, the FWHM of the X_A and the D^0, X is estimated to be approximately 10 meV, factor of 2.5 less than the sample grown at 1150 °C. Such a narrow spectrum width is an indication of an improvement of the crystalline quality of the AlN epilayer due to the higher growth temperature.

To look more in detail into the spectroscopic properties of AlN epilayers, luminescence studies of a wide range of the spectrum were carried out. Similar to the GaN yellow luminescence band, we observed a violet luminescence band in AlN. A nearly similar line shape of the broadband luminescence in GaN and AlN suggests that their origin could be from the same kind of defects present in both materials. Figure 4.32 (right) shows an overall spectral view of the luminescence of sample Y1153. In addition to the relatively weak NBE luminescence at about 6 eV, a broader luminescence band is observed in between 2.8 to 4.5 eV in the violet region. There are essentially three identifiable transitions at about 3.05 eV, 3.55 eV, and a shoulder at about 4.06 eV. There are several interpretations regarding the deep level transitions (DLTs) in violet band. However, there is no consensus even on the qualitative nature of these tran-

sitions. Dadgar and Bastek *et al.* [61, 62] assigned the transitions at about 3.2 eV and 3.8 eV to the oxygen-DX-center and silicon-DX-center, respectively. A DX-center forms a deep state within the band gap where "D" stands for a participating donor and the "X" for the second unknown defect. Furthermore, the transition at about 4.6 eV and 5 eV were attributed to the Al-vacancy and nitrogen-vacancy, respectively. However, a sound justification for these assignments is not mentioned. Others reported that oxygen [43, 185] or carbon [43] impurities give rise to an intense and broad violet luminescence band. Strassburg *et al.* [186] also investigated the deep luminescence and compared the data with elemental analysis using glow discharge mass spectrometry (GDMS). They came to the conclusion that neither oxygen nor silicon impurities are straightly correlated with the transition in the observed violet luminescence band and ruled out that an impurity element alone is generating such emission band. Theoretical calculations have indicated that the cation vacancy V_{Al} and its complex with donors in undoped and Si-doped AlN layers have small formation energies and easily create negatively charged defect states with acceptor character during the crystal growth [87, 89, 187]. Meanwhile, the formation energy of V_{Al}-O_N complexes is lower than that of an isolated V_{Al} because of their opposite charge characters. Therefore, Mattila and Nieminen [87] suggested that the complex formation between cation vacancies and substitutional oxygen donors e.g. V_{Al}-O_N, is indeed a very likely process. Evidence for the presence of cation vacancies in the luminescence processes also comes from the experimental results by Fan *et al.* [14]. They reported that the formation energy of the triply negatively charged V_{Al}^{-3} is very low during the growth of AlN. The possibility of V_{Al}^{-2} as the origin of a deep acceptor can be excluded due to its higher formation energy than (V_{Al}-complex)$^{-2}$. The transition mechanism comes from the donor-to-acceptor pair (DAP) transitions between a shallow donor and different acceptor levels, namely, V_{Al}^{-3}, and its complexes. According to Fan *et al.*, the electron energy of the V_{Al}^{-3} level is approximately 0.5 eV higher than that of the (V_{Al}-complex)$^{-2}$. This value was determined by both, experimental measurement and theoretical calculation. In Fig. 4.32 (right), we also see two transitions at the lower energy side (at 3.05 eV and 3.55 eV), separated by 0.5 eV. Thus, the transitions at 3.05 eV and 3.55 eV might be associated with V_{Al}^{-3} and (V_{Al}-complex)$^{-2}$ acceptor levels, respectively. Since the Si impurity level of our sample was below the detection limit of SIMS ($\leq 10^{17}$ cm^{-3}), the V_{Al} may form a complex with oxygen (1-2 $\times 10^{18}$ cm^{-3}) incorporated into the layer. The shoulder at 4.06 eV may be associated with a deep level acceptor impurity transition due to the cation vacancy complex with one negative charge (V_{Al}-complex)$^{-1}$, such as (V_{Al}-2O)$^{-1}$ which has a higher formation energy [14, 87].

The emission of such a broad and intense violet luminescence indicates the presence of large amounts of point defects in our AlN epilayer which may have an adverse effect on the electrical conductivity. We will discuss on intentional doping and its effects on the properties of AlN in the next chapter. Besides point defects, the X-ray (see previous sections) and the TEM investigations (see above) showed that the AlN epilayers also contain considerable amounts of extended defects, especially edge-type threading dislocations. The latter commonly do not contribute to the luminescence, although they may significantly affect the optical and electrical properties of the material by trapping carriers or gettering the point defects.

Table 4.8: Measured characterization results of approx. 500 nm and 1 μm thick optimized AlN epilayers.

Parameters	Results for the thickness of	
	500 nm	1 μm
AFM RMS surface roughness (1 ×1 μm^2 scanning)	0.21 nm	0.2 nm
Hexagonal pit density	$< 10^5$ cm^{-2}	$< 10^5$ cm^{-2}
FWHM of HRXRD (002) reflection	35 arcsec	25 arcsec
FWHM of HRXRD (102) reflection	1349 arcsec	1051 arcsec
FWHM of HRXRD (114) reflection	301 arcsec	290 arcsec
Screw-type TDs from TEM	10^7 cm^{-2}	
Edge-type TDs from TEM	3.5×10^{10} cm^{-2}	
FWHM of low temp.(T = 8K) CL NBE peak	$\approx$ 10 meV	$\approx$ 10 meV
In-plane tensile strain	-0.05%	-0.01%

Nevertheless, the overall characterization results show that we have achieved a high quality 500 nm thick undoped AlN epilayers in the existing facility and the best results reported so far in the AIXTRON AIX200RF reactor. Table 4.8 presents a summary of the results after the optimization of growth procedures.

To analyze the thickness dependent properties of an AlN epilayer, we deposited an approximately 1 μm thick layer using the same optimized growth parameters as described above. Table 4.8 shows the comparative characterization results of approx. 500 nm and 1 μm thick optimized AlN epilayers. Similar as described by others [188], we observed a slight improvement in the crystal quality of our undoped AlN layer. The FWHM of the X-ray rocking curves for all the (002), (102) and (114)-reflections is significantly reduced. We calculated an out-of-plane strain $\epsilon_\perp$ to be -0.01% which is lower than that of the 500 nm thick layer (-0.05%). It shows that a 1 μm thick layer is more relaxed than a 500 nm thick layer. We observed an emergence of few cracks on the surface of the epilayer. This may be due to the release of the in-plane tensile strain after exceeding the critical thickness. The FWHM of X-ray values give estimated screw and edge-type TDs N_S and N_E to be 1.4×10^6 cm^{-2} and 8.8×10^9 cm^{-2}, respectively. It shows a remarkable reduction of the dislocation density after increasing the layer thickness. However, the surface morphology and the CL near band-edge excitonic emission were almost similar to the 500 nm thick sample. Furthermore, the position of the recombination line of excitons bound to neutral donors D_0X and the free A exciton X_A transition were shifted to the higher energy side at 6.024 and 6.034 eV, respectively, indicating the thicker layer is almost unstrained which is in-line with the results obtained from the X-ray measurements.

To see the effects of even larger epilayer thickness on the properties of AlN, we employed a multi-step growth technique at a fixed growth temperature of 1199 °C. Details of this technique are described below.

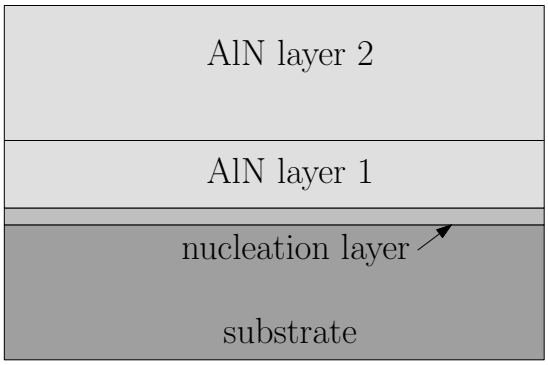

Figure 4.33: Schematic illustration of the AlN epilayer deposition with different V–III ratio over a medium-temperature (MT) oxygen doped AlN nucleation layer (NL) on sapphire substrate.

4.4 Multi-step growth on sapphire

Since our reactor is built with quartz glass, it is not possible to continuously expose it to a high temperature of 1199 °C for a very long time to deposit an epilayer thicker than 1 μm. Therefore, a multi-step growth process was employed. In this technique, the growth rate was increased by increasing TMAl flow-rate at various growth steps to achieve the required thicknesses. As illustrated in Fig. 4.33, we deposited an approximately 200 nm thick AlN (layer 1) using our optimized two-step growth process and parameters of Tab.4.6. During the growth of layer 2, we increased the TMAl flow-rate from 11.3 μmole/min to 22 μmole/min for the growth of 1.5 and 2.0 μm thick layers and up to 54 μmole/min for the growth of the 2.5 μm thick layer. The flow-rate of TMAl was increased slowly within 90 seconds.

Figure 4.34 illustrates the measured FWHM for the (002)- and (102)-reflections against various thicknesses of the AlN epilayers. We observed very low values of the FWHM for the (002)-reflection ($\leq$ 50 arcsec) for thin samples. However, it increased with increasing thickness ($>$ 1 μm). There are basically two reasons for such a broadening of the (002) rocking curves. First, the imperfections of the epilayer are increased with higher growth rates. The cross-sectional TEM WBDF image of Fig. 4.35 (a) under $\mathbf{g}$ = 0002 condition shows an increased number of screw and mixed type TDs in comparison to the similar investigation of the 500 nm thick sample (see Fig. 4.26 (top)). Although some TDs are annihilated by forming TD loops, many new TDs emerged in the course of increasing thickness. Second, the visibility of the correlation peak due to the high density of homogeneously distributed pure edge-type threading dislocations might be vanishing with increasing imperfectness. A similar result for a GaN layer deposited over an oxygen-doped AlN NL was also reported by Bläsing *et al.* [164] and Hertkorn *et al.* [78]. However, as illustrated in Fig. 4.34, the measured FWHM for the (102)-reflection strongly decreases with increasing epilayer thicknesses similar as observed by others [188]. Figure 4.35 (b) under $\mathbf{g} = \bar{1}100$ condition exhibits that some of the edge-type TDs are bended with increasing epilayer thicknesses and annihilated

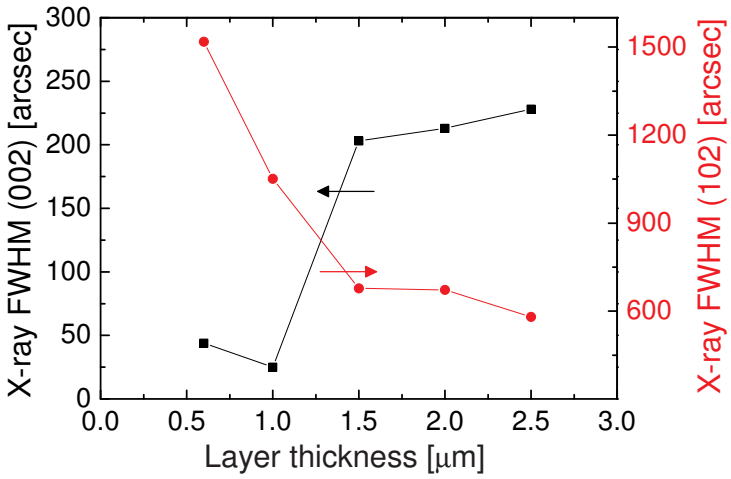

Figure 4.34: Change in FWHM of X-ray rocking curves of symmetric (002)- and skew-symmetric (102)-reflections with respect to the layer thicknesses.

by loop formation. Imura *et al.* [113] also observed similar results and reported that the transition of the growth mode by thickness variation can reduce the number of dislocations, as these dislocations of opposite signs are forced to redirect towards each other resulting in dipole half-loop formation.

The calculated screw and edge-type TDs N_S and N_E are tabulated in Tab. 4.9. Unfortunately, it was not possible to investigate these samples by plan-view TEM because of difficulties in sample preparation. By counting the number of dislocations

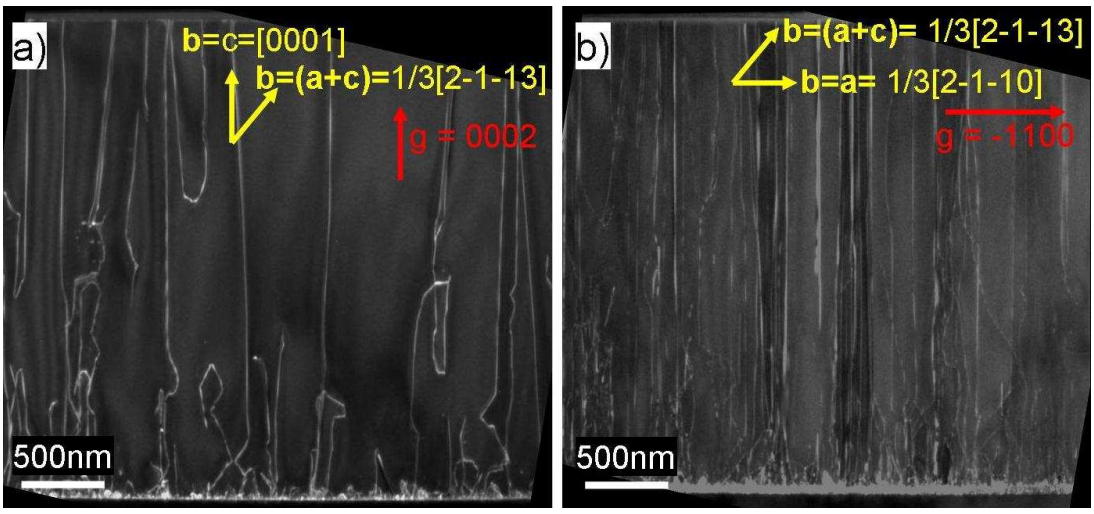

Figure 4.35: Cross-sectional TEM WBDF image of a 2 μm thick AlN epilayer exploiting the (0002) (a) and ($\bar{1}$100) reflections (b). The Burgers vectors **b** of the TDs in the respective WBDF image are also illustrated. TD loops and emergence of screw-type TDs are seen in (a). Bending and loop formation of edge-type TDs are seen in (b).

Table 4.9: Calculated screw and edge type TDs N_S and N_E for varying epilayer thickness.

Sample	Layer Thickness	N_S	N_E
	μm	cm^{-2}	cm^{-2}
Y1153	0.5	4.2×10^{6}	1.8×10^{10}
Y1249	1.0	1.4×10^{6}	8.8×10^{9}
Y1233	1.5	9.0×10^{7}	3.6×10^{9}
Y1234	2.0	9.9×10^{7}	3.5×10^{9}
Y1235	2.5	1.1×10^{8}	2.6×10^{9}

per length in the cross-sectional TEM WBDF image considering the depth of the TEM samples, the dislocation density can be estimated to be a factor of two higher than the calculated value from the FWHM of X-ray rocking curves. This is verified by counting the number of pits in AFM images. Hence, X-ray systematically underestimates the dislocation density by a factor of two.

Figure 4.36 shows $1\times1\,\mu$m^2 (left) and $10\times10\,\mu$m^2 (right) AFM micrographs of the 2.5 μm thick AlN epilayer. The RMS surface roughness of the $1\times1\,\mu$m^2 scanned image is 0.16 nm. The surface is atomically flat having terraces with monoatomic step height. The average terrace width is about 75 nm. By considering monoatomic step height and

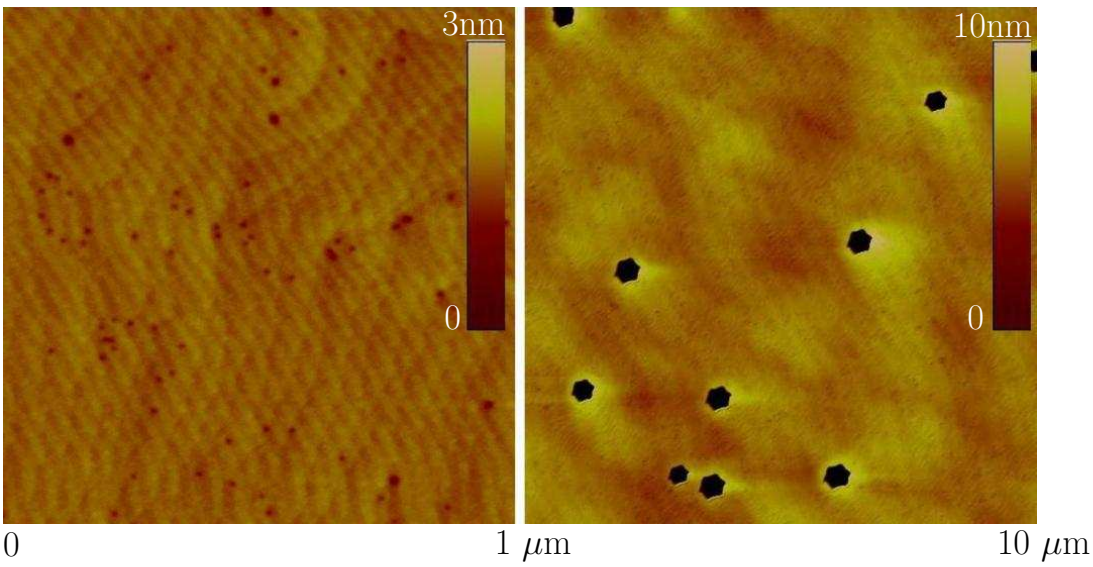

Figure 4.36: AFM images of 2.5 μm thick AlN epilayer. $1\times1\,\mu$m^2 scanned image (left) exhibiting atomically flat and clearly resolved terraces and atomic step height. Scattered small pits are also visible. $10\times10\,\mu$m^2 scanned image (right) exhibiting large hexagonal pits. The terraces are also visible.

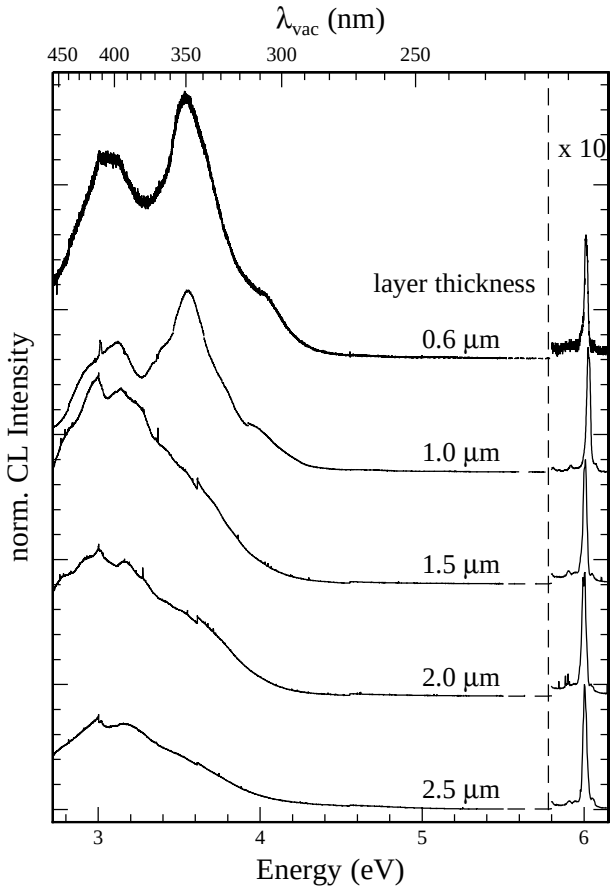

Figure 4.37: Overview of low-temperature (T=8K) CL spectra of AlN with changing epilayer thickness. The spectra are normalized to the intensity of NBE luminescence. A change in the intensity of violet luminescence with the epilayer thickness is clearly observed.

the average terrace width, we obtained the tilt angle of the AlN surface plane to be about 0.2 °which is close to the sapphire misorientation angle i.e. 0.3 °miscut to the m-plane. The density of the scattered small pits, associated with edge-type TDs, is about 7×10^9 cm^{-2}. This value is almost two to three times higher than the estimated N_E. The average diameter of the opening of these small pits is about 15 nm, significantly larger than what we observed on the surface of thin epilayers. Such increase in diameter is attributed to the propagation of TDs in conical shape. Few large size (diameter $\geq$ 50 nm) pits are also seen at the 1×1 μm^2 scanned image which are associated with screw and/or mixed-type TDs. However, very large size (diameter $\geq$ 400 nm) hexagonal pits, associated with screw and/or mixed-type TDs, are seen at the 10×10 μm^2 scanned image. The average density of these pits is about 1×10^7 cm^{-2}. We observed that the density of small pits is increased with decreasing epilayer thickness but the density of large hexagonal pits is almost independent of the epilayer thickness. Moreover, the size of both, the small and the large hexagonal pits increased with increasing epilayer thickness. The RMS surface roughness of the 1×1 μm^2 scanned image of all samples is

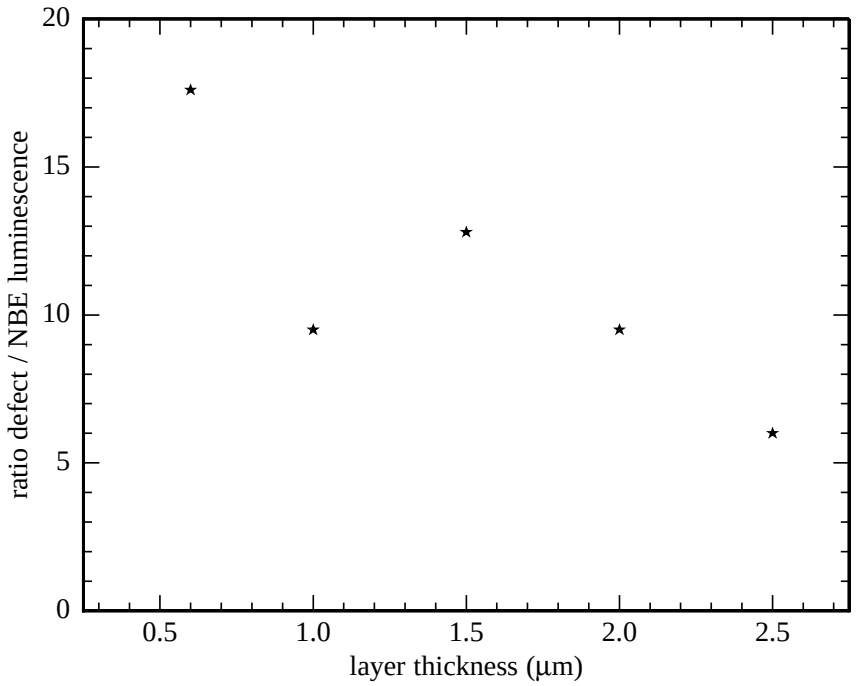

Figure 4.38: CL intensity ratio of the NBE to the defect related DLT with respect to the epilayer thickness.

below 0.2 nm.

Low-temperature (T=8 K) CL measurements were carried out by R.A.R. Leute during his diploma thesis to investigate the influences of epilayer thickness on the spectroscopic properties of AlN [189]. Figure 4.37 shows the CL spectra of all samples. The intensity of the spectra is normalized to the intensity of the ten times magnified NBE luminescence for a more precise comparison. It is clearly seen that the overall integrated intensity of the defect related deep-level-transitions (DLT) at the violet luminescence band decreases with increasing epilayer thickness. The intensity of the transition at around 3.55 eV is dominant in the 0.5 and 1.0 μm thick samples. It is largely reduced in other thicker (1.5 to 2.5 μm) samples. It is noted that the growth rate of these thicker samples was higher than the first two 0.5 and 1.0 μm thick samples. We observed that the influence of the layer thickness to improve the quality is more pronounced than the deteriorating effect of higher growth rates. Such a reduction in the intensity of the transition at around 3.55 eV in thicker samples may be attributed to a high supply of TMAl during the growth. It shows that the Al-rich growth condition helps to minimize the point defects due to aluminum vacancies and their complexes. Another explanation is that the reduced density of edge-type TDs in thicker epilayers also reduces the gettering of the point defects which ultimately minimizes the defect related transitions. The ratio of the NBE to the DLT with respect to the AlN epilayer thickness is shown in Fig. 4.38. For a quantitative analysis, the integration limit of the NBE and the DLT intensities is limited from 5.85 to 6.2 eV and 2.8 to 5.0 eV, respectively. It is clearly seen that the DLT can be minimized by increasing the epilayer thickness. Unfortunately,

the samples thicker than 1.3 μm were not crack free. The crack density increased with the increase of thickness. The average distance between the cracks was about 3 mm in the 1.5 μm thick sample whereas it was about 500 μm in the 2.5 μm thick layer. We conclude that cracking is one of the severe problems and a major issue in thick layer growth of AlN. Therefore, a so-called crack critical thickness limits the increase of the layer thickness at least on sapphire substrate.

4.5 Using Indium as Surfactant

Indium has been found to be an effective surfactant for the growth of group-III nitride films due to its low solubility in AlN or GaN at a high growth temperature. Thermodynamically, indium or indium compounds are not predicted to be stable (easily decompose) at the temperatures used in this study. There are already few reports stating the use of indium as a surfactant element in the growth of GaN [190] and AlN/GaN heterostructures [191, 192]. Not only by decreasing the surface free energy but also by enhancing the surface mobility of adsorbed species, In can remarkably influence the surface quality of GaN and AlN. Recently, a theoretical study on the basis of first-principle total-energy calculations within the density-functional theory was carried out by Zhuang *et al.* [193] about the effect of an In-adlayer on AlN with Al- and N-polar layers. It is reported that the surfactant effect of In is attributed to a much weaker In-Al bond than the Al-N bond on the Al-polar AlN surface and the bigger average diffusion coefficient for Al atoms on the Al-polar AlN surface. For the Al-polar surface, there is a larger driving force for surface segregation of In so that it behaves as a surfactant and the diffusion barrier energy of Al atoms becomes smaller. Therefore, the addition of In can modify the surface kinetics, increase the Al mean path at the surface, promote step-flow mode, and improve the morphology of the grown AlN layers. Earlier, Neugebauer *et al.* [194] pointed out that the presence of an In adlayer on the surface quantitatively affects the diffusion of N adatoms: Lateral transport of N adatoms on the surface is not realized by diffusion on the top surface layer but below the In adlayer. This mechanism reduces the N diffusion barrier dramatically (by more than a factor of two) and opens an efficient and hitherto unexpected diffusion channel for lateral surface transport. Significantly enhanced adatom diffusivity on the surface favors step-flow growth and thus allows to achieve a smooth surface morphology. The alteration of surface diffusion kinetics may reduce the tensile strain and eventually result in a crack-free layer.

We supplied a little quantity of indium (In) (0.33 μmole/min) into the reactor throughout the growth period of high temperature AlN epilayer using trimethylindium (TMIn) as a source. Figure 4.39 shows AFM images of 1.5 μm thick AlN epilayers without (left) and with (right) In supply during the growth.

Using In as a surfactant, we obtained atomically very flat and step-flow like surface morphology in AlN. The surface contains a relatively lower number of small pits. However, the RMS surface roughness of both images is nearly equal, i.e. 0.16 nm. Meanwhile, we obtained almost similar X-ray rocking curve measurements for both samples.

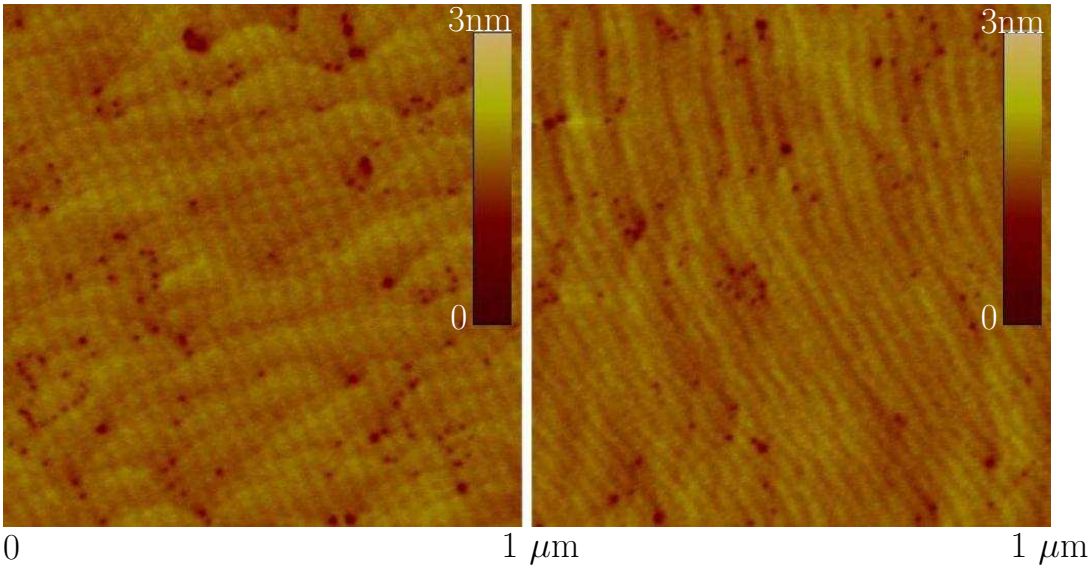

Figure 4.39: AFM images of 1.5 μm thick AlN epilayers without (left) and with (right) In supply during the growth.

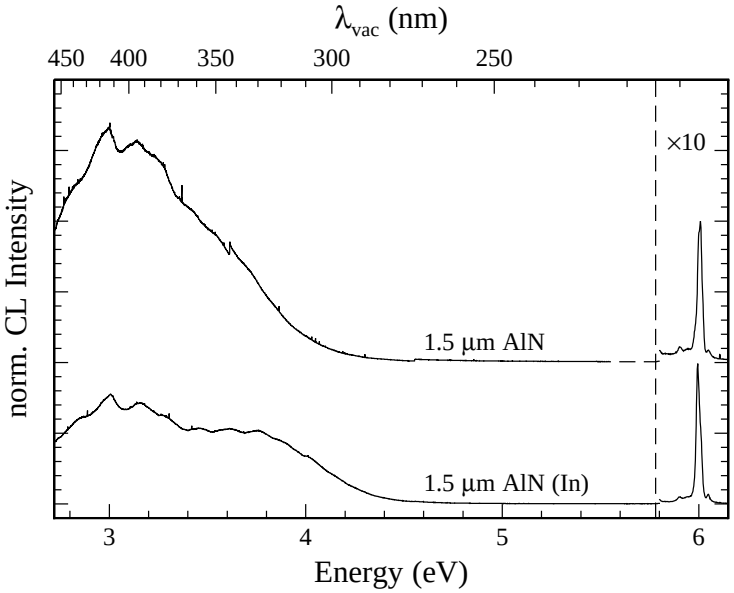

Figure 4.40: Overview of low-temperature (T = 8 K) CL spectra of AlN without and with In as a surfactant element. The spectra are normalized to the intensity of the NBE luminescence. A decrease in the intensity of the violet luminescence in the sample with In as a surfactant element is clearly observed.

Figure 4.40 shows a direct comparison of the low-temperature (T = 8 K) wide range CL spectra between 1.5 μm thick AlN epilayers without (left) and with (right) In as a surfactant element. One can see a clear decrease in the intensity of the defect related luminescence DLT for the sample with In as a surfactant. In addition, the Fabry-

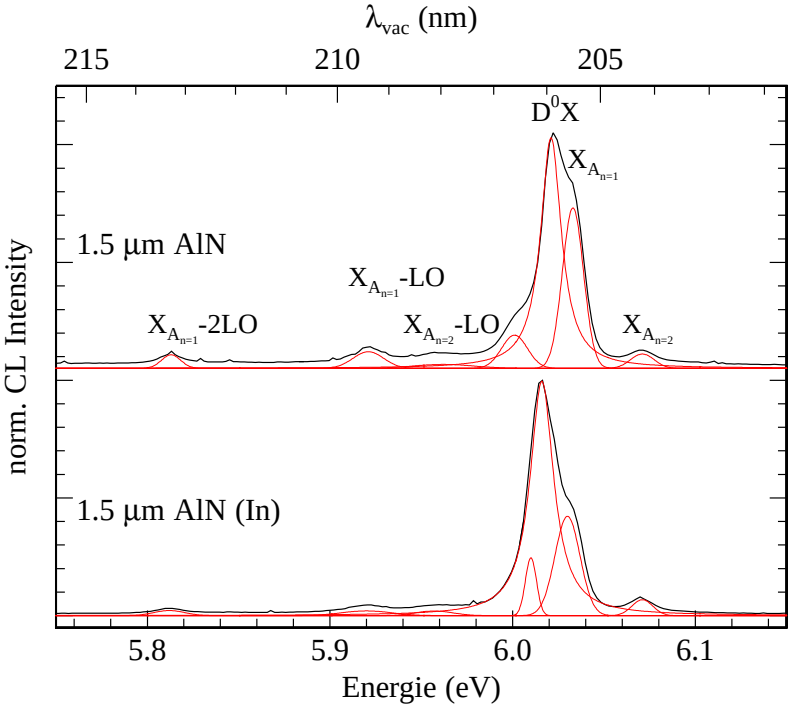

Figure 4.41: NBE CL spectra of AlN at low-temperature (T = 8 K) without and with In as a surfactant element. Indium has almost no influences on the NBE luminescence.

Perot oscillations of the violet luminescence band further confirm a smooth surface of the layer. The epilayer thickness was calculated to be 1.63 μm using the Fabry-Perot oscillations (11 maxima at the interval from 300 nm to 490 nm) and a refractive index of AlN i.e. 2.36 [189]. Figure 4.41 shows a similar characteristics of the NBE luminescence of both samples. The FWHM of the free A exciton X_A and excitons bound to neutral donors (D^0, X) is estimated to be approximately 8 meV for both samples. These observations show that indium has no influence on the NBE luminescence and it acts exclusively on the surface diffusion of species. Furthermore, SIMS data showed no detectable In in the In-doped sample.

Thus, the above results have shown that In can be used as a surfactant to improve the surface quality and achieve a successful deposition of a crack-free 1.5 μm thick AlN epilayer on sapphire substrate without undesirable influences on the physical properties of the epilayer and even reduced deep level transitions.

4.6 *In-situ* deposited SiN_x as defect-reducing interlayer

The defect density reduction by an *in situ* technique using silicon (Si) as an anti-surfactant was first described by Tanaka *et al.* [195]. The treatment of a nitride layer with NH_3 and SiH_4 leads to a fractional coverage of the surface with porous SiN_x. The SiN_x acts as a nano-mask that stops the propagation of threading dislocations from

the underneath layer into the overlying layer and reduces the defect density. It has been successfully employed as interlayers between GaN layers grown on foreign substrates [76, 78, 196, 197]. Deposition of a SiN_x layer would lead to a 3D growth mode of the succeeding layer. The subsequently grown layer must be coalesced completely after a certain thickness to impact positively the layer quality. However, there are several reports that with increasing Al-content in the AlGaN layer, the effectiveness of an *in situ* SiN_x mask decreases [79]. This is basically ascribed to a very low Al adatom mobility which impedes a lateral growth of the subsequently growing layer. Hence, the employment of an *in situ* SiN_x mask technique was not expected to be effective for the improvement of the material quality of high Al-content AlGaN or pure AlN crystals. Engl *et al.* [76] did not observe dislocation termination at the SiN_x interface in the $Al_{0.1}Ga_{0.9}N$ layer. However, K. Forghani [198] reported a reduction of TDs in an $Al_{0.2}Ga_{0.8}N$ layer using the *in situ* SiN_x mask technique. Therefore, we have also tried the same technique in the growth of pure AlN.

We deposited an approximately 100 nm thick AlN layer using our optimized two-step growth process. The growth of AlN was interrupted to deposit a SiN_x layer at 1070 °C under 104 mbar of reactor pressure. We supplied 0.38 μmol/min of SiH_4 and 22 mmol/min of NH_3 for 15 minutes in H_2 and N_2 ambient. Then, an approximately 900 nm thick AlN layer was deposited under the same growth condition as the underlying layer. Figure 4.42 shows cross-sectional TEM WBDF images of AlN with SiN_x interlayer under $\mathbf{g}$ = (0002) and $(2\overline{1}10)$ conditions. We observe an efficient dislocation annihilation, specially for the a-type TDs at the SiN_x interface (b) although the annihilation of c and (a+c)-type TDs are also seen at some region (a). However, the annihilation effect of the pure edge a-type TDs does not occur homogeneously over the whole SiN_x

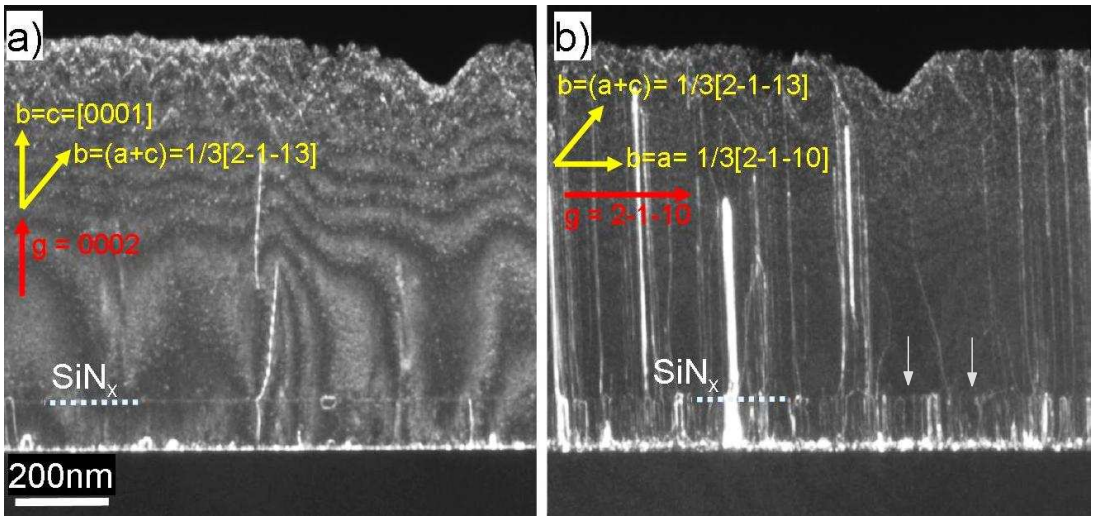

Figure 4.42: Cross-sectional TEM WBDF image of AlN with SiN_x interlayer exploiting the (0002) (a) and $(2\overline{1}10)$ reflections (b). The Burgers vectors $\mathbf{b}$ of the TDs in the respective WBDF image are also illustrated. TD annihilations with loop formation at the SiN_x as pointed out by arrows are clearly seen.

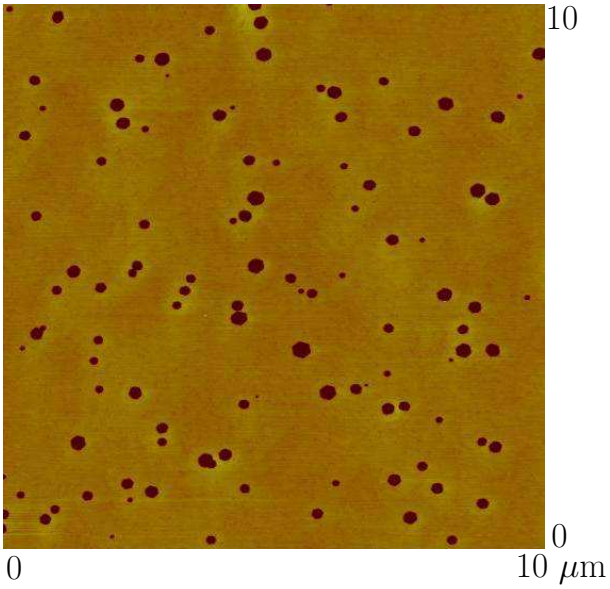

Figure 4.43: AFM image ($10 \times 10\ \mu m^2$) of an AlN layer grown over a SiN_x intermediate layer.

layer in our sample. In some regions of the SiN_x layer the propagation of the TDs is completely stopped and the annihilation process is highly efficient (lower arrows). More significantly, SiN_x anti-surfactant also induces lateral overgrowth of AlN on the nano-mask. However, the SiN_x layer plays a role of quasi-substrate interface with high lattice mismatch which results in the strain on the overlaying layer. We observe some TDs are bending in the course of propagation in the overlying layer of AlN. Such bending may be attributed to the strain of the layer. The bended TDs finally open at the surface as large etch pits. A rough surface with a large number of large hexagonal pits is observed in the AFM image in Fig. 4.43. However, the space between the larger pits is still very smooth. Meanwhile, the X-ray rocking curve measurements for (002)- and (102)-reflections show a broadening for the (002)-reflection curve but a narrowing for the (102)-reflection curve. The increased density of large hexagonal pits in AFM observation is also corelated with the broadening of the (002) peak. This may be attributed to a possible increase of stacking faults and the generation of misfit dislocations due to the quasi-substrate nature of the SiN_x layer although some of the screw-type TDs were annihilated at the SiN_x layer interface. However, the narrowing of the (102)-reflection curve is attributed to the reduction of edge-type TDs as shown in the TEM image. Table 4.10 presents a summary of the characterization results of a 1.0 μm thick AlN epilayer without and with *in situ* SiN_x layer. This result shows that AlN can be epitaxially grown over *in situ* deposited SiN_x layer and the TDs can be reduced although a large number of hexagonal pits was emerged. However, such pits may be suppressed by increasing the growth temperature and further optimization in future.

Table 4.10: Characterization results of 1.0 μm thick AlN epilayer without and with *in situ* SiN_x layer.

Parameters	without SiN_x layer	with SiN_x layer
AFM RMS surface roughness (nm)	0.213	17.79
X-ray FWHM for (002)-reflection (arcsec)	25	173
X-ray FWHM for (102)-reflection (arcsec)	1051	856
N_S (cm^{-2})	1.4×10^6	6.5×10^7
N_E (cm^{-2})	8.8×10^9	3.3×10^9

4.7 AlN on Different Substrates

We have successfully optimized the growth parameters and developed a growth process for the deposition of AlN epilayers on sapphire substrate. We used the same growth parameters for the growth of AlN on SiC and native AlN substrates. This gives us an opportunity to compare the properties of the AlN epilayer grown on different substrates.

4.7.1 Growth on SiC

We found that the crystal and the surface qualities of AlN epilayers grown on SiC were inferior to the epilayer grown on sapphire substrate by employing the same two-step growth processes. Therefore, we directly deposited AlN (500 nm thick) on SiC substrate without using a medium temperature nucleation layer. Prior to the epilayer deposition, the substrate was thermally cleaned using H_2 for 20 minutes at 1100 °C followed by a nitridation step with the supply of 900 sccm of NH_3 for 10 minutes at the same temperature. Later on, the NH_3 flow-rate was reduced to 250 sccm while ramping up the temperature till 1199 °C.

Figure 4.44 shows an AFM image of the directly grown AlN epilayer on SiC. The surface is atomically flat having terraces with one or two atomic steps height. The average terrace width is about 100 nm and the step height is about 0.5 nm. However, the density of large-sized pits (diameter $\geq$ 100 nm) is about 3×10^8 cm^{-2} which is almost three orders of magnitudes higher than in AlN on sapphire whereas the density of scattered small pits is about 1×10^{10} cm^{-2} which is almost a fourth less. The measured RMS surface roughness is 0.2 nm excluding the large-sized pits. The FWHM for the (002)- and (102)-reflections of X-ray rocking curves was measured to be 196 arcsec and 668 arcsec, respectively, which are almost four times higher and more than half less than the respective values of AlN on sapphire. We have estimated $N_S = 8.4 \times 10^8$ cm^{-2} and $N_E = 3.5 \times 10^9$ cm^{-2} from the corresponding X-ray measurements. It means the edge-type TDs are drastically reduced in AlN on SiC whereas screw-type TDs are increased. The cross-sectional WBDF TEM micrographs in Fig. 4.45 shows screw-type TDs in (a) and edge-type TDs in (b). While comparing it with Fig. 4.26, we can clearly see that the

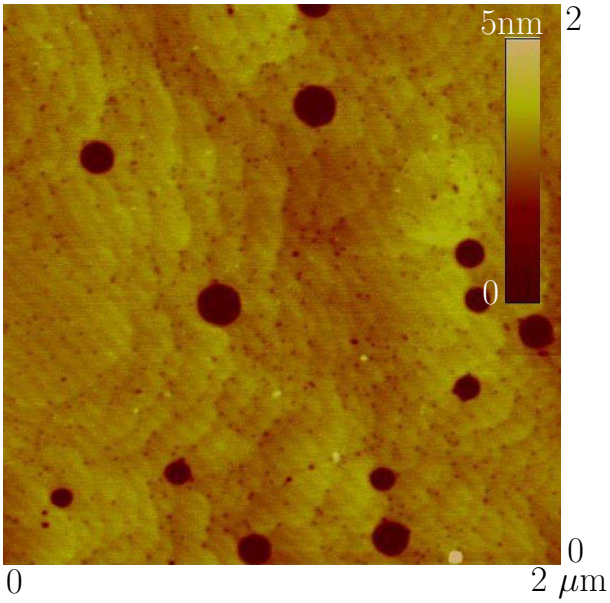

Figure 4.44: AFM image of 2 ×2 μm^2 scanned AlN epilayer on SiC exhibiting atomically flat and clearly resolved terrace width with atomic step height on the surface. However, large pits having diameter ≥ along with small pits are also seen .

nucleation of TDs at the interface between the AlN epilayer and the SiC substrate is relatively small. The number of edge-type TDs threading through the entire epilayer is also very low. Many of these TDs are bent and bundled together. AlN on sapphire had a high density of screw-component TDs near the interface, but few of them propagated toward the free surface, because most of them were annihilated during the growth. For AlN on SiC, there were fewer screw-component TDs near the interface, but most of them propagated toward the surface. This different microstructure could be attributed

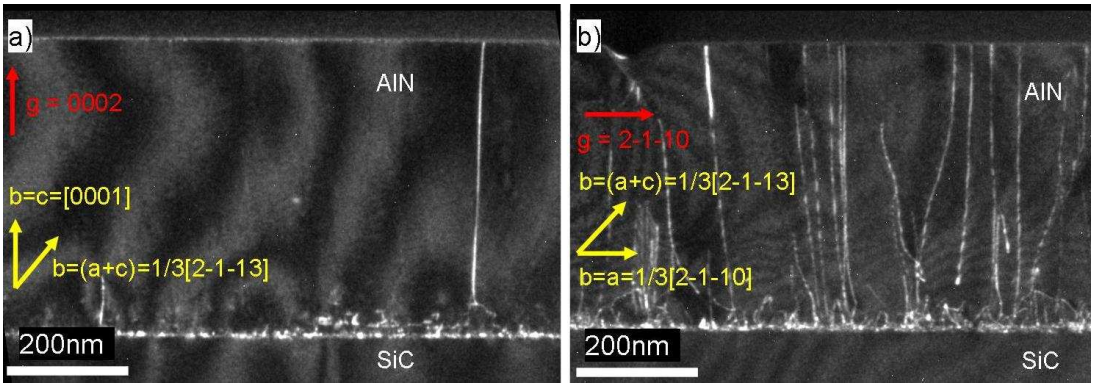

Figure 4.45: Cross-sectional TEM WBDF image of AlN on SiC exploiting the (0002) (a) and $(2\bar{1}\bar{1}0)$ reflections (b). The Burgers vectors **b** of the TDs in the respective WBDF image are also illustrated.

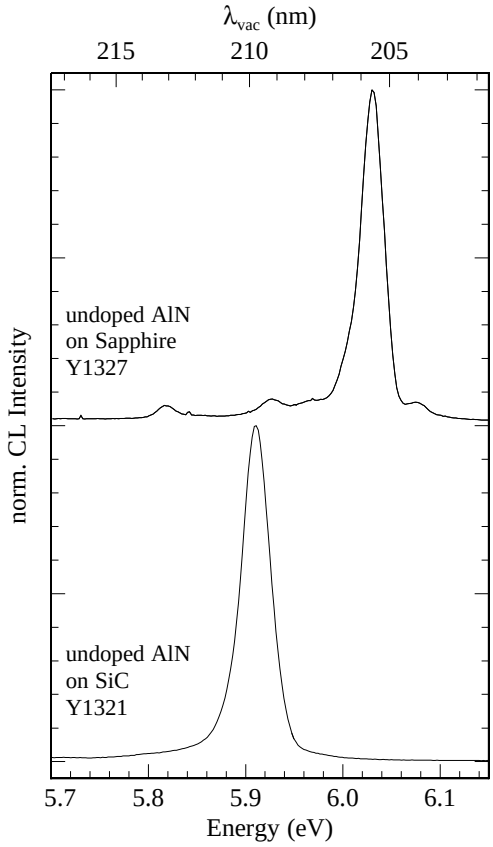

Figure 4.46: Low-temperature (T = 8 K) CL spectra exhibiting NBE luminescence of AlN directly grown on SiC and AlN on sapphire under the same growth conditions.

to the difference in lattice mismatch in the two systems. The low temperature (T = 8 K) CL spectra exhibiting the near-band-edge luminescence of AlN grown on SiC and grown on sapphire under similar growth conditions are shown in Fig. 4.46. The peak position of AlN grown on SiC is shifted to lower energies which is a consequence of a different strain situation due to a large mismatch in thermal expansion coefficients of AlN and SiC. The in-plane tensile strain of AlN on SiC is calculated to be 0.16 to 0.19% wheres it is 0.04 to 0.07% on sapphire. Raman studies carried out by R.A.R. Leute [189] also show the similar strain situation in these layers.

Figure 4.47 shows a direct comparison of the wide range CL spectra of the AlN epilayers deposited on sapphire and SiC at low-temperature (T = 8 K). The luminescence intensity of the spectra is not normalized in this case. We clearly see that the NBE luminescence intensity of AlN on SiC is nearly an order of magnitude higher than that of AlN on sapphire. On the other hand, the intensity of the defect related transitions at violet luminescence band is largely reduced in AlN on SiC. These observations show that the growth mode of the overlaying epilayer is substrate dependent. In our experiments, we found that the crystalline and luminescence properties of an AlN epilayer grown on SiC are better than on sapphire substrate. However, the AlN epilayer is strained and the surface is heavily pitted when grown on SiC. We apparently expect

that the large pits can be suppressed by growing the epilayer at a temperature higher than 1200 °C. This is based on our experimental evidences of growing AlN on sapphire at different growth temperatures from 1110 °C to 1199 °C.

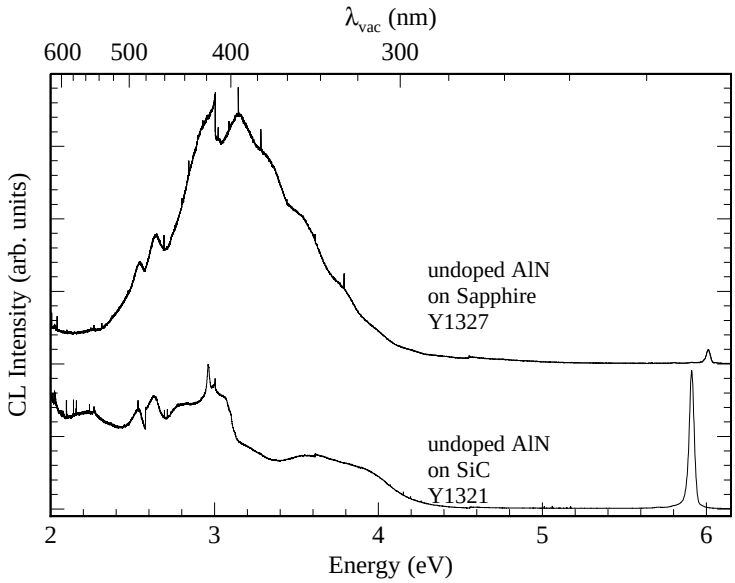

Figure 4.47: Overview of low-temperature (T = 8K) CL spectra of AlN on SiC and on sapphire. The luminescence intensity of the spectra is not normalized. The spectrum of AlN on SiC exhibits higher NBE luminescence intensity and lower violet band intensity.

4.7.2 Growth on native AlN substrate

We received few test pieces of bulk AlN substrates from Dr. Matthias Bickermann of University of Nuernberg-Erlangen. AlN bulk single crystals were grown by physical vapour transport (PVT), i.e. sublimation of AlN powder and re-condensation of the gaseous species on a seed located at the top of the crucible. Growth was performed in a tungsten setup at temperatures of 2100...2200 °C and at thermal gradients between (hotter) source and (colder) seed of 10...15 K/cm. N_2 was used as inert gas; for details see [199]. 1-inch diameter AlN templates grown on 6H-SiC were used as seeds for AlN bulk growth. Such templates provide large-area seeds, but they are often cracked (cf. studies of Makarov *et al.* [200]). These cracks as well as defects (micropipes, dislocations, low angle grain boundaries) from the SiC seed propagate into the AlN layer and subsequently into the growing bulk crystal. It was found that the low growth rates mitigate crack propagation; slow cooling as well as optimization of the thermal field inside the crucible can prevent formation of new cracks after growth [201]. A sample was cut out from the grown crystal and subsequently polished on both {0001} faces by standard wafering techniques. However, the surface was not very smooth. The main part of the sample appears yellowish brown to the eye. The mean density of screw-type TDs as evaluated by wet chemical etching is about 4×10^4 cm^{-2}; the density of edge-type TDs was estimated to be in the range of 10^5– 10^6 cm^{-2}. The sample shows

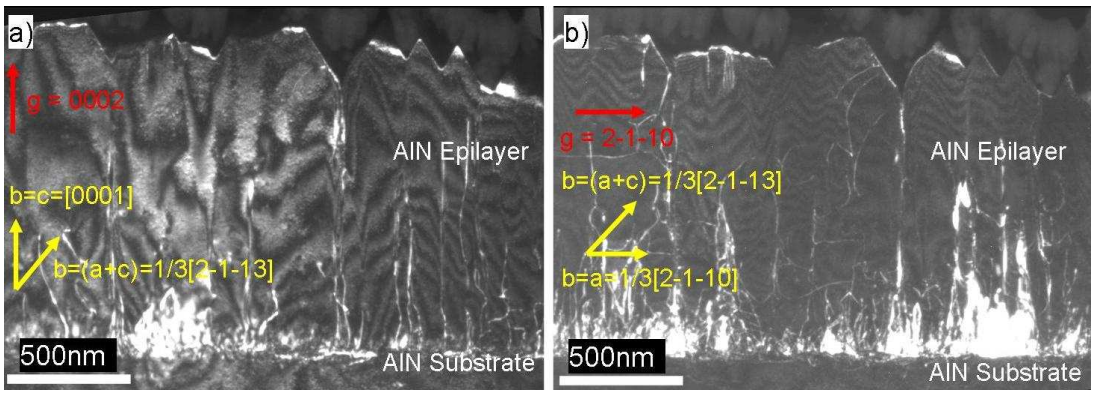

Figure 4.48: Cross-sectional TEM WBDF image of AlN on native AlN substrate exploiting the (0002) (a) and $(2\overline{1}10)$ reflections (b). The Burgers vectors **b** of the TDs in the respective WBDF image are also illustrated.

small-angle grain boundaries which are spaced 0.5 – 1.5 mm apart from each other. This mosaic structure is mostly inherited from the quality of the SiC and the AlN-on-SiC template used as seed. Structural properties of the sample are discussed in detail in [201].

An approximately 1.0 μm thick AlN epilayer was directly deposited under the same growth conditions as described for the growth of AlN on SiC. As expected, the AFM observations revealed a very rough surface since the substrate was not epi-ready. Figure 4.48 shows a cross-sectional TEM WBDF image of AlN on the native AlN substrate exploiting the (0002) and $(2\overline{1}10)$ reflections. It is revealed that the epilayer is grown in a columnar structures with column diameters in the range of 100 to 500 nm. The domains of such structures are clearly visible. It may be attributed to the roughly polished surface and/or the possible polycrystal structure of the bulk AlN substrate. We also did not observe a single peak in the X-ray rocking curve measurements from both the substrate before epilayer growth and AlN epilayer. We observed a broad peak with many fringes. The broadening of the peak may be due to the modulation of the peaks from different neighboring tilted domains. Although the interface shows that a large number of TDs were generated in the beginning of the growth, the majority of them was annihilated within an epilayer thickness of 300 nm. Unlike heteroepitaxy, the edge-type TDs are not threading through the entire layer thickness. Both, the screw- and the edge-type TD densities are reduced in the course of the epilayer thickness. The top part of the layer has a very low dislocation density. It clearly indicates the advantage of homoepitaxial growth of AlN.

However, the low-temperature (T = 8 K) CL spectrum of our homoepitaxial AlN layer (Fig. 4.49) is not very promising. The NBE luminescence from this sample is broader (FWHM $\approx$ 48 meV) than the luminescences from the bulk substrate (FWHM $\approx$ 19 meV) and the optimized AlN epilayer on sapphire (FWHM $\approx$ 10 meV). It may be due to the modulation effect of the tilted domains. Like AlN on sapphire, both, the homoepitaxial AlN and the bulk AlN, demonstrated strong deep level transitions in the violet band (Fig. 4.50) which are again attributed to Al vacancies and their complexes

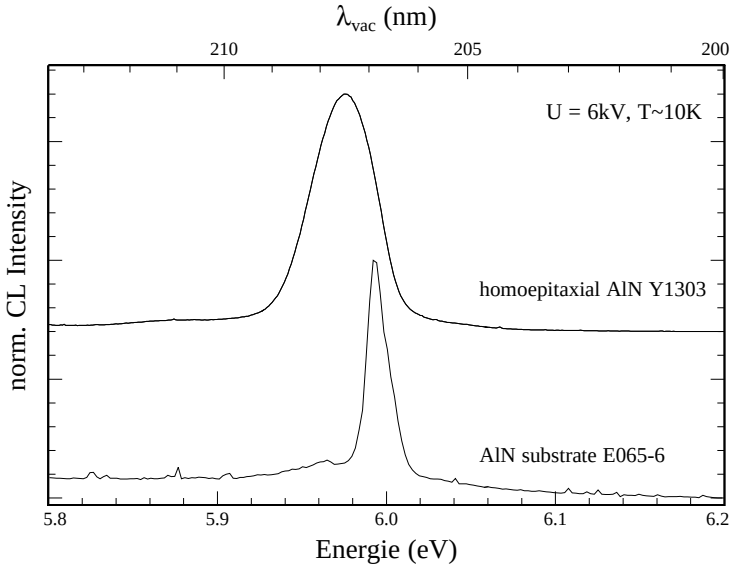

Figure 4.49: Low-temperature (T = 8 K) CL spectra exhibiting the NBE luminescence of the AlN substrate, and the AlN epilayers directly grown on AlN substrate.

[202]. We need more growth runs and intensive investigations to justify the epilayer quality of homoepitaxial AlN which could be a future work.

However, our investigations suggest that a very high quality of AlN epilayer with a low TD density could be deposited on AlN substrate using our optimized growth parameters if the substrate is epi-ready and the growth temperature is higher than 1200 °C.

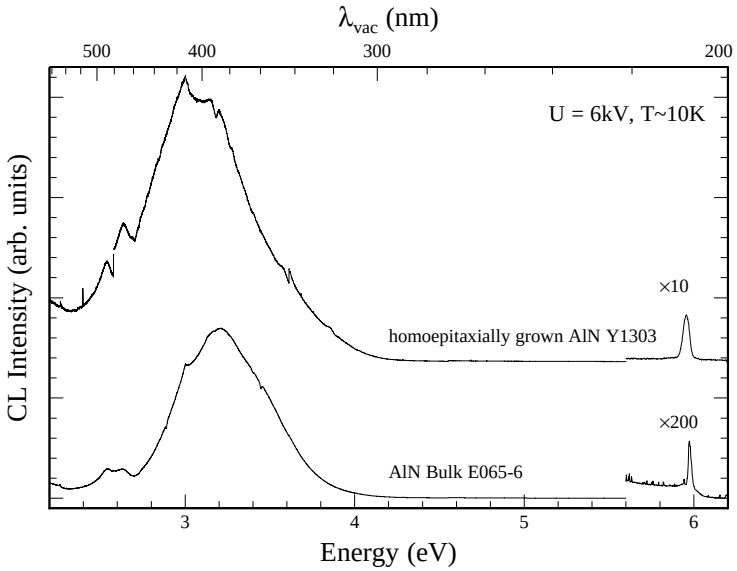

Figure 4.50: Overview of low-temperature (T = 8K) CL spectra of the AlN substrate, and the AlN epilayers directly grown on AlN substrate.

Chapter 5

Si Doping of AlN

The effective doping of high Al content AlGaN and AlN remains a vital issue for the employment of these semiconductors in electronic and optoelectronic device structures. The limited conductivity in n-type AlN layers constitutes a severe impediment for the progress of AlN-based device applications. Therefore, investigations of the doping of these materials are very important for both basic research and application levels. In this chapter we present a brief preview of silicon (Si) doping of AlN epilayers to obtain n-type electrical conductivity. Si-doping of AlN has inherent limitations and difficulties which will be explained. Next, we will discuss our systematic studies of its impact on structural and spectroscopic properties of AlN. Finally, the electrical measurements of n-type conduction in the AlN epilayers will be presented.

5.1 Introduction

When the semiconductor is doped, new states are created within the energy gap. The electron (or hole) states associated with donors (or acceptors) are usually a small fraction of an electron volt (eV) away from the bottom of the conduction band (or top of the valance band). Shallow donors are impurities which require little energy - typically around the thermal energy or less - to ionize and contribute free carriers to semiconductors. Therefore, the impurity which has a low ionization energy is always a preferable dopant element in semiconductors.

In group-III nitrides, a group-IV atom (C, Si, Ge) is a donor when incorporated on the cation site. The n-type doping of GaN and InN has never been a problem. In fact, as-grown nominally undoped GaN and InN layers have often exhibited unintentional n-type conductivity, the cause of which was widely debated. In contrast, undoped AlN epilayers are typically highly resistive. In GaN and InGaN, silicon readily forms a shallow donor and allows the growth of highly conductive layers [203]. The activation energy for the ionization of Si donors in GaN is determined to be in the range of 12 to 17 meV [204] whereas it increases with increasing Al content in AlGaN [205]. Although Si is a potential n-type dopant in AlN, the activation energy for the donor ionization $E_{a,D}$ is reported to be in the range of 86 to 312 meV [12,206] and increases with the increase of Si concentration [207]. With such a high donor ionization energy, it is difficult to obtain

sufficiently many free-carriers for n-type conductivity in AlN epilayers. Till today, only a few groups have reported the electrical conductivity in Si doped AlN epilayers. Taniyasu *et al.* [206] recently reported a high room-temperature electron mobility μ_n of 426 $cm^2V^{-1}s^{-1}$ and 285 $cm^2V^{-1}s^{-1}$ in lowly Si-doped ([Si]=3.5 $\times 10^{17}$ cm^{-3}) AlN epilayers on native AlN and SiC substrates, respectively. The free carrier concentration n was reported to be 7.4 $\times 10^{14}$ cm^{-3} in the homoepitaxially grown epilayer. They estimated the donor concentration N_D and the acceptor concentration N_A to be 3.0 $\times 10^{17}$ cm^{-3} and 2.6 $\times 10^{16}$ cm^{-3}, respectively, assuming the following charge neutrality equation

$$\frac{n(n+N_A)}{N_D-(n+N_A)} \approx \frac{N_C}{g} exp\left(-\frac{E_{a,D}}{k_B T}\right), \tag{5.1}$$

where N_C is the effective density of states in the conduction band, g is the donor degeneracy factor, which is 2, k_B is the Boltzmann constant, T is the sample temperature, and $E_{a,D}$ = 282 meV. The N_D of 3.0 $\times 10^{17}$ cm^{-3} agreed well with the Si doping concentration of 3.5 $\times 10^{17}$ cm^{-3} which indicate that almost all of the Si atoms were ionized and they claimed that Si acts as a shallow donor in AlN. But the measured low free carrier concentration (almost three orders magnitude lower than the donor concentration) and the estimated very high donor ionization energy (almost an order of magnitude higher than thermal energy) certainly rise many questions whether Si is stabilized in *DX* configurations or just partially ionized so that the n-type doping is always limited in AlN. A transition from a shallow to a deep state by lowering energy by a large lattice relaxation and the capture of a second electron forms a *DX*-center within the band gap where "D" stands for a participating donor and "X" for the second unknown defect. The transition is accompanied by a strong relaxation of the impurity off the substitutional site [208, 209]. In the *DX* configuration the defect is negatively charged, i.e., it is a deep acceptor and will, therefore, trap free carriers. Several first-principles studies have addressed the issue whether the Si donors undergo a *DX* transition in AlGaN and convert to negatively charged deep levels. However, the theoretical predictions are largely contradictory. Bogusławski and Bernholc [210] and Skierbiszewski *et al.* [211] predicted a stable *DX* configuration for $Al_xGa_{1-x}N$ alloys with compositions higher than about 0.5 which quenches the doping efficiency. In earlier experimental reports, it was found that Si remains a shallow donor in $Al_xGa_{1-x}N$ alloys up to x = 0.44 and the conductivity was found to be strongly declined at Al mole fractions exceeding 0.5 [212, 213]. For higher Al content $Al_xGa_{1-x}N$ and pure AlN, several groups have reported experimental results arguing that Si undergoes a shallow-deep transition [205, 211]. Zeisel *et al.* [214] obtained a free electron concentration of 2 $\times 10^{15}$ cm^{-3} at room temperature and an activation energy of 320 meV of the *DX*-center in Si-doped AlN (AlN:Si) on sapphire grown by MBE. It was one of the first experimental reports of n-type conductivity of AlN demonstrating that Si is a viable dopant element in highly resistive AlN. However, no mobility was mentioned in that report. Since then, only a few reports on the achievement of measurable electrical conductivity in AlN at room temperature have been reported [12, 13, 215]. However, Stampfl and Van de Walle in their earlier comprehensive theoretical studies [216, 217] have argued that Si donors would remain shallow throughout the alloy range and do not undergo a DX transition, whereas oxygen undergoes this transition. The shallow-deep *DX* transition of oxygen

in AlN and in high Al content $Al_xGa_{1-x}N$ might be a reason for the drop of the free carrier concentration.

The low activation ratio (due to a large ionization energy) even can not be compensated by high Si doping concentrations because of the self-compensation effect of Si donors. In group-III nitrides, the group-IV atom becomes an acceptor when incorporated on the anion site instead of the cation site. Thus, a problem inherent to doping with group-IV elements is self-compensation, i.e., simultaneous incorporation of the dopant on both cation and anion sublattices [210]. The large bandgap enhances the self-compensation of the donor atoms. Taniyasu *et al.* [205] reported that when the Si concentration [Si] was more than $3.3\times10^{19}\,cm^{-3}$, the AlN epilayer becomes highly resistive due to the self-compensation of Si donors. The additionally incorporated Si (antisite Si (Si_N)) forms an acceptor state and compensates the remaining Si donors. This indicates that the self-compensation plays a negative role at higher [Si] and limits the upper doping level of Si for AlN and high Al content $Al_xGa_{1-x}N$.

Another responsible factor for a very low free electron concentration in Si-doped AlN epilayers on sapphire substrate is the compensation of the carriers by cation vacancies V_{Al} and their complexes (V_{Al}-Si_{Al}) [216]. Stampfl and Van de Walle found that the formation energy of the Al vacancy, particularly in the triply negative charge state, is significantly reduced when the Fermi-level position of the Si-doped AlN is shifted towards the conduction band. In chapter 4, we have already discussed the association of the deep level transitions to the V_{Al} and its complexes at the broad violet band region of low temperature (T = 8 K) CL spectra of undoped AlN epilayers. Therefore, it would be an interesting research to investigate how the deep level transition at the violet band of the CL spectrum is affected by [Si]. We will elaborate it in the later section of this chapter.

Furthermore, the crystalline and surface properties of AlN layers are largely affected by introducing Si dopants. We explore the mechanism by which Si causes morphological changes in AlN which was still not well understood. Additionally, the Si atom has a smaller atomic radius than the Al atom, therefore, substitution for Al may induce a large lattice strain. All these effects are discussed in the later sections.

5.2 Experimental

Si-doping was performed using diluted silane (SiH_4) in H_2 as a Si dopant source through a double dilution configuration of mass–flow controllers (MFCs). A typical structure as illustrated in Fig. 5.1 (left) was grown by depositing a 250 nm thick Si-doped AlN layer on top of a 250 nm thick optimized undoped AlN buffer layer at a growth temperature of 1190 °C. The basic growth parameters of the Si-doped layer were similar to those of the undoped buffer layer as tabulated in Tab.4.6. We varied [Si] from $4\times10^{17}\,cm^{-3}$ to $9\times10^{19}\,cm^{-3}$ in order to investigate its effects on the surface, crystal quality, and strain in the AlN epilayer. However, the maximum amount of Si-doping appears to be limited by cracks that develop in epilayers with high [Si]. The [Si] was extrapolated from our growth parameters using other AlN samples as reference which had been measured by

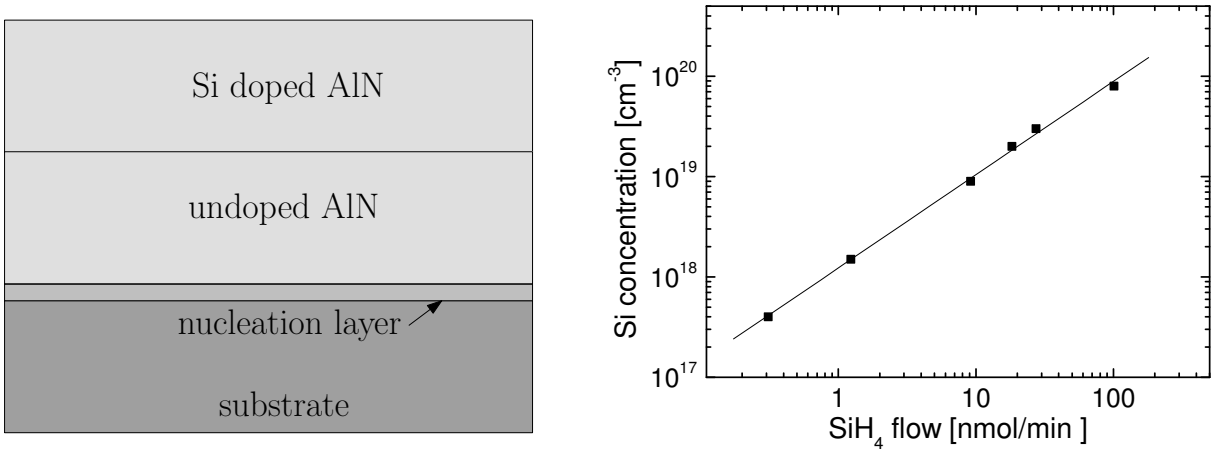

Figure 5.1: Si-doped AlN epilayer (approx. 250 nm thick) deposited on top of an undoped AlN epilayer (approx. 250 nm thick) over a medium-temperature nucleation layer (left). Si concentration [Si] measured by SIMS vs SiH_4 flow (right).

secondary ion mass spectroscopy (SIMS)[3]. SIMS depth profiles reveal a homogeneous incorporation of Si in the AlN epilayers up to [Si] of $9\times10^{19}\,cm^{-3}$. Figure 5.1 (right) shows a plot of measured [Si] against the SiH_4 flow rate. A good linearity of the plot demonstrates the good solubility of the Si dopant in the AlN epilayer.

5.3 Effects on structural properties

Si-doping of high Al content AlGaN and AlN is very challenging not only in obtaining good electrical properties but also a good structural quality. Even though Si is readily incorporated into these epilayers, both the surface and the crystal properties are remarkably influenced by its varying concentration. In the growth of GaN, Si has been established as an antisurfactant [218] and similar roughening effects were observed in AlN layers [13] in contrary to reports of the surfactant effect of Si in the MBE growth of AlN by Lebedev *et. al* [70] and Hermann *et. al* [219]. Figure 5.2 shows AFM micrographs of Si-doped AlN layers with various Si concentration. We clearly see an increase of surface roughening accompanied by depression, grooves and the emergence of a large number of pits in comparison to the undoped AlN epilayer (see Fig. 4.19(c)). The AFM micrographs show that both the size and the depth of the pits increase with increasing [Si]. In the heavily doped sample (d), some pits are connected to each other through dark grooves forming networks.

Cross-sectional TEM investigations (Fig. 5.3) of three different doping levels showed that the edge-type TDs in all samples were almost straightly propagating in the undoped buffer layers with a line direction normal to the (0001) growth plane similar to 500 nm thick undoped samples (see Fig. 4.25 (b)). It is readily seen that the edge-type TDs, penetrating the underneath undoped layer, propagate straight to the top in the

[3]SIMS measurements were carried out by L. Kirste, T. Fuchs, and M. Grimm of the Fraunhofer Institute for Applied Solid State Physics, Freiburg.

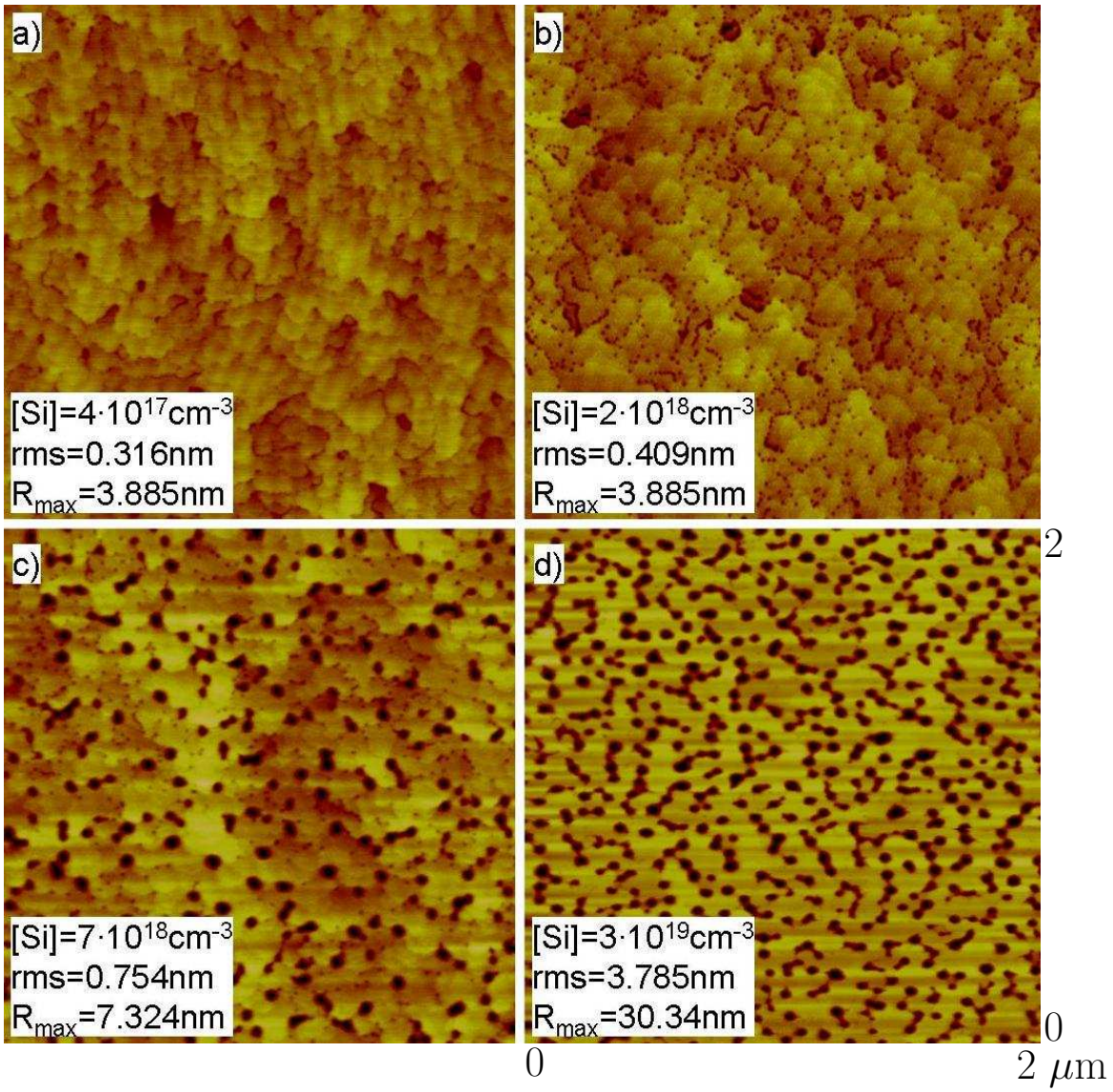

Figure 5.2: $2\times2\ \mu m^2$ scanned AFM images exhibiting surface morphology of Si-doped AlN epilayers with [Si] of: (a)4×10^{17} cm^{-3}, (b) 1.5×10^{18} cm^{-3}, (c) 7×10^{18} cm^{-3}, and (d) 3×10^{19} cm^{-3}.

case of the low doped samples (see Fig. 5.3(a)), whereas some of the TDs changed the propagation direction at or above the interface in the case of moderate to high doping (Fig. 5.3(b) and (c)). Cantu *et. al* [220] have earlier reported that the inclination of TDs in Si-doped $Al_{0.49}Ga_{0.51}N$ layers increases with the Si-doping level. The average angle of TD inclination at or above the interface between undoped and doped layers seems to increase with increasing [Si]. However, the bent TDs still maintain their edge character. TEM images reveal that the bent neighboring TDs come closer to each other, bunch together, and finally culminate into a V-shaped pit. Due to a stronger bending, TDs bunch earlier in highly doped samples that causes the roots of V-shaped pits nucleating

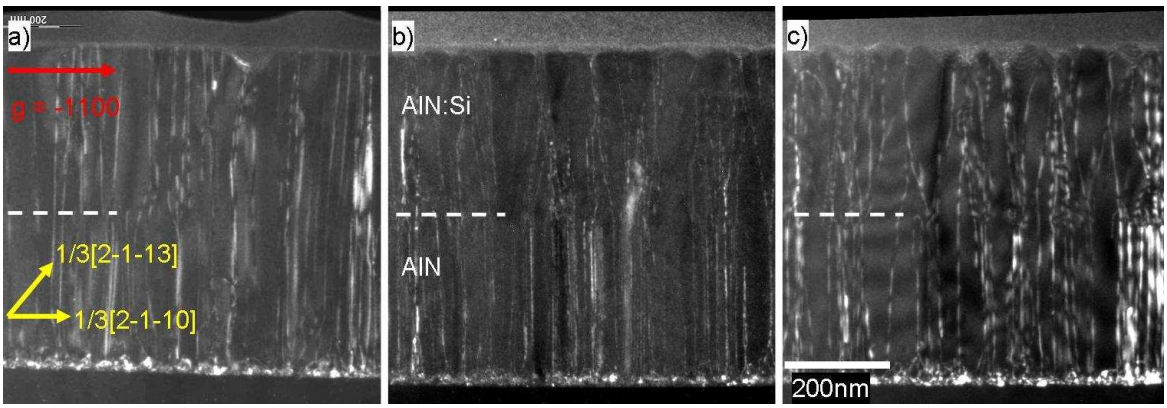

Figure 5.3: TEM cross-sectional view illustrating edge-type and/or mixed TDs of a Si-doped layer on the top of undoped AlN (the white dotted line shows the interface) where [Si]≈ $1.5\times10^{18}\,cm^{-3}$ (a), $2\times10^{19}\,cm^{-3}$ (b), and $9\times10^{19}\,cm^{-3}$ (c). Emergence of V-pits when TDs came closer together after bending.

earlier which later on emerge as a deep pit as observed in AFM and TEM micrographs. These pits have a wider opening at the surface. TEM cross sectional studies also demonstrate the evolution of some new defect networks related with screw-type TDs in the Si-doped area (Fig. 5.4(a)). However, some screw-type TDs are annihilated at or above the interface between undoped and doped layers with the formation of TD loops (Fig. 5.4(c)). Furthermore, the TEM studies show no segregation of Si atoms in our samples.

Figure 5.5 shows ω scans at (002)-reflection of X-ray rocking curves for a very low ([Si]=$4\times10^{17}\,cm^{-3}$) and a high ([Si]=$3\times10^{19}\,cm^{-3}$) doped sample. The low doped sample (plot (i)) exhibits a narrow intense single peak whereas the moderate and high doped

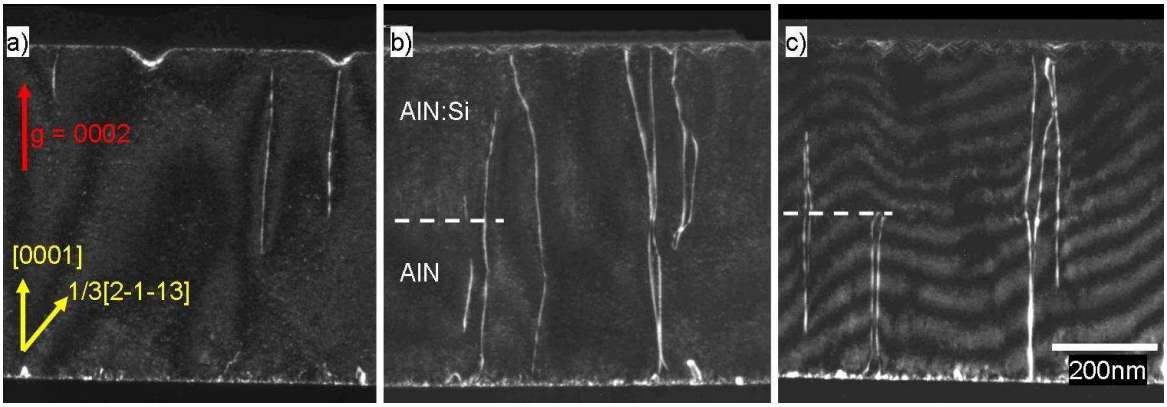

Figure 5.4: TEM cross-sectional view illustrating screw-type and/or mixed TDs of a Si-doped layer on the top of undoped AlN (the white dotted line shows the interface) where [Si]≈ $1.5\times10^{18}\,cm^{-3}$ (a), $2\times10^{19}\,cm^{-3}$ (b), and $9\times10^{19}\,cm^{-3}$ (c). Some TDs are generated in the Si-doped region and some are annihilated at the interface to higher [Si].

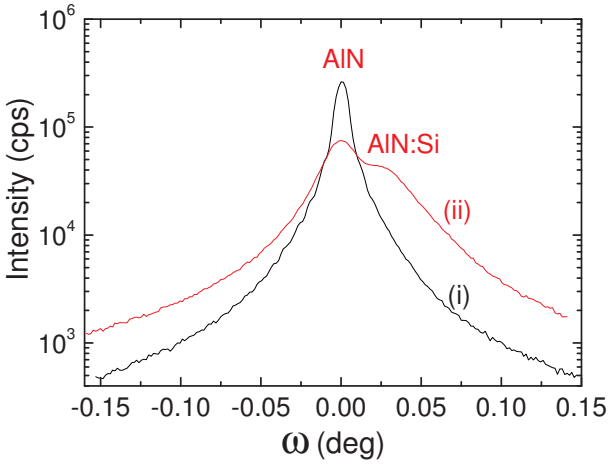

Figure 5.5: ω scan at (002)-reflection of X-ray rocking curve (left) of Si-doped samples, [Si]=4 $\times 10^{17}$ cm^{-3} (plot (i)) and [Si]=3 $\times 10^{19}$ cm^{-3} (plot (ii)).

samples (plot (ii)) exhibit two clearly resolved peaks. The intense one at the left and relatively broad one at the shoulder are corresponding (002)-reflection peaks from the underneath undoped buffer and the top doped layers, respectively. This indicates a different strain situation in these two layers. It apparently suggests that Si incorporation is responsible for the stress evolution in the AlN:Si layer which induces the edge-type TD bending as discussed above. The appearance of a single peak at a very low [Si] might be due to a convolution effect of unresolved proximate two peaks from doped and undoped layers.

Figure 5.6 (left) displays the evaluated strain in AlN:Si layers at different [Si] using Eq. 2.6. We found that the in-plane tensile strain in the AlN:Si layers increases with increasing [Si] up to approx. 2 $\times 10^{19}$ cm^{-3}, whereas it decreases for higher concentra-

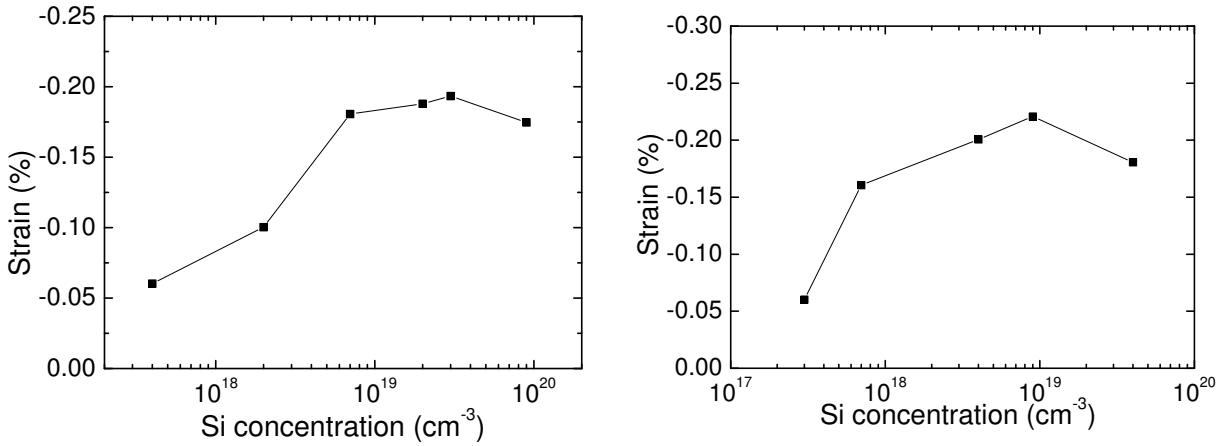

Figure 5.6: In-plane tensile strain of Si-doped AlN layers at various Si concentrations determined from the HRXRD rocking curve measurements. Series of samples grown at 1190 °C (left) and 1150 °C (right)



Figure 5.7: Optical microscopy images of AlN:Si samples with [Si]=1.5×10^{18} cm^{-3}, sample Y1155 (a), 3×10^{19} cm^{-3}, sample Y1157 (b), and 9×10^{19} cm^{-3}, sample Y1179 (c). Cracks were visible only at the edge of sample Y1155. In the other 2 samples, cracks were homogeneously distributed throughout the surface.

tions. This behavior was further verified by low temperature CL measurements which will be presented later in this chapter. We had previously deposited a series of similar structures of doped and undoped AlN epilayers at the growth temperature of 1150 °C. Unlike to the samples grown at 1190 °C this series of samples did not exhibit two distinct X-ray peaks from the underneath undoped buffer and the top doped layers due to an inferior crystal quality of the underneath buffer layer. Instead, we observed a single relatively broad convoluted peaks. The estimated strain at different [Si] is presented in Fig. 5.6 (right) which also exhibited a similar strain situation as of the samples grown at 1190 °C.

Figure 5.7 shows optical microscopy images of three different doping levels, ranging from low (1.5×10^{18} cm^{-3}, sample Y1155) (a), via moderate (3×10^{19} cm^{-3}, sample Y1157) (b), to high (9×10^{19} cm^{-3}, sample Y1179) (c). The surface of the very low doped ([Si]$\leq10^{18}$ cm^{-3}) AlN:Si layer was crack-free. A few straight crack lines were visible at the edge of the low doped sample as demonstrated in image (a). The total number of cracks on a half of the two inch sample surface was nearly 15. The number of such straight crack lines were increased with increasing [Si]. However, the cracks started emerging at different directions when [Si] $\geq 10^{19}$ cm^{-3}. The average distance between cracks in the moderately doped sample was about 80 to 100 μm as demonstrated in image (b). The highly doped sample was severely cracked and micro-cracks are clearly visible in every direction as demonstrated in image (c). The average distance between cracks was about 2 μm. Even a peeling off of the layer was occasionally observed especially at the edge of this sample. This corroborates the evidence of the relaxation of tensile stress by cracks for [Si] higher than 2×10^{19} cm^{-3} in the AlN:Si layer.

Our experiments show that a slight excess [Si] has an adverse effect on the surface quality of AlN epilayers causing increased roughness, and crack formation limiting the doping capability. AFM, TEM and X-ray investigations suggest that the deteriorating surface quality is attributed to the nucleation of pits in the Si-doped AlN epilayer that corresponds to an interaction between Si induced in-plane tensile strain with the close proximity to the arrival of bundles of inclined edge-type TDs. A large density of deep pits in the strained epilayer may provide a mechanism of strain release or relaxation

causing the layer cracking of the Si-doped samples in addition to the consequence of the inherited properties of increasing in-plane tensile strain. Interestingly, we observed that In as a surfactant slightly helps to reduce the cracks on Si-doped layers without affecting surface and crystal quality as in the growth of undoped AlN epilayer. Similarly, instead of abrupt switching of a large amount of SiH_4 in the reactor, a slow ramping flow also helps to reduce the cracks.

Figure 5.8 illustrates the change in FWHM of X-ray rocking curves of symmetric (002)- and skew-symmetric (102)-reflections with respect to the [Si]. Surprisingly, the HRXRD (002) peak is narrower (≈40 arcsec) for the very low doped ([Si]=4×10^{17} cm^{-3}) sample as compared to its undoped counterpart (≈60 arcsec). This is attributed to the annihilation of some of the screw-type TDs at or above the interface between undoped and doped layers. However, the FWHM of the (002)-reflection increased with increasing [Si] up to a level of 10^{19} cm^{-3} and then slightly decreased for higher concentrations. The broadening of X-ray peaks can be attributed to an excess number of newly emerged screw type TDs over the annihilated ones, the surface roughening due to increasing pit density, and the virtual broadening due to the convolution effect of peaks from doped and undoped layers. The slight decrease of the FWHM at very high [Si] may be attributed to the increased TD annihilation due to the large amount of [Si]. The relaxation by cracks for [Si] > 10^{19} cm^{-3} might be another reason for smaller (002)-reflection. However, the FWHM of the (102)-reflection is almost the same (≈ 1500 arcsec) in all samples. This also verifies our remarks on TEM analysis that the edge-type TDs (N_E≈10^{10} cm^{-2}) are generally not annihilated even after strong bending and indifferent with respect to [Si].

5.4 Effects on spectroscopic properties

In this section, we present low temperature (T = 8 K) CL spectra of Si-doped AlN layers and effects of different [Si] on both the near-band-edge (NBE) and deep-level transitions (DLT).

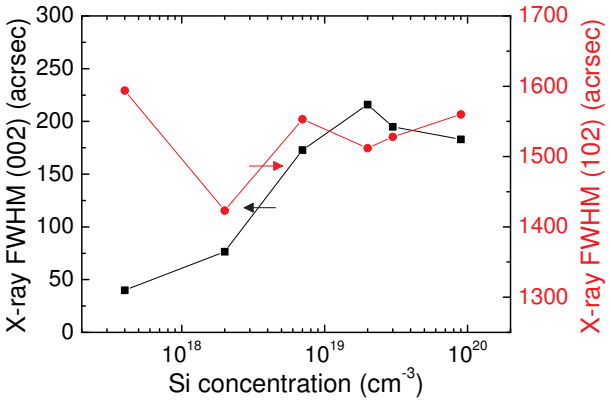

Figure 5.8: Change in FWHM of X-ray rocking curves of symmetric (002)- and skew-symmetric (102)-reflections with respect to the Si concentration.

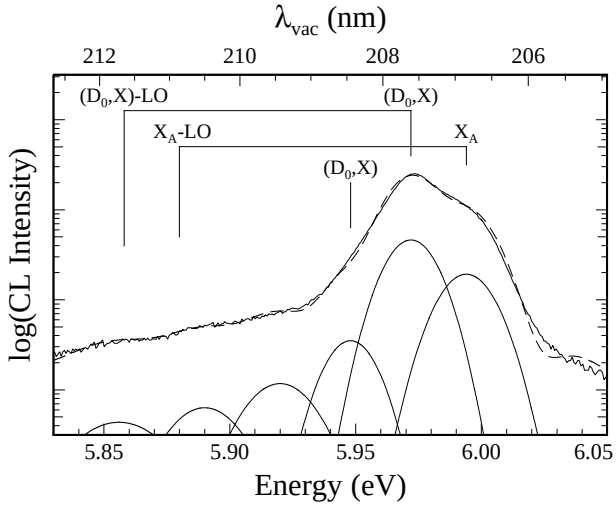

Figure 5.9: Low temperature CL spectrum of sample Y1155 with [Si]=1.5 ×10^{18} cm^{-3}. Three main contributions are seen in the near-band-edge luminescence. Additionally, Gaussian fitting curves are also shown.

5.4.1 Influence on near-band-edge luminescence

Figure 5.9 shows the CL spectrum of sample Y1155 with a [Si] = 1.5 ×10^{18} cm^{-3} and Gaussian fitting curves in the vicinity of 6.0 eV. Three main contributions are observed at the NBE luminescence. The contributions at 5.995 eV and 5.972 eV (dominant line) are assigned to the free A exciton X_A and excitons bound to neutral donors D^0, X, respectively. The FWHM of these transitions is about 20 meV which is almost two times broader than similar transitions in undoped layers. Like in undoped layers, we also observed a transition at 5.95 eV corresponding to D^0, X. However, the donor for this transition is still in question.

Temperature-dependent CL measurements were carried out on a similar sample to confirm the assignment of these transitions [183]. A localization energy of the donor bound exciton, $E_{loc,DX}$ of about 22 meV was determined from the distance between the line positions of the D^0, X and X_A transitions. $E_{loc,DX}$ of all other samples with different [Si] lies in between 22 and 29 meV with a tendency that the higher doped samples have a slightly larger localization energy. One reason for this behavior could possibly be another unknown transition with a localization energy of about 10-15 meV that might play a minor role in the spectra in low doped samples, unfortunately it can not be resolved. For this reason, the transition that was seen in the undoped AlN layers (see Fig. 4.32 (left) is not taken into account here.

The recorded NBE CL spectra from undoped (as a reference sample) and Si-doped samples with various [Si] ranging from 4 ×10^{17} cm^{-3} to 9 ×10^{19} cm^{-3} grown at 1190 °C are collectively shown in Fig. 5.10 (left). The NBE luminescence is monotonically shifted to smaller energies (red shift) when the [Si] in the samples increased up to a concentration of about 2 ×10^{19} cm^{-3}. When the [Si] was increased further, then the NBE luminescence again shifted back to higher energies (blue shift). A shift of the NBE luminescence

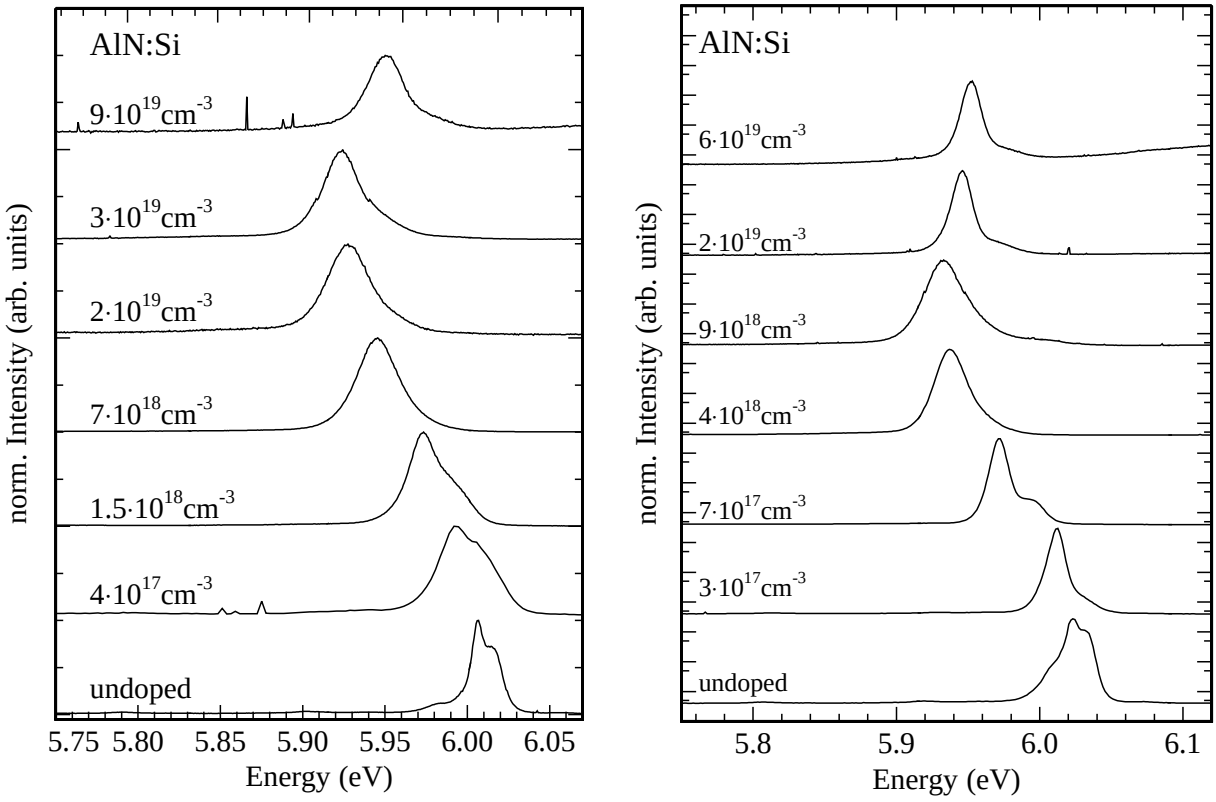

Figure 5.10: Red shifting of CL peak of AlN layers till a Si concentration of 10^{19} cm^{-3} and blue shifting for higher concentrations for series of samples grown at 1190 °C (left) and 1150 °C (right)

band to smaller energies with increasing [Si] was already reported by Nam *et al.* [221] on MOVPE grown samples in the range of 1.5×10^{17} cm^{-3} to 1.5×10^{18} cm^{-3} and Monroy *et al.* [222] on MBE grown samples till [Si] = 5.2×10^{21} cm^{-3}. The red shift of NBE luminescence in those reports was ascribed to a band-edge re-normalization by Nam *et. al* and occurrence of potential fluctuations (or alloying) for higher silicon doping concentrations by Monroy *et al*. However, these explanations can not answer the subsequent reverse shifting (blue shift) of NBE luminescence at higher concentrations ([Si] $\geq 3\times10^{19}$ cm^{-3}) as shown in Fig. 5.10. Our explanation for the red shift is rather a consequence of tensile strain introduced by doping with Si as also measured by X-ray (see above). The sample series grown at 1150 °C also exhibited a similar shift of the NBE luminescence as shown in Fig. 5.10 (right). For high Si concentrations ([Si] $\geq$ 2×10^{19} cm^{-3}), cracks cause strain relaxation and the NBE luminescence shifts back to higher energies.

Figure 5.11 (left) shows the corresponding Raman E_2^{high} modes for the sample series grown at 1190 °C. Similar to the evolution of two peaks in X-ray rocking curves (see Fig. 5.5), a double peak of E_2^{high} mode is also observed in the Raman spectra for the moderately and highly doped samples. The high-energy component at the position of 656 cm^1 is assumed originating from the undoped AlN buffer layer. The low-energy component shifts down for [Si] up to 3×10^{19} cm^{-3}, and shifts back again at the highest

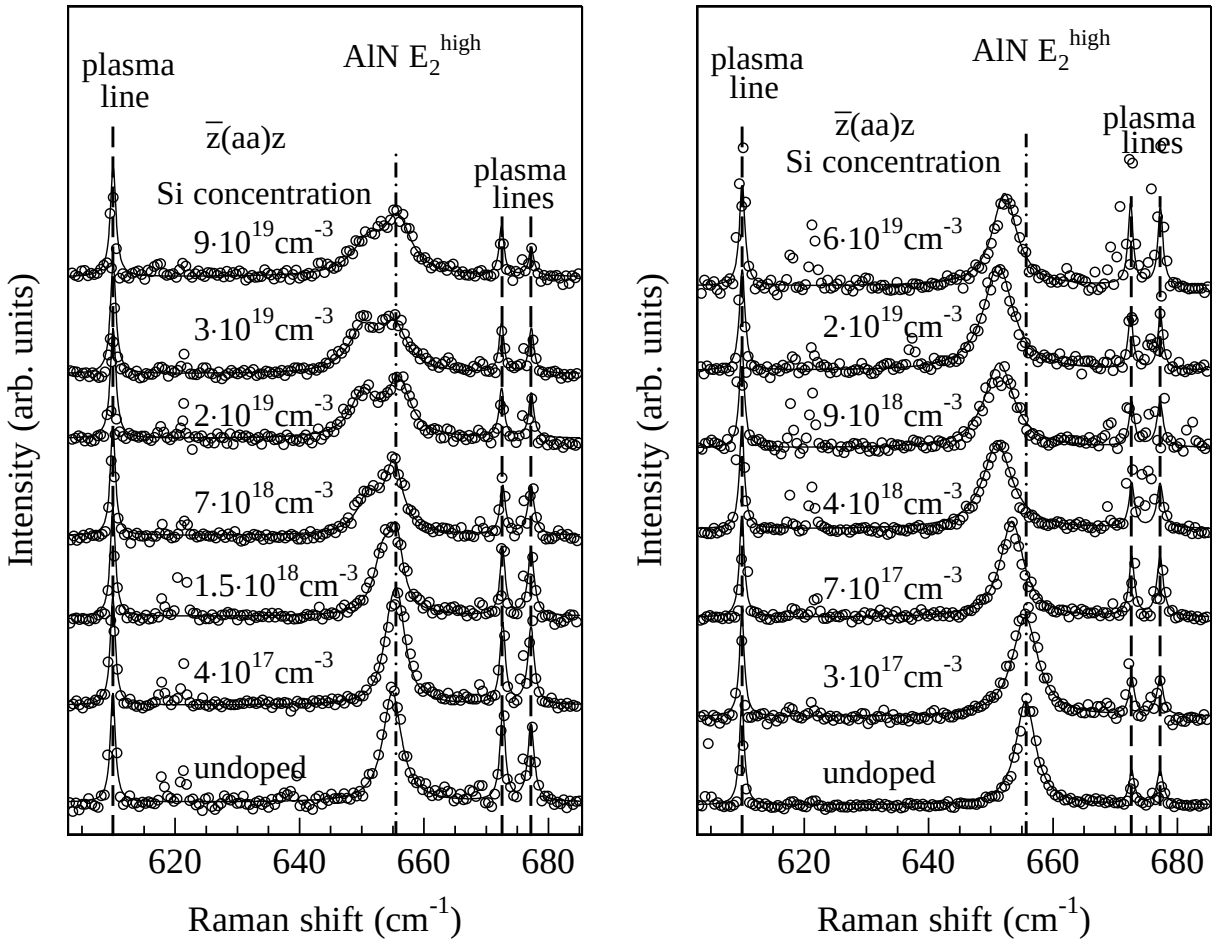

Figure 5.11: Raman spectra of the E_2^{high} mode for the Si-doped and the undoped AlN reference samples grown at 1190 °C (left) and 1150 °C (right). The vertical lines mark the position of the E_2^{high} mode of unstrained AlN.

doping level of 9×10^{19} cm^{-3} whereas the high-energy component is not shifted. Figure 5.11 (right) shows the corresponding Raman E_2^{high} modes for the sample series grown at 1150 °C. In the Raman measurements, we found only one single shifted peak, similar to the X-ray measurements. However, we again observed that the E_2^{high} mode shifts to lower wavenumbers for [Si] up to 9×10^{18} cm^{-3}, and shifts back for the higher doping levels.

An important finding is that the tensile strain as determined by X-ray measurements can be correlated perfectly with the observed Raman shift [183]. Thus, the only explanation for the CL shift consistent with the experimental data is in terms of strain effects caused by the Si doping. A clue to the decrease of such strain above a doping level of 1-3 $\times 10^{19}$ cm^{-3} is given by the observation of a high density of micro-cracks in these highly doped samples as mentioned above. The formation of cracks relaxes the strain in the layers, and therefore the NBE emission shifts back towards the position observed in the undoped layer.

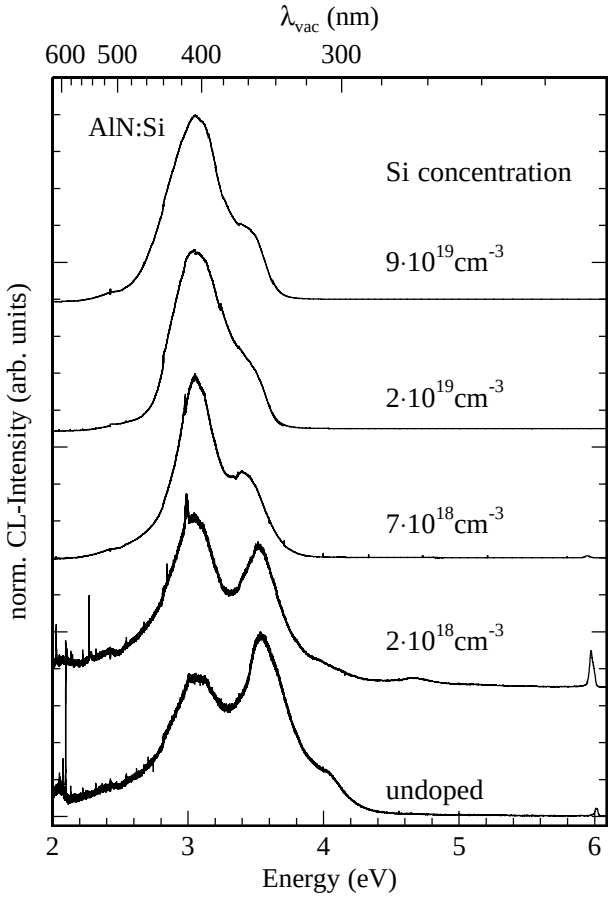

Figure 5.12: Overview of low-temperature (T = 10 K) CL spectra, normalized to the intensity at around 3 eV, for the Si-doped and the undoped samples grown at 1190 °C. The intensity ratio between the peaks at about 3 eV and the near-band-edge luminescence at 6 eV increases with increasing Si concentrations and shows a minimum for [Si]=2×10^{18} cm^{-3}.

5.4.2 Influence on violet band luminescence

As explained in the previous chapter, there are essentially three identifiable transitions at about 3.05 eV, 3.55 eV, and 4.06 eV in low-temperature CL spectra of undoped AlN. Figure 5.12 shows a collective overview of CL spectra (violet band DLT to NBE luminescence) from undoped (as a reference sample) and Si-doped samples with various [Si]. The spectra are normalized to the intensity at around 3 eV. Like the undoped sample, all Si-doped samples exhibited the violet band transitions. However, the dominant transition is coming from 3.05 eV which is in contrast to the undoped layer in which the dominant transition is at 3.55 eV. In the undoped layer, the Fermi level lies approximately in the middle of the band gap. In this case, the formation energy for (V_{Al}-complex)$^{-2}$ may become lower than the formation energy of V_{Al}^{-3}, therefore the dominant transition might be coming from the (V_{Al}-complex)$^{-2}$ charge states. Since Si is supposed to be acting as a shallow donor in AlN, a shift of the Fermi level toward the

conduction band can be expected with Si incorporation. The formation energy of V_{Al}^{-3} – supposed to act as triple acceptors – consistently becomes lower than the formation energy of (V_{Al}-complex)$^{-2}$ for a shift of the Fermi level toward the conduction band while doping the layer with Si [89, 217]. Figure 5.12 clearly shows that the intensity ratio of the two peaks at 3.05 eV and 3.55 eV changes systematically with the Si-doping, pushing up the 3.05 eV peak intensity at higher concentrations. This behavior is consistent with results of theoretical calculations by Mattila and Nieminen [87]. The argument of lowering the formation energy of the Al vacancy was also put forward by Gorczyca *et. al* [187]. Although the behavior of the Al vacancy in AlN is very similar to that of the Ga vacancy in GaN, the formation energy of the Al vacancy becomes significantly lower than that of the Ga vacancy for high values of the Fermi level due to a larger band gap of AlN. Therefore, the emission at 3.05 eV, which is attributed to V_{Al}^{-3}, becomes the dominating transition with increasing [Si] in AlN. Being an acceptor like defect, the V_{Al}^{-3} acts as a compensating center.

Similarly, the intensity ratio between the DLT at around 3 eV and the NBE at around 6 eV also changes with [Si]. It is very high for heavily doped samples. We observe a minimum intensity ratio for the sample with [Si]=2×10^{18} cm^{-3}. It also shows that the Al vacancy and its complex are increased with increasing [Si]. More Al vacancies may be formed due to the increasing competition between Si and Al atoms to fill the lattice and finally none of these atoms succeed to fill the lattice. Another possible explanation can be the gettering of point defects at the facets of increased depth and size of V-pits with increasing [Si].

5.5 Electrical Properties

Unlike GaN and InN, as-grown undoped AlN is electrically highly resistive. We have carried out two-point *I-V* measurements of our intentionally undoped AlN layers to examine the temperature dependent resistivity using a transmission line model (TLM) test structure (see Fig. 5.13). The resistivity is estimated in the range of 10^9 Ω·cm and 100 Ω·cm at room temperature and 1000 °C, respectively. Such a high resistivity of undoped AlN is attributed to a large donor ionization energy and the compensation of the free carriers by negatively charged cation vacancies, their complexes, and/or deep level acceptor impurities as discussed in the previous section. We estimated the activation energy of the donors in undoped AlN epilayers to be approximately 330 meV at higher temperatures. However, the source of donors in undoped AlN is still unknown.

Another big problem in AlN is the difficulty in obtaining Ohmic contact formation due to its high work function i.e. about 5.3 eV [223, 224]. Additionally, one or two monolayers of native oxide may be formed on the top of the deposited AlN due to the inherent characteristics of AlN. Such native oxide of Al not only becomes a hindrance for an Ohmic contact formation but also eliminates the advantage of the low (negative) electron affinity [225] of AlN. In order to overcome the difficulties of obtaining Ohmic contacts, we carried out particularly the following experiments: (a) Etching away a few nanometers of the top layer of AlN by dry (reactive ion etching (RIE)) or chemical

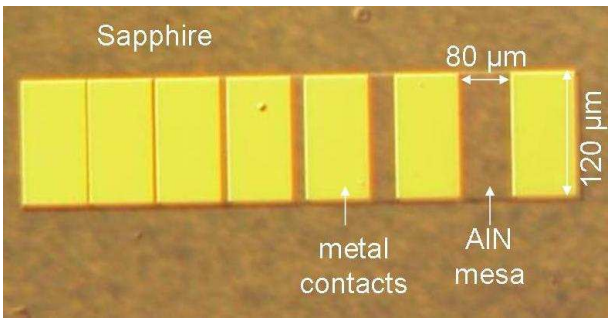

Figure 5.13: TLM pattern with mesa etching. The layer widths between the contacts are 80, 40, 20, 10, and 5 μm.

etching (using a warm solution of H_3PO_4 or KOH or HCl) before metallization, and (b) *in situ* deposition of an about 8 nm thick GaN layer on top of the AlN layers and etching away the GaN layer by RIE after metallization and rapid thermal annealing (RTA). Detailed studies of these experiments are described in Lu Xianming's master thesis [226].

Similar to intentionally undoped AlN, we carried out two-point current-voltage (*I-V*) measurements in a temperature range between 400 °C and 1000 °C to examine the temperature dependence of the resistivity of our AlN:Si layers with various [Si]. We could not carry out reliable measurements in most of our samples at a temperature below 400 °C due to the very high resistivity. Meanwhile, it was also not possible to carry out conventional van der Pauw Hall measurements due to the cracking as well as high resistivity of the layers.

Before metalization, an oxide dip of all samples was carried out in a warm (≈ 100 °C) HCl:H_2O (1:1) solution for 1 minute and they were immediately placed into a metal evaporation chamber. The n-type contact was formed by depositing a conventional stack of Ti/Al/Ni/Au (15/200/20/100 nm). The contact was annealed at 890 °C (maximum achievable temperature in our rapid thermal annealer (RTA)) - lower alloying temperatures were not sufficient - under N_2 atmosphere for 1 minute.

A general view of the resistivity of the AlN:Si layers with various [Si] as a function of reciprocal temperature is shown in Fig. 5.14 (left). The figure depicts a decrease in resistivity of AlN:Si layers with increasing temperature for all samples. One should notice that these resistivities contain both, the contact resistance and the layer resistivity, which itself depends on carrier concentration and mobility. The slope of plots is different for different [Si]. The highly doped sample exhibits a strong slope. In addition to a strong compensation of free carriers by V_{Al}^{-3} acceptors, Si donors are also self compensated in the highly doped sample [12]. Such effects strongly decrease the free carrier concentration. Meanwhile, donor ion scattering and neutral impurity scattering effects are increased in the highly doped sample which reduce the mobility of the free carriers. The cumulative effects of both the reduced amount of free carriers and the decreased mobility finally may increase the resistivity of the highly doped layer. Figure 5.14 (right) shows a comparison of the electrical resistivity of AlN:Si layers with different [Si] at 400 °C. A minimum resistivity of 22 Ω·cm is obtained for [Si] =

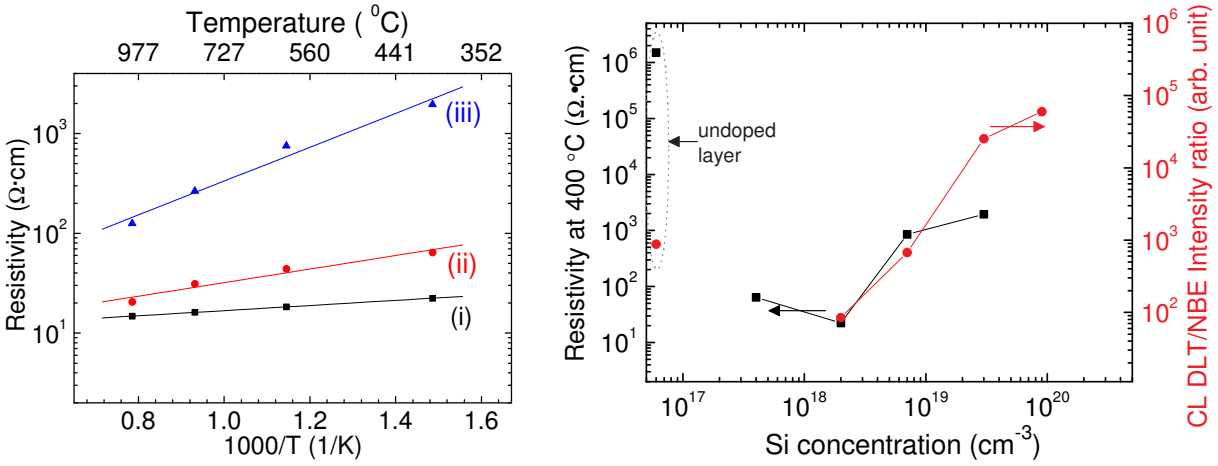

Figure 5.14: Variation of resistivity of AlN:Si layers with reciprocal temperature (left). Plots (i), (ii), and (iii) are for [Si] = 2×10^{18} cm^{-3}, 4×10^{17} cm^{-3}, and 3×10^{19} cm^{-3}, respectively. Change in resistivity of the AlN:Si layer at 400 °C and low temperature CL DLT/NBE luminescence intensity ratio against [Si] (right).

2×10^{18} cm^{-3}. High-temperature electrical measurements yield resistivities which are larger toward lower and higher Si concentrations. The possible reason for higher resistivity in the low doped ([Si] = 4×10^{17} cm^{-3}) sample is insufficient free carrier concentration. Meanwhile, the plot of low-temp CL DLT/NBE intensity ratio against [Si] strongly supports our arguments. We found a minimum value of the DLT/NBE intensity ratio when [Si] = 2×10^{18} cm^{-3} (see Fig. 5.10). At this Si level, the compensation effect is minimum. This corroborates the argument that the increased amount of V_{Al}^{-3} which act as triple acceptors effectively captures the free carriers from the ionized Si donors with increasing [Si]. However, other reasons e.g. non-optimized contacts or material defects (grain boundaries, cracks of the layer, etc) can not be ruled out for the low conductivity of our AlN:Si layers.

For Van der Pauw Hall measurements, neither the simple In contact alloying as applied on GaN nor the surface treatment with acids to remove possible oxides worked properly. Therefore, we have grown a thin GaN layer (about 8 nm) on top of our AlN:Si layers as briefly mentioned in the beginning of this section. After alloying the contacts at a high temperature of 950 °C (in the RTA facility of Mattson GmbH, Dornstadt) for 30 sec , the GaN layer was etched away by RIE on the remaining open surface. Now, the electrical measurements could be performed by Van der Pauw-Hall measurements. However, only the sample which was doped with [Si] = 2×10^{18} cm^{-3} exhibited measurable electrical properties. We obtained a fair electrical conductivity σ of 0.002 $(\Omega\,\mathrm{cm})^{-1}$, free electron concentration n of 4×10^{14} cm^{-3}, and carrier mobility μ_n of 30 cm^{2}V^{-1}s^{-1} in this sample. Figure 5.15 shows the variation of the electrical resistivity ρ with temperature for this sample. We determined the activation energy of the donor ionization $E_{a,D}$ in the range of 200 meV at lower temperature region using typical Arrhenius equation $\rho(T) = \rho_0 \exp(E_{a,D}/k_BT)$. If we substitute the value of n, N_D (assuming fully ionized Si donors, i.e. N_D=[Si]) and $E_{a,D}$ into Eq. 5.1, we obtain the acceptor concentration N_A to be 1.5×10^{18} cm^{-3} which is almost 75% of the Si donor

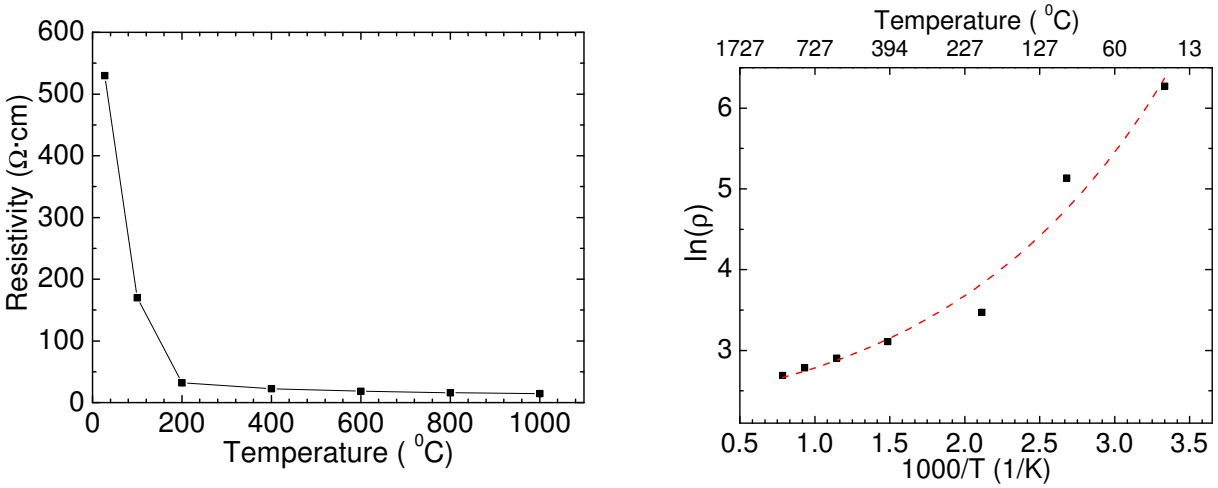

Figure 5.15: Variation of electrical resistivity with temperature (left) and corresponding Arrhenius plot (right) for [Si]=2 ×10^{18} cm^{-3}.

concentration. The quantitative amount of [Si] and the measured n clearly indicate the possible compensation of a huge amount of Si donors by the defects which are acting as acceptors. If we consider N_A in the range of 3.5 ×10^{16} cm^{-3}, similar to the value used by Taniyasu *et al.* [206], then we would expect the free carrier concentration to be in the range of 10^{16} cm^{-3} for $E_{a,D}$ = 200 meV. However, the partial ionization of Si donors also can not be ruled out for the measurement of a low free carrier concentration in our sample.

Figures 5.15 (left) and (right) show a non-linear behavior of the resistivity ρ with temperature T and the corresponding Arrhenius plot, respectively. Typically, a constant slope of the Arrhenius plot is expected throughout all temperatures. However, we observed a steeper slope below 200 °C than at higher temperatures. From the typical Arrhenius equation $\ln(\rho) \propto (E_{a,D}/T)$, we estimated $E_{a,D}$ of 50 meV at high temperature region (400 to 1000 °C) which is almost four times lower than at low temperature region (below 200 °C). Hermann *et al.* [207] have also observed a sudden decrease in the activation energy (45 meV) for a very high Si concentrations (2.3 ×10^{21} cm^{-3}) and the increase in conductivity. They attributed it to the formation of an impurity band. Estimation of different activation energies at different temperature regions in our samples suggests that the conductivity of the Si doped AlN epilayer is influenced not only by the activation of shallow Si donors but also by other mechanism, e.g. carrier hopping at higher temperature region. Si donors may have bounded to different type of defect centers, e.g. vacancies and their complexes and they might form various deep level energy states. At high temperatures, the neutral defect levels could be ionized and carrier transport might take place between different states by hopping conduction process [227–229]. Abtew *et al.* [228] have reported that the activation energy of an amorphous semiconductor, such as a-Si and a-Si:H is temperature dependent if localized energy states are present in the material. In this case, the pre-factor of the Arrhenius equation ρ_0 can be written as $\rho_0 \propto \exp(E_{a,D}/k_B T_M)$ [228] where T_M is a material dependent parameter that shows how quickly the activation energy decreases with temperature. This expression

is also called Meyer-Neldel rule (MNR) [230]. Previously, Schmidt *et al.* [231] have also reported that the emission of charge carriers from deep electron traps in ZnO (similar wide bandgap material) follows the MNR. Irmscher *et al.* [232] observed a temperature variation of the conductance of Si doped AlN bulk crystals due to the thermal activation of electrons from the acceptor-like electron traps in the range from 0.5 to 1 eV below the conduction band edge. Kasu *et al.* [233] have also earlier reported the presence of hopping conduction in heavily Si doped (1.5×10^{21} cm^{-3}) AlN layers. Therefore, we assume that the combination of regular shallow donors ($E_{a,D}$ of 200 meV) and the ionization of deep levels at high temperature (leading to hopping conductivity) increases the carrier concentration of the Si doped AlN epilayer at high temperature region. Consequently, the conductivity of the layer at high temperature region is increased although the carrier mobility is affected by the thermal lattice vibrations and we estimated a low activation energy from the typical Arrhenius equation. Since the resistivity is primarily dependent on the Si concentration for the AlN:Si layers and extremely high for the undoped layer, we have no doubt that Si is the major contributing donor for the conductivity of the AlN:Si layers and its activation energy is about 200 meV which was estimated at low temperature region.

Our experiments show that the attempt to incorporate Si donors is accompanied by the spontaneous generation of large numbers of native defects, acting as acceptors. Although the compensation by native defects is not an insurmountable problem, a high degree of compensation is often unavoidable. Unlike in GaN, this problem is obviously more severe in AlN. Moreover, the self–compensation depends on the growth conditions, such as the degree of the thermal equilibrium and the surface stoichiometry. Therefore, an electron concentration above the value obtained at our growth conditions can probably be achieved by improving the material quality. The material quality can probably be improved by growing AlN layers at a very low V/III ratio i.e. under highly Al-rich conditions and low NH_3 flow. To grow ultra-flat smooth surface and very high crystalline quality layers at very low V/III ratio, the growth temperature should be employed above 1250 °C which may facilitate 2D-growth mode. At such a high growth temperature, Al adatoms acquire sufficient thermal energy which increases the diffusion length. We realized that the solubility of Si is independent of the growth temperature. We had grown Si-doped samples at 1150 °C and 1190 °C. SIMS measurements show a consistent result of Si incorporation at both growth temperatures. Meanwhile, there is a high possibility of overgrowing AlN on the facets of V-pits which ultimately reduces the pit density. It may also help to annihilate the TDs which suppress the V-pit formation and ultimately reduces the gettering of point defects. The reduction of the intensity of defect related deep level transitions at the violet band in the luminescence spectrum is the most indispensable condition to improve the electrical properties of AlN:Si. However, the reduction of point defects will finally minimize the defect related luminescence transitions. Moreover, the oxygen contamination can be further reduced by improving the material quality which also facilitates the n-type electrical conductivity of AlN:Si.

Chapter 6

MOVPE Growth of High Al Content AlGaN

The material development of the ternary alloy AlGaN is one key to group-III nitride-based device applications. Low Al content $Al_xGa_{1-x}N$ ($x \leq 0.5$) layers have been used in several electronic and optoelectronic devices since the inception of the nitride-based technology. However, the growth of a good quality $Al_xGa_{1-x}N$ epilayer of high Al content and its usage in devices are still in the infant stage. This chapter includes the growth and characterization of $Al_xGa_{1-x}N$ ($x \geq 0.5$) layers grown under similar growth conditions as our optimized AlN as described in the previous chapters. We will particularly focus on the issue of controlling the Al composition in the solid phase. Finally, we will present structural and spectroscopic properties of the $Al_xGa_{1-x}N$ epilayers.

6.1 Introduction

AlGaN is basically used as a barrier layer in AlGaN/GaN heterostructures. Owing to the polarization properties of GaN and AlGaN, typically a two dimensional electron gas (2DEG) is formed at the interface with large carrier concentration and mobility. Such structures are the basis for GaN based heterostructure field effect transistors (HFETs) and high electron mobility transistors (HEMTs) for high–power high–frequency applications [8, 9, 52]. Meanwhile, there may also be a possibility of using AlGaN as a channel layer in AlN/AlGaN heterostructures. Such heterostructures could be employed in the fabrication of very high-temperature/high-power/high-frequency electronic devices in future. The intrinsic carrier concentration of GaN increases with the increase of temperature. It influences the free-carrier concentration of heterostructures at high temperature. In this case, a precise control of carrier density would be difficult in the devices. The wide bandgap energy of AlGaN with increasing Al content leads to a low intrinsic carrier concentration enabling a more precise control of free-carrier concentration over a wide range of temperatures. This, in turn, allows the device to be operable especially at high temperatures under harsh conditions. Therefore, a possible minimization of the effects of intrinsic carriers in the device operation at high temperatures is one of the major advantages of using high Al content AlGaN as a channel layer. If the

low-field mobility of carriers could be increased, then there would be a huge possibility of successfully employing AlGaN as a channel layer because of lowering sensitivity to ionized impurity scattering with increasing Al content. The mobility of 2DEG electrons in AlGaN is primarily limited by optical phonon scattering and alloy disorder scattering processes [234]. While growing $Al_xGa_{1-x}N$ with $x \geq 0.5$, a lattice mismatch with the GaN template can lead to the generation of dislocations at the interface and cracks on the surface of the overgrown strained layers. Therefore, it is imperative to use AlN as a buffer layer because of a close lattice match between the underneath AlN layer and the overgrown high Al content AlGaN layer. The growth of $Al_xGa_{1-x}N$ for electronic device structures is generally carried out on GaN templates due to the high quality of GaN layers that can currently be grown. However, even for the AlGaN/GaN heterostructures, using AlN as a buffer layer could be more advantageous because of its superior physical and chemical properties over GaN [235,236]. Especially, undoped AlN is highly resistive and the problem of leakage control in the buffer layer could be minimized during high temperature operation. For this, the material quality of AlN should be good enough because the buffer layer selection critically affects the overgrown AlGaN quality.

In recent years, high Al-content AlGaN alloys have attracted even greater interest as an important photonics material because of their applications in deep ultraviolet (UV) optoelectronic devices, such as deep UV light emitting diodes (LEDs) [3,4] and solar-blind photodetectors [237]. However, $Al_xGa_{1-x}N$ on GaN template cannot be used for light emitters with emission wavelength $\leq$360 nm due to the absorption in this layer. However, the quality of high Al content AlGaN directly grown on foreign substrates is not expected to be good enough because of more complex ternary material system. Therefore, these devices need to be grown on AlN templates. The quality of the AlGaN material for high Al compositions needs a radical improvement to reach the higher radiative efficiencies desired for deep UV LEDs and lasers. Meanwhile, like AlN, the growth of high quality AlGaN alloys of high Al-content is very difficult. Basically, the efficient incorporation of Al (without material loss) and the material quality are the main issues. Some important factors, like a low flow of NH_3 and low growth pressure to suppress the gas phase pre-reactions between Al and N precursors, and a very high growth temperature for the sufficient mobility of Al-adatoms, should be taken into consideration for the growth of high Al content AlGaN layers [238]. In the previous chapter, we have successfully developed a process and determined parameters for the growth of pure AlN layers. In this chapter, we discuss the growth and characterization of $Al_xGa_{1-x}N$ ($x \geq 0.5$) layers by employing a similar optimized process for the high-temperature AlN growth.

6.2 Experimental

We have used the conventional precursors TMAl, NH_3, and trimethylgallium (TMGa) for the growth of AlGaN layers. We have grown two sets of samples with a typical structure as illustrated in Fig. 6.1. In the first set (Series 1), an about 700 nm thick AlGaN layer at 1190 °C was deposited on top of an about 60 nm thick optimized high

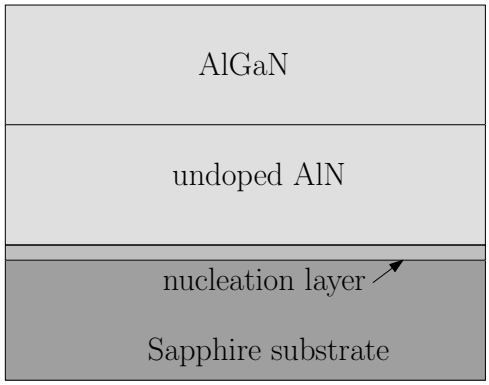

Figure 6.1: Illustration of AlGaN epilayer deposited on the top of undoped high-temperature AlN epilayer over a medium-temperature (MT) nucleation layer (NL).

temperature AlN buffer layer. The basic growth parameters of AlGaN were similar to the underneath AlN buffer layer as tabulated in Tab. 4.6. To change the composition of Al in AlGaN, we have controlled the TMGa flow. In the second set of samples (Series 2), we deposited an about 300 nm thick AlGaN layer at 1199 °C on top of an about 900 nm thick optimized high temperature AlN buffer layer. The thick AlN buffer layer was grown using the multi-step growth process as described in chapter 4. The AlGaN layers in both series were deposited under similar growth conditions (except the growth temperature) as tabulated in Tab. 4.6 except the two samples of series 2 having 78% and 88% of Al content. Instead of decreasing the TMGa flow rate in the growth of these two samples, the TMAl flow rate was increased because of the lower limitation of the flows in MFCs connected with the Ga line in our system.

6.3 Al Composition in AlGaN

The Al composition $x_{\mathrm{Al}}^{\mathrm{solid}}$ in AlGaN layer was evaluated using

$$x_{\mathrm{Al}}^{\mathrm{solid}} = \frac{c_{\mathrm{meas}}^{\mathrm{AlGaN}} - c_{\mathrm{theo}}^{\mathrm{GaN}}}{c_{\mathrm{theo}}^{\mathrm{AlN}} - c_{\mathrm{theo}}^{\mathrm{GaN}}}, \tag{6.1}$$

where $c_{\mathrm{meas}}^{\mathrm{AlGaN}}$ is the measured c-lattice constant of the AlGaN layer, and $c_{\mathrm{theo}}^{\mathrm{GaN}}$ and $c_{\mathrm{theo}}^{\mathrm{AlN}}$ are theoretically calculated c-lattice constants of relaxed GaN and AlN layers, respectively. $c_{\mathrm{meas}}^{\mathrm{AlGaN}}$ was determined using the X-ray peak positions of the (002) reflection of AlGaN from ω-2θ scan. The value of ω was corrected by the difference between the measured and the theoretical (20.84 °) peak positions of the (002) reflection of sapphire substrate. Unlike the AlGaN layers on GaN template, we expect a compressive biaxial strain in our AlGaN layers on AlN template. However, it was not possible to calculate the biaxial strain in these samples. The skew-symmetric (102) and asymmetric (114) reflections of both, the high Al content AlGaN and the underneath AlN, layers were broad and their peak positions were very close to each other. We obtained a convoluted single broad peak of these reflections from all the samples. Therefore, it was not possible to evaluate

the a-lattice constant of the AlGaN layers and so the biaxial strain. Thus, some errors in the composition calculation can not be ruled out since the effect of strain was not taken into account.

The Al composition $x_{\mathrm{Al}}^{\mathrm{gas}}$ in the gas phase is calculated using

$$x_{\mathrm{Al}}^{\mathrm{gas}} = \frac{2 \times j_{\mathrm{molar}}^{\mathrm{Al}}}{2 \times j_{\mathrm{molar}}^{\mathrm{Al}} + j_{\mathrm{molar}}^{\mathrm{Ga}}}, \tag{6.2}$$

where $j_{\mathrm{molar}}^{\mathrm{Al}}$ and $j_{\mathrm{molar}}^{\mathrm{Ga}}$ are molar flows of TMAl and TMGa, respectively. These molar flows j_{molar} (measured e.g. in moles/min) are determined from the respective well-known vapor pressure data taking into account the respective bubbler carrier gas flows, temperatures, and pressures [122]. TMAl evaporates as a dimeric molecule [122,126], i.e. every molecule in the vapor contains two Al atoms, not just one. Therefore, a factor of two is taken into account.

Figure 6.2 (left) shows a plot of the Al composition $x_{\mathrm{Al}}^{\mathrm{solid}}$ in solid-phase AlGaN against the gas-phase composition $x_{\mathrm{Al}}^{\mathrm{gas}}$ for the samples grown at 1190 °C. The data points are either on or slightly above the straight line with increasing Al mole fractions. This demonstrates a successful suppression of parasitic pre-reactions between TMAl and NH_3 precursors. The molar flows of TMAl (constant) and TMGa (varying) along with the growth rates of $Al_xGa_{1-x}N$ with different Al compositions and their corresponding binaries (GaN and AlN) are tabulated in Table 6.1. The AlGaN growth rate decreased with increasing Al content. As expected, the growth rate of the corresponding binary GaN decreased with decreasing TMGa molar flow. However, the growth rate of the binary AlN slightly increased even though the TMAl molar flow rate was kept constant. It might be due to the presence of other species like Ga.

A plot of the Al composition $x_{\mathrm{Al}}^{\mathrm{solid}}$ in the AlGaN epilayers against the gas-phase composition $x_{\mathrm{Al}}^{\mathrm{gas}}$ for the samples grown at 1199 °C is shown in Fig. 6.2 (right). The

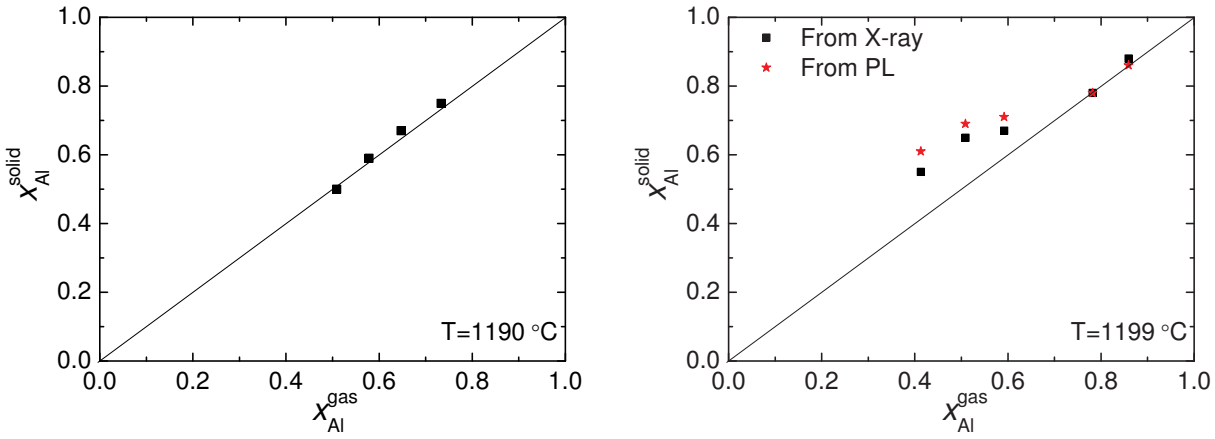

Figure 6.2: Al composition $x_{\mathrm{Al}}^{\mathrm{solid}}$ in AlGaN layers determined from X-ray measurements against the gas-phase composition $x_{\mathrm{Al}}^{\mathrm{gas}}$ for the samples grown at 1190 °C (left) and 1199 °C (right). Stars indicate Al compositions $x_{\mathrm{Al}}^{\mathrm{solid}}$ in AlGaN layers determined from PL measurements.

Table 6.1: MO precursor flow rates and growth rates of $Al_xGa_{1-x}N$ and corresponding binaries at the growth temperature of 1190 °C.

Sample	TMAl flow rate μmol/min	TMGa flow rate μmol/min	Growth rate AlGaN nm/hr	AlN nm/hr	GaN nm/hr
$Al_{0.5}Ga_{0.5}N$	9	9	477	239	238
$Al_{0.59}Ga_{0.41}N$	9	7	426	251	175
$Al_{0.67}Ga_{0.33}N$	9	5	375	251	124
$Al_{0.75}Ga_{0.25}N$	9	3	340	255	85

Al content was evaluated using X-ray and PL measurements. A deviation of 8 to -2% was observed in the results of the two measurements from lower to higher Al content samples. Such deviation comes from the neglected biaxial strain effect and the measurement errors, too. The molar flows of TMAl and TMGa along with the growth rates of $Al_xGa_{1-x}N$ with different Al compositions and their corresponding binaries (GaN and AlN) are tabulated in Table 6.2. The first three samples of $Al_xGa_{1-x}N$ where $x_{Al} \leq 0.67$ were grown at a constant TMAl molar flow of 9 μmol/min. The data points for these samples are above the straight line in Fig. 6.2 (right) showing a slight deviation from the linear relationship. It shows that the Ga incorporation efficiency is reduced at higher growth temperature. Such a decrease in incorporation efficiency may be attributed to the desorption of Ga atoms at high temperature. If we specifically compare the data on row 1 in Table 6.1 and on row 2 in Table 6.2, we can clearly see a significantly decreased growth rate of the binary GaN under the same growth condition at two different growth temperatures. Meanwhile, the growth rate of the binary AlN is also slightly decreased while growing at higher temperature which is in agreement with our earlier observations while growing undoped AlN epilayers as described in chapter 3. It means a loss of Al species occurs at higher growth temperature even though the data points in Fig. 6.2 (right) are displayed above the straight line. However, due to a competition in the incorporation between Al and Ga atoms into the AlGaN epilayers, Al becomes more favorable to be incorporated at higher temperature that results in higher Al content in the deposited AlGaN despite the loss of Al species. Another perspective to this phenomena is that the deposition ratio of AlN and GaN in AlGaN depends on the driving force imparted by the partial pressure of group III elements. Okada *et al* [238] could quantify this thermodynamical behavior of the AlGaN system at high temperatures. Accordingly, any increase of the growth temperature leads to a partial pressure decrease. At high temperatures, the partial pressure of Ga is extremely small compared with that of Al. Consequently, the Al content of AlGaN increases with the increase of the growth temperature.

Figure 6.3 shows a comparison between the normalized growth rates of the binaries, AlN and GaN, in AlGaN layers against the TMGa molar flow for the two sets of samples. The growth rate is normalized to the corresponding molar flow rates of

Table 6.2: MO precursor flow rates and growth rates of $Al_xGa_{1-x}N$ and corresponding binaries at the growth temperature of 1199 °C.

Sample	TMAl flow rate μmol/min	TMGa flow rate μmol/min	Growth rate AlGaN nm/hr	AlN nm/hr	GaN nm/hr
$Al_{0.55}Ga_{0.45}N$	9	13	352	214	138
$Al_{0.65}Ga_{0.35}N$	9	9	279	189	88
$Al_{0.67}Ga_{0.33}N$	9	6	273	192	81
$Al_{0.78}Ga_{0.22}N$	22	6	537	421	116
$Al_{0.88}Ga_{0.12}N$	22	4	479	411	68

TMGa and TMAl. We can clearly see the shift of plots towards lower growth rates for the samples grown at 1199 °C. This shows the material consumption inefficiency with increasing growth temperature. It depicts a decrease in normalized growth rate of the binary GaN at higher growth temperature with increasing TMGa flow rates. If we compare the data on row 3 and 4 in Table 6.2, we can see an increase of the growth rates for both binaries. However, the normalized growth rate of AlN is decreased with the increase of TMAl molar flow rate. This is attributed to a loss of Al species in the gas-phase reactions. The growth rate of the binary GaN is increased by 43% which is higher than the possible errors for the determination of Al content in AlGaN. The explanation for increasing growth rate of GaN is still unknown.

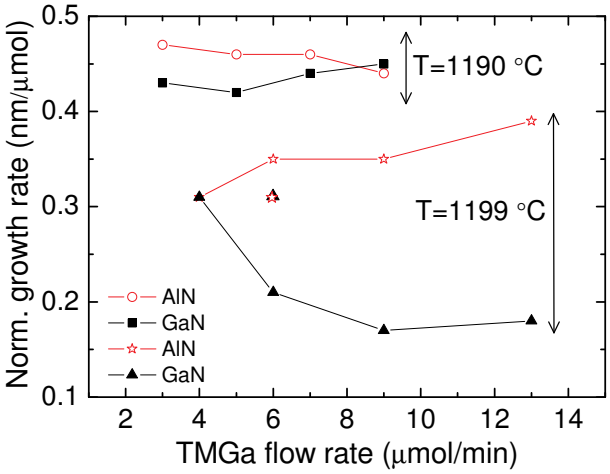

Figure 6.3: Normalized growth rates of AlN and GaN in AlGaN layers against the TMGa molar flow for two sets of samples grown at 1190 °C and 1199 °C. The GaN growth rate decreases at higher growth temperature.

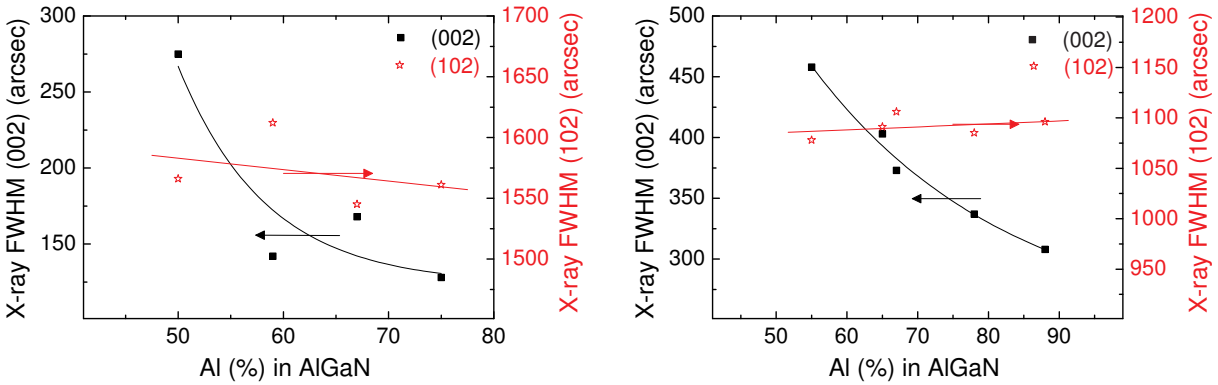

Figure 6.4: Change in FWHM of x-ray rocking curves for the symmetric (002)- and skew-symmetric (102)-reflections with respect to the Al content in AlGaN for the samples grown at 1190 °C (left) and 1199 °C (right).

6.4 Structural and Spectroscopic Properties

Figure 6.4 illustrates the plot of the FWHM of the X-ray rocking curves of the symmetric (002)- and skew-symmetric (102)-reflections with respect to the Al content in AlGaN for both sets of samples grown at 1190 °C (left) and 1199 °C (right). A trend of decreasing FWHM for the (002)-reflection with increasing Al content is observed in both sets whereas the FWHM for the (102)-reflection does not show a clear trend. As explained earlier, instead of two peaks, each from AlGaN and the underneath AlN, we observed a single peak for the (102)-reflection. However, the AlGaN samples in series 2, grown over a thick buffer layer of AlN, have shown relatively smaller values of FWHM for the (102)-reflection than the samples from series 1. These values are also smaller than the values of the underlying AlN layers (approx. 1200 arcsec). It means that some of the edge-type dislocations might be annihilated at or above the interface between the AlGaN and AlN layers. Therefore, the twist mosaicity rotating around the c-axis improves from the underlying AlN to the AlGaN. But the FWHMs for the (002)-reflection in this series of samples are higher than those from series 1 and for the underlying layer too. This may be attributed to a possible emergence of new screw type dislocations and stacking faults in the overgrown AlGaN layers.

Figure 6.5 shows AFM micrographs of the $Al_{0.75}Ga_{0.25}N$ layer from series 1. A high density of dimples are forming as ripples on the surface. The depth and width of the dimples are approximately 2.5 nm and 450 nm, respectively. Meanwhile, atomic steps are visible on the $2 \times 2\,\mu m^2$ scanned image. Such steps have an average width of 50 nm and a height of 2 or 3 atomic layers. The surface morphologies of all other samples in this series have also shown similar features and have a measured RMS surface roughness of about 0.45 nm on a $2 \times 2\,\mu m^2$ scan.

Similarly, fig. 6.6 shows AFM micrographs of the $Al_{0.78}Ga_{0.22}N$ layer from series 2. In this series of samples, the density of dimple-like features and ripples are drastically reduced. The surface is more flat. However, the amount of small pits on the $2 \times 2\,\mu m^2$ scan is high. Such pits may be attributed to the openings of edge-type TDs and point defects. Some large pits are also observed in the $10 \times 10\,\mu m^2$ scans. These pits may be

attributed to the openings of screw-type TDs. The surface morphologies of all other samples in this series have also shown similar features and have a measured RMS surface roughness of about 0.35 nm on $2 \times 2\,\mu m^2$ scans which is lower than the value measured in series 1.

Low-temperature (T = 10 K) photoluminescence (PL) measurements were carried out on the samples of series 2 [189]. The near-band-edge (NBE) spectra are depicted collectively in Fig. 6.7 (left). The intensity of the NBE transitions is gradually decreasing due to the enhancement of nonradiative recombination processes with increasing Al concentration measured by X-ray without considering strain [239]. The dependence of the line positions of the NBE luminescence with the Al content of the AlGaN layers is shown in Figure 6.7 (right). A theoretical curve is also shown with a bowing factor of 0.9. We see a deviation of up to 100 meV for the measured points from the theoretical curve. Such a deviation may come from the strain in the layer which is not considered in these measurements. We expect the data points above the line for compressive strain. As expected, the deviation is large in low Al content layers because the compressive biaxial strain might be increased with decreasing Al content.

The dependence of the FWHM of the exciton luminescence with the Al content x of $Al_xGa_{1-x}N$ is shown in Fig. 6.8. We can see an increase of the FWHM of the exciton luminescence with increasing alloy compositions (decreasing Al content in our samples and increasing Al content in the low Al content (< 50%) samples grown by Lipski and Forghani) due to the effect of alloy broadening as predicted by Lee *et al.* [240]. This is also in line with the FWHM for the (002)-reflection of X-ray measurements demonstrating that the crystal quality is deteriorating with increasing alloy composition i.e. decreasing

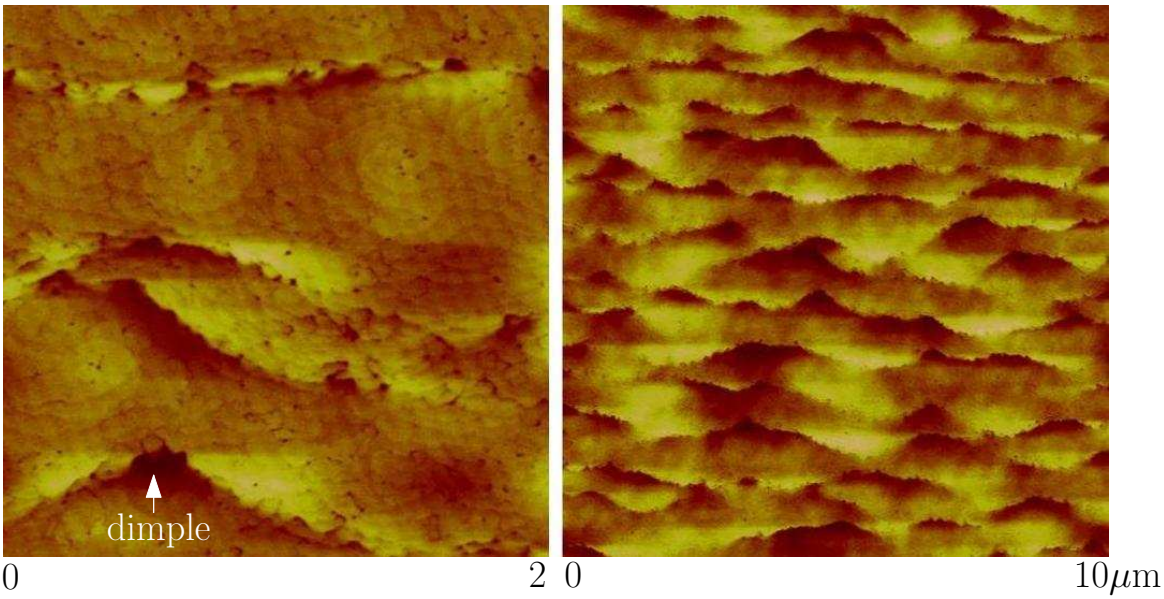

Figure 6.5: $2 \times 2\,\mu m^2$ (left) and $10 \times 10\,\mu m^2$ (right) AFM scans exhibiting the surface morphology of an $Al_{0.75}Ga_{0.25}N$ layer grown at 1190 °C. A high density of dimples and trenches are seen.

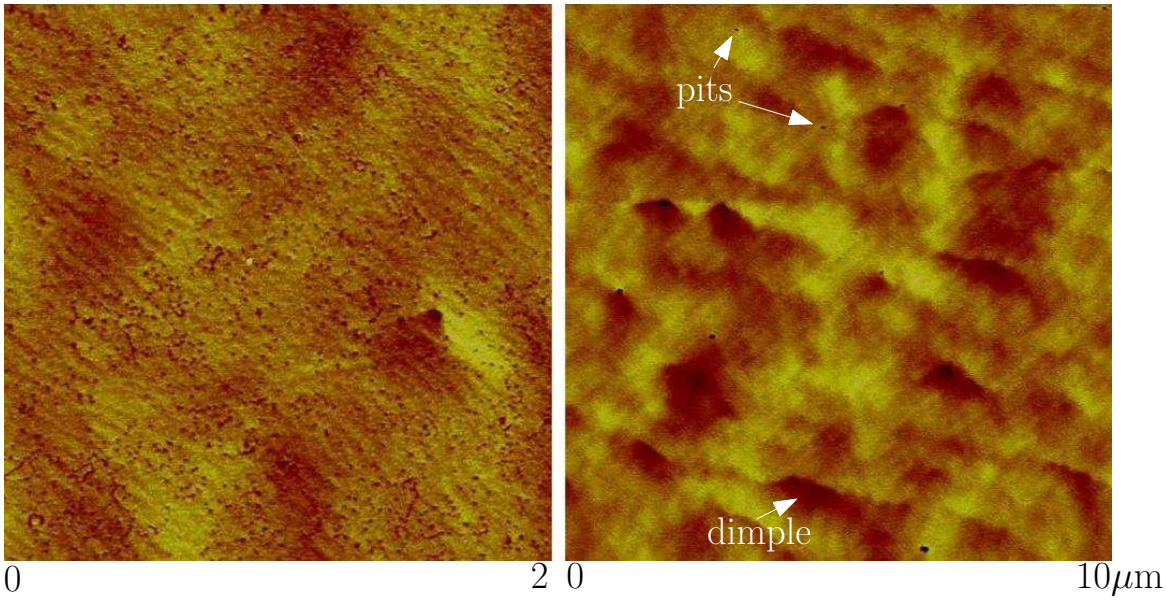

Figure 6.6: $2\times2\,\mu m^2$ (left) and $10\times10\,\mu m^2$ (right) AFM scans exhibiting the surface morphology of an $Al_{0.78}Ga_{0.22}N$ layer grown at 1199 °C. Small pits on the left and occasional dimples and large pits on the right images are seen.

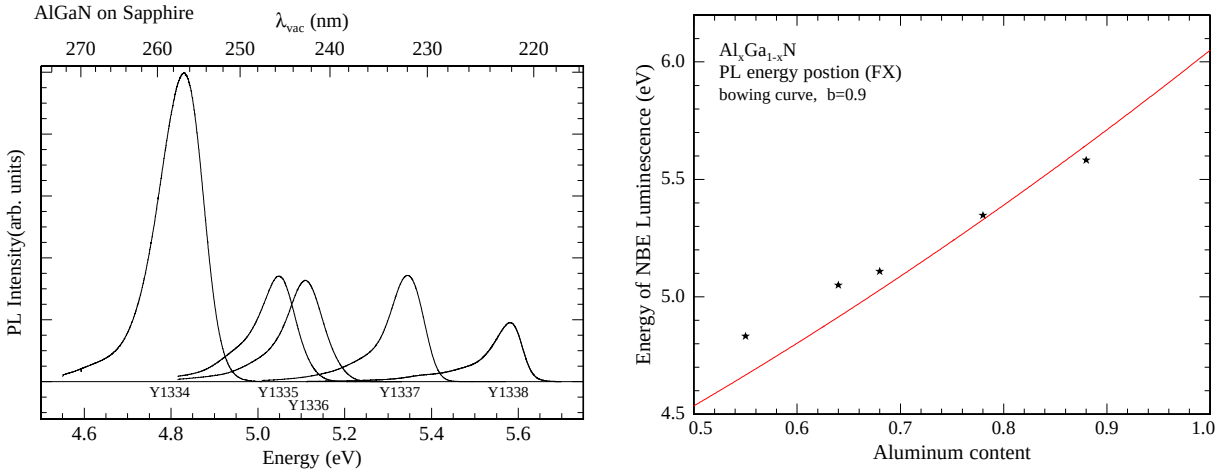

Figure 6.7: NBE PL spectra of $Al_xGa_{1-x}N$ (left) and the dependence of the energy of the excitons luminescence on the Al content (right).

Al content in our case. We observed the maximum FWHM when $x \approx 55\%$ and minimum for binaries. There are several reports showing the broadening of PL linewidths with increasing Al content [198, 241] at some extent, as seen in Fig. 6.8, and decreasing again when the Al content was exceeding 75% or more [239, 242]. Nepal *et al* [242] have suggested that the FWHM primarily depends on two terms, FWHM(x) $\propto$ x(1-x)·$dE_g(x)/dx$, where $dE_g(x)/dx$ is change of bandgap energy with respect to Al content. The second term makes the FWHM(x) nonsymmetric and they obtained maximum value at $x \approx 70\%$. In our case, the PL linewidth already started decreasing when the Al

content was exceeding 50% following the symmetricity of FWHM(x) $\propto$ x(1-x) [240]. It is expected because our growth condition is more favorable to high Al content layers. We suggest that the effect of alloy broadening on the luminescence linewidth depends not only on the physical parameters but also on the growth condition. In order to understand the effect of growth condition on alloy broadening, a detailed line shape analysis has to be carried out which could be a future work.

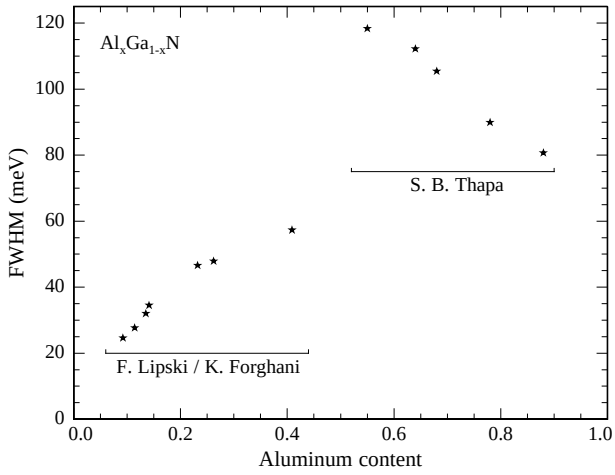

Figure 6.8: Dependence of the energy of the exciton luminescence half width on the Al content of AlGaN on our samples and samples grown by F. Lipski and K. Forghani.

Our experiments and the results show that a good quality of high Al content AlGaN can be achieved using similar growth conditions as for pure AlN. We successfully suppressed the gas-phase pre-reactions between TMAl and NH_3 and increased the incorporation efficiency of Al. However, the increased growth temperature decreases the incorporation efficiency of Ga.

Chapter 7

Heterostructures for Potential Devices based on AlN

In the previous chapters, we have extensively studied the growth and characterization of undoped and Si-doped AlN epilayers as well as high Al content AlGaN epilayers that were grown under similar growth conditions. For the realization of electronic and optoelectronic devices based on these materials, the epilayer quality of these materials should be further improved. Nevertheless, it is imperative to explore possible applications and understand the limitations. In this chapter, we will discuss implications of these materials in few structures that can be employed in future electronic and optoelectronic devices.

7.1 Heterostructures for Electronic Devices

$Al_xGa_{1-x}N$/GaN heterostructures have been widely used in electronic devices like HEMTs, and FETs/MISFETs/MODFETs for numerous applications since a decade [8,9]. This is because group-III-based wide bandgap semiconductors have superior material properties compared to silicon or GaAs, such as a high breakdown field ($3.3\,MV\,cm^{-1}$) and a high electron saturation velocity ($2.5\times10^7\,cm\,s^{-1}$). More importantly, they have a high density two-dimensional electron gas (2DEG) induced at the heterostructure interface due to the polarization effects even if the low Al content AlGaN barrier layer consists of an undoped layer. By increasing the breakdown voltage and applying materials with a higher breakdown field to the channel layer, these structures can be utilized to meet the future demands of much higher power applications, e.g. high-voltage high-power rectifiers. AlN has a breakdown voltage ($12\,MV\,cm^{-1}$) about four times higher than that of GaN, and the electron saturation velocity ($2.2\times10^7\,cm\,s^{-1}$) is almost the same as that of GaN. Therefore, AlN or high Al content AlGaN might be suitable materials to be used in the devices that demand an increase of the breakdown voltage. Using this concept we have proposed a structure employing AlN as a barrier layer and AlGaN as a channel layer instead of the conventional $Al_xGa_{1-x}N$/GaN heterostructure although the quality of the barrier with high Al content significantly reduces the mobility. The large conduction band offset provided by these heterostructures offers the

potential for high carrier confinement.

Due to its high resistivity and high thermal conductivity, AlN is more suitable than conventional GaN to be used as buffer layer so that the problem of the leakage current in electronic devices could effectively be addressed during high temperature operation. A report by Arulkumaran *et al.* [243] demonstrating an enhancement of the breakdown voltage in AlGaN/GaN HEMTs using a thick AlN buffer layer further inspires the use of AlN.

AlN/AlGaN heterostructure

Similar as in $Al_xGa_{1-x}N$/GaN heterostructures, we expect the formation of a triangular quantum well in the $Al_xGa_{1-x}N$ channel with a high density 2DEG depending on the Fermi level position due to the highly polarized nature of $Al_xGa_{1-x}N$ and the strain induced piezoelectric fields. Moreover, this structure may also be a promising candidate for the development of micro-electro-mechanical-system (MEMS) and piezo sensors for extreme environment operations because of excellent piezoelectric properties of AlN in comparison to other member of group-III nitrides (see Tab. 2.2). In MEMS technology, the lower AlGaN channel layer may represent the mechanical active layer, while the upper AlN barrier layer supplies the piezoelectrically active layer for actuation and the confinement of a 2D electron gas (at the lower interface). The 2DEG may serve as back electrode for the piezoelectric actuation and as read-out. The AlN barrier layer contributes to the total piezoelectric response. Using such structures in MEMS creates new and exciting opportunities for miniaturizing, reducing power consumption, and improving the performance and functionality of many devices. Till the date, there are only a few reports on the implementation of AlGaN as a channel layer [244, 245] in device structures. Such structures demonstrate a possible realization of AlGaN channel HEMTs for high voltage switching and microwave power applications in future. However, all of these researchers have used low Al content (≤38%) AlGaN channel layers and slightly higher Al content AlGaN barrier layers instead of AlN.

Looking into the future prospects, we have carried out band structure simulations of AlN/$Al_xGa_{1-x}N$ heterostructures using the software "BandEng" (one dimensional

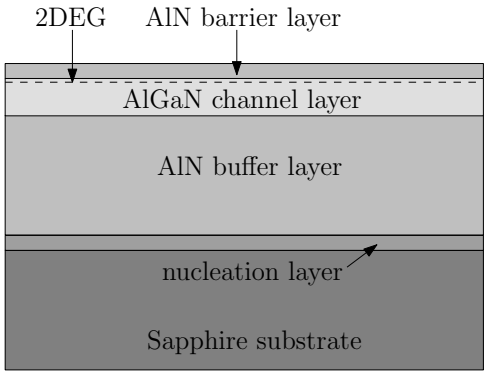

Figure 7.1: Schematic of AlN/AlGaN/AlN double-heterostructure.

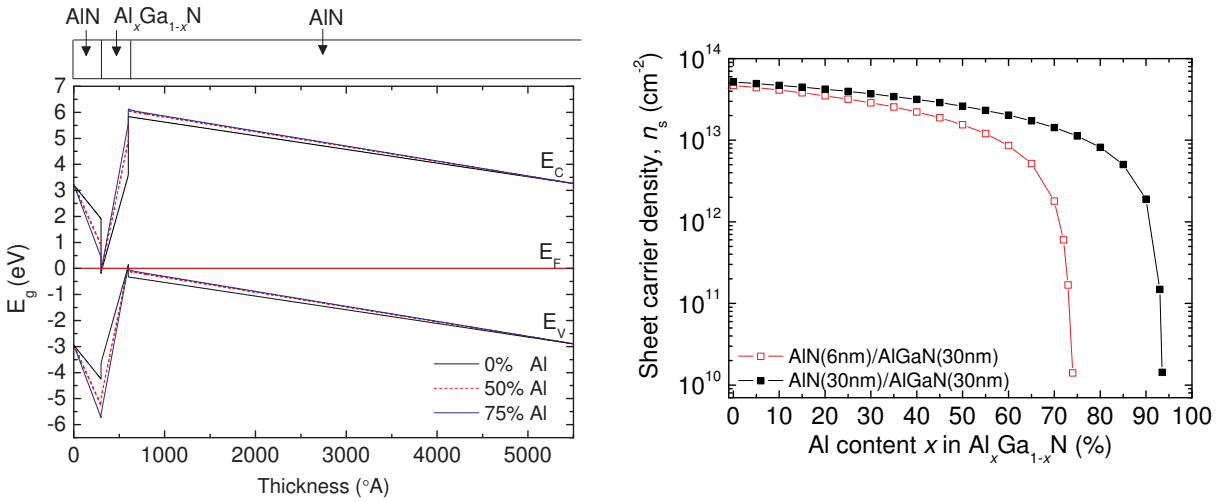

Figure 7.2: Overview of energy band diagram of AlN/AlGaN(50% and 75%)/AlN double-heterostructure at equilibrium (left) and interface sheet career density n_s vs Al molar fraction x of AlGaN for the AlN barrier layer thicknesses of 6 and 30 nm (right) in the simulated structures using BandEng.

Schrödinger-Poisson-equation solver) developed by M. Grundmann [246]. Figure 7.1 illustrates the schematic of a proposed heterostructure consisting of the AlN barrier layer on top preceded by an $Al_xGa_{1-x}N$ channel layer deposited over an undoped AlN buffer layer.

In these calculations, we changed three parameters: The Al molar fraction x, the thicknesses of the barrier and the channel layers. The simulation results showed a high interface sheet career density n_s if both layers were thicker. Figure 7.2 (left) illustrates an overview of the energy band diagram of an AlN/AlGaN/AlN (30/30/500 nm) double-heterostructure at equilibrium for the Al molar fraction x = 0%, 50% and 75%. The conduction band offset of 2.1 eV, 1.05 eV and 534 meV and the corresponding interface sheet career density n_s of 5.5×10^{13} cm^{-2}, 1.73×10^{13} cm^{-2} and 1.9×10^{12} cm^{-2} are formed for the Al mole fractions of x = 0%, 50% and 75%, respectively. Such a decrease in n_s with increasing x is attributed to the decreased confinement for the 2DEG. Figure 7.2 (right) shows n_s vs Al molar fraction x of AlGaN for the AlN barrier layer thicknesses of 6 and 30 nm. The simulation results show a sharp decrease in n_s if the Al molar fraction x is above 60% and 80% in 6 nm and 30 nm thick barrier layers, respectively.

We have grown a structure (see Fig. 7.1) containing a 30 nm thick $Al_xGa_{1-x}N$ layer on top of our optimized AlN buffer layer (500 nm), covered by another 30 nm of AlN. We covered the structure with a 10 nm thick GaN layer in order to improve the electrical contact formation and processed Ti/Al/Ni/Au (15/200/20/80) metal contacts. After alloying the contacts at 900 °C for 30 sec, the GaN was etched away by RIE on the remaining open surface. By low-temperature CL measurements, we could verify that the $Al_xGa_{1-x}N$ layer was grown with reasonable optical quality as shown in Fig. 7.3 (left). The spectrum shows an intense peak at about 5.365 eV due to an Al content of about 79% in the AlGaN layer. We can observe a much weaker near-band edge luminescence of the thin AlN top layer. The composition was further confirmed by

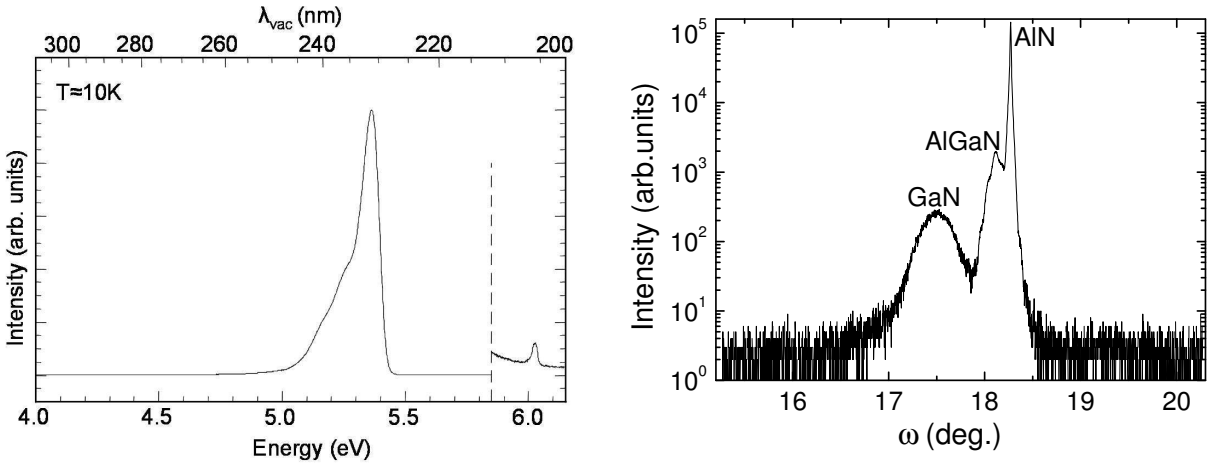

Figure 7.3: Low-temperature (10 K) CL spectrum (left) and X-ray diffraction for (002)-reflection (right) of the AlN/$Al_{0.79}Ga_{0.21}$N/AlN double hetero structure. The GaN peak at X-ray was measured before etching.

X-ray measurements in Fig. 7.3 (right). A GaN peak was seen before etching away, however, it vanished after etching away. We have grown a similar structure, as mentioned above, with a 6 nm thick AlN barrier layer. We carried out two-point *I-V* electrical measurements on this sample. Such a heterostructure showed a lateral electrical resistivity of 17 Ω·cm considering a thickness of 10 nm. From resistivities at various temperatures, we found an activation energy of about 70 meV. Unfortunately, we could not carry out Van der Pauw Hall measurements in both 30 nm and 6 nm thick barrier layer heterostructures even when the Al composition was reduced to 50%. There might be several reasons: high contact resistance, inhomogeneity of the layer, rough interface, severely limited mobility due to different scattering mechanisms (e.g. strong alloy disorder, interface roughness and optical phonons). More extensive and comprehensive investigations are needed to understand these problems.

AlN/GaN heterostructure

Besides a strong piezoelectric polarization caused by the significant lattice mismatch between AlN and GaN, the spontaneous polarization in AlN is very large and only about 3-5 times smaller than that of typical ferroelectric perovskites [247, 248]. However, much less work has been done on AlN/GaN heterostructures mainly due to the difficulty in growing high-quality AlN barrier layers on GaN. The biggest issue in the growth of such structure is the emergence of cracks in the AlN barrier layer due to a large lattice mismatch to the underneath GaN channel layer. To accommodate such lattice-mismatch, the addition of indium to the barrier layer has been investigated for improving device performance [249, 250]. Nevertheless, few studies have already been reported in the expectation of higher sheet carrier density in AlN/GaN heterostructures for high-power and high-frequency operations [251, 252]. Owing to the large conduction band offset between AlN and GaN (about 2.1 eV from simulation), the high-field characteristics of HEMTs are also improved due to the prevention of real-

space transfer of electrons from the channel into the barrier region under forward gate bias and/or electron transfer to higher satellite valleys of the conduction band in the barrier which have lower effective masses [251]. Another advantage of this structure is the decreased alloy disorder scattering and gate leakage current as compared to the conventional AlGaN/GaN HEMTs and FETs [253]. In addition to obvious applications in high transconductance, low threshold voltage HEMTs, the high-density, high-mobility 2DEGs at ultrashallow single AlN/GaN heterojunctions can enable a variety of devices such as high performance transparent biosensors, plasma-wave terahertz emitters, and other applications where a highly conductive channel buried a few nanometers under the surface is desirable [251, 254].

The band gap simulation (see Fig. 7.2) shows that a high sheet carrier concentration upto $n_s \approx 5\times10^{13}\,\mathrm{cm}^{-2}$ can be achieved in AlN/GaN heterostructures which is near the polarization limit. However, in reality it is very difficult to achieve such high carrier concentration. This is because the thickness of the AlN barrier layer grown on GaN should be kept below a certain critical thickness, due to the large lattice mismatch between AlN and GaN (2.47% for AlN on GaN). Consequently, n_s becomes much smaller than the expected value from very large polarizations in AlN due to the large surface depletion effect caused by the thin AlN barrier layer. Cao *et al.* [251] reported a high mobility μ of $1600\,\mathrm{cm}^2\mathrm{V}^{-1}\mathrm{s}^{-1}$ and n_s of approx. $3\times10^{13}\,\mathrm{cm}^{-2}$ at 300 K in ultrathin (2.3 nm AlN/GaN) heterojunctions grown by MBE. However, the electrical properties of such heterostructures grown in MOVPE are very poor. Very recently, Seo *et al.* [252] reported a Hall mobility of $948\,\mathrm{cm}^2\mathrm{V}^{-1}\mathrm{s}^{-1}$ at room temperature for an *in situ* Si_3N_4 passivated AlN/GaN heterostructure grown by MOVPE. The reported carrier concentration is $6.8\times10^{12}\,\mathrm{cm}^{-2}$ which is very low in comparison to the MBE grown sample.

In this work, we have deposited AlN/GaN (6/30 nm) heterostructures separately

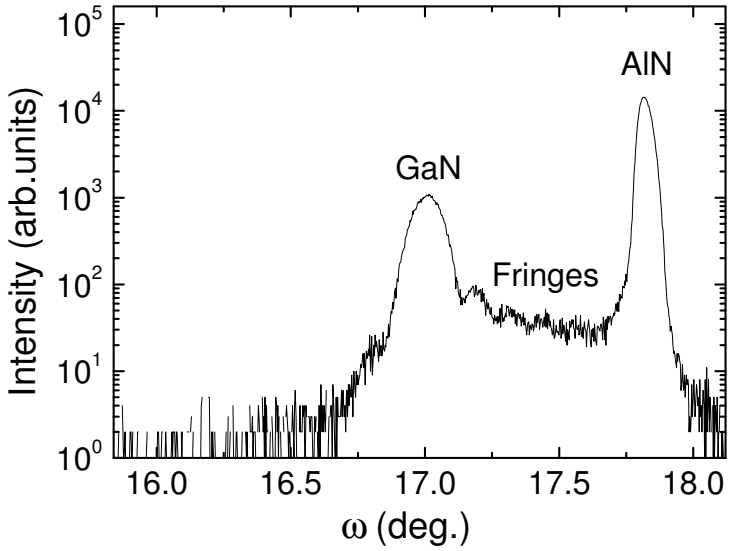

Figure 7.4: X-ray diffraction of the AlN/GaN/AlN double hetero structure.

on both GaN and optimized AlN buffer layers. The GaN channel layer was grown at a relatively low temperature of 1150 °C whereas the AlN barrier layer was grown under our optimized growth conditions. No cracks were observed at the surface in optical microscopy. AFM observations exhibited a smooth surface. Figure 7.4 shows X-ray diffraction peaks of AlN and GaN in $\omega - 2\theta$ scan for the (002)-reflection of an AlN/GaN/AlN double heterostructure. The fringes indicate a sharp interface between AlN and GaN layers. On these structures, we directly deposited a conventional stack of Ti/Al/Ni/Au (15/200/20/100 nm) by evaporation for contact formation after an oxide dip of the samples in a warm (≈ 100 °C) HCl:H_2O (1:1) solution for 1 minute. The contact was annealed at 890 °C under N_2 atmosphere for 1 minute.

Van der Pauw Hall measurements were performed at room temperature and at 77 K. We obtained a free carrier Hall mobility μ_n of 375 $cm^2V^{-1}s^{-1}$ and 520 $cm^2V^{-1}s^{-1}$ at room temperature and 572 $cm^2V^{-1}s^{-1}$ and 936 $cm^2V^{-1}s^{-1}$ at 77 K for the AlN/GaN heterostructures grown on GaN and AlN buffer layers, respectively, whereas the sheet career density n_s was measured to be 3.9×10^{13} cm^{-2} and 1.4×10^{13} cm^{-2} in the respective structures. The former structure exhibited a sheet resistance R_s of 428 Ω/□ whereas the later showed a high value of 831 Ω/□. The strain situation of each layer is different in both structures. The GaN channel layer on top of the AlN buffer layer is normally compressive whereas the GaN buffer layer is assumed to be more relaxed. AlN deposited on top of the compressively strained GaN has naturally less tensile strain than the layer deposited on the relaxed GaN buffer layer. It may be one reason why we obtained a low n_s in our AlN/GaN/AlN heterostructures. Our AlN buffer layer has still a larger number of TDs in comparison to the optimized GaN layer which may cause compensation of free carriers. This may be another reason for the decrease of n_s. The increased μ in the AlN/GaN/AlN heterostructure may be attributed to less electron-electron scattering due to a decreased n_s. Nevertheless, the above results still show a comparable results of our structures with similar structures grown by others using MOVPE.

7.2 Heterostructures for Optoelectronic Devices

AlN is emerging as an active material for deep ultraviolet (DUV) optotelectronic emitters and detectors operating in the 200-340 nm wavelength range. Such devices are important for many applications, including water purification, biochemical agent detection, medical research/health care and high-density data storage [255]. Taniyasu *et al.* [2] for the first time in 2006 reported a DUV LED operating at 210 nm, the shortest wavelength light emitter based on AlN. But the external quantum efficiency of the on-wafer device was reported to be very low in the order of 10^{-6}% because of no sufficient electron-hole confinement and carrier injection into the emitting layer of AlN. A key problem in such devices is the limited conductivity that can be obtained in the n- and p-type AlN layers. We have determined the activation energy of Si in AlN to be approximately 200 meV and others have also reported in the same range of 180 to 300 meV. Meanwhile, the p-type doping is a much bigger problem. An acceptor ionization energy $E_{a,A}$ for magnesium (Mg) in AlN has been reported to be larger than 600 meV [2, 14]. With such activation energies it will always be difficult to get a de-

sirable carrier concentration in AlN at room temperature. Therefore it is very difficult to employ AlN as an efficient active material in LEDs or lasers [256]. However, AlN has still a huge potential to be used in combination with $Al_xGa_{1-x}N$ materials in the structures of optoelectronic devices. Basically, a low TD density AlN is a highly attractive material to be used as a buffer layer in AlGaN based DUV structures due to its transparency to the operating wavelengths. AlN can also be a promising candidate for DUV Schottky barrier photodetectors as reported by Dahal *et al.* [257]. Such photodetectors can address serious problems of Si photodiodes i.e. degradation under UV irradiation and unnecessarily high and broadband responsivity at longer wavelengths [258]. Moreover, AlN/AlGaN superlattices (SLs) are also employed as a dislocation filter to reduce TDs and tensile strain in the subsequently grown layers of the DUV structure [259, 260].

Furthermore, thin AlN/GaN superlattice structures (SLS) can be used for the fabrication of quantum cascade lasers (QCLs) [261]. Unlike conventional laser diodes, QCL is a bandgap independent control-by-design optoelectronic device. It relies on intersubband (ISB) transitions between electron confined states and the desired wavelength of operation can be obtained through a proper choice of the layer thicknesses. The AlN/GaN SLS has attracted new attention because the large conduction band offset provided by their heterostructures offers the potential to push the conventional ISB device operation (mid-infrared to the THz spectral range using GaAs/AlGaAs, InGaAs/AlInAs or antimonides) to much shorter wavelengths, namely the 1.3-1.55 μm range used for fibre optics telecommunications. MBE is still a dominant technique for fabricating AlN/GaN SLS for short-wavelength ISB devices because of the possibility of precise control of layer thicknesses down to one monolayer [262, 263]. Actually, it is still a challenging task in MOVPE technology to achieve abrupt heterojunctions by a precise control of the layer thickness. However, MOVPE has an advantage for the general production of nitride-based optoelectronic devices as explained in chapter 2 and 3. For this reason, studies on the growth of AlN/GaN SLS by MOVPE have still a

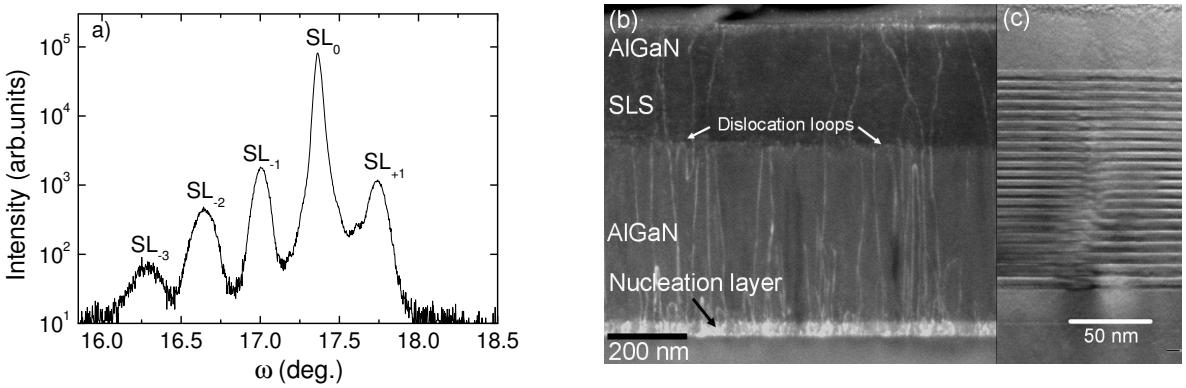

Figure 7.5: HRXRD measurement of the ω-2θ scan (002)-reflection of AlN/GaN superlattice (left). TEM-bright-field image of the superlattice structure (right). Bright and dark layers in the superlattice structure are AlN and GaN, respectively.

considerable significance.

We have grown AlN/GaN SLs consisting of 21 periods of each 4 nm thick AlN and GaN layers. The structure was grown on a 500 nm thick $Al_{0.5}Ga_{0.5}N$ buffer layer over a thin layer of optimized high temperature AlN layer and covered with a 40 nm thick $Al_{0.5}Ga_{0.5}N$ cap. The growth interruption time was kept 5 s after each layer grown of AlN and GaN. A HRXRD measurements of the ω-2θ scan (002)-reflection was performed to verify the periodicity and HRTEM was used to examine the abruptness of the interfaces of the SLS. Indeed, it shows the superlattice related satellite peaks (SL) confirming the good periodicity of the layers (Fig. 7.5 (left)). The defects and the abruptness of the interfaces of the superlattice structure were investigated by transmission electron microscopy (TEM) as shown in Fig. 7.5 (right). The bright layer is AlN and the dark GaN. TEM cross section studies confirm the excellent uniformity and the flatness of the SLS structure. The interfaces of AlN on GaN are sharper than those of GaN on AlN. SIMS measurements[5] (Fig. 7.6) of this sample also confirm the uniformity of the structure. However, the occasional change in the shape of the curve (as shown by arrows) shows an intermixing of the layers. Moreover, as shown in the TEM-dark-field image (Fig. 7.5(right, b)), many of the threading dislocations (TDs) coming through the AlGaN buffer layer are bent at the interface between buffer layer and SL which formed dislocation loops and stopped there.

These results show that a thin AlN–GaN SLs can be grown using MOVPE but the issue of the intermixing of the layers still needs to be carefully addressed to employ it in the device structure. However, such SLs can also be employed for the TD reduction in the overlying layer.

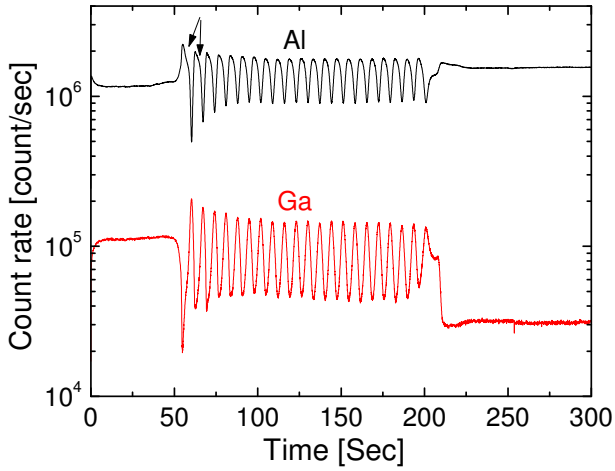

Figure 7.6: SIMS measurement confirming uniform AlN/GaN superlattices on the AlGaN buffer layer capped again by AlGaN.

[5]SIMS measurements were carried out by Dr. Christoph Schnuerer-Patschan and Dr. Ulrich Ehrke of Cameca GmbH, Munich.

Chapter 8

Summary and Conclusions

In this thesis, investigations on the MOVPE growth of AlN, Si-doped AlN, $Al_xGa_{1-x}N$ ($x \geq 0.5$), and AlN/$Al_xGa_{1-x}N$ ($0 \leq x \leq 0.8$) heterostructures were systematically carried out.

The major problems in the growth of a high quality AlN epilayer are the gas-phase parasitic pre-reactions between the Al MO precursor and NH_3 and the 3D growth mode of the layer due to a low surface mobility of the Al species. To minimize the gas-phase pre-reactions, we modified the susceptor design of an AIX200RF reactor by shifting the substrate position from the conventional downstream middle place to the upstream gas inlet position. This arrangement decreased the residence time of precursors at the heated zone of the reactor and minimized the gas-phase parasitic pre-reactions. We optimized the conventional two-step growth process and the parameters. Oxygen doping at the beginning of the deposition of the mid-temperature (870 °C) AlN nucleation layer followed by a cooling down process before ramping up of the growth temperature had positive impacts on the quality of the final high temperature AlN epilayer. The layer was grown in N_2 and H_2 ambient at the ratio of 2:1 using a low V-III product by supplying a minimum flow of both, NH_3 (11.2 mmol/min) and TMAl (11.3 μmol/min) precursors. In this condition, the growth rate was approx. 220 nm/hr. The lower growth rate, in addition to a higher growth temperature of 1199 °C and a lower reactor pressure of 35 mbar, facilitated the growth-mode from 3D to 2D. These growth conditions have addressed a low surface mobility issue of Al species at some extents. As a result, we obtained a 500 nm thick epilayer of AlN with a very smooth and atomically flat surface. The density of large hexagonal pits (diameter $\geq$ 50 nm) on the surface was less than 10^5 cm^{-2}. The measured RMS surface roughness (1×1 μm^2 scan) was 0.21 nm and the FWHM of the X-ray (002)- and (102)-reflections were 35 and 1350 arcsec, respectively. TEM investigations showed that the TDs were originating at the nucleation layer and threading through the entire layer. The screw- and edge-type TD density was about 10^7 cm^{-2} and 3.5×10^{10} cm^{-2}. The near-band-edge peak was well resolved at around 6.0 eV in CL investigations. The FWHM of the low-temperature (T = 8 K) CL NBE was about 10 meV. However, we recorded broad intense peaks at around 3 eV at the violet band region. These peaks were attributed to Al vacancies and their complexes. The peak intensity and FWHM of the X-ray (102)-reflection were drastically reduced by increasing the layer thickness but the layers above 1.2 μm thicknesses were

not crack free. We introduced indium as a surfactant during the high-temperature growth of the AlN epilayer and obtained a very high quality 1.5 μm thick crack-free epilayer. The measured FWHM of X-ray (102)-reflection of this layer was 680 arcsec which corresponds to an edge-type TD density of about 4×10^{9} cm^{-2}. The intensity of deep level transitions at the violet band region was also drastically reduced.

Additionally, we deposited AlN on a SiC substrate without a NL under similar optimized growth conditions. The crystalline and spectroscopic quality of AlN on SiC was superior than on the layer grown on sapphire but the surface was heavily pitted with large hexagonal pits. Furthermore, we demonstrated the homoepitaxial growth of AlN on bulk AlN crystals with a low density of edge-type TDs.

Si-doping of AlN has inherent limitations and difficulties. We observed adverse effects on the surface and crystal quality of AlN by Si doping. TEM investigations showed that the edge-type TDs, coming through the underneath undoped layer, were propagating straight to the top in the case of a low doped sample whereas they were strongly bent at or above the interface in the case of high doped samples. The bent neighboring TDs came closer, bunched together, and finally formed a V-pit defect. The density, size, and depth of such pits increased with increasing [Si]. The FWHM of the X-ray (002)-reflection was increasing up to [Si] = 2×10^{19} cm^{-3} and decreasing for higher concentrations whereas the FWHM for the (102)-reflection was unaffected. The X-ray evaluations, shifting of NBE peaks in CL and E_2-mode in Raman spectra showed that the in-plane tensile strain in the AlN:Si layers increased with increasing [Si] up to approx. 2×10^{19} cm^{-3}, and decreased for higher concentrations. A lot of cracks were clearly visible on the surface of relatively highly doped ([Si]$\geq 2\times10^{19}$ cm^{-3}) samples under optical microscopy investigations. The intensity ratio of the two peaks at 3 eV and at 3.5 eV measured by CL was changed systematically with the Si doping, pushing up the 3 eV peak intensity at higher concentrations. Similarly, the intensity ratio between the deep level transitions and the near band-edge luminescence was also changing with [Si]. We observed a minimum intensity ratio for the sample with [Si] = 2×10^{18} cm^{-3}. By room temperature Van der Pauw Hall measurements, we found a fair electrical conductivity of 0.002 $(\Omega\,\mathrm{cm})^{-1}$, free electron concentration of 4×10^{14} cm^{-3}, and carrier mobility of 30 cm^{2}V^{-1}s^{-1}. We found different activation energies at low and high temperature regions from the Arrhenius plot. This suggests that Si may have formed both, shallow and different deep level energy states. We evaluated the activation energy of Si as a shallow donor to be about 200 meV in the low temperature region. At high temperature electrical measurements, we observed higher resistivity for both, higher as well as lower [Si] as compared to [Si] = 2×10^{18} cm^{-3}. This corroborates the argument that Al vacancies were formed which act as triple acceptors and compensate the Si donors with increasing Si. We conclude that the effective n-type doping of AlN could be achieved only if the acceptor like defect centers (Al vacancies and their complexes, and TDs) were drastically reduced.

Two series of $Al_xGa_{1-x}N$ ($x \geq 0.5$) layers were grown at two different growth temperatures of 1190 °C and 1199 °C under similar growth conditions on top of the optimized AlN layer. We found that the incorporation efficiency of Al was higher than Ga at the higher growth temperature, although the growth rate of both binaries, AlN and GaN decreased. The FWHM of the X-ray (002)-reflection and the photoluminescence was

increased with increasing alloy composition (decreasing Al content) whereas it was not affected for X-ray (102)-reflection. However, the X-ray width for (102)-reflection was narrower for the samples grown at higher temperature. It means some of the edge-type dislocations might be annihilated at or above the interface between the AlGaN and underneath the AlN layer. However, the surfaces of all samples were not uniform and a high density of dimple like depletions was observed.

AlN/$Al_{0.79}Ga_{0.21}N$ heterostructures for potential electronics device applications were grown on AlN/Sapphire templates. It was not possible to measure Hall mobility in the AlGaN alloy channel even when the Al composition was reduced to 50%. However, two-point *I-V* electrical measurements showed lateral electrical resistivity of 17 Ω·cm when the barrier layer was 6 nm thin. Meanwhile, we compared the electrical properties of AlN/GaN heterostructures grown on AlN/Sapphire and GaN/Sapphire templates. We measured a higher room–temperature free carrier mobility in the heterostructure on the former template (520 $cm^2V^{-1}s^{-1}$) than on the latter one (375 $cm^2V^{-1}s^{-1}$). But the carrier concentration on the former template (1.4×10^{13} cm^{-2}) was lower than on the latter one (3.9×10^{13} cm^{-2}).

A successful growth of 21 periods of AlN/GaN (4/4 nm) superlattice structure that could be used for the short-wavelength ISB devices was also demonstrated.

This thesis has clearly pointed out the fact that a high growth temperature, more than 1200 °C, is a necessary growth condition to improve the quality of the AlN epilayers further. Furthermore, the reactor should be designed in such a fashion that the residence time of the precursors at the heated zone should be short. In the case of the availability of such high temperature reactor, our newly developed multi-step growth process could be successfully employed to obtain an excellent quality of AlN. According to this process, an initial layer could be deposited using our optimized growth condition for a thin (500 nm) layer. The high growth temperature enhances the coalescence process so that many small islands would merge into large islands. To increase the thickness of the layer, the growth rate can be increased by increasing the flow rate of TMAl. It means the subsequent layers would be grown at Al-rich condition. Due to the acquirement of the sufficient thermal energy, the mean diffusion length of the adsorbed Al adatoms would be increased so that the growth mode always remains in 2D-mode which finally hopefully results in an excellent quality of the epilayer.

Our experiments show that the attempt to incorporate Si donors is accompanied by the spontaneous generation of large numbers of acceptor like native defects coming from Al vacancies and the formation of V-pits. The Al vacancies could be minimized by growing the layer at Al-rich growth condition. Meanwhile, with a high thermal energy, there is a high possibility of overgrowing AlN on the facets of the V-pits so that their formation probability could be minimized. A decrease in V-pits ultimately would reduce the gettering of point defects. The reduction of point defects will finally minimize the defect related luminescence transitions at the violet region of the CL spectrum which is the most indispensable condition for the improvement of the electrical properties of AlN:Si. Moreover, the oxygen contamination can be also reduced by improving the material quality. Therefore, we expect good electrical properties and control of carrier concentration in high temperature grown AlN layers.

Own Publications

- J. Hertkorn, S.B. Thapa, T. Wunderer, F. Scholz, Z.H. Wu, Q.Y. Wei, F.A. Ponce, M.A. Moram, C.J. Humphreys, C. Vierheilig, and U.T. Schwarz, "Highly conductive modulation doped composition graded p-AlGaN/(AlN)/GaN multi heterostructures grown by metalorganic vapor phase epitaxy", *J. Appl. Phys.* **106**, 013720 (2009).

- R.A.R. Leute, M. Feneberg, R. Sauer, K. Thonke, S.B. Thapa, F. Scholz, Y. Taniyasu, and M. Kasu, "Photoluminescence of highly excited AlN: Biexcitons and exciton exciton scattering", *Appl. Phys. Lett.* **95**, 031903 (2009).

- O. Klein, J. Biskupek, U. Kaiser, K. Forghani, S.B. Thapa, and F. Scholz, "Simulation supported analysis of the effect of SiN_x interlayers in AlGaN on the dislocation density reduction", *Journal of Physics: Conference Series* **209**, 012018 (2010).

- F. Scholz, S.B. Thapa, M. Fikry, J. Hertkorn, T. Wunderer, F. Lipski, A. Reiser, Y. Xie, M. Feneberg, K. Thonke, R. Sauer, M. Dürrschnabel, L.D. Yao, and D. Gerthsen, "Epitaxial growth of coaxial GaInN-GaN hetero-nanotubes", *IOP Conference Series: Materials Science and Engineering (MSE)* **6**, 012002 (2009).

- F. Lipski, S.B. Thapa, J. Hertkorn, T. Wunderer, S. Schwaiger, F. Scholz, M. Feneberg, M. Wiedenmann, K. Thonke, H. Hochmuth, M. Lorenz, and M. Grundmann, "Studies towards freestanding GaN in hydride vapor phase epitaxy by in-situ etching of a sacrificial ZnO buffer layer", *phys. stat. sol. (c)* **6**, S352 (2009).

- G.M. Prinz, M. Feneberg, M. Schirra, K. Thonke, R. Sauer, S.B. Thapa, and F. Scholz, "Silicon-doping induced strain of AlN layers: a comparative luminescence and Raman study", *phys. stat. sol. (RRL)* **2**, 215 (2008).

- S.B. Thapa, J. Hertkorn, F. Scholz, G.M. Prinz, R.A.R. Leute, M. Feneberg, K. Thonke, R. Sauer, O. Klein, J. Biskupek, and U. Kaiser, "Growth and studies of Si-doped AlN layers", *J. Cryst. Growth* **310**, 4939 (2008).

- A.V. Lobanova, E.V. Yakovlev, R.A. Talalaev, S.B. Thapa, F. Scholz, "Growth conditions and surface morphology of AlN MOVPE", *J. Cryst. Growth* **310**, 4935 (2008).

- J. Hertkorn, F. Lipski, P. Brückner, S.B. Thapa, T. Wunderer, F. Scholz, A. Chuvilin, U. Kaiser, M. Beer, and J. Zweck, "Process optimization for the effective reduction of threading dislocations in MOVPE grown GaN using in situ deposited SiN_x masks", *J. Cryst. Growth* **310**, 4867 (2008).

- S.B. Thapa, J. Hertkorn, T. Wunderer, F. Lipski, F. Scholz, A. Reiser, Y. Xie, M. Feneberg, K. Thonke, R. Sauer, M. Dürrschnabel, L.D. Yao, and D. Gerthsen, "MOVPE growth of GaN around ZnO nanopillars", *J. Cryst. Growth* **310**, 5139 (2008).

- S.B. Thapa, J. Hertkorn, F. Scholz, G.M. Prinz, R.A.R. Leute, M. Feneberg, K. Thonke, R. Sauer, O. Klein, J. Biskupek, and U. Kaiser, "MOVPE growth of high quality AlN and effects of Si incorporation", *phys. stat. sol. (c)* **5**, 1774 (2008).

- J. Hertkorn, P. Brückner, S.B. Thapa, T. Wunderer, F. Scholz, M. Beer, and J. Zweck, "Optimization of nucleation and buffer layer growth for improved GaN quality", *J. Cryst. Growth* **308**, 30 (2007).

- S.B. Thapa, J. Hertkorn, F. Scholz, G.M. Prinz, R.A.R. Leute, M. Feneberg, K. Thonke, and R. Sauer, "MOVPE growth of high quality AlN and effects of Si doping", Extended Abstract Booklet Bratislava, Slovakia, *12th European Workshop for Metalorganic Vapour Phase Epitaxy, EWMOVPE-XII,* 65 (2007).

- S.B. Thapa, J. Hertkorn, T. Wunderer, F. Lipski, F. Scholz, A. Reiser, Y. Xie, M. Feneberg, K. Thonke, R. Sauer, M. Dürrschnabel, L.D. Yao, and D. Gerthsen, "Heteroepitaxial growth of GaN on ZnO by MOVPE", Extended Abstract Booklet Bratislava, Slovakia, *12th European Workshop for Metalorganic Vapour Phase Epitaxy, EWMOVPE-XII,* 135 (2007).

- L. Gu, V. Srot, W. Sigle, C. Koch, P. van Aken, F. Scholz, S.B. Thapa, C. Kirchner, M. Jetter, and M. Rühle, "Bandgap measurements of direct and indirect semiconductors using monochromated elctrons", *Phys. Rev. B* **75**, 195214 (2007).

- S.B. Thapa, C. Kirchner, F. Scholz, G.M. Prinz, K. Thonke, J. Biskupek, U. Kaiser, and D. Hofstetter, "Structural and spectroscopic properties of AlN layers grown by MOVPE", *J. Cryst. Growth* **298**, 383 (2007).

Conference/Workshop Presentations:

- S.B. Thapa, J. Hertkorn, F. Scholz, G.M. Prinz, R.A.R. Leute, M. Feneberg, K. Thonke, R. Sauer, O. Klein, J. Biskupek, and U. Kaiser, "Growth and studies of Si-doped AlN layers", Oral presentation, *14th International Conference on Metal Organic Vapour Phase Epitaxy*, June 2-6, 2008, Metz, France.

- S.B. Thapa, J. Hertkorn, T. Wunderer, F. Lipski, F. Scholz, A. Reiser, Y. Xie, M. Feneberg, K. Thonke, R. Sauer, M. Dürrschnabel, L.D. Yao, and D. Gerthsen ,"MOVPE growth of GaN around ZnO nanopillars", Poster presentation, *14th International Conference on Metal Organic Vapour Phase Epitaxy*, June 2-6, 2008, Metz, France.

- S.B. Thapa, J. Hertkorn, F. Scholz, G.M. Prinz, R.A.R. Leute, M. Feneberg, K. Thonke, R. Sauer, O. Klein, J. Biskupek, and U. Kaiser, "MOVPE growth of high quality AlN and effects of Si incorporation", Oral presentation, *7th International Conference of Nitride Semiconductors*, Sept. 16-21, 2007, Las Vegas, USA.

- S.B. Thapa, J. Hertkorn, F. Scholz, G.M. Prinz, R.A.R. Leute, M. Feneberg, K. Thonke, and R. Sauer, "MOVPE growth of high quality AlN and effects of Si doping", Poster presentation, *12th European Workshop for Metalorganic Vapour Phase Epitaxy (EWMOVPE-XII)*, June 3-6, 2007, Bratislava, Slovakia.

- S.B. Thapa, J. Hertkorn, T. Wunderer, F. Lipski, F. Scholz, A. Reiser, Y. Xie, M. Feneberg, K. Thonke, R. Sauer, M. Dürrschnabel, L.D. Yao, and D. Gerthsen, "Heteroepitaxial growth of GaN on ZnO by MOVPE", Poster presentation, *12th European Workshop for Metalorganic Vapour Phase Epitaxy (EWMOVPE-XII)*, June 3-6, 2007, Bratislava, Slovakia.

- S.B. Thapa, J. Hertkorn, F. Scholz, G.M. Prinz, K. Thonke, and R. Sauer, "Effect of initial growth process on structural and spectroscopic properties of AlN", Oral presentation, *Deutsche Gesellschaft für Kristallwachstum und Kristallzüchtung Workshop on III-V Epitaxy (DGKK 2006)*, Dec. 7-8, 2006, Ulm, Germany.

- S.B. Thapa, C. Kirchner, F. Scholz, G.M. Prinz, K. Thonke, R. Sauer, A. Chuvilin, J. Biskupek, U. Kaiser, and D. Hofstetter, "Structural and spectroscopic properties of AlN layers grown by MOVPE", Poster presentation, *13th International Conference on Metal Organic Vapour Phase Epitaxy*, May 22-26, 2006, Miyazaki, Japan.

- S.B. Thapa, C. Kirchner, F. Scholz, D. Hofstetter , A. Minkow, G.M. Prinz, K. Thonke, and R. Sauer, "Structural properties of AlN grown by MOVPE", Oral presentation, *Deutsche Gesellschaft für Kristallwachstum und Kristallzüchtung Workshop on III-V Epitaxy (DGKK 2005)*, Dec. 8-9, 2005, Duisburg, Germany.

Bibliography

[1] S. Nakamura, and S.F. Chichibu, *Introduction to Nitride Semiconductor Blue Lasers and Light Emitting Diodes*, Taylor and Francis, London, 2000.

[2] Y. Taniyasu, M. Kasu, and T. Makimoto, "An aluminium nitride light-emitting diode with a wavelength of 210 nanometers", *Nature* **441**, 325 (2006).

[3] T.M. Katona, T. Margalith, C. Moe, M.C. Schmidt, C. Matt, S. Nakamura, J.S. Speck, S.P. DenBaars, and P. Steven, "Growth and fabrication of short-wavelength UV LEDs", *Proc. SPIE* **5187**, 250 (2004).

[4] M. Shatalov, Z. Gong, M. Gaevski, S. Wu, W. Sun, V. Adivarahan, and M.A. Khan, "Reliability of AlGaN-based deep UV LEDs on sapphire", *Proc. SPIE* **6134**, 61340P (2006).

[5] R.D. Dupuis, J.B. Limb, J. Liu, J. Ryou, C. Horne, and D. Yoo, "InGaN MQW green LEDs using p-InGaN and p-InGaN/p-GaN superlattices as p-type layers", *Proc. SPIE* **6894**, 68941D (2008).

[6] F. Bernardini, V. Fiorentini, and D. Vanderbilt, "Spontaneous polarization and piezoelectric constants of III-V nitrides", *Phys. Rev. B* **56**, R10024 (1997).

[7] O. Ambacher, J. Smart, J.R. Shealy, N.G. Weimann, K. Chu, M. Murphy, W.J. Schaff, L.F. Eastman, R. Dimitrov, L. Wittmer, M. Stutzmann, W. Rieger, and J. Hilsenbeck, "Two-dimensional electron gases induced by spontaneous and piezoelectric polarization charges in N- and Ga-face AlGaN/GaN heterostructures", *J. Appl. Phys.* **85**, 3222 (1999).

[8] Y.-F. Wu, B.P. Keller, S. Keller, D. Kapolnek, S.P. Denbaars, and U.K. Mishra, "Measured power performance of AlGaN/GaN MODFETs", *IEEE Electron Device Lett.* **17**, 455 (1996).

[9] L. Shen, S. Heikman, B. Moran, R. Coffie, N.-Q. Zhang, D. Buttari, I.P. Smorchkova, S. Keller, S.P. DenBaars, and U.K. Mishra, "AlGaN/AlN/GaN High-Power Microwave HEMT", *IEEE Electron Device Lett.* **22**, 457 (2001).

[10] H. Amano, N. Sawaki, I. Akasaki, and Y. Toyoda, "Metalorganic vapor phase epitaxial growth of a high quality GaN film using an AlN buffer layer", *Appl. Phys. Lett.* **48**, 353 (1986).

[11] H. Amano, M. Kito, K. Hiramatsu, and I. Akasaki, "P-type Conduction in Mg-doped GaN Treated with Low-energy Electron Beam Irradiation (LEEBI)", *Jpn. J. Appl. Phys.* **28**, L2112 (1989).

[12] Y. Taniyasu, M. Kasu, and T. Makimoto, "Electrical conduction properties of n-type Si-doped AlN with high electron mobility (>100 $cm^2V^{-1}s^{-1}$)", *Appl. Phys. Lett.* **85**, 4672 (2004).

[13] T. Ive, O. Brandt, H. Kostial, K.J. Friedland, L. Däweritz, and K.H. Ploog, "Controlled n-type doping of AlN:Si films grown on 6H-SiC(0001) by plasma-assisted molecular beam epitaxy", *Appl. Phys. Lett.* **86**, 024106 (2005).

[14] Z.Y. Fan, J.Y. Lin, and H.X. Jiang, "Achieving conductive high Al-content AlGaN alloys for deep UV photonics", *Proc. SPIE* **55**, 647911-1 (2007).

[15] C. Caliendo, and P. Imperatori, "Structural, optical, and acoustic characterization of high-quality AlN thick films sputtered on Al2O3(0001) at low temperature for GHz-band electroacoustic devices applications", *J. Appl. Phys.* **96**, 2610 (2004).

[16] C.M. Yang, K. Uehara, S.K. Kim, S. Kameda, H. Nakase, and K. Tsubouchi, "Highly c-axis-oriented AlN film using MOCVD for 5GHz-band FBAR filter", *IEEE Symposium on Ultrasonics* **1**, 170 (2003).

[17] I. Waki, C. Kumtornkittikul, Y. Shimogaki, and Y. Nakano, "Shortest intersubband transition wavelength (1.68 μm) achieved in AlN/GaN multiple quantum wells by metalorganic vapor phase epitaxy", *Appl. Phys. Lett.* **82**, 4465 (2002).

[18] D. Hofstetter, S. Schad, H. Wu, W.J. Schaff, and L.F. Eastman, "GaN/AlN-based quantum-well infrared photodetector for 1.55 μm", *Appl. Phys. Lett.* **83**, 572 (2003).

[19] D. Gerthsen, B. Neubauer, Ch. Dieker, R. Lantier, A. Rizzi, and H. Lueth, "Molecular beam epitaxy (MBE) growth and structural properties of GaN and AlN on 3C-SiC(0 0 1) substrates", *J. Cryst. Growth* **200**, 353 (1999).

[20] V. Lebedev, V. Cimalla, U. Kaiser, Ch. Foerster, J. Pezoldt, J. Biskupek, and O. Ambacher, "Effect of nanoscale surface morphology on the phase stability of 3C-AlN films on Si.111.", *J. Appl. Phys.* **97**, 114306 (2005).

[21] D.J. As, S. Potthast, J. Fernandez, K. Lischka, H. Nagasawa, and M. Abe, "Cubic GaN/AlGaN Schottky-barrier devices on 3C-SiC substrates", *Microelectronic Engineering* **83**, 34 (2006).

[22] T. Lei, M. Fanciulli, R.J. Molnar, T.D. Moustakas, R.J. Graham, and J. Scanlon, "Epitaxial growth of zinc blende and wurtzitic gallium nitride thin films on (001) silicon", *Appl. Phys. Lett.* **59**, 944 (1991).

[23] D. Chandrasekhar, D.J. Smith, S. Strite, M.E. Lin, and H. Morkoç, "Characterization of Group III-nitride semiconductors by high-resolution electron microscopy", *J. Cryst. Growth* **152**, 135 (1995).

[24] J.G. Lozano, F.M. Morales, R. García, D. González, V. Lebedev, Ch.Y. Wang, V. Cimalla, and O. Ambacher, "Cubic InN growth on sapphire (0001) using cubic indium oxide as buffer layer", *Appl. Phys. Lett.* **90**, 091901 (2007).

[25] H. Morkoç, *Handbook of Nitride Semiconductors and Devices, Volume 1: Materials Properties, Physics and Growth.* WILEY-VCH Verlag GmbH and Co. KGaA, Weinheim, 2008.

[26] S.J. Pearton, *Optoelectronic Properties of Semiconductors and Superlattices, M.O. Manasreh, series editor, Volume 7 GaN and Related Materials II.* Gordon and Breach Science Publishers, 2000, Amsteldijk.

[27] J. Neugebauer, "Ab initio Analysis of Surface Structure and Adatom Kinetics of Group-III Nitrides ", *phys. stat. sol. (b)* **227**, 93 (2001).

[28] M. Stutzmann, O. Ambacher, M. Eickhoff, U. Karrer, A. Lima Pimenta, R. Neuberger, J. Schalwig, R. Dimitrov, P.J. Schuck, and R.D. Grober, "Playing with Polarity", *phys. stat. sol. (b)* **228**, 505 (2001).

[29] S. Adachi, *Properties of Group-IV, III-V and II-VI Semiconductors,* John Wiley and Sons, Ltd., West Sussex, 2005.

[30] J. Li, K.B. Nam, M.L. Nakarmi, J.Y. Lin, H.X. Jiang, P. Carrier, and S.-H. Wei, "Band structure and fundamental optical transitions in wurtzite AlN", *Appl. Phys. Lett.* **83**, 5163 (2003).

[31] Y.-N. Xu, and W.Y. Ching, "Electronic, optical, and structural properties of some wurtzite crystals", *Phys. Rev. B* **48**, 4335 (1993).

[32] O. Ambacher, J. Majewski, C. Miskys, A. Link, M. Hermann, M. Eickhoff, M. Stutzmann, F. Bernardini, V. Fiorentini, V. Tilak, B. Schaff, and L.F. Eastman, "Pyroelectric properties of Al(In)GaN/GaN hetero and quantum well structures", *J. Phys.: Condensed Matter* **14**, 3399 (2002).

[33] K. Lawniczak-Jablonska, T. Suski, I. Gorczyca, N.E. Christensen, K.E. Attenkofer, R.C.C. Perera, E.M. Gullikson, J.H. Underwood, D.L. Ederer, and Z. Liliental Weber, "Electronic states in valence and conduction bands of group-III nitrides: Experiment and theory", *Phys. Rev. B* **61**, 16623 (2000).

[34] D. Fritsch, H. Schmidt, and M. Grundmann, "Band-structure pseudopotential calculation of zinc-blende and wurtzite AlN, GaN, and InN", *Phys. Rev. B* **67**, 235205 (2003).

[35] A. Rubio, J.L. Corkill, M.L. Cohen, E.L. Shirley, and S.G. Louie, "Quasiparticle band structure of AlN and GaN", *Phys. Rev. B* **48**, 11810 (1993).

[36] A. Kobayashi, O.F. Sankey, S.M. Volz, and J.D. Dow, "Semiempirical tight-binding band structures of wurtzite semiconductors: AlN, Cds, CdSe, and ZnO", *Phys. Rev. B* **28**, 935 (1983).

[37] W.Y. Ching, and B.N. Harmon, "Electronic structure of AlN", *Phys. Rev. B* **34**, 5305 (1986).

[38] E. Ruiz, S. Alvarez, and P. Alemany, "Electronic structure and properties of AlN", *Phys. Rev. B* **49**, 7115 (1994).

[39] P. Rinke, M. Winkelnkemper, A. Qteish, D. Bimberg, J. Neugebauer, and M. Scheffler, "Consistent set of band parameters for the group-III nitrides AlN, GaN, and InN", *Phys. Rev. B* **77**, 075202 (2008).

[40] G.D. Chen, M. Smith, J.Y. Lin, H.X. Jiang, S.-H. Wei, M. Asif Khan, and C.J. Sun, "Fundamental optical transitions in GaN", *Appl. Phys. Lett.* **68**, 2784 (1996).

[41] W.M. Yim, E.J. Stofko, P.J. Zanzucchi, J.I. Pankove, M. Ettenberg, and S.L. Gilbert, "Epitaxially grown AlN and its optical band gap", *J. Appl. Phys.* **44**, 292 (1973).

[42] P.B. Perry, and R.F. Rutz, "The optical absorption edge of single-crystal AlN prepared by a closed-spaced vapor process", *Appl. Phys. Lett.* **33**, 319 (1978).

[43] X. Tang, F. Hossain, K. Wongchotigul, and M.G. Spencer, "Near band-edge transition in aluminum nitride thin films grown by metal organic chemical vapor deposition", *Appl. Phys. Lett.* **72**, 1501 (1998).

[44] M. Goano, E. Bellotti, E. Ghillino, C. Garetto, G. Ghione, and K.F. Brennan, "Band structure nonlocal pseudopotential calculation of the III-nitride wurtzite phase materials system. Part II. Ternary alloys $Al_xGa_{1-x}N$, $In_xGa_{1-x}N$, and $In_xAl_{1-x}N$", *J. Appl. Phys.* **88**, 6476 (2000).

[45] H. Kawanishi, E. Niikura, M. Yamamoto, and S. Takeda, "Experimental energy difference between heavy- or light-hole valence band and crystal-field split-off-hole valence band in $Al_xGa_{1-x}N$", *Appl. Phys. Lett.* **89**, 251107 (2006).

[46] F. Bernardini, and V. Fiorentini, "Nonlinear macroscopic polarization in III-V nitride alloys", *Phys. Rev. B* **64**, 085207 (2001).

[47] F. Bernardini, and V. Fiorentini, "Erratum: Nonlinear macroscopic polarization in III-V nitride alloys ", *Phys. Rev. B* **65**, 085207 (2001).

[48] A.F. Wright, "Elastic properties of zinc-blende and wurtzite AlN, GaN, and InN", *J. Appl. Phys.* **82**, 2833 (1997).

[49] C. Deger, E. Born, H. Angerer, O. Ambacher, M. Stutzmann, J. Homsteiner, E. Riha, and G. Fischerauer, "Sound velocity of $Al_xGa_{1-x}N$ thin films obtained by surface acoustic-wave measurements", *Appl. Phys. Lett.* **72**, 2400 (1998).

[50] V. Fiorentini, F. Bernardini, F. Della Sala, A. Di Carlo, and P. Lugli, "Effects of macroscopic polarization in III-V nitride multiple quantum wells", *Phys. Rev. B* **60**, 8849 (1999).

[51] F. Bernardini, and V. Fiorentini, "Nonlinear Behavior of Spontaneous and Piezoelectric Polarization in III-V Nitride Alloys", *phys. stat. sol. (a)* **190**, 65 (2002).

[52] O. Ambacher, B. Foutz, J. Smart, J.R. Shealy, N.G. Weimann, K. Chu, M. Murphy, A.J. Sierakowski, W.J. Schaff, L.F. Eastman, R. Dimitrov, A. Mitchell, and M. Stutzmann, "Two dimensional electron gases induced by spontaneous and piezoelectric polarization in undoped and doped AlGaN/GaN heterostructures", *J. Appl. Phys.* **87**, 334 (2000).

[53] U.K. Mishra, P. Parikh, and Yi-F. Wu, "AlGaN/GaN HEMTs - An Overview of Device Operation and Applications", *Proc. IEEE.* **90**, 1022 (2002).

[54] H. Hirayama, "Quaternary InAlGaN–based high-efficiency ultraviolet light-emitting diodes", *J. Appl. Phys.* **97**, 091101 (2005).

[55] T. Takeuchi, S. Sota, M. Katsuragawa, M. Komori, H. Takeuchi, H. Amano, and I. Akasaki, "Quantum-Confined Stark Effect due to Piezoelectric Fields in GaInN Strained Quantum Wells", *Jpn. J. Appl. Phys.* **36**, L382 (1997).

[56] T. Deguchi, K. Sekiguchi, A. Nakamura, T. Sota, R. Matsuo, S. Chichibu and S. Nakamura, "Quantum-Confined Stark Effect in an AlGaN/GaN/AlGaN Single Quantum Well Structure", *Jpn. J. Appl. Phys.* **38**, L914 (1999).

[57] G.A. Slack, and T.F. McNelly "Growth of high purity AlN crystals", *J. Cryst. Growth* **34**, 263 (1976).

[58] C.J. Sun, P. Kung, A. Saxler, H. Ohsato, K. Haritos, and M. Razeghi, "A crystallographic model of (00.1) aluminum nitride epitaxial thin film growth on (00.1) sapphire substrate", *J. Appl. Phys.* **75** (8), 3964 (1994).

[59] K. Dovidenko, S. Oktyabrsky, J. Narayan, and M. Razeghi, "Aluminum nitride films on different orientation of sapphire and silicon", *J. Appl. Phys.* **79** (5), 2439 (1996).

[60] C.J. Sun, and M. Razeghi, "Comparison of the physical properties of GaN thin films deposited on (0001) and $(01\bar{1}2)$ sapphire substrates", *Appl. Phys. Lett.* **63**, 973 (1993).

[61] A. Dadgar, A. Krost, J. Christen, B. Bastek, F. Bertram, A. Krtschil, T. Hempel, J. Bläsing, U. Haboeck, A. Hoffmann, "MOVPE growth of high-quality AlN", *J. Cryst. Growth* **297**, 306 (2006).

[62] B. Bastek, J. Christen, F. Bertram, T. Hempel, A. Dadgar, and A. Krost, "Cathodoluminescence of point defects in high quality AlN MOVPE epilayers", Poster at the ICDS 24, Albuquerque, 2007.

[63] G. Vogg, C.R. Miskys, J.A. Garrido, M. Hermann, M. Eickhoff, and M. Stutzmann, "High quality heteroepitaxial AlN films on diamond", *J. Appl. Phys.* **96**, 895 (2004).

[64] K. Masu, Y. Nakamura, T. Yamazaki, T. Shibata, M. Takahashi, and K. Tsubouchi, "Transmission Electron Microscopic Observation of AlN/α-Al_2O_3 Heteroepitaxial Interface with Initial Nitriding AlN Layer", *Jpn. J. Appl. Phys.* **34**, L760 (1995).

[65] K. Uehara, Y. Aota, S. Kameda, H. Nakase, and K. Tsubouchi, "Low Propagation Loss of Atomically-Flat Surface AlN with Low Dislocation Density for 5-GHz Band SAW Devices", *Proc. 2005 IEEE Symposium on Ultrasonics*, 455 (2005).

[66] Th. Kehagias, Ph. Komninou, G. Nouet, P. Ruterana, and Th. Karakostas, "Misfit relaxation of the AlN/α-Al_2O_3 (0001) interface", *Phys. Rev. B* **64**, 195329 (2001).

[67] S.J. Rosner, E.C. Carr, M.J. Ludowise, G. Girolami, and H.I. Erikson "Correlation of cathodoluminescence inhomogeneity with microstructural defects in epitaxial GaN grown by metalorganic chemical-vapor deposition ", *Appl. Phys. Lett.* **70**, 420 (1997).

[68] T. Sugahara, H. Sato, M. Hao, Y. Naoi, S. Kurai, S. Tottori, K. Yamashita, K. Nishino, L.T. Romano, and S. Sakai, "Direct Evidence that Dislocations are Non-Radiative Recombination Centers in GaN", *Jpn. J. Appl. Phys.* **37**, L398 (1998).

[69] N.G. Weimann, L.F. Eastman, D. Doppalpudi, H.M. Ng, and T.D. Moustakas, "Scattering of electrons at threading dislocations in GaN", *J. Appl. Phys.* **83**, 3656 (1998).

[70] V. Lebedev, F.M. Morales, H. Romanus, S. Krischok, G. Ecke, V. Cimalla, M. Himmerlick, T. Stauden, D. Cengher, and O. Ambacher, "The role of Si as surfactant and donor in molecular-beam epitaxy of AlN", *J. Appl. Phys.* **98**, 093508 (2005).

[71] A.F. Wright, and J. Furthmüller, "Theoretical investigation of edge dislocations in AlN", *Appl. Phys. Lett.* **72**, 3467 (1998).

[72] X.H. Wu, L.M. Brown, D. Kapolnek, S. Keller, B. Keller, S.P. DenBaars, and S.J. Speck, "Defect structure of metal-organic chemical vapor deposition-grown epitaxial (0001) GaN/Al_2O_3 ", *J. Appl. Phys.* **80**, 3228 (1996).

[73] F.A. Ponce, D. Cherns, W.T. Young, and J.W. Steeds, "Characterization of dislocations in GaN by transmission electron diffraction and microscopy techniques", *Appl. Phys. Lett.* **69**, 770 (1996).

[74] A. Sakai, H. Sunakawa, and A. Usui, "Transmission electron microscopy of defects in GaN films formed by epitaxial lateral overgrowth", *Appl. Phys. Lett.* **73**, 481 (1998).

[75] H. Marchand, X. Wu, J. Ibbetson, P. Fini, P. Kozodoy, S. Keller, J. Speck, S. Denbaars, and U.K. Mishra, "Microstructure of GaN laterally overgrown by metalorganic chemical vapor deposition", *Appl. Phys. Lett.* **73**, 747 (1998).

[76] K. Engl, M. Beer, N. Gmeinwieser, U.T. Schwarz, J. Zweck, W. Wegscheider, S. Miller, A. Miler, H.-J. Lugauer, G. Brüderl, A. Lell and V. Härle, "Influence of an in situ-deposited SiN_x intermediate layer inside GaN and AlGaN layers on SiC substrates", *J. Cryst. Growth* **289**, 6 (2006).

[77] M.J. Kappers, R. Datta, R.A. Oliver, F.D.G. Rayment, M.E. Vickers, and C.J. Humphreys, "Threading dislocation reduction in (0001) GaN thin films using SiN_x interlayers", *J. Cryst. Growth* **300**, 70 (2007).

[78] J. Hertkorn, F. Lipski, P. Brückner, T. Wunderer, S.B. Thapa, F. Scholz, A. Chuvilin, U. Kaiser, M. Beer, and J. Zweck, "Process optimization for the effective reduction of threading dislocations in MOVPE grown GaN using in situ deposited SiN_x masks", *J. Cryst. Growth* **310**, 4867 (2008).

[79] T. Detchprohm, S. Sano, S. Mochizuki, S. Kamiyama, H. Amano, and I. Akasaki, "Growth Mechanism and Characterization of Low-Dislocation-Density AlGaN Single Crystals Grown on Periodically Grooved Substrates", *phys. stat. sol. (c)* **188**, 799 (2001).

[80] J. Mei, F.A. Ponce, R.S. Qhalid Fareed, J.W. Yang, and M. Asif Khan, "Dislocation generation at the coalescence of aluminum nitride lateral epitaxy on shallow-grooved sapphire substrates", *Appl. Phys. Lett.* **90**, 221909 (2007).

[81] M. Imura, K. Nakano, N. Fujimoto, N. Okada, K. Balakrishnan, M. Iwaya, S. Kamiyama, H. Amano, I. Akasaki, T. Noro, T. Takagi, and A. Bandoh "Dislocations in AlN Epilayers Grown on Sapphire Substrate by High-Temperature Metal-Organic Vapor Phase Epitaxy", *Jpn. J. Appl. Phys.* **46**, 1458 (2007).

[82] Z. Liliental-Weber, Y. Chen, S. Ruvimov, and J. Washburn "Formation mechanism of nanotubes in GaN", *Phys. Rev. Lett.* **79**, 2835 (1997).

[83] C.J. Sun, M.Z. Anwar, Q. Chen, J.W. Yang, M.A. Khan, M.S. Shur, A.D. Bykhovski, Z. Liliental-Weber, C. Kisielowski, M. Smith, J.Y. Lin, and H.X. Xiang, "Quantum shift of band-edge stimulated emission in InGaN-GaN multiple quantum well light-emitting diodes", *Appl. Phys. Lett.* **70**, 2978 (1997).

[84] X.H. Wu, C. Elsass, S. Keller, A. Abare, P. Petroff, S.P. DenBaars, and J.S. Speck, "Structural origin of V-defects and correlation with localized excitonic centers in InGaN/GaN multiple quantum wells ", *Appl. Phys. Lett.* **72**, 692 (1998).

[85] C.G. Van de Walle, and J. Neugebauer, "First-principles calculations for defects and impurities: Applications to III-nitrides", *J. Appl. Phys.* **95**, 3851 (2004).

[86] M.A. Reshchikov, and H. Morkoç, "Luminescence properties of defects in GaN", *J. Appl. Phys.* **97**, 061301 (2005).

[87] T. Mattila and R.M. Nieminen, "Point-defect complexes and broadband luminescence in GaN and AlN", *Phys. Rev. B* **55**, 9571 (1997).

[88] A. Fara, F. Bernardini, and V. Fiorentini, "Theoretical evidence for the semi-insulating character of AlN", *J. Appl. Phys.* **85**, 2001 (1999).

[89] C. Stampfl, and C.G. Van de Walle, "Theoretical investigation of native defects, impurities, and complexes in aluminum nitride", *Phys. Rev. B* **65**, 155212 (2002).

[90] T.L. Chu, D.W. Ing, and A.J. Noreika, "Epitaxial growth of aluminum nitride", *Electrochemical Technology* **6**, 56 (1968).

[91] Y. Kumagai, T. Yamane, and A. Koukitu "Growth of thick AlN layers by hydrie vapor-phase epitaxy", *J. Cryst. Growth* **281**, 62 (2005).

[92] V. Soukhoveev, O. Kovalenkev, , V. Ivantsov, A. Syrkin, A. Usikov, V. Maslennikov, and V. Dmitriev "Recent results on AlN growth by HVPE and fabrication of free standing AlN wafers", *phys. stat. sol. (c)* **3**, 1653 (2006).

[93] M. Bickermann, B.M. Epelbaum, M. Kazan, Z. Herro, P. Masri, and A. Winnacker "Growth and characterization of bulk AlN substrates grown by PVT", *phys. stat. sol. (a)* **202**, 531 (2005).

[94] P. Lu, J.H. Edgar, C. Cao, K. Hohn, R. Dalmau, R. Schlesser, and Z. Sitar "Bulk AlN Crystal Growth on SiC Seeds and Defects Study", in Proc. *Mater. Res. Soc. Symp.*, **955**, 0955-I03-07 (2007).

[95] A. Kakanakova-Georgieva, G.K. Gueorguiev, R. Yakimova, and E. Janzén "Effect of impurity incorporation on crystallization in AlN sublimation epitaxy", *J. Appl. Phys.* **96**, 5293 (2004).

[96] F. Tuomisto, J.-M. Maeki, T.Yu. Chemekova, Yu.N. Makarov, O.V. Avdeev, E.N. Mokhov, A.S. Segal, M.G. Ramm, S. Davis, G. Huminic, H. Helava, M. Bickermann, and B.M. Epelbaum "Characterization of bulk AlN crystals with positron annihilation spectroscopy", *J. Cryst. Growth* **310**, 3998 (2008).

[97] M. Bockowski, B. Lucznik, I. Grzegory, S. Krukowski, M. Wroblewski, and S. Porowski "High-pressure direct synthesis of aluminium nitride", *J. Phys.: Cond. Matt.* **14**, 11237 (2002).

[98] H. Isobe, F. Kawamura, M. Kawahara, M. Yashimura, Y. Mori, and T. Sasaki "Synthesis of AlN Grains and Liquid-Phase-Epitaxy (LPE) Growth of AlN Films Using Sn-Ca Mixed Flux", *Jpn. J. Appl. Phys.* **44**, L488 (2005).

[99] R.D. Vispute, H. Wu and J. Narayan "High quality epitaxial aluminum nitride layers on sapphire by pulsed laser deposition", *Appl. Phys. Lett.* **67** (11), 1549 (1995).

[100] A. Basillais, C. Boulmer-Leborgne, J. Mathias, N. Laidani, A. Laurent, and J. Perrière "Influence of the growth conditions on the composition of aluminum nitride films by laser ablation", *Appl. Phys. A* **71**, 619 (2000).

[101] S. Tungasmita, J. Birth, P.O.A. Persson, K. Jarrendahl, and L. Hultman, "Enhanced quality of epitaxial AlN thin films on 6H-SiC by ultra-high vacuum ion-assisted reactive dc magnetron sputter deposition", *Appl. Phys. Lett.* **76**, 170 (2000).

[102] M. Kamp, M. Mayer, A. Pelzmann, A. Theis, H.Y. Chung, H. Sternschulte, O. Marti, and K.J. Ebeling, "NH_3 as Nitrogen Source in MBE Growth of GaN", *Proceedings of Topical Workshop on III-V Nitrides*, Nagoya, Japan, 1995

[103] S. Guha, N.A. Bojarczuk, and D.W. Kisker, "Surface lifetimes of Ga and growth behavior on GaN (0001) surfaces during molecular beam epitaxy", *Appl. Phys. Lett.* **69**, 2879 (1996).

[104] R. Boger, M. Fiederle, L. Kirste, M. Maier, and J. Wagner, "Molecular beam epitaxy and doping of AlN at high growth temperatures", *J. Phys. D: Appl. Phys.* **39**, 4616 (2006).

[105] Z.Y. Fan, G. Rong, N. Newman, and D.J. Smith, "Defect annihilation in AlN thin films by ultrahigh temperature processing", *Appl. Phys. Lett.* **76**, 1839 (2000).

[106] Z.C. Feng, (Editor), *III-Nitride Semiconductor Materials,* Imperial College Press, London, 2006.

[107] S. Yoshida, S. Misawa, Y. Fujii, S. Takada, H. Hayakawa, S. Gonda and A. Itoh, "Reactive molecular beam epitaxy of aluminium nitride", *J. Vac. Sci. Technol.* **16**, 990 (1979).

[108] J.R. Heffelfinger, D.L. Medlin, and K.F. McCarty, "On the initial stage of AlN thin-film growth onto (0001) oriented Al_2O_3 substrates by molecular beam epitaxy", *J. Appl. Phys.* **85**, 466 (1999).

[109] N. Faleev, H. Lu, and W.J. Schaff, "Low density of threading dislocations in AlN grown on sapphire", *J. Appl. Phys.* **101**, 093516 (2007).

[110] X.Q. Shen, Y. Tanizu, T. Ide, and H. Okumura, "Ultra-flat and high-quality AlN thin films on sapphire (0001) substrates grown by rf-MBE", *phys. stat. sol. (c)* **0**, 2511 (2003).

[111] H.M. Manasevit, F.M. Erdmann, and W.I. Simpson, "The use of metalorganics in the preparation of semiconductor materials", *J. Electrochem. Soc.* **118**, 1864 (1971).

[112] J. Bai, T. Wang, P.J. Parbrook, K.B. Lee, and A.G. Cullis, "A study of dislocations in Aln and GaN films grown on sapphire substrates", *J. Cryst. Growth* **282**, 290 (2005).

[113] M. Imura, K. Nakano, N. Fujimoto, N. Okada, K. Balakrishnan, M. Iwaya, S. Kamiyama, H. Amano, I. Akasaki, T. Noro, T. Takagi, and A. Bandoh, "High-Temperature Metal-Organic Vapor Phase Epitaxial Growth of AlN on Sapphire by Multi Transition Growth Mode Method Varying V/III Ratio", *Jpn. J. Appl. Phys.* **45**, 8639 (2006).

[114] Q.S. Paduanoa, D.W. Weyburne, J. Jasinski, and Z. Liliental-Weber, "Effect of initial process conditions on the structural properties of AlN films", *J. Cryst. Growth* **261**, 259 (2004).

[115] R.S.Q. Fareed, J.P. Zhang, R. Gaska, G. Tamulaitis, J. Mickevicius, R. Aleksiejunas, M.S. Shur, and M.A. Khan, "Migration Enhanced MOCVD (MEMOCVD) buffers for increased carrier lifetime in GaN and AlGaN epilayers on sapphire and SiC substrates", *phys. stat. sol. (c)* **2**, 2095 (2005).

[116] Y.A. Xi, K.X. Chen, F. Mont, J.K. Kim, C. Wetzel, E.F. Schubert, W. Liu, X. Li, and J.A. Smart, "Very high quality AlN grown on (0001) sapphire by metal-organic vapor phase epitaxy", *Appl. Phys. Lett.* **89**, 103106 (2006).

[117] H. Yu, D. Caliskan, and E. Ozbay, "Growth of high crystalline quality semi-insulating GaN layers for high electron mobility transistor applications", *J. Appl. Phys.* **100**, 033501 (2006).

[118] V. Srikant, J. Speck, and D. Clarke, "Mosaic structure in epitaxial thin films having large lattice mismatch", *J. Appl. Phys.* **82**, 4286 (1997).

[119] S.R. Lee, A.M. West, A.A. Allerman, K.E. Waldrip, D.M. Follstaedt, P.P. Provencio, D.D. Koleske, and C.R. Abernathy, "Effect of threading dislocations on the Bragg peakwidths of GaN, AlGaN, and AlN heterolayers", *Appl. Phys. Lett.* **86**, 241904 (2005).

[120] T. Metzger, R. Höpler, E. Born, O. Ambacher, M. Stutzmann, R. Stömmer, M. Schuster, H. Göbel, S. Christiansen, M. Albrecht, and H.P. Strunk, "Defect structure of epitaxial GaN films determined by transmission electron microscopy and triple axis X-ray diffractometry", *Philos. Mag. A* **77**, 1013 (1998).

[121] C.G. Dunn, and E.F. Koch, "Comparison of dislocation densities of primary and secondary recrystallization grains of Si-Fe", *Acta Metall.* **5**, 548 (1957).

[122] G.B. Stringfellow, *Orgametallic Vapor-Phase Epitaxy: Theory and Practice*, Academic Press Inc, 2nd Edition, San Diego, 1999.

[123] N.E. Kaluza, *MOVPE Growth and Characterization of $Al_xGa_{1-x}N$/GaN Heterostructures for HEMT Application*, Ph.D. Thesis, RWTH, Aachen, 2003.

[124] C. Kirchner, *Metallorganische Gasphasenepitaxie für optoelektronische und elektronische Bauelemente im Materialsystem AlGaInN*, Ph.D. Thesis, Ulm University, Ulm, 2001.

[125] D.W. Shaw, "Kinetic aspects in the vapour phase epitaxy of III-V compounds", *J. Cryst. Growth* **31**, 130 (1975).

[126] K.S. Pitzer, and H.S. Gutowsky, "Electron Deficient Molecules: II Aluminum Alkyls", *J. Amer. Chem. Soc.* **68**, 2204 (1946).

[127] A.W. Laubengayer, and W.F. Gilliam, "The Alkyls of the Third Group Elements. I. Vapor Phase Studies of the Alkyls of Aluminum, Gallium and Indium", *J. Amer. Chem. Soc.* **63**, 477 (1941).

[128] C.H. Henrickson, and D.P. Eyman, "Lewis acidity of alanes. Interactions of trimethylalane with sulfides", *Inorg. Chem.* **6**, 1461 (1967).

[129] D.W. Squire, C. Dulcey, and M.C. Lin, "Mechanistic studies of the decomposition of trimethylaluminum on heated surfaces", *J. Vac. Sci. Technol.* **B3**, 1513 (1985).

[130] M. Tirtowidjojo, and R. Pollard, "Equilibrium gas phase species for MOCVD of $Al_xGa_{1-x}As$", *J. Cryst. Growth* **77**, 200 (1986).

[131] S. DenBaars, B. Maa, P. Dapkus, A. Danner, and H.C. Lee, "Homogeneous and heterogeneous thermal decomposition rates of trimethylgallium and arsine and their relevance to the growth of GaAs by MOCVD", *J. Cryst. Growth* **77**, 188 (1986).

[132] C. Larsen, N. Buchan, S. Li, and G. Stringfellow, "Decomposition mechanisms of trimethylgallium", *J. Cryst. Growth* **102**, 103 (1990).

[133] S. Oikawa, M. Tsuda, M. Morishita, M. Mashita, and Y. Kuniya, "Elementary process of the thermal decomposition of alkyl gallium", *J. Cryst. Growth* **91**, 471 (1988).

[134] S. Liu, and D. Stevenson, "Growth Kinetics and Catalytic Effects in the Vapor Phase Epitaxy of Gallium Nitride", *J. Electrochem. Soc.* **125**, 1161 (1978).

[135] N. Singh, A. Murell, D. Harrison, and J. Foord, "The adsorption and thermal decomposition of PH_3 and NH_3 on GaAs(100)", *J. Phys.: Condens. Matter* **3**, S167 (1991).

[136] R. Sheknar, and K. Jensen, "Temperature programmed desorption investigations of hydrogen and ammonia reactions on GaN", *Surf. Sci.* **381**, L581 (1997).

[137] F.C. Sauls, L.V. Interrante, and Z. Jiang, "Ammine(trimethyl)aluminum formation and pyrolytic methane loss: thermodynamics, kinetics, and mechanism", *Inorg. Chem.* **29**, 2989 (1990).

[138] B.S. Ault, "Matrix isolation study of the reactions of trimethylaluminum with ammonia", *J. Phys. Chem.* **96**, 7908 (1992).

[139] J. Han, J.J. Figiel, M.H. Crawford, M.A. Banas, M.E. Bartram, R.M. Biefeld, Y.K. Song, and A.V. Nurmikko, "OMVPE growth and gas-phase reactions of AlGaN for UV emitters", *J. Cryst. Growth* **195**, 291 (1998).

[140] T.G. Mihopoulos, V. Gupta, and K.F. Jensen, "A reaction-transport model for AlGaN MOVPE growth", *J. Cryst. Growth* **195**, 733 (1998).

[141] J.R. Creighton, W.G. Breiland, M.E. Coltrin, and R.P. Pawlowski, "Gas-phase nanoparticle formation during AlGaN metalorganic vapor phase epitaxy", *Appl. Phys. Lett.* **81**, 2626 (2002).

[142] J.R. Creighton, G.T. Wang, W.G. Breiland, and M.E. Coltrin, "Nature of the parasitic chemistry during AlGaInN OMVPE", *J. Cryst. Growth* **261**, 204 (2004).

[143] S.C. Choi, J.-H. Kim, J.Y. Choi, K.J. Lee, K.Y. Lim, and G.M. Yang, "Al concentration control of epitaxial AlGaN alloys and interface control of GaN/AlGaN quantum well structures", *J. Appl. Phys.* **87**, 172 (2002).

[144] A.A. Allerman, M.H. Crawford, A.J. Fischer, K.H.A. Bogart, S.R. Lee, D.M. Follstaedt, P.P. Provencio, D.D. Koleske, "Growth and design of deep-UV (240-290 nm) light emitting diodes using AlGaN alloys", *J. Cryst. Growth* **272**, 227 (2004).

[145] S. Keller, G. Parish, P.T. Fini, S. Heikman, C.-H. Chen, N. Zhang, S.P. DenBaars, and U.K. Mishra, "Metalorganic chemical vapor deposition of high mobility AlGaN/GaN heterostructures", *J. Appl. Phys.* **86**, 5850 (1999).

[146] E.V. Yakovlev, R.A. Talalaev, A.N. Vorob'ev, and Yu.N. Makarov,"Critical issues in group-III nitride MOVPE modeling", *Electrochem. Soc. Proc.* **08**, 258 (2003).

[147] A.V. Lobanova, K.M. Mazaev, R.A. Talalaev, M. Leys, S. Boeykens, K. Cheng, and S. Degroote, "Effect of V/III ratio in AlN and AlGaN MOVPE", *J. Cryst. Growth* **287**, 601 (2006).

[148] A.V. Lobanova, E.V. Yakovlev, R.A. Talalaev, S.B. Thapa, and F. Scholz, "Growth conditions and surface morphology of AlN MOVPE", *J. Cryst. Growth* **310**, 4935 (2008).

[149] S.Yu. Karpov, V.G. Prokofyev, E.V. Yakovlev, R.A. Talalaev, Yu.N. Makarov, "Novel approach to simulation of group-III nitride growth by MOVPE", *MRS. Internet J. Nitride Semicond. Res.* **4**, 4 (1999).

[150] E.V. Yakovlev, R.A. Talalaev, N. Kaluza, H. Hardtdegen, and H.L. Bay, "Influence of reactor inlet configuration on the AlGaN growth efficiency", *J. Cryst. Growth* **298**, 413 (2007).

[151] K. Uchida, A. Watanabe, F. Yano, M. Kouguchi, T. Tanaka, and S. Minagawa, "Nitridation process of sapphire substrate surface and its effect on the growth of GaN", *J. Appl. Phys.* **79**, 3487 (1996).

[152] T. Hashimoto, Y. Terakoshi, M. Ishida, M. Yuri, O. Imafuji, T. Sugino, A. Yoshikawa, and K. Itoh, "Effect of V/III ratio in AlN and AlGaN MOVPE", *J. Cryst. Growth* **189**, 254 (1998).

[153] M. Seelamann-Eggebert, H. Zimmermann, H. Obloh, R. Niebuhr, and B. Wachtendorf, "Plasma cleaning and nitridation of sapphire substrates for $Al_xGa_{1-x}N$ epitaxy as studied by X-ray photoelectron diffraction", *J. Vac. Sci. Technol.* **A16**, 2008 (1998).

[154] F. Dwikusuma, and T.F. Kuech, "X-ray photoelectron spectroscopic study on sapphire nitridation for GaN growth by hydride vapor phase epitaxy: Nitridation mechanism", *J. Appl. Phys.* **94**, 5656 (2003).

[155] M. Yeadon, M.T. Marshall, F. Hamdani, S. Pekin, and H. Morkoç, "*In situ* transmission electron microscopy of AlN growth by nitridation of (0001) α-Al_2O_3", *J. Appl. Phys.* **83**, 2847 (1998).

[156] K.S. Kim, S.H. Kim, and D.R. Lee, "Structures of nitridated layers on sapphire studied by X-ray reflectivity and diffraction", *Appl. Phys. Lett.* **76**, 1552 (2000).

[157] Y. Wu, A. Hanlon, J.F. Kaeding, R. Sharma, P.T. Fini, S. Nakamura, and J.S. Speck, "Effect of nitridation on polarity, microstructure, and morphology of AlN films", *Appl. Phys. Lett.* **84**, 912 (2004).

[158] Q. Paduano, and D. Weyburne, "Two-step Process for the Metalorganic Chemical Vapor Deposition Growth of High Quality AlN Films on Sapphire", *Jpn. J. Appl. Phys.* **42**, 1590 (2003).

[159] W. Hu, C. Jiao, H. Wei, P. Zhang, T. Kang, R. Zhang, and X. Liu, "Effect of Nitridation on Morphology, Structural Properties and Stress of AlN Films", *Chin. Phys. Lett.* **25**, 4364 (2008).

[160] S. Nakamura, "GaN Growth Using GaN Buffer Layer", *Jpn. J. Appl. Phys.* **30**, L1705 (1991).

[161] B. Kuhn and F. Scholz, "An Oxygen Doped Nucleation Layer for the Growth of High Optical Quality GaN on Sapphire", *phys. stat. sol. (a)* **188**, 629 (2001).

[162] G. Rosazza, T. Baffie, M. Jeymond, and N. Eustathopoulos, "Contact angles and spreading kinetics of Al and AlCu alloys on sintered AlN", *Mater. Sci. Eng. A* **298**, 34 (2001).

[163] N.Y. Taranets, V.I. Nizhenko, V.V. Poluyanskaya, and Y.V. Naidich, "GeAl and SnAl alloys capillary properties in contact with aluminum nitride", *Acta. Mater.* **50**, 5147 (2001).

[164] J. Bläsing, A. Krost, J. Hertkorn, F. Scholz, L. Kirste, A. Chuvilin, and U. Kaiser, "Oxygen induced strain field homogenization in AlN nucleation layers and its impact on GaN grown by metal organic vapor phase epitaxy on sapphire: An x-ray diffraction study", *J. Appl. Phys.* **105**, 033504 (2009).

[165] J. Hertkorn, *Verbesserung der lateralen Stromführung in hocheffizienten Halbleiterlichtquellen.*, Ph.D. Thesis, Ulm University, Ulm, 2009.

[166] L. Sugiura, K. Itaya, J. Nishio, H. Fujimoto, and Y. Kokubun, "Effects of thermal treatment of low-temperature GaN buffer layers on the quality of subsequent GaN layers", *J. Appl. Phys.* **82**, 4877 (1997).

[167] K. Nakamura, O. Makino, A. Tachibana, and K. Matsumoto, "Quantum chemical study of parasitic reaction in III–V nitride semiconductor crystal growth", *J. Organometallic Chem.* **611**, 514 (2000).

[168] M. Yoshida, H. Watanabe, and F. Uesugi, "Mass Spectrometric Study of $Ga(CH_3)_3$ and $Ga(C_2H_5)_3$ Decomposition Reaction in H_2 and N_2", *J. Electrochem. Soc.* **132**, 677 (1985).

[169] B. Beaumont, P. Gibart, and J.P. Faurie, "Nitrogen precursors in metalorganic vapor phase epitaxy of (Al,Ga)N", *J. Cryst. Growth* **156**, 140 (1995).

[170] N. Kaluza, R. Steins, Y.S. Cho, Z. Sofer, and H. Hardtdegen, "*In-Situ* Monitoring of Parameters Influencing Temperature in MOVPE Nitride Growth ", *11th European Workshop on MOVPE Proc.*, pp. 179, Lausanne, Switzerland, June 5th-8th, (2005).

[171] J.L. Vossen, and W. Kern, *Thin Film Processes II*, Academic Press Inc., San Diego, 1991.

[172] O. Ambacher, "Growth and applications of Group III-nitrides", *J. Phys. D: Appl. Phys.* **31**, 2653 (1998).

[173] R. Steins, H. Hardtdegen, N. Kaluza, M.v.d. Ahe, Y.S. Cho, and Z. Sofer, "Optimisation of GaN high-temperature growth using N_2 as carrier gas", *11th European Workshop on MOVPE Proc.*, pp. 341, Lausanne, Switzerland, June 5th-8th, (2005).

[174] V. Wagner, O. Parillaud, H.J. Bühlmann, M. Illegems, S. Gradecak, P. Stadelmann, T. Riemann, and J. Christen, "Influence of the carrier gas composition on morphology, dislocations, and microscopic luminescence properties of selectively grown GaN by hydride vapor phase epitaxy", *J. Appl. Phys.* **92**, 1307 (2002).

[175] K. Uehara, Y. Aota, S. Kameda, H. Nakase, Y. Isota, and K. Tsubouchi,"Growth of Atomically Flat-Surface Aluminum Nitride Epitaxial Film by Metalorganic Chemical Vapor Deposition", *Jpn. J. Appl. Phys.* **44**, 2987 (2005).

[176] P.M. Dryburgh, "The estimation of minimum growth temperature for crystals grown from the gas phase", *J. Cryst. Growth* **87**, 397 (1988).

[177] A. Koukitu, and Y. Kumagai, "Thermodynamic analysis of group III nitrides grown by metalorganic vapour-phase epitaxy (MOVPE), hydride (or halide) vapour-phase epitaxy (HVPE) and molecular beam epitaxy (MBE)", *J. Phys.: Condens. Matter* **13**, 6907 (2001).

[178] Y. Ohaba, and A. Hatano, "Growth of High-Quality AlN and AlN/GaN/AlN Heterostructure on Sapphire Substrate", *Jpn. J. Appl. Phys.* **35**, L1013 (1996).

[179] S. Vezian, F. Natali, F. Semond, and J. Massies, "From spiral growth to kinetic roughening in molecular-beam epitaxy of GaN(0001)", *Phys. Rev. B* **69**, 125329 (2004).

[180] A. Matsuse, N. Grandjean, B. Damilano, and J. Massies, "Surface morphology of AlN and size dispersion of GaN quantum dots", *J. Cryst. Growth* **274**, 387 (2005).

[181] O. Klein, J. Biskupek, U. Kaiser, K. Forghani, S.B. Thapa, and F. Scholz, "Simulation supported analysis of the effect of SiN_x interlayers in AlGaN on the dislocation density reduction", *Journal of Physics: Conference Series* **209**, 012018 (2010).

[182] T. Hino, S. Tomiya, T. Miyajima, K. Yanashima, S. Hashimoto, and M. Ikeda, "Characterization of threading dislocations in GaN epitaxial layers", *Appl. Phys. Lett.* **76**, 3421 (2000).

[183] G.M. Prinz, *Optische Spektroskopie an Halbleitern mit großer Bandlücke und ZnO-Nanostrukturen*, Ph.D. Thesis, Ulm University, Ulm, 2008.

[184] E. Silveira, J.A. Freitas Jr., M. Kneissl, D.W. Treat, N.M. Johnson, G.A. Slack, and L.J. Schowalter, "Near-bandedge cathodoluminescence of an AlN homoepitaxial film", *Appl. Phys. Lett.* **84**, 3501 (2004).

[185] R.A. Youngman, and J.H. Harris, "Luminescence Studies of Oxygen-Related Defects In Aluminum Nitride", *J. Am. Ceram. Soc.* **73**, 3238 (1990).

[186] M. Strassburg, J. Senawiratne, N. Dietz, U. Haboeck, A. Hoffmann, V. Noveski, R. Schlesser, and Z. Sitar, "The growth and optical properties of large, high-quality AlN single crystals", *J. Appl. Phys.* **96**, 5870 (2004).

[187] I. Gorczyca, N.E. Christensen and A. Svane, "Influence of hydrostatic pressure on cation vacancies in GaN, AlN, and GaAs", *Phys. Rev. B* **66**, 075210 (2002).

[188] B.N. Pantha, R. Dahal, M.L. Nakarmi, N. Nepal, J. Li, J.Y. Lin, H.X. Jiang, Q.S. Paduano, and D. Weyburne, "Correlation between optoelectronic and structural properties and epilayer thickness of AlN", *Appl. Phys. Lett.* **90**, 241101 (2007).

[189] R.A.R. Leute, *Optische Spektroskopie an dotiertem Aluminium-Nitrid*, Diplomarbeit, Institute of Semiconductor Physics, Ulm University, Ulm, 2009.

[190] F. Widmann, B. Daudin, G. Feuillet, N. Pelekanos, and J.L. Rouvière, "Improved quality GaN grown by molecular beam epitaxy using In as a surfactant", *Appl. Phys. Lett.* **73**, 2642 (1998).

[191] S. Keller, S. Heikman, I. Ben-Yaacov, L. Shen, S.P. DenBaars, and U.K. Mishra, "Indium-surfactant-assisted growth of high-mobility AlN/GaN multilayer structures by metalorganic chemical vapor deposition", *Appl. Phys. Lett.* **79**, 3449 (2001).

[192] S. Nicolay, E. Feltin, J.-F. Carlin, M. Mosca, L. Nevou, M. Tchernycheva, F.H. Julien, M. Illegems, and N. Grandjean, "Indium surfactant effect on AlN/GaN heterostructures grown by metal-organic vapor-phase epitaxy: Applications to intersubband transitions", *Appl. Phys. Lett.* **88**, 151902 (2006).

[193] Q. Zhuang, W. Lin, and J. Kang, "Effect of In-Adlayer on AlN (0001) and (000-1) Polar Surfaces", *J. Phys. Chem. C* **113**, 10185 (2009).

[194] J. Neugebauer, T.K. Zywietz, M. Scheffler, J.E. Northrup, H. Chen, and R.M. Feenstra, "Adatom Kinetics On and Below the Surface: The Existence of a New Diffusion Channel", *Phys. Rev. Lett.* **90**, 056101 (2003).

[195] S. Tanaka, M. Takeuchi, and Y. Aoyagi, "Anti-Surfactant in III–Nitride Epitaxy –Quantum Dot Formation and Dislocation Termination–", *Jpn. J. Appl. Phys.* **39**, L831 (2000).

[196] K. Pakula, R. Bozek, J.M. Baranowski, J. Jasinski, and Z. Liliental-Weber, "Reduction of dislocation density in heteroepitaxial GaN: role of SiH_4 treatment", *J. Cryst. Growth* **267**, 1 (2004).

[197] A. Dadgar, M. Poschenriede, A. Reiher, J. Bläsing, J. Christen, A. Krtschil, T. Finger, T. Hempel, A. Diez, and A. Krost, "Reduction of stress at the initial stages of GaN growth on Si(111)", *Appl. Phys. Lett.* **82**, 28 (2003).

[198] K. Forghani, *Investigations on MOVPE growth of AlGaN heterostructures for UV LED applications*, Master Thesis, Institute of Optoelectronics, Ulm University, Ulm, 2008.

[199] B.M. Epelbaum, M. Bickermann, and A. Winnacker, "Approaches to seeded PVT growth of AIN crystals", *J. Cryst. Growth* **275**, e479 (2005).

[200] Yu. N. Makarov, O.V. Avdeev, I.S. Barash, D.S. Bazarevskiy, T.Yu. Chemekova, E.N. Mokhov, S.S. Nagalyuk, A.D. Roenkov, A.S. Segal, Yu.A. Vodakov, M.G. Ramm, S. Davis, G. Huminic, and H. Helava, "Experimental and theoretical analysis of sublimation growth of AlN bulk crystals", *J. Cryst. Growth* **310**, 881 (2008).

[201] M. Bickermann, B.M. Epelbaum, O. Filip, P. Heimann, S. Nagata, and A. Winnacker, "Structural properties of aluminum nitride bulk single crystals grown by PVT", *phys. stat. sol. (c)* **5**, 1502 (2008).

[202] M. Bickermann, B.M. Epelbaum, O. Filip, P. Heimann, S. Nagata, and A. Winnacker, "Point defect content and optical transitions in bulk aluminum nitride crystals", *phys. stat. sol. (b)* **246**, 1181 (2009).

[203] L.B. Rowland, K. Doverspike, and D.K. Gaskill, "Silicon doping of GaN using disilane", *Appl. Phys. Lett.* **66**, 1495 (1995).

[204] W. Götz, N.M. Johnson, C. Chen, H. Liu, C. Kuo, W. Imler, "Activation energies of Si donors in GaN", *Appl. Phys. Lett.* **68**, 3144 (1996).

[205] Y. Taniyasu, M. Kasu, and N. Kobayashi, "Intentional control of n-type conduction for Si-doped AlN and $Al_xGa_{1-x}N$ ($0.42 \leq x \leq 1$)", *Appl. Phys. Lett.* **81**, 1255 (2002).

[206] Y. Taniyasu, M. Kasu, and T. Makimoto, "Increased electron mobility in n–type Si–doped AlN by reducing dislocation density", *Appl. Phys. Lett.* **89**, 182112 (2006).

[207] M. Hermann, F. Furtmayr, A. Bergmaier, G. Dollinger, M. Stutzmann and M. Eickhoff, "Highly Si-doped AlN grown by plasma-assisted molecular-beam epitaxy", *Appl. Phys. Lett.* **86**, 192108 (2005).

[208] D.V. Lang and R.A. Logan, "Large-Lattice-Relaxation Model for Persistent Photoconductivity in Compound Semiconductors", *Phys. Rev. Lett.* **39**, 635 (1977).

[209] D.J. Chadi and K.J. Chang, "Theory of the Atomic and Electronic Structure of *DX* Centers in GaAs and $Al_xGa_{1-x}As$ Alloys", *Phys. Rev. Lett.* **61**, 873 (1988).

[210] P. Bogusławski, and J. Bernholc, "Doping properties of C, Si, and Ge impurities in GaN and AlN", *Phys. Rev. B* **56**, 9496 (1997).

[211] C. Skierbiszewski, T. Suski, M. Leszcynski, M. Shin, M. Skowronski, M.D. Bremser, and R.F. Davis, "Evidence for localized Si-donor state and its metastable properties in AlGaN", *Appl. Phys. Lett.* **74**, 3833 (1999).

[212] A.Y. Polyakov, N.B. Smirnov, A.V. Govorkov, M.G. Milvidskii, J.M. Redwing, M. Shin, M. Skowronski, D.W. Greve, and R.G. Wilson, "Properties of Si donors and persistent photoconductivity in AlGaN", *Solid-State Electron.* **42**, 627 (1998).

[213] M.D. McCluskey, N.M. Johnson, C.G. Van de Walle, D.P. Bour, M. Kneissl, and W. Walukiewicz, "Metastability of Oxygen Donors in AlGaN", *Phys. Rev. Lett.* **80**, 4008 (1998).

[214] R. Zeisel, M.W. Bayerl, S.T.B. Goennenwein, R. Dimitrov, O. Ambacher, M.S. Brandt, and M. Stutzmann, "*DX*-behavior of Si in AlN", *Phys. Rev. B* **61**, R16283 (2000).

[215] B. Borisov, V. Kuryatkov, Yu. Kudryavtsev, R. Asomoza, S. Nikishin, D.Y. Song, M. Holtz, and H. Temkin "Si-doped $Al_xGa_{1-x}N$ ($0.56 \leq x \leq 1$) layers grown by molecular beam epitaxy with ammonia", *Appl. Phys. Lett.* **87**, 132106 (2005).

[216] C. Stampfl, and C.G. Van de Walle, "Doping of $Al_xGa_{1-x}N$", *Appl. Phys. Lett.* **72**, 459 (1998).

[217] C.G. Van de Walle, "*DX*-center formation in wurtzite and zinc-blende $Al_xGa_{1-x}N$", *Phys. Rev. B* **57**, R2033 (1998).

[218] A. Munkholm, C. Thompson, M.V. Ramana Murty, J.A. Eastman, O. Auciello, G.B. Stephenson, P. Fini, S.P. DenBaars, and J.S. Speck,, "Layer-by-layer growth of GaN induced by silicon", *Appl. Phys. Lett.* **77**, 1626 (2000).

[219] M. Hermann, F. Furtmayr, F.M. Morales, O. Ambacher, M. Stutzmann, and M. Eickhoff, "Impact of silicon incorporation on the formation of structural defects in AlN", *J. Appl. Phys.* **100**, 113531 (2006).

[220] P. Cantu, F. Wu, P. Waltereit, S. Keller, A.E. Romanov, U.K. Mishra, S.P. DenBaars, and J.S. Speck, "Si doping effect on strain reduction in compressively strained Al_0.49Ga_0.51N thin films", *Appl. Phys. Lett.* **83**, 674 (2003).

[221] K.B. Nam, M.L. Nakarmi, J. Li, J.Y. Lin, and H.X. Jiang, "Photoluminescence studies of Si-doped AlN epilayers", *Appl. Phys. Lett.* **83**, 2787 (2003).

[222] E. Monroy, J. Zenneck, G. Cherkashinin, O. Ambacher, M. Hermann, M. Stutzmann, and M. Eickhoff, "Luminescence properties of highly Si-doped AlN", *Appl. Phys. Lett.* **88**, 071906 (2006).

[223] J. Pelletier, D. Gervais, and C. Pomot, "Application of wide-gap semiconductors to surface ionization: Work functions of AlN and SiC single crystals", *J. Appl. Phys.* **55**, 994 (1984).

[224] Y.J. Lin, "Nonalloyed Ohmic Formation for p-Type AlGaN with p-Type GaN Capping Layers Using Ohmic Recessed Technique", *Jpn. J. Appl. Phys.* **45**, L86 (2006).

[225] M. Kasu and N. Kobayashi, "Field-emission characteristics and large current density of heavily Si-doped AlN and $Al_xGa_{1-x}N$ ($0.38 \leq x < 1$)", *Appl. Phys. Lett.* **79**, 3642 (2001).

[226] L. Xianming, *The Studies of AlN/AlGaN Heterostructure Grown by MOVPE*, Master Thesis, Institute of Optoelectronics, Ulm University, Ulm, 2007.

[227] M. Placidi, A. Pérez-Tomś, J.C. Moreno, E. Frayssinet, F. Semond, A. Constant, P. Godignon, N. Mestres, A. Crespi, and J. Millán, "Interfacial properties of AlN and oxidized AlN on Si", *Surface Science* **604**, 63 (2010).

[228] T.A. Abtew, M. Zhang, Y. Pan, and D.A. Drabold, "Electrical conductivity and MeyerNeldel rule: The role of localized states in hydrogenated amorphous silicon", *J. Non-Cryst. Solids* **354**, 2909 (2008).

[229] A. Hartstein, and A.B. Fowler, "High temperature 'variable range hopping' conductivity in silicon inversion layers", *J. Phys. C: Solid State Phys.* **8**, L249 (1975).

[230] The Meyer-Neldel Rule, doi:10.4028/www.scientific.net/DDF.192-193.

[231] H. Schmidt, M. Wiebe, B. Dittes, and M. Grundmann, "Meyer-Neldel rule in ZnO", *Appl. Phys. Lett.* **91**, 071906 (2007).

[232] K. Irmscher, T. Schulz, M. Albrecht, C. Hartmann, J. Wollweber, and R. Fornari, "Compensating defects in Si-doped AlN bulk crystals", *Physica B* **401**, 323 (2007).

[233] M. Kasu and N. Kobayashi, "Spontaneous Ridge Formation and Its Effect on Field Emission of Heavily Si-Doped AlN", *phys. stat. sol. (a)* **188**, 779 (2001).

[234] S. Rajan, S.P. DenBaars,U.K. Mishra, H. Xing, and D. Jena, "Electron mobility in graded AlGaN alloys", *Appl. Phys. Lett.* **88**, 042103 (2006).

[235] F.A. Ponce, J.S. Major, Jr., W.E. Plano, and D.F. Welch, "Crystalline structure of AlGaN epitaxy on sapphire using AlN buffer layers", *Appl. Phys. Lett.* **65**, 2302 (1994).

[236] N. Kuwano, T. Tsuruda, Y. Kida, H. Miyake, K. Hiramatsu, and T. Shibata, "TEM analysis of threading dislocations in crack-free $Al_xGa_{1x}N$ grown on an AlN(0001) template", *phys. stat. sol. (a)* **7**, 2444 (2003).

[237] T. Tut, T. Yelboga, E. Ulker, and E. Ozbay,"Solar-blind AlGaN-based *p-i-n* photodetectors with high breakdown voltage and detectivity", *Appl. Phys. Lett.* **92**, 103502 (2008).

[238] N. Okada, N. Fujimoto, T. Kitano, G. Narita, M. Imura, K. Balakrishnan, M. Iwaya, S. Kamiyama, H. Amano, I. Akasaki, K. Shimono, T. Noro, T. Takagi, and A. Bandoh, "Thermodynamic Aspects of Growth of AlGaN by High-Temperature Metal Organic Vapor Phase Epitaxy", *Jpn. J. Appl. Phys.* **45**, 2502 (2006).

[239] G. Coli, K.K. Bajaj, J. Li, J.Y. Lin, and H.X. Jiang, "Excitonic luminescence linewidths in AlGaN alloys with high aluminum concentrations", *Appl. Phys. Lett.* **80**, 2907 (2002).

[240] S.M. Lee, and K.K. Bajaj, "A quantum statistical theory of linewidths of radiative transitions due to compositional disordering in semiconductor alloys", *J. Appl. Phys.* **73**, 1788 (1993).

[241] A.N. Westmeyer, S. Mahajan, and K.K. Bajaj, J.Y. Lin, H.X. Jiang, D.D. Koleske, and R.T. Senger, "Determination of energy-band offsets between GaN and AlN using excitonic luminescence transition in AlGaN alloys", *J. Appl. Phys.* **99**, 013705 (2006).

[242] N. Nepal, J. Li, M.L. Nakarmi, J.Y. Lin, and H.X. Jiang, "Exciton localization in AlGaN alloys", *Appl. Phys. Lett.* **88**, 062103 (2006).

[243] S. Arulkumaran, T. Egawa, S. Matsui, and H. Ishikawa, "Enhancement of breakdown voltage by AlN buffer layer thickness in AlGaN/GaN high-electron-mobility transistors on 4 in. diameter silicon", *Appl. Phys. Lett.* **86**, 123503 (2005).

[244] T. Nanjo, M. Takeuchi, and M. Suita, "Remarkable breakdown voltage enhancement in AlGaN channel high electron mobility transistors", *Appl. Phys. Lett.* **92**, 263502 (2008).

[245] A. Raman, S. Dasgupta, S. Rajan, J.S. Speck, and U.K. Mishra, "AlGaN Channel High Electron Mobility Transistors: Device Performance and Power-Switching Figure of Merit", *Jpn. J. Appl. Phys.* **47**, 3359 (2008).

[246] M. Grundmann, University of California, Santa Barbara. http://my.ece.ucsb.edu/mgrundmann/bandeng.htm.

[247] W. Zhong, R.D. King-Smith, and D. Vanderbilt, "Giant LO-TO splittings in perovskite ferroelectrics", *Phys. Rev. Lett.* **72**, 3618 (1994).

[248] F. Bernardini, and V. Fiorentini, "Spontaneous versus Piezoelectric Polarization in III-V Nitrides: Conceptual Aspects and Practical Consequences", *phys. stat. sol. (b)* **216**, 391 (1999).

[249] M. Gonschorek, J.-F. Carlin, E. Feltin, M.A. Py, and N. Grandjean, "High electron mobility in nearly lattice-matched AlInN/AlN/GaN heterostructure field effect transistors", *Appl. Phys. Lett.* **89**, 062106 (2006).

[250] M. Miyoshi, Y. Kuraoka, M. Tanaka, and T. Egawa, "Metalorganic Chemical Vapor Deposition and Material Characterization of Lattice-Matched InAlN/GaN Two-Dimensional Electron Gas Heterostructures", *Appl. Phys. Express* **1**, 081102 (2008).

[251] Y. Cao, K. Wang, and D. Jena, "Electron transport properties of low sheet-resistance two-dimensional electron gases in ultrathin AlN/GaN heterojunctions grown by MBE", *phys. stat. sol. (c)* **5**, 1873 (2008).

[252] S. Seo, G.Y. Zhao, and D. Pavlidis, "Power characteristics of AlN/GaN MISFETs on sapphire substrate", *Electron. Lett.* **3**, 44 (2008).

[253] S. Seo, K. Ghose, D. Pavlidis, and S. Schmidt"AlN/GaN MISFET for High Frequency Applications: Physical simulation and Experimental Evaluation", *Proc. of the 2nd European Microwave Integrated Circuits Conference*, 219 (2007).

[254] M. Higashiwaki, T. Matsui, and T. Mimura, "AlN/GaN insulated-gate HFETs using Cat-CVD SiN_x", *IEEE Electron Device Lett.* **27**, 719 (2006).

[255] C.J. Collins, A.V. Sampath, G.A. Garrett, G.A. Saeney, H. Shen, M. Wraback, A.Yu. Nikiforov, G.S. Cargill, and V. Dierolf, "Enhanced room-temperature luminescence efficiency through carrier localization in $Al_xGa_{1-x}N$ alloys", *Appl. Phys. Lett.* **86**, 031916 (2005).

[256] B. Monemar, P.P. Paskov, J.P. Bergman, A.A. Toropov, and T.V. Shubina, "Recent developments in the III-nitride materials", *phys. stat. sol. (b)* **244**, 1759 (2007).

[257] R. Dahal, T.M. Al Tahtamouni, Z.Y. Fan, J.Y. Lin, and H.X. Jiang, "Hybrid AlN-SiC deep ultraviolet Schottky barrier photodetectors", *Appl. Phys. Lett.* **90**, 263505 (2007).

[258] T. Saito, T. Hitora, H. Hitora, H. Kawai, I. Saito, and E. Yamaguchi, "UV/VUV photodetectors using group III–nitride semiconductors", *phys. stat. sol. (b)* **6**, S658 (2009).

[259] Da-Bing Li, M. Aoki,T. Katsuno, H. Miyake, K. Hiramatsu, T. Shibata, "Influence of growth interruption and Si doping on the structural and optical properties of $Al_xGa_{1-x}N$/AlN (x > 0.5) multiple quantum wells ", *J. Cryst. Growth* **298**, 500 (2007).

[260] K. Nagamatsu, N. Okada, H. Sugimura, H. Tsuzuki, F. Mori, K. Iidaa, A. Bando, M. Iwaya, S. Kamiyama, H. Amano, I. Akasaki, "High-efficiency AlGaN-based UV light-emitting diode on laterally overgrown AlN", *J. Cryst. Growth* **310**, 2316 (2008).

[261] Y. Inoue, H. Nagasawa, N. Sone, K. Ishino, A. Ishida, H. Fujiyasu, J.J. Kim, H. Makino, T. Yao, S. Sakakibara, and M. Kuwabara, "Fabrication and characterization of short period AlN/GaN quantum cascade laser structures", *J. Cryst. Growth* **265**, 65 (2004).

[262] M. Tchernycheva, L. Nevou, L. Doyennette, F.H. Julien, E. Warde, F. Guillot, E. Monroy, E. Bellet-Amalric, T. Remmele, and M. Albrecht, "Systematic experimental and theoretical investigation of intersubband absorption in GaN/AlN quantum wells", *Phys. Rev. B* **73**, 125347 (2006).

[263] X.Y. Liu, P. Holmström, P. Jänes, L. Thylen, and T.G. Andersson, "Intersubband absorption at 1.5 - 3.5 μm GaN/AlN multiple quantum wells grown by molecular beam epitaxy on sapphire", *phys. stat. sol. (b)* **244**, 2892 (2007).

Curriculum Vitae

Personal Data

Name:	Sarad Bahadur Thapa
Birthdate/birthplace:	10th November 1968/ Kathmandu, Nepal
Nationality:	Nepali
Family:	Married/2 children

Education

1984	School Leaving Certificate (Grade 10), Bhanubhakta Memorial Secondary School, Kathmandu, Nepal
06/1984 – 07/1987	Proficiency Certificate Level (Science), Amrit Science Campus, Kathmandu, Nepal
08/1988 – 10/1993	B.Sc. Engineering (Electrical and Electronics), Bangladesh University of Engineering and Technology, Dhaka, Bangladesh
04/2002 – 01/2005	M.Sc. Communications Technology, Ulm University, Ulm, Germany

Professional Career and Research

04/1994 – 02/2002	Telecom Engineer, Nepal Telecom, Nepal
04/2005 – 01/2009	Research Assistant (Working for Ph.D.), Institute of Optoelectronics, Ulm University, Germany
01/2009 – till the date	Scientific Staff, Institute of Optics, Information, and Photonics, Friedrich-Alexander University of Erlangen- Nuremberg, Erlangen, Germany

Ulm, 15.07.2010